

π^0 - h^\pm Jet Correlations in $d + \text{Au}$ Collisions at $\sqrt{s_{NN}} = 200 \text{ GeV}$

A dissertation presented to
the faculty of
the College of Arts and Sciences of Ohio University

In partial fulfillment
of the requirements for the degree
Doctor of Philosophy

Bing Xia

December 2014

© 2014 Bing Xia. All Rights Reserved.

This dissertation titled
 π^0 - h^\pm Jet Correlations in $d + \text{Au}$ Collisions at $\sqrt{s_{NN}} = 200 \text{ GeV}$

by
BING XIA

has been approved for
the Department of Physics and Astronomy
and the College of Arts and Sciences by

Justin Frantz
Associate Professor of Physics and Astronomy

Robert Frank
Dean, College of Arts and Sciences

ABSTRACT

XIA, BING, Ph.D., December 2014, Physics

π^0 - h^\pm Jet Correlations in $d + \text{Au}$ Collisions at $\sqrt{s_{NN}} = 200$ GeV (232 pp.)

Director of Dissertation: Justin Frantz

Various quark gluon plasma signatures have been experimentally established in Au+Au and Pb+Pb collisions at RHIC and LHC, such as elliptical flow and jet quenching. For decades, the quark gluon plasma was believed not to be created in $p+A$ collisions. However, recent experimental discoveries of collective flow in $p+\text{Pb}$ and $d+\text{Au}$ collisions indicate a hot nuclear medium and a thermal equilibrium in such small systems. An energy loss analysis would be a good alternative measurement for such pictures.

Di-hadron correlation measurements are widely used in jet analysis. In this study, π^0 - h^\pm azimuthal correlations and the per trigger yields in $d+\text{Au}$ collisions at $\sqrt{s_{NN}} = 200$ GeV are measured and compared with $p+p$ collisions at the same energy. In order to cancel out part of the systematic uncertainties and measure the subtle jet modifications, a new quantity RI is proposed and measured from data. In central $d+\text{Au}$ collisions, RI shows a clear suppression in large z_T regions and a delicate enhancement of about 2σ in low z_T regions. Such jet modifications are qualitatively similar, but in a much smaller scale, to the ones observed in central Au+Au collisions, which are attributed to the jet quenching and energy loss in a quark gluon plasma created in central Au+Au collisions.

No theory is available to explain this new experimental phenomenon. To constrain the cold nuclear matter effects, we perform a series of simulations to investigate the possible physics origin of these modifications. Various k_T setting in Pythia and Hijing simulations are not able to reproduce the features observed in data. Also, the gluon jet mixing and nuclear modification of the parton distribution

functions are studied. None of them are sufficient to explain the RI modification observed in central d +Au collisions.

No significant away-side I_{dA} modifications is observed in peripheral d +Au collisions. This result suggests that previous unexpected R_{dA} enhancement in peripheral d +Au collisions from π^0 and jet reconstruction analysis might come from an issue with the determination of N_{coll} scale factor instead of a real enhancement in physics data.

Regardless of the theoretical origin, the data provide constraints that should be able to set concrete limits on the contributions of various cold nuclear or possibly hot QGP-like effects.

To My Parents

ACKNOWLEDGMENTS

I would like to express my gratitude to all the guidance and financial aids from my advisor Justin Frantz.

I want to express my appreciation for Dimitri Kochenov's helps at Brookhaven. And our road trip was a particular fun.

I would like to say thanks to all my office-mates: Anthony Paul Ramirez, Harsha Attanayake, Tyler Danley. We shared all kinds of ideas, knowledge and days with pleasure.

My analysis is based on previous work contributed by Matthew Nguyen, Megan Connors, Jutin Frantz and John Chen. Their analysis notes and codes lead my first step in this area.

Without hundreds of PHENIXers, there won't be such high quality data for this analysis. I do appreciate their hard work, helps and suggestions, especially those from HHJers. I hope my analysis could contribute a little to our collaboration.

I learned a lot from the courses offered by exceptional people in Ohio University. The experience is largely beyond the courses themselves. It comes from the great attitude and character shown by these people. It includes, but is not limited to, Roger Rollins, Louis Wright, David Chelberg, Jundong Liu, David Juedes and Hossein Javadi Asl.

I would like to share the results with all the people mentioned above after gaining so much from them.

TABLE OF CONTENTS

	Page
Abstract	3
Dedication	5
Acknowledgments	6
List of Tables	10
List of Figures	11
1 Introduction	15
1.1 Quantum Chromodynamics	15
1.1.1 Microscopic Picture of World	15
1.1.2 History of QCD	18
1.1.3 Formulation of QCD	22
1.1.4 Calculation of QCD	26
1.2 Quark-Gluon Plasma and Heavy Ion Collisions	30
1.2.1 Elliptic Flow, Hydrodynamics and Equilibrium	33
1.2.2 Jet Quenching and Energy Loss	37
1.3 Cold Nuclear Matter Effect	39
1.3.1 Nuclear Modification of Parton Distribution	40
1.3.2 Cronin Effect	45
1.3.3 Radiative Energy Loss	46
1.3.4 Gluon Saturation	47
1.3.5 k_T Effect	48
1.4 Collective Effect in d +Au Collisions	49
1.5 Statement of Purpose	58
2 Experimental Facilities	60
2.1 RHIC	60
2.2 PHENIX	61
2.2.1 Event Trigger and Characterization	62
2.2.1.1 Beam-Beam Counters	62
2.2.1.2 Zero Degree Calorimeters	64
2.2.1.3 The Centrality Definition	65
2.2.1.4 Triggers	67
2.2.2 Charged Particle Tracking	69
2.2.2.1 Drift Chamber	70
2.2.2.2 Pad Chamber	72

2.2.3	Photon Reconstruction	73
2.2.3.1	Electromagnetic Calorimeter	73
2.2.3.2	Muon Piston Calorimeter	76
2.2.4	Electron Identification	76
3	Data Analysis	78
3.1	PHENIX Data Set	78
3.2	Particle Identification	79
3.2.1	Choice of Particle Types	79
3.2.2	Photon Identification	79
3.2.3	π^0 and η Identification	81
3.2.4	Charged Hadrons Identification	83
3.3	d +Au Centrality Categorization	85
3.4	p_T and Centrality Selection	89
3.5	Event and Particle Selections for Final Results	90
3.6	Two Particle Correlation	91
3.6.1	Notations for Mathematical Framework	94
3.6.2	Acceptance Correction and Event Mixing	95
3.6.3	Two-Source Model and Combinatorial Background	96
3.7	Quality Assurance	100
3.8	Dead and Hot Towers	101
3.9	Combinatorics for Reconstructed π^0	102
3.10	Charged Hadron Efficiency	109
3.10.1	d +Au Collisions	110
3.10.2	p + p Collisions	112
3.11	Rapidity Acceptance Correction	115
3.12	Uncertainties in Measurements	126
4	Results	134
4.1	Correlation Functions and Jet Functions	134
4.2	Jet Widths	148
4.3	Near and Away Side I_{dA}	157
4.4	Double Ratio RI	159
5	Discussions	167
5.1	Introduction to Discussion	167
5.2	New Questions for Small Heavy Ion Collision Systems	168
5.3	Comparison to Peripheral R_{dA} Results	168
5.4	Establishment of Centrality Dependent Nuclear Effect for RI	170
5.5	Interpretation of RI	174
5.6	PYTHIA Studies of the k_T Effect	178
5.7	PYTHIA Study of Quark Gluon Jet Mixing	182
5.8	Nuclear Modification of Parton Distribution Functions	187

5.9 HIJING Simulations	192
5.10 Summary	202
References	206
Appendix A: Acceptance Correction	219
Appendix B: Mean and Variance Estimation in Histograms	225
Index	229

LIST OF TABLES

Table	Page
2.1 LVL2 Trigger Algorithm	70
3.1 Data Set Summary	78
3.2 S/B Ratio and Fitting Coefficients of π^0 Combinatorics	103
3.3 The uncertainty of $R_{\Delta\eta}$ corrections in 0-20% d+Au collisions	125
3.4 Uncertainties and Their Contributions. Here, C means corrected and the systematics is included. Y means the systematics is included. P means the systematics is included and treated carefully because of partial cancelness. 0 means the systematics is cancelled out. We believe that all Type B uncertainties are uncorrelated with each other, so we use the square root of the quadratic sum of all Type B uncertainties as the final over-all Type B uncertainty.	133
4.1 The size of the bleeding effect correction on the awayside in 0-20% d+Au collisions (The unit of p_T is GeV/c)	158

LIST OF FIGURES

Figure	Page
1.1 Elementary Particles in Standard Model	16
1.2 QCD Interaction Vertices in Feynman Diagram	27
1.3 Strong Interaction Running Coupling	29
1.4 Quark-Gluon Plasma Phase Transition Temperature	31
1.5 Elliptical Flow and Reaction Plane	34
1.6 Elliptic Flow and Hydrodynamics Model Prediction	35
1.7 Particle Yields Ratio and Statistical Model Prediction	36
1.8 $\pi^0 R_{AA}$	38
1.9 Jet Quenching in Two Particle Correlations	39
1.10 An example of Parton Distribution Function	42
1.11 Gluon PDF's Uncertainty	43
1.12 Fraction of LO Parton Scattering Process in π^0 Trigger Events	43
1.13 An Illustration of nPDF	44
1.14 Cronin Peak at Different Pseudorapidity	46
1.15 Color Glass Condensate	48
1.16 Ridge Structure in Central p +Pb Collisions	50
1.17 Shoulder Structure in Central Au+Au Collisions	51
1.18 Triangular Fluctuation in Glauber MC Simulation	52
1.19 v_2 of p +Pb from CMS and ATLAS	54
1.20 v_3 of p +Pb and Pb+Pb from CMS	55
1.21 Eccentricity Scaled Anisotropy vs Multiplicity	56
1.22 Mass Ordering in p +Pb Collisions	57
1.23 v_2 Mass Ordering in d +Au Collisions	57
2.1 Experimental Facilities	60
2.2 PHENIX Acceptance	62
2.3 PHENIX Configuration	63
2.4 Beam-Beam Counter	64
2.5 Zero Degree Calorimeter	64
2.6 Illustration of Centrality Class Binning	66
2.7 Centrality Determination in PHENIX	68
2.8 Drift Chamber Construction and Wire Arrangement	72
2.9 Track Reconstruction in Drift Chamber	73
2.10 EMCal	74
2.11 Muon Piston Calorimeter	76
2.12 Ring Imaging Cherenkov Detector	77
3.1 Two Particle Azimuthal Correlation Illustration	92
3.2 Cartoon Plot of Two-Particle Correlation Distribution in Azimuthal Angle	93

3.3	χ^2 Value of DC in All Runs	102
3.4	DC Efficiency in a Bad Run	103
3.5	Acceptance Correction in a Bad Run	104
3.6	EMC Tower Hit Distribution	105
3.7	EMC Tower Dead Hot Map	105
3.8	π^0 Combinatorics	106
3.9	Jet Function of Low Band	107
3.10	Jet Function of High Band	108
3.11	Size of π^0 Combinatorics Correction	109
3.12	MC/Bootstrap Comparison for Run6 p+p Collisions	110
3.13	Charged Hadron Efficiency in 0-20% Centrality d+Au Collisions	112
3.14	Charged Hadron Efficiency in 20-40% Centrality d+Au Collisions	113
3.15	Charged Hadron Efficiency in 40-60% Centrality d+Au Collisions	113
3.16	Charged Hadron Efficiency in 60-88% Centrality d+Au Collisions	114
3.17	Charged Hadron Efficiency Comparison	114
3.18	Charged Hadron Efficiency in $p+p$ Collisions	115
3.19	Function of $\Delta\eta$ Correction	116
3.20	Nearsid Width for 0 - 20% Centrality	117
3.21	Nearsid Width for 20 - 40% Centrality	118
3.22	Nearsid Width for 40 - 60% Centrality	119
3.23	Nearsid Width for 60 - 88% Centrality	120
3.24	Awayside Width for 0 - 20% Centrality	121
3.25	Awayside Width for 20 - 40% Centrality	122
3.26	Awayside Width for 40 - 60% Centrality	123
3.27	Awayside Width for 60 - 88% Centrality	124
3.28	Nearside Rapidity Acceptance Correction for 0 - 20% Centrality	125
3.29	Nearside Rapidity Acceptance Correction for 20 - 40% Centrality	126
3.30	Nearside Rapidity Acceptance Correction for 40 - 60% Centrality	127
3.31	Nearside Rapidity Acceptance Correction for 60 - 88% Centrality	128
4.1	Mixed Background Substitution Check	135
4.2	Jet Function Samples for 0 - 20% Centrality	136
4.3	Correlation Functions for 0 - 5% Centrality	138
4.4	Correlation Functions for 0 - 20% Centrality	139
4.5	Correlation Functions for 20 - 40% Centrality	140
4.6	Correlation Functions for 40 - 60% Centrality	141
4.7	Correlation Functions for 60 - 88% Centrality	142
4.8	Jet Functions for 0 - 5% Centrality	143
4.9	Jet Functions for 0 - 20% Centrality	144
4.10	Jet Functions for 20 - 40% Centrality	145
4.11	Jet Functions for 40 - 60% Centrality	146
4.12	Jet Functions for 60 - 88% Centrality	147
4.13	Nearsid Width for 0 - 20% Centrality	149

4.14	Nearsid Width for 20 - 40% Centrality	150
4.15	Nearsid Width for 40 - 60% Centrality	151
4.16	Nearsid Width for 60 - 88% Centrality	152
4.17	Awayside Width for 0 - 20% Centrality	153
4.18	Awayside Width for 20 - 40% Centrality	154
4.19	Awayside Width for 40 - 60% Centrality	155
4.20	Awayside Width for 60 - 88% Centrality	156
4.21	Nearsid I_{dA-z_T} Plot in $d+Au$ with 0 - 20% Centrality	159
4.22	Nearsid I_{dA-z_T} Plot in $d+Au$ with 20 - 40% Centrality	160
4.23	Nearsid I_{dA-z_T} Plot in $d+Au$ with 40 - 60% Centrality	161
4.24	Nearsid I_{dA-z_T} Plot in $d+Au$ with 60 - 88% Centrality	162
4.25	Awayside I_{dA-z_T} Plot in $d+Au$ with 0 - 20% Centrality	162
4.26	Awayside I_{dA-z_T} Plot in $d+Au$ with 20 - 40% Centrality	163
4.27	Awayside I_{dA-z_T} Plot in $d+Au$ with 40 - 60% Centrality	163
4.28	Awayside I_{dA-z_T} Plot in $d+Au$ with 60 - 88% Centrality	164
4.29	RI vs z_T Plot in $d+Au$ with 0 - 20% Centrality	164
4.30	RI vs z_T Plot in $d+Au$ with 20 - 40% Centrality	165
4.31	RI vs z_T Plot in $d+Au$ with 40 - 60% Centrality	165
4.32	RI vs z_T Plot in $d+Au$ with 60 - 88% Centrality	166
5.1	Away-side I_{dA} in Peripheral $d+Au$ Collisions from Isolated $\gamma-h^\pm$ Analysis	167
5.2	R_{dA} Anomaly	170
5.3	Away-side I_{dA} In Peripheral $d+Au$ Collisions	171
5.4	Centrality Dependence of Slope of RI vs z_T	172
5.5	Centrality Dependence of RI values in Low and High z_T Regions	173
5.6	Ratio of RI values in Low and High z_T Regions	174
5.7	Correlation Functions in Central Au+Au Collisions	175
5.8	Away Side I_{AA} Plot in Central Au+Au Collisions	176
5.9	ATLAS Jet Measurement in Pb+Pb Collisions	177
5.10	RI Comparison with Au+Au	178
5.11	k_T Effect in p+p and d+Au Collision Measured by STAR	180
5.12	k_T Effect On RI	181
5.13	Probability Distributions for Hard Scattering Subprocesses in π^0 Triggered Events	183
5.14	RI in Class A and Class B Events	184
5.15	RI Modifications in 100% $q \rightarrow g$ Conversions	186
5.16	RI Modifications in 100% $q \leftrightarrow g$ Conversions	187
5.17	nPDF Effect On Jet Functions	188
5.18	nPDF Effect On RI	189
5.19	x vs Q^2 of Triggered Events in PYTHIA	190
5.20	nPDF when $6 \leq Q \leq 7$ GeV/ c	191
5.21	Overview of CTEQ6M PDF Sets	191
5.22	Overview of NNLO MSTW2008 PDF Sets	192

5.23	Sea u d nPDF Effect On RI	193
5.24	Valence u Quark Distribution in EPS09s nPDF	194
5.25	EPS09s Effect On RI	195
5.26	HIJING Particle η Distributions	196
5.27	PHOBOS Charged Hadrons	197
5.28	RI from HIJING with $k_T = 0.44$ GeV/ c	198
5.29	Width Comparison Between HIJING and PYTHIA	199
5.30	RI from HIJING $k_T = 2.0$ GeV/ c and PYTHIA $k_T = 2.8$ GeV/ c	199
5.31	Jet Functions from HIJING $k_T = 2.0$ GeV/ c and PYTHIA $k_T = 2.8$ GeV/ c	200
5.32	Jet Width in HIJING	201
5.33	Statistical Precision of CMS p +Pb Measurement	205

1 INTRODUCTION

1.1 Quantum Chromodynamics

1.1.1 Microscopic Picture of World. The *Standard Model* (SM) is a collection of theories, which incorporate special relativity (Lorentz invariance) and gauge theory (gauge invariance), describing the electromagnetic, weak and strong interactions in particle physics. Though gravity is not included in the Standard Model, the gravitational interaction is insignificant at the subatomic scale, even compared with the weak interaction. The Standard Model is the most successful model to describe the underlying principles of fundamental particles. One major goal of science is to understand matter. What is the matter (nature)? Where does it come from (origin)? Besides the little known dark matter and dark energy,¹ the building blocks of the matter are the *elementary particles*. According to the Standard Model, the known elementary particles can be categorized as the *quarks*, *leptons* (including *neutrinos*), *gauge bosons* and the *Higgs boson(s)*, see Figure 1.1. The graviton is postulated as a massless, spin-2 boson, which mediates the gravitational force. However, the quantum field theory that includes the gravity is not renormalizable, and the graviton has never been experimentally observed. The unification of all the four interactions remains to a theory beyond the current Standard Model, maybe even beyond the quantum field theory.

There are three generations of quarks, leptons and neutrinos. In principle, there could be a fourth generation of neutrinos, for example, the sterile neutrinos,

¹ The existence of dark matter is indicated by extra gravitational effects, besides the known baryon matter, in astronomical observations, such as the gravitational lens, the motion of galaxies. The nature of the dark matter might be a weakly interacting massive particle (WIMP), or some other non-baryon particles. Dark energy is a pure hypothetical descriptive concept to “explain”, or say to name, the observed accelerating expansion of the universe, which is more than the current estimation based on the known gravitational matter including the dark matter.

² http://en.wikipedia.org/wiki/Standard_Model

mass →	$\approx 2.3 \text{ MeV}/c^2$	$\approx 1.275 \text{ GeV}/c^2$	$\approx 173.07 \text{ GeV}/c^2$	0	$\approx 126 \text{ GeV}/c^2$
charge →	$2/3$	$2/3$	$2/3$	0	0
spin →	$1/2$	$1/2$	$1/2$	1	0
	u up	c charm	t top	g gluon	H Higgs boson
QUARKS					
	$\approx 4.8 \text{ MeV}/c^2$	$\approx 95 \text{ MeV}/c^2$	$\approx 4.18 \text{ GeV}/c^2$	0	
	$-1/3$	$-1/3$	$-1/3$	0	
	$1/2$	$1/2$	$1/2$	1	
	d down	s strange	b bottom	γ photon	
	$0.511 \text{ MeV}/c^2$	$105.7 \text{ MeV}/c^2$	$1.777 \text{ GeV}/c^2$	$91.2 \text{ GeV}/c^2$	
	-1	-1	-1	0	
	$1/2$	$1/2$	$1/2$	1	
	e electron	μ muon	τ tau	Z Z boson	
LEPTONS					
	$< 2.2 \text{ eV}/c^2$	$< 0.17 \text{ MeV}/c^2$	$< 15.5 \text{ MeV}/c^2$	$80.4 \text{ GeV}/c^2$	
	0	0	0	± 1	
	$1/2$	$1/2$	$1/2$	1	
	ν_e electron neutrino	ν_μ muon neutrino	ν_τ tau neutrino	W W boson	
					GAUGE BOSONS

Figure 1.1: A table of the elementary particles in the Standard Model²

which do not interact with known particles via the electroweak interaction (or strong interaction, of course). It is one candidate for dark matter. Until today, this type of neutrinos remains hypothetical.

The gauge bosons are the force carriers in the Standard Model. The photon is the intermediate gauge boson of the electromagnetic interaction, and W^\pm and Z^0 are the ones for the weak interaction. The gluons are the strong interaction's force carriers. The Higgs boson(s) is predicted by the Higgs mechanism[1][2][3] in 1964, and during the time of the research of this thesis, CMS (Compact Muon Solenoid, an experiment collaboration at LHC) and ATLAS (A Toroidal LHC Apparatus, an

experiment collaboration at LHC) have published the first papers [4][5] about the discovery of a neutral boson with mass around 125 GeV, which is compatible with the Standard Model Higgs boson(s), and thus completes the discovery of all particles in the Standard Model.

In the Standard Model, the particle view of the world is embodied by *quantum field theory* (QFT). The quantum field theory is a theory to describe particles as excited states, through second quantization, of fields defined on the space-time point. The Standard Model is a $SU(3) \otimes SU(2)_L \otimes U(1)_Y$ gauge theory, and the gauge theories are proven to be renormalizable by 't Hooft and Veltman in the early seventies [6](massless) [7](massive) [8](complete proof).

The field theory *quantum chromodynamics* (QCD), as part of the Standard Model, is a quantum field theory describing the strong interaction between the particles that are color charged. QCD is a $SU(3)$ gauge theory, which means that the color $SU(3)$ local gauge symmetry generates the dynamics for the strong interaction. The $SU(3)$ symmetry in QCD is a non-Abelian symmetry, different than the $U(1)$ symmetry in quantum electrodynamic (QED), though the Lagrangians are similar. Therefore, there are some extra rich features only in QCD, which are not present in QED. We will discuss them in Section 1.1.3 and 1.1.4. In the Standard Model, all the fundamental interactions are generated by some local gauge symmetry. The strong interaction is described by $SU(3)_C$ color gauge symmetry. The electroweak interaction is described by a $SU(2)_L \otimes U(1)_Y$ gauge theory. The gauge boson fields are generated as $W_\mu^1, W_\mu^2, W_\mu^3$ and B_μ . After a local gauge symmetry breaking (referred as the *spontaneous symmetry breaking*), the boson fields mix to $W^\pm \equiv (W^1 \mp iW^2)/\sqrt{2}$ and $Z \equiv -B \sin \theta_W + W^3 \cos \theta_W$, and the W^\pm, Z , the Higgs fields acquire masses (the *Higgs mechanism*). The fermion fields

can interact with the Higgs fields via the Yukawa coupling, which gives mass to the leptons and quarks.

This is our current understanding of the particle world in a theoretical way called the Standard Model. There are quite a lot parameters needed from the experiments, and there are things it can't explain. Nevertheless, this is a triumph in physics history.

1.1.2 History of QCD. Initially, the strong interaction is termed as the force that binds nucleons together inside of nuclei. Yukawa proposed that such a strong nuclear force is carried by an intermediate boson [9]. The Yukawa theory of the interaction between fermions (ψ) and bosons (ϕ) can be expressed by the Lagrangian density

$$\mathcal{L} = \mathcal{L}_{\text{Dirac}} + \mathcal{L}_{\text{Klein-Gorden}} + g\bar{\psi}\psi\phi. \quad (1.1)$$

Then the potential can be calculate as [10]

$$V(r) = -\frac{g^2}{4\pi} \frac{1}{r} e^{-m_\phi r} \quad (1.2)$$

with range about $1/m_\phi = \hbar/m_\phi c$. From the experimental measurement of the size of the nucleons, Yukawa predicted the mass of the exchanged boson to be around 100 MeV, which turns out to be the pion. However, this effective interpretation has a serious flaw, which treats the nucleons as elementary particles. A more fundamental strong interaction theory had yet to be established, waiting for the arrival of the quark model, color hypothesis and Yang-Mills gauge theory.

The first step of the quark model started with the *isospin* (isotopic spin or isobaric spin) proposed by Heisenberg [11] based on the almost identical mass of the proton and neutron. The isospin is an abstract space spanned by the proton and neutron, which is essentially the SU(2) flavor symmetry of up and down quarks (or say, isospin rotation invariance in the strong interaction from Noether's theorem).

This symmetry is an close-to-exact symmetry in the sense of the smallness of u and d quark's "bare" mass and small electromagnetic correction [12].

However, with the invention of new detectors, such as the bubble chamber, and the operation of new particle accelerators, the boom of "elementary" particles came. The particle family got crowded and messy. This could be reflected by Lamb's Noble Prize speech in 1955 that "*I have heard it said that the finder of a new elementary particle used to be rewarded by a Nobel Prize, but such a discovery now ought to be punished by a \$10,000 fine*". The chaotic state ended with the so called "eightfold way" proposed by Gell-Mann [13], which is the periodic table of elementary particles. Every baryon or meson could find its own spot in a octet, nonet, decuplet or singlet. By the time, Ω^- was not yet discovered. Gell-Mann predicted such a particle with $J = \frac{3}{2}$, $Q = -1$, $S = -3$ and mass around 1680 MeV, and it was discovered at Brookhaven National Laboratory (BNL) [14]. The eight fold way was put on the firm ground. To explain this particular pattern observed in elementary particles, Gell-Mann [15] and Zweig [16][17] independently proposed the *quark model* that mesons and baryons are composed of even more fundamental fermions with fractional charges. Later, the *deep inelastic scattering* (DIS) data supported the proposed composite structure of nucleons, though the physics community had not yet accepted the quark model completely since free quarks have never been observed experimentally. This phenomena is called quark confinement, and that's why Feynman used partons to describe the constitutes of hadrons. The approximate SU(3) symmetry in the quark model is from the flavor symmetry between u , d and s quarks in the strong interaction . The mesons are composed of a quark and an anti-quark, or say, $\mathbf{3} \otimes \bar{\mathbf{3}} = \mathbf{8} \oplus \mathbf{1}$ in SU(3) representations. Though the octet and singlet states might mix with each other, such as ϕ , ω . This is called ϕ - ω mixing, and the mixing angle $\sin \theta = 0.76$, close to ideal mixing $\sqrt{2/3}$, where ω is

$(u\bar{u} + d\bar{d})/\sqrt{2}$ and ϕ is $s\bar{s}$, see [18]. The baryons are composed of three quarks, or say, $\mathbf{3} \otimes \mathbf{3} \otimes \mathbf{3} = (\mathbf{6} \otimes \mathbf{3}) \oplus (\bar{\mathbf{3}} \otimes \mathbf{3}) = \mathbf{10} \oplus \mathbf{8} \oplus \mathbf{8} \oplus \mathbf{1}$. The decuplet is completely symmetric in flavor, the singlet is completely antisymmetric, and the two octets are partial symmetric [12]. However, such symmetry consideration has a problem in some ground states. For example, Δ^{++} with $J_3 = \frac{3}{2}$ and $L = 0$, its wave function should be $u(\uparrow)u(\uparrow)u(\uparrow)$, which is symmetric. Based on the Pauli exclusive principle, the fermion's wave function should be antisymmetric. Therefore, there should be some hidden quantum number(s).³ This was noticed and argued by Greenberg [19]. Later, Han and Nambu proposed another SU(3) symmetry besides the normal flavor symmetry [20]. Then the singlet state of the new SU(3) symmetry is antisymmetric, and the newly introduced quantum number saved the quark model. The new SU(3) gauge symmetry comes from a new degree of freedom, *color*. Also, the number of colors could be obtained by experimental data of R , see [12] [21].

$$R \equiv \frac{e^+ + e^- \rightarrow \text{hadrons}}{e^+ + e^- \rightarrow \mu^+ + \mu^-} \quad (1.3)$$

R is about 4 at energies about 10 - 40 GeV. The theoretical calculation considering all the quark antiquark pair contributions (except the top quark, since its mass is about 180 GeV/ c^2 , too heavy) is $(\frac{2}{3})^2 + (\frac{1}{3})^2 + (\frac{2}{3})^2 + (\frac{1}{3})^2 + (\frac{2}{3})^2 = \frac{11}{9}$. There is a factor difference about 3, which comes from the degree of freedom of color. Other evidence comes from pion decays ($\pi^0 \rightarrow \gamma + \gamma$). The decay rate is

$$\Gamma(\pi^0 \rightarrow \gamma + \gamma) = N_C^2 (Q_u^2 - Q_d^2)^2 \frac{\alpha^2 m_{\pi^0}^3}{64\pi^3 F_\pi^2} = 0.84 N_C^2 \text{ (eV)}. \quad (1.4)$$

Here $\alpha = \frac{e^2}{4\pi}$ is the *fine structure constant*, F_π is pion decay constant, taken as 91 MeV. The experiment value for the decay rate is 7.84 eV, then $N_C = 3$ [18] [22].

³ Also, there are some other difficulties in the quark model. First, the mysterious quark confinement. Second, there is no compelling reason in the quark model to support the fact that there is no $qqq\bar{q}$ or $qqq\bar{q}$ states in nature

Despite the reluctance of the physics community to undoubtedly accept the quark model, it was convincingly secured by the Bjorken scaling in deep inelastic electron-proton scattering [23]. Firstly, in the elastic electron-proton scatterings ($e + p \rightarrow e + p$), the electric and magnetic *form factors* $G_E(q^2)$ and $G_M(q^2)$ (linear combinations of $F_{1,2}(q^2)$, related to the proton's charge and magnetic distributions) could be determined by $\frac{d\sigma}{d\Omega}(\theta, \phi)$ data and fitted, up to 10 GeV, as a “dipole” function of $(\frac{1}{1-q^2/0.71})^{-2}$. This is consistent with an exponential distribution in radius space and deviated from a point-like structure. Furthermore, in the inelastic electron-proton scatterings ($e + p \rightarrow e + X$), the *Bjorken scaling* is observed, which is a phenomena that in the large Q^2 ($Q^2 \triangleq -q^2 > 0$) transfer scatterings the form factor $W_1(\nu, Q^2)$ and $W_2(\nu, Q^2)$ depend on x only ($x \triangleq \frac{Q^2}{2m\nu} = -\frac{q^2}{2p \cdot q}$ and $\nu = E - E'$), or say, $MW_1(\nu, Q^2) \rightarrow F_1(\omega)$ and $\nu W_2(\nu, Q^2) \rightarrow F_2(\omega)$, where $\omega = \frac{2q \cdot p}{Q^2} = \frac{2M\nu}{Q^2}$. This is consistent with the picture that the virtual photon scatters with a free point-like charged parton and the parton takes a fraction of the longitudinal momentum / energy of the proton (and this fraction turns out to be the *Bjorken scaling variable* x). The *Callan-Gross relation* ($2xF_1 = F_2$) shows that the parton has spin $\frac{1}{2}$. This is compelling evidence for the quark model. Besides that, the structure function shows the existence of sea quarks and some kind of partons which interact neither electromagnetically nor weakly - the gluons. And the gluons' total momentum is almost half (46%) of the proton's momentum. Later on, jets were observed in high energy collisions. A *jet* is essentially a bunch of hadrons fragmented from an outgoing parton during a hard scattering. This is another supporting evidence for the existence of gluons and quarks, despite that they are always confined inside of hadrons.

Back to the age of nuclear strong interaction, there was a major development in theory, *Yang-Mills theory* [24]⁴. It is a non-Abelian gauge theory on the isospin space. The local gauge symmetry was introduced by Weyl [25], however it's not on SU(2) space and it is Abelian. Yang-Mills theory is carried out with the SU(2) Lie group, the non-Abelian nature brings the feature-rich Lie algebra to generate the dynamics. As we know, the strong interaction is resulted from the SU(3) color symmetry, not the SU(2) isospin symmetry. The application of Yang-Mills theory to the strong interaction was carried out after the discoveries of the quark model and the color concept. The dawn of the quantum chromodynamics came finally. After that, the theories about the strong interaction converged to Yang-Mills idea, which is the only one to satisfy the renormalizability conditions [26], and formed the current quantum chromodynamics.

1.1.3 Formulation of QCD. This section is not meant to be a complete derivation, just a outline. The content could be easily obtained from [12] [23] [18].

Let's start from the Lagrangian density for a free quark field (with some quark flavor)

$$\mathcal{L}_{\text{quark}} = \sum_{j=1}^3 \bar{\psi}_j (i\gamma^\mu \partial_\mu - m) \psi_j \quad (1.5)$$

where j denotes three color charges: r , g and b , and the four vector index summation is omitted according to the Einstein summation convention. If we abbreviate the color summation into one convenient notion ψ

$$\psi \triangleq \begin{pmatrix} \psi_r \\ \psi_g \\ \psi_b \end{pmatrix} \quad (1.6)$$

⁴ Here, Yang-Mills theory is specific term for the one proposed by Yang and Mills in 1950's, not a general term for the gauge theories based on their idea.

and

$$\bar{\psi} = \begin{pmatrix} \bar{\psi}_r & \bar{\psi}_g & \bar{\psi}_b \end{pmatrix} \quad (1.7)$$

Then we introduce a local (space-time dependent) gauge transformation, a rotation in the color space, and require gauge invariance. The reason we do this is because the flavor invariance is a global one, as we know the global symmetry won't generate any dynamics. The operator has to be unitary in the first place. It acts on the color space, and doesn't touch the space-time part, such as γ^μ .

$$\psi \rightarrow U\psi \quad \text{and} \quad \bar{\psi} \rightarrow \bar{\psi}U^\dagger \quad (1.8)$$

and

$$U^\dagger U = 1 \quad (\text{Unitary}). \quad (1.9)$$

For the unitary matrix, it could be represent by a Hermitian matrix in the form

$$U = e^{iH} \quad \text{with} \quad H^\dagger = H \quad (1.10)$$

For a 3×3 Hermitian matrix, we can decompose it into 9 linear independent matrices,

$$H = \theta I + \mathbf{a} \cdot \mathbf{T}. \quad (1.11)$$

We may choose the Gell-Mann matrix $\lambda_1, \dots, \lambda_8$ for \mathbf{T} . Anyway, this form is general. T_a with $a = 1, \dots, 8$ are a set of linear independent traceless 3×3 matrices. The $e^{\mathbf{a} \cdot \mathbf{T}}$ part belongs to SU(3) Lie group (if we add the phase part, it would be U(3) group). And we will get an additional gluon field, which is a color singlet. We will see the gluon field is massless. Then the hadrons, which are color neutral, can exchange a colorless gluon. Due to its zero mass, it carries a long range strong force. This contradicts the experimental fact. So we rule out the U(3) symmetry by the experiment observations. To demand the SU(3) local ($\mathbf{a} = \mathbf{a}(x)$) gauge invariance

requirement, we consider an infinitesimal transformation ($|\mathbf{a}| \rightarrow 0$)

$$\psi(x) \rightarrow (1 + ia_a T_a) \psi(x). \quad (1.12)$$

And get the SU(3) generators T_a 's, which follow the non-Abelian Lie bracket relations,

$$[T_a, T_b] = if_{abc} T_c \quad (1.13)$$

where f_{abc} is the structure constant in the SU(3) Lie group. In the infinitesimal local gauge transformation, we see that the derivatives behave like

$$\partial_\mu \psi \rightarrow (1 + ia_a T_a) \partial_\mu \psi + iT_a \psi \partial_\mu a_a. \quad (1.14)$$

The additional term here violate the gauge invariance of the Lagrangian density \mathcal{L}_0 , so we apply the trick we've learned in QED by using the *gauge covariant derivative*

$$D_\mu = \partial_\mu - igT_a A_\mu^a \quad (1.15)$$

and introduce eight new vector boson fields A_μ^a (we call them the *gluon fields* in QCD, or *gauge fields* in the gauge theory) to absorb the additional term. The transformation of \mathbf{A}_μ is

$$A_\mu^a \rightarrow A_\mu^a + \frac{1}{g} \partial_\mu a_a \quad (1.16)$$

where g is the coupling constant, we shall find this later. However, the desired relation is not simply valid as we expect here,

$$D_\mu \psi \not\rightarrow e^{i\mathbf{a}\mathbf{T}} D_\mu \psi. \quad (1.17)$$

This is because the non-Abelian nature of SU(3) group, see Equation 1.13. The second term of D_μ won't easily go away when commuting with the gauge transform

operator,

$$\gamma^\mu T_a \psi \rightarrow \gamma^\mu T_a (1 + i a_b T_b) \psi \quad (1.18)$$

$$= (1 + a_b T_b) \gamma^\mu T_a \psi + i a_b \gamma^\mu (T_a T_b - T_b T_a) \psi \quad (1.19)$$

$$= (1 + a_b T_b) \gamma^\mu T_a \psi - a_b \gamma^\mu f_{abc} T_c \psi \quad (1.20)$$

$$\neq (1 + a_b T_b) \gamma^\mu T_a \psi. \quad (1.21)$$

The easiest solution to this is to rewrite Equation 1.16

$$A_\mu^a \rightarrow A_\mu^a + \frac{1}{g} \partial_\mu a_a - f_{abc} a_b A_\mu^c. \quad (1.22)$$

Also, we need to take in the free gluon Lagrangian density part

$$\mathcal{L}_{\text{gluon}} = -\frac{1}{4} F^{\mu\nu} F_{\mu\nu} \quad \text{with} \quad (1.23)$$

$$F_{\mu\nu} = \partial_\mu A_\nu - \partial_\nu A_\mu. \quad (1.24)$$

Due to the additional term in in Equation 1.22, the invariance doesn't hold any more. So we rewrite the gluon field strength tensor $F_{\mu\nu}$ as

$$F_{\mu\nu}^a = \partial_\mu A_\nu^a - \partial_\nu A_\mu^a + g f_{abc} A_\mu^b A_\nu^c \quad (1.25)$$

$$= -\frac{1}{g} [D_\mu, D_\nu]. \quad (1.26)$$

Then we get the Lagrangian density of QCD

$$\mathcal{L}_{\text{QCD}} = \sum_{f,i,j} \bar{\psi}_{f,i} (i \gamma^\mu D_\mu - m_q) \psi_{f,j} - \frac{1}{4} \sum_a F_{\mu\nu}^a F_a^{\mu\nu}. \quad (1.27)$$

Here, the color indices i, j run from 1 to $N_C = 3$. N_C means 3 types of color charges (r, g, b colors). The flavor index f runs from 1 to $N_f = 6$. N_f means 6 types of quark flavors (u, d, c, s, t, b quarks). The indices a, b, c run from 1 to $N_C^2 - 1 = 8$. They reflect 8 types of gluons, corresponding to the dimensionality of SU(3) gauge group. The $\psi_{f,i}$ is the spin- $\frac{1}{2}$ quark scalar field with flavor f and color i . The m_f is

the quark mass of flavor f . D_μ and $F_{\mu\nu}^a$ are defined in Equation 1.15, 1.25. A_μ^a are the spin-1 gluon vector fields.

Now we see g is g_s , the QCD *coupling constant*, with

$$\alpha_s = \frac{g_s^2}{4\pi}. \quad (1.28)$$

Also, we may group \mathcal{L}_{QCD} into two parts.

$$\mathcal{L}_{\text{QCD}} = \mathcal{L}_0 + \mathcal{L}_{\text{int}} \quad (1.29)$$

$$\begin{aligned} \mathcal{L}_0 = & \sum_{f,i,j} \bar{\psi}_{f,i} (i\gamma^\mu \partial_\mu - m_q)_{ij} \psi_{f,j} \\ & - \frac{1}{4} \sum_a [(\partial_\mu A_\nu^a)(\partial^\mu A_a^\nu) - (\partial^\mu A_a^\nu)(\partial_\mu A_\nu^a)] \end{aligned} \quad (1.30)$$

$$\begin{aligned} \mathcal{L}_{\text{int}} = & \sum_{f,i,j} g_s A_\mu^a \bar{\psi}_{f,i} \gamma^\mu T_a \psi_{f,j} - g_s f_{abc} A_b^\mu A_c^\nu (\partial_\mu A_\nu^a) \\ & - \frac{1}{4} g_s^2 (f_{abc} A_b^\mu A_c^\nu) (f_{ade} A_\mu^d A_\nu^e) \end{aligned} \quad (1.31)$$

The two terms in \mathcal{L}_0 are the propagator of the free quark and gluon respectively.

The first term $gA\bar{\psi}\psi$ in \mathcal{L}_{int} is a coupling similar in QED ($e\bar{\psi}\gamma^\mu\psi A_\mu$), which represents a $gq\bar{q}$ interaction. The later two terms AAA , $AAAA$ in \mathcal{L}_{int} are novel, they represent ggg and $gggg$ coupling. The Feynman vertices are shown in Figure 1.2. This QCD unique feature comes from the non-Abelian nature of SU(3) symmetry. The self coupling of gluons make the strong interaction much different than QED. The color screen effect behaves much differently in non-Abelian QCD and leads to the running coupling and asymptotic freedom.

1.1.4 Calculation of QCD. Initially, the QCD coupling constant value was experimentally measured to be greater than 1. This fact causes a failure of the perturbation calculation method by the Feynmann diagram expansion. The Bjorken scaling, mentioned in Section 1.1.2, needs a negative β -function. Or say, the β -function for the strong interaction needs to be ultraviolet asymptotically free.

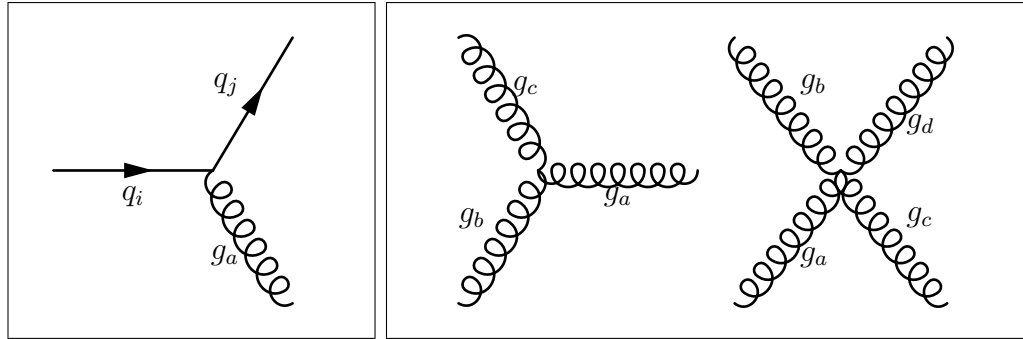


Figure 1.2: QCD interaction vertices in Feynman diagram. The one on the left is similar to QED coupling, the other two self-coupling between gluons are from the non-Abelian nature of QCD, which make QCD much richer.

The *asymptotic freedom* means that the QCD interaction constant is small at a high energy scale or at small length scales. This feature makes perturbative QCD possible at high energies, and makes color charge “anti-screened” at large length scales, therefore gives the Bjorken scaling (close to free quarks in a small nucleon). The β -function, a renormalization group equation, relates the coupling constant g with the energy scale μ_R in a renormalizable gauge theory, and it can be expand as a series of powers of g .

$$\beta(g) = \frac{1}{\mu_R} \frac{\partial g}{\partial \mu_R} = -(b_0 \alpha_s^2 + b_1 \alpha_s^3 + b_2 \alpha_s^4 + \dots). \quad (1.32)$$

According to the renormalization group theory, in a renormalizable quantum field theory, the coupling constant always depends on (or say redefined as a function depending on) the momentum transfer Q^2 , as shown in the β -function, when considering all the corrections from higher order Feynman diagrams and using the renormalized quantities. This is called a *running coupling*. In 1972, 't Hooft wrote the correct negative result on the board as a reply to Symanzik in a conference,

however none of them pursued it later ⁵. In 1973, Politzer, Gross and Wilczek discovered that a non-Abelian gauge theory is indeed asymptotically free [27] [28] [29]. The consequence of such a discovery in the strong interaction was shown in a following paper [30]. In Abelian QED, the dependence is only logarithmically

$$\alpha(Q^2) = \frac{\alpha(\mu^2)}{1 - \frac{\alpha(\mu^2)}{3\pi} \log\left(\frac{Q^2}{\mu^2}\right)} \quad (1.33)$$

$$= \frac{\alpha(0)}{1 - \frac{\alpha(0)}{3\pi} \log\left(\frac{Q^2}{m^2}\right)} \quad (1.34)$$

In non-Abelian QCD, the running coupling constant is

$$\alpha_s(Q^2) = \frac{\alpha_s(\mu^2)}{1 + b_0\alpha_s(\mu^2) \log(Q^2/\mu^2) + \mathcal{O}(\alpha_s^2)}. \quad (1.35)$$

Consider the 1-loop correction,

$$\alpha_s(Q^2) \doteq \frac{\alpha_s(\mu^2)}{1 + \frac{\alpha_s(\mu^2)}{12\pi} (11n_c - 2n_f) \log(Q^2/\mu^2)} \quad (1.36)$$

$$= \frac{12\pi}{(33 - 2n_f) \log(Q^2/\Lambda^2)}. \quad (1.37)$$

$$\text{where } \Lambda^2 = \mu^2 \exp\left(\frac{-12\pi}{(33 - 2n_f)\alpha_s(\mu^2)}\right). \quad (1.38)$$

The *QCD scale* Λ denotes the energy scale where the effective coupling constant gets to infinity, and its value is about 217 MeV. As we see, $33 - 2n_f < 0$, this leads to the asymptotic freedom and “anti-screen” of color charge. For 2 and 3 loops corrections [31],

$$b_1 = (153 - 19n_f)/(24\pi^2)$$

$$b_2 = (2857 - \frac{5033}{9}n_f + \frac{325}{27}n_f^2)/(128\pi^3).$$

For higher orders, please refer [32] [33]. The running coupling in QCD is shown Figure 1.3 in [34] [31].

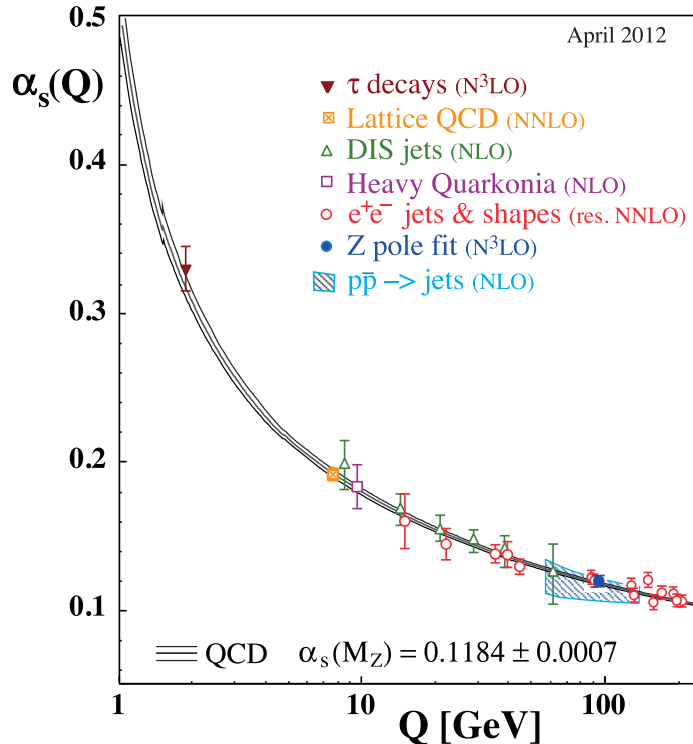


Figure 1.3: Summary of measurements of the strong interaction α_s as function of energy scale Q . This demonstrates running coupling constant and asymptotic freedom in QCD [34] [31].

As a consequence of the running coupling and asymptotic freedom, in high momentum transfer or small length scale, one can carry out a perturbative calculation in the quantum chromodynamics. Much like in QED, we just consider a few orders of Feynman diagrams in pQCD calculations when α_s is small. This is called *perturbative QCD* (pQCD). However, quarks and gluons are always trapped in hadrons. To cope with this fact, the *factorization theorem* allows us to separate/factorize the short-distance (large Q^2 , perturbative) processes (such as parton parton hard scattering) and long-distance (small Q^2 , non-perturbative)

⁵ See advanced information provided in http://www.nobelprize.org/nobel_prizes/physics/laureates/2004/advanced.html

processes (such as hadronization) [35]. Therefore, pQCD could be applied to calculate the measurable quantities in hadronic productions.

On the other side of the asymptotic freedom, the running coupling constant gets very large in the infrared region. The perturbative QCD is only applicable in high energy. *Lattice QCD* was proposed by Wilson [36] as a non-perturbative method. In the lattice QCD, the 4 dimensional Euclidean space is discretized as a lattice with some spacing. The quark fields are placed on the sites and the gauge boson fields are placed on the links between neighboring sites. The finite space distance corresponds to a cut-off in the momentum. Continuum theory is then recovered by extrapolation when we push the spacing to infinitesimal. The lattice QCD has a wide range of applications, which greatly extend the reach of QCD calculations. However, lattice QCD can't be a cure to all QCD questions, and we need experimental data to test all predictions from QCD theories. Furthermore, its extensive computation cost is another practical issue. Data from nuclear experiments, especially those in intermediate energies where pQCD is not applicable, as well as phenomenological models, are indispensable for understanding and testing QCD.

1.2 Quark-Gluon Plasma and Heavy Ion Collisions

Considering the asymptotic freedom and running coupling at small length scales, Collins and Perry suggested that there might be free quarks in the dense center of neutron stars [37]. This idea is in the high density, low temperature regime of QCD. Later, Shuryak looked into the high temperature nuclear phase transition, and proposed a deconfined state of nuclear matter, the *quark-gluon plasma* (QGP):

When the energy density ε exceeds some typical hadronic value (~ 1 GeV/fm³), matter no longer consists of separate hadrons (protons, neutrons, etc.), but as their fundamental constituents, quarks and

gluons. Because of the apparent analogy with similar phenomena in atomic physics we may call this phase of matter the QCD (or quark-gluon) plasma.

From a dimensional argument, we can infer the critical temperature $T_C \sim 170$ MeV when the critical energy density $\varepsilon_C \sim 1 \text{ GeV}/\text{fm}^3$ [38]. This is pretty close to the value of QCD scale Λ , therefore this phase transition is out of the capability of the perturbative QCD. The numerical calculation from the lattice QCD showed that the quark-gluon plasma phase transition happens at the critical temperature about $170 \text{ MeV} \approx 10^{12} \text{ K}$, see Figure 1.4 from [39].

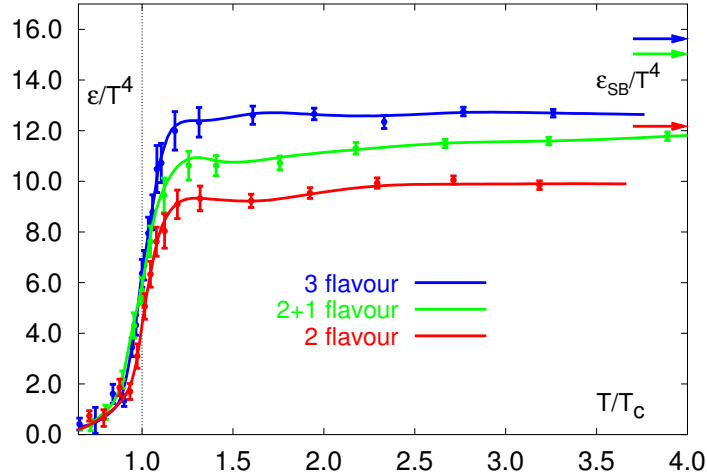


Figure 1.4: Lattice QCD results for ε/T^4 as a function of temperature scaled by T_C . When one heavier quark is included (labeled as 2+1 flavor in the plot), T_C is (173 ± 8) MeV. As shown in the plot, the degree of freedom increases dramatically near T_C . ε_{SB} is the Stefan-Boltzmann limits, which denotes the energy density contributed from the degrees of freedom from bosons ($\frac{\pi^2}{30}T^4$ from each) and fermions ($\frac{7}{8}\frac{\pi^2}{30}T^4$ from each) [39] [38].

The quark-gluon plasma is believed to have existed in the first few microseconds of the universe. One might be tempted to trace signals back to that primordial time to infer QGP's properties and the early universe. One candidate is the color neutral photon. However, the photon signals from that era are buried by the ones from a much later stage when the hadrons were already formed. Current left-over photons of the primordial universe come from the moment when the photons decoupled from the electrons and neutral hydrogen atoms started to form. These photon remnant are referred as the *cosmic microwave background*. Therefore, the signatures of QGP in the early universe are hard to trace back by astronomy observations.

Nevertheless, we can achieve such a high temperature, high energy density environment in laboratories to create a miniscule fireball, a.k.a. a quark gluon plasma, by colliding heavy ions with each other. This is the *heavy ion collision*. And such colliders are called *heavy ion colliders*. Such experimental attempts have lasted for more than two decades. The *energy of each pair of colliding nucleons in the center of mass frame* ($\sqrt{s_{NN}}$) increased from 1 GeV at Bevalac of the Lawrence Berkeley National Laboratory (LBNL), to 5 GeV at the Alternating Gradient Synchrotron (AGS) of the Brookhaven National Laboratory (BNL), to 17 GeV in the Super Proton Synchrotron (SPS) of the European Organization for Nuclear Research (CERN). No definite evidence had been found until SPS indicated the existence of a dense state of matter, possibly partonic [40]. The Relativistic Heavy Ion Collider (RHIC) was built with the goal of searching for the quark-gluon plasma, and started operation in 2000 with $\sqrt{s_{NN}}$ up to 200 GeV. The e^+e^- pair production from direct photons agrees with a temperature at least 300 MeV at the time 0.6 fm/c after collisions [41], this is well above T_C from LQCD calculation. The data from RHIC has revealed quite a lot of QGP signatures and found that the new state of matter is strongly coupled. The original picture for the quark-gluon plasma

is more like an ideal gas, so now the QGP is referred as the *strongly coupled quark-gluon plasma* (sQGP). Along the Large Hadron Collider (LHC) commissioned at CERN in the year of 2009, the energy frontier again rises with $\sqrt{s_{NN}}$ up to 2.76 TeV in Pb+Pb collisions and 5.02 TeV in p +Pb collisions. New measurements came out, such as less (direct) quarkonium suppression in low p_T region at LHC though its higher energies and higher temperature which is explained by the re-combination mechanism in QGP [42] [43] [44], momentum imbalance and jet-quenching from full jet reconstruction analysis [45] [46] [47], W and Z bosons observations [48] [49] [50]. The most striking one is long range correlations, even sizable v_2 and v_3 values, discovered in small systems, such as p +A collisions. We will discuss it in detail in Section 1.4. This seemingly collective behavior agrees with the picture that there is a thermally equilibrated state in a short time after the collisions (order of fm/c seconds). Though the system size is small, the number density can be high. If there are enough particles and the ratio between mean free path and system size is small, a statistical equilibrium could be reached. This is unexpected, and needs further investigation to confirm or dispute this idea. This is one of the motivations of this thesis research.

1.2.1 Elliptic Flow, Hydrodynamics and Equilibrium. When two nuclei collide with each other, the nuclear matter overlaps in an ellipsoid shape. Such a spacial anisotropy leads to a momentum anisotropy, and leaves the observable hadron production in a spacial anisotropy, which is called *elliptical flow*, See Figure 1.5. The hadron production is dominated by the elliptical flow, or say the 2nd order Fourier coefficient v_2

$$\frac{d^2 N}{d\phi dp_T} = N_0 \left[1 + \sum_{n=1}^{\infty} 2v_n(p_T) \cos(n(\phi - \Psi_n)) \right] \quad (1.39)$$

$$\approx N_0 \left[1 + 2v_2(p_T) \cos(2(\phi - \Psi_{RP})) \right] \quad (1.40)$$

where Ψ_{RP} denotes the azimuthal angle of the *reaction plane*, which is the plane defined by the impact parameter direction x and the beam direction z in Figure 1.5. ϕ is the azimuthal angle of a emitted particle. All the azimuthal angles are defined in the x - y plane. And v_n can be calculated by

$$v_n = \langle \cos(n[\phi - \Psi_{\text{RP}}]) \rangle \quad (1.41)$$

The elliptic flow at RHIC was first reported by [51], then [52]. Both used the

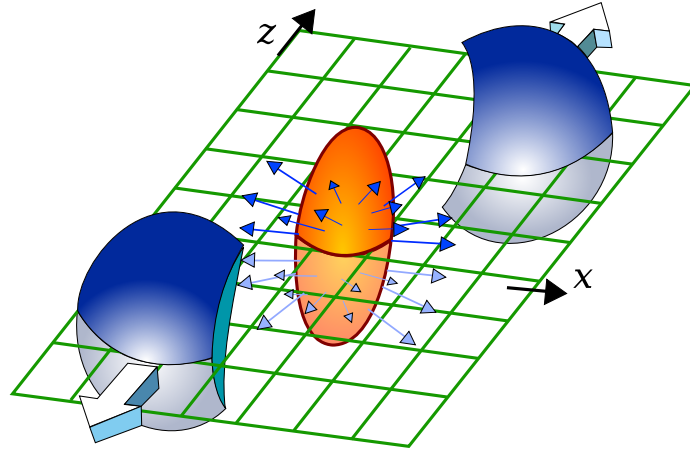


Figure 1.5: Elliptical flow and reaction plane⁶

reaction plane method mentioned in Equation 1.39. An alternative method is using the two particle correlation, discussed in Section 3.6 in details,

$$\frac{dN^{\text{AB}}}{d\Delta\phi} \propto 1 + \sum_{n=1}^{\infty} 2\langle v_n^A v_n^B \rangle \cos(n\Delta\phi). \quad (1.42)$$

Both methods are equivalent to first order. The two particle correlation method has a few advantages. First, it doesn't require a full azimuthal coverage; Second, it doesn't use event-by-event reaction plane determination; Third, it could have more

⁶ <https://www.phenix.bnl.gov/WWW/run/drawing/index.html>

information than the flow, such as the jet correlations. The first correlations result was published in [53].

The elliptic flow data agree with the hydrodynamics model very well, see Figure 1.6. This has a strong indication that local thermal equilibrium is established early in collisions and the QGP experiences a hydrodynamical evolution. The thermal equilibrium in such a short time can't be established within an ideal gas model, therefore, sQGP and ideal liquid is the new picture we get from RHIC's data. The viscosity value can be extracted from the elliptic flow measurements, and the viscosity entropy ratio (η/s) is surprisingly small, almost close to the quantum limit predicted by the uncertainty principle ($\eta/s \gtrsim \hbar$ with dimensional argument) [54] and the AdS/CFT calculation ($\eta/s \geq \frac{\hbar}{4\pi}$) [55] [55]. This is a universal feature of a strongly interacting system, and independent of the detailed structure.

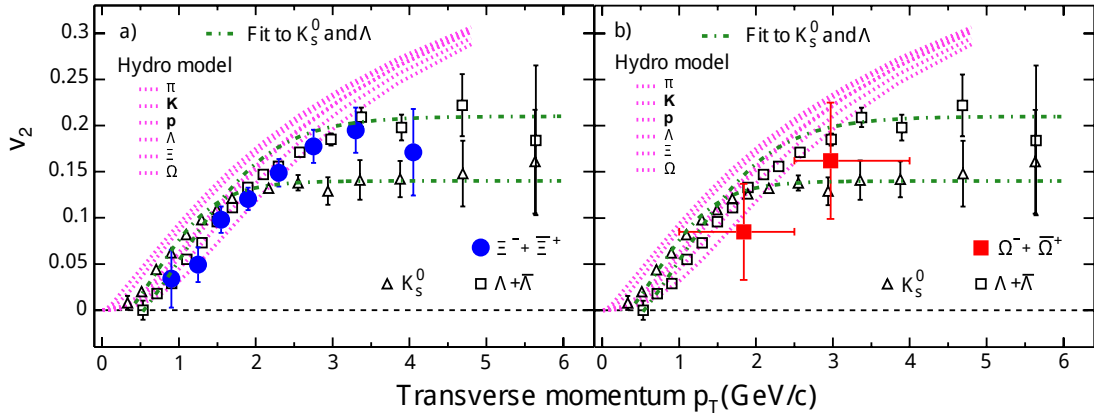


Figure 1.6: p_T dependent v_2 values for various hadron species in minimum-bias Au+Au collisions at $\sqrt{s_{NN}} = 200$ GeV [56]. K_s^0 and $\bar{\Lambda}$ data are from [57]. Ξ and Ω data are from [58]. The dot-dashed lines are fitting curves. The dotted curves are hydrodynamics calculation results.

The statistical model has been applied to calculate the particle yields ratio by Fermi [59] and Hagedorn [60]. The data from RHIC agree with the statistical models, see Figure 1.7, which might indicate a chemical equilibrium is achieved before hadronization.

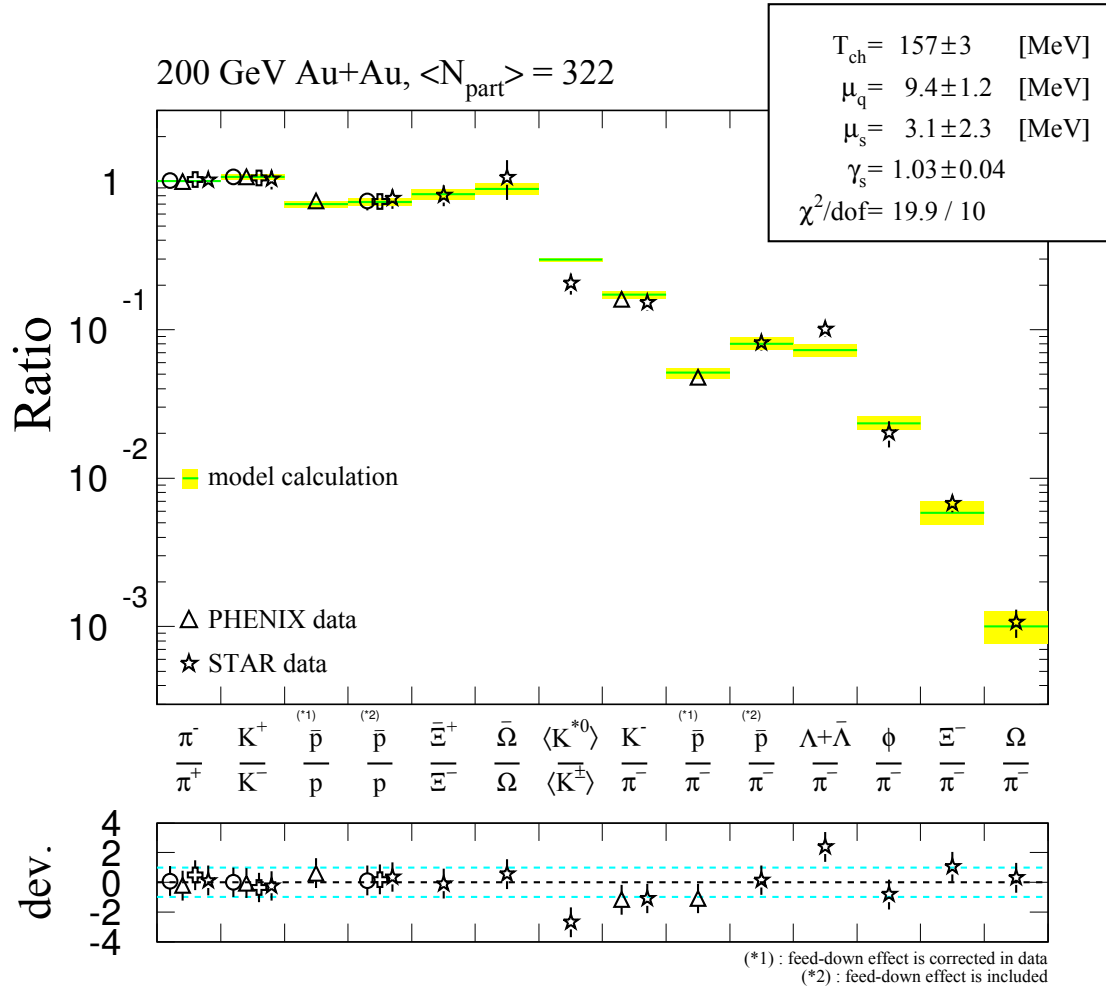


Figure 1.7: Identified particle yields ratios. The data are from PHENIX (triangles), STAR (stars), BRAHMS (circles), and PHOBOS (crosses) in central Au+Au collisions at $\sqrt{s_{NN}} = 200$ GeV [38]. The statistical model is from [61].

1.2.2 Jet Quenching and Energy Loss. Hard scatterings of partons happen well before the formation of the quark-gluon plasma. The scattered partons have to travel through, radiate gluons and lose energies to the hot QCD medium. Then the jets associated with those partons should be softer and wider. It was suggested that the *energy loss* in a deconfined color medium is larger than in a hadronic medium [62]. A significant consequence is the depletion of high p_T hadrons, such a phenomenon is called *jet quenching*.

The first observation was published in [63], where a *nuclear modification factor* R_{AA} is defined as

$$R_{AA}(p_T) = \frac{(1/N_{\text{evt}}) d^2 N^{A+A} / dp_T d\eta}{(\langle N_{\text{binary}} \rangle / \sigma_{\text{inel}}^{N+N}) d^2 \sigma^{N+N} / dp_T d\eta} \quad (1.43)$$

where $\langle N_{\text{binary}} \rangle$ is the average number of inelastic $N+N$ collisions per event. R_{AA} compares A+A yields with a sum of independent $N+N$ collisions (binary scaling). Jet quenching is shown by $R_{AA} < 1$ at high p_T regions with various particle species in A+A collisions at RHIC and LHC. π^0 R_{AA} in central, peripheral Au+Au collisions and $p+p$ collisions are shown in Figure 1.8

Besides the single particle method, two particle correlation provides insight into the jet quenching as well [64]. I_{AA} is defined as a quantity to compare A+A collisions with a $p+p$ reference

$$I_{AA}(\Delta\phi_1, \Delta\phi_2) = \frac{\int_{\Delta\phi_1}^{\Delta\phi_2} d\Delta\phi \frac{dn_{AA}^{AB}}{d\Delta\phi}}{\int_{\Delta\phi_1}^{\Delta\phi_2} d\Delta\phi \frac{dn_{pp}^{AB}}{d\Delta\phi}} \quad (1.44)$$

where n means counts per event per trigger particle pair yields.

Jet quenching is manifested by missing or suppressed awayside jet (see Figure 1.9a) and $I_{AA} < 1$ (see Figure 1.9b) in central A+A collisions.

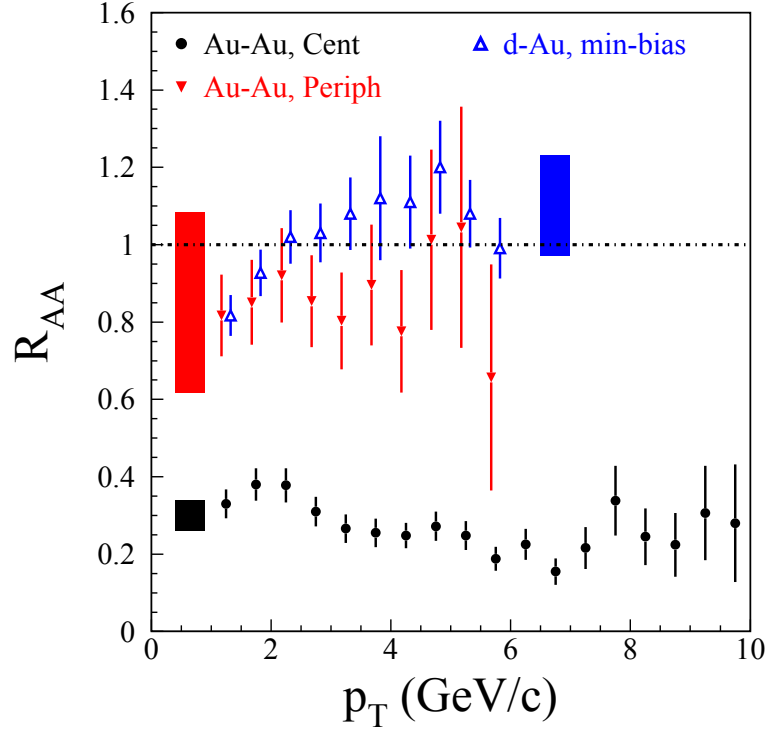
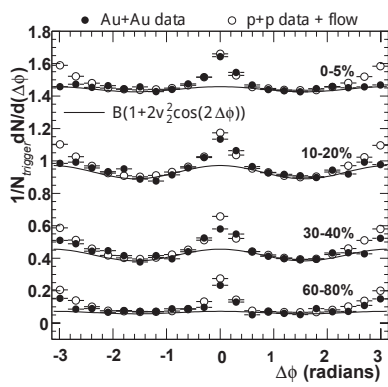


Figure 1.8: R_{AA} of π^0 in central, peripheral Au+Au and d +Au collisions. Jet quenching appears in large p_T regions in central Au+Au collisions [38].

High p_T particles are more likely coming from the region near the surface of the hot QCD medium. This is called *surface bias*. Consequently, the single particle yields can't give too much information about the interior of the medium. In two particle correlations, the leading triggers are usually chosen as high p_T particles, which tends to be from the near surface area, in other words, the partner particles have to travel a long distance inside the medium to survive. They undergo more medium interactions and modifications. This is one advantage of the two particle correlation method in the study of medium modifications.



(a) Suppressed away-side jet

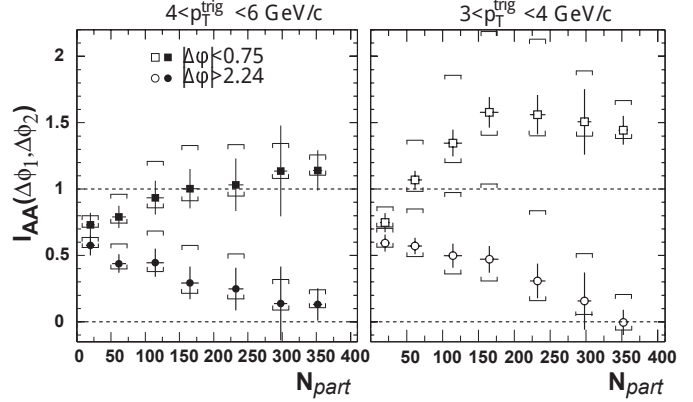
(b) I_{AA} in central Au+Au collisions

Figure 1.9: Jet quenching in two particle correlations. In (a), the awayside jet without flow contribution is suppressed down to less than 0.2 in central Au+Au collisions. In (b), the awayside jet's $I_{AA} < 1$ in central Au+Au collisions. While the nearside jet's I_{AA} is not suppressed. [64]

1.3 Cold Nuclear Matter Effect

The comparisons between heavy ion collisions and $p+p$ collisions, such as R_{AA} , I_{AA} , have revealed a clear difference between these two system. However, in order to put the QGP argument on the solid ground, we need to disentangle the hot medium effect and the *cold nuclear effect* (CNM). The cold nuclear effect is the observed phenomena describing the final production differences between the nucleus (or nucleon) nucleus collisions and the nucleon nucleon collisions without any presence of the opaque hot color medium, or say, quark-gluon plasma. Traditionally $d+Au$ collisions are believed not to create QGP. Even if QGP is created in such a small system, its effect is much smaller than the one in A+A collisions. Therefore, the $d+Au$ collisions at RHIC and $p+Pb$ at LHC serve as a good baseline for the A+A

collisions in the quark-gluon plasma search. Sometimes, we may refer the cold nuclear matter effect as one of initial state effects, and the hot medium effect as the final state effect. The cold nuclear matter effect includes the modifications of parton distributions [65], parton rescatterings [66] and a number of others. Here, the name *parton* is proposed by Feynman as a generic word for the particle constituent inside of a nucleon, which means a quark or a gluon. PHENIX charged hadron production data from d +Au collisions at RHIC have shown such modifications in forward / backward rapidity [67] and midrapidity [68].

The cold nuclear matter effect includes:

- Nuclear Modification of Parton Distribution
- Cronin Effect
- Gluon Saturation
- Radiative Energy Loss
- k_T Effect

And, they may not be distinctively different. They might have common physics origin, or similar observable effects on the other hand.

1.3.1 Nuclear Modification of Parton Distribution. According to the factorization theorem (see Section 1.1.4), the calculation of the inclusive cross section could be factorized into the parton distribution function $f(x, Q^2)$, the fragmentation function $D(z)$ and a perturbatively calculable differential cross section.

$$d\sigma^{p+p \rightarrow h+X} = \sum_{abc} \int dx_a dx_b dz_c f_{a/p}(x_a, Q^2) f_{b/p}(x_b, Q^2) d\hat{\sigma}^{a+b \rightarrow c+d}(Q^2) D_{c \rightarrow h}(z_h). \quad (1.45)$$

The *parton distribution function* (PDF) $f(x, Q^2)$ is the parton probability density function in terms of its *longitudinal momentum fraction* x in a free nucleon and the energy scale Q^2 .

$$x \triangleq \frac{p_L^{\text{parton}}}{p_L^{\text{nucleon}}}. \quad (1.46)$$

The parton distribution function is obtained by a global analysis of the data from the deep inelastic scattering, *Drell-Yan process* ($q + q' \rightarrow \gamma/Z \rightarrow l + l'$), W -lepton asymmetry, inclusive jet and other measurements. The most commonly used parton distribution function sets include CTEQ by CTEQ collaboration, HERA by H1 and ZEUS collaborations. An example PDF from CTEQ6 is shown in Figure 1.10 from [69]. However, the uncertainty of the gluon distribution function is still large even with recent DIS and inclusive jet data in CTEQ6, see Figure 1.11. In the hard scattering events at RHIC energy, the gluon processes dominate in the interesting physics, such as the π^0 triggered events, see Figure 1.12. In this analysis, the events triggered by π^0 with $5 < p_T < 15$ are analysed. This is one reason that we need to keep it in mind.

One way to construct the parton distribution function inside a nucleus $f_{q/A}(x)$ is to use a simple convolution between the parton distribution function $f_{q/p}(y)$ and the distribution of nucleon momenta inside of a nucleon $f_{p/A}(z)$,

$$f_{q/A}(x) = \iint f_{q/p}(y) f_{p/A}(z) \delta(x - yz) dy dz.$$

Analysis of the muon DIS data in the iron and deuterium, the parton distribution function is modified when the nucleon is part of a nucleus [71]. In the same way, the parton distribution in a nucleus is not a naive sum of the PDFs from constituent nucleons. This leads to the *nuclear parton distribution function* (nPDF). The nuclear modification to the free proton PDF is quantified by

$$R_i^A(x, Q^2) \triangleq \frac{f_i^A(x, Q^2)}{f_i(x, Q^2)}. \quad (1.47)$$

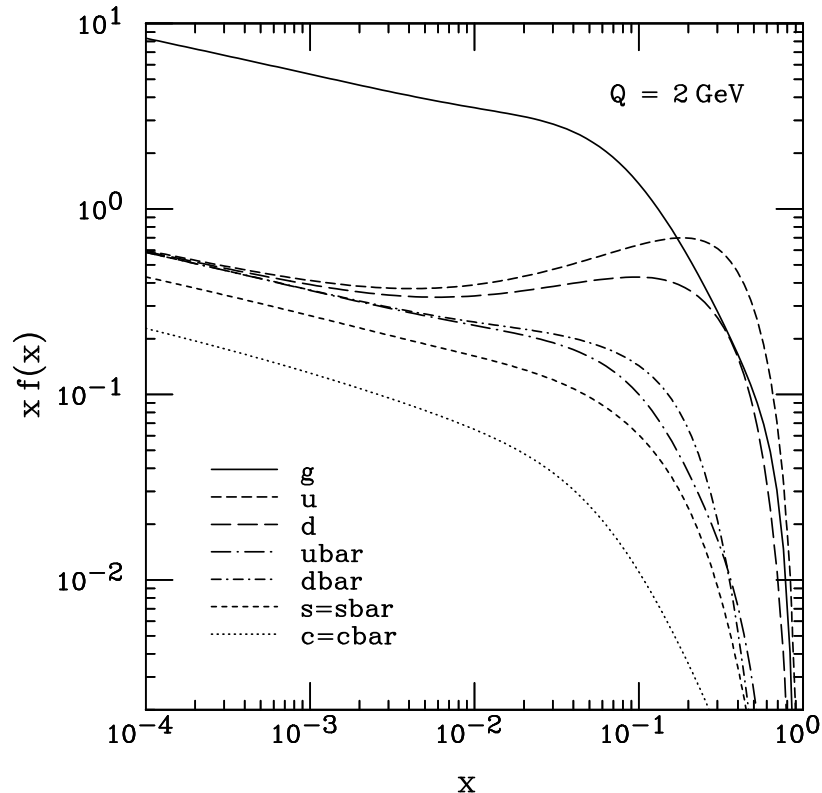


Figure 1.10: Overview of the CTEQ6M parton distribution function at $Q = 2 \text{ GeV}$ [69]

Here, $f_i^A(x, Q^2)$ is the free nucleon PDF, and $f_i^A(x, Q^2)$ is the PDF of a nucleon inside of a nucleus of species i . An illustration of the nPDF is shown in Figure 1.13.

There are a few known nuclear effects in different nPDF regions shown in Figure 1.13. They are listed as below:

- Shadowing effect ($x \lesssim 0.04$)

In small momentum fraction x ($x \lesssim 0.04$) region, the space distributions of partons are large due to the uncertainty principle. The destructive interference between wave functions of partons in different nucleons causes the number of low x partons decreased. This phenomena is called *shadowing effect*. Part of it

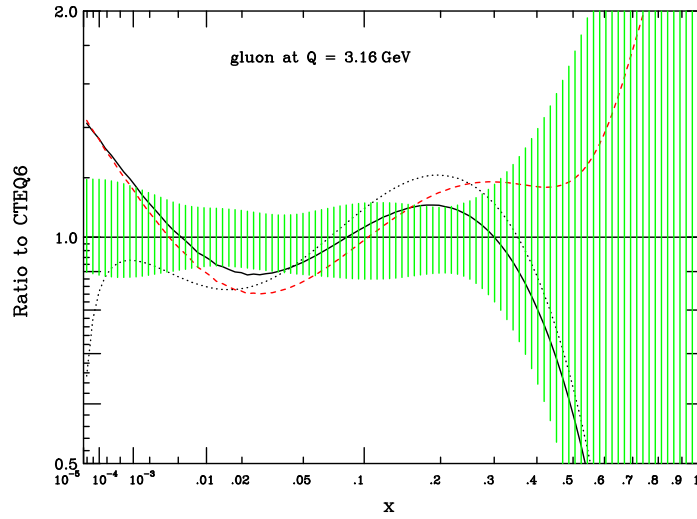


Figure 1.11: The uncertainty of CTEQ6 gluon parton distribution functions at $Q^2 = 10 \text{ GeV}^2$ [69]

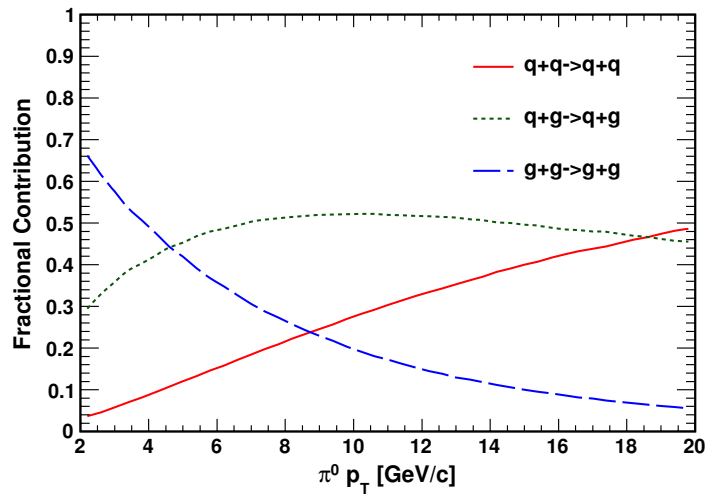


Figure 1.12: The fractional contribution of parton scattering processes to π^0 triggered events in $p+p$ collisions at $\sqrt{s_{NN}} = 200 \text{ GeV}$. The other processes are less than 1% and not shown [70].

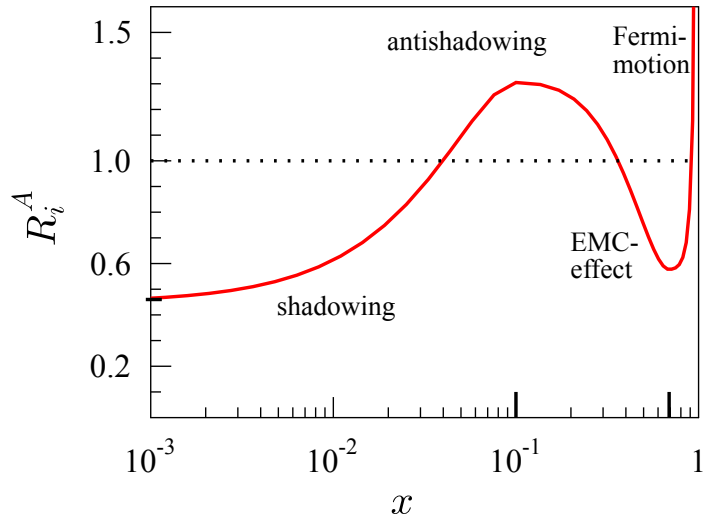


Figure 1.13: An illustration of nPDF with different modification regions marked [65]

could be attributed to parton fusions, where wave functions of partons in different nucleons start to overlap with each other. This effect is greater for gluons, since the low momentum gluons dominate sea quarks at low x .

- Anti-shadowing effect ($0.04 \lesssim x \lesssim 0.3$)

The constructive interference between partons in different nucleons results in an enhancement at larger x ($0.04 \lesssim x \lesssim 0.3$). This is the *anti-shadowing effect*.

- EMC effect ($0.3 \lesssim x \lesssim 0.8$)

The *EMC effect* refers to the unexpected deficit in the region of $0.3 \lesssim x \lesssim 0.8$ discovered in muon DIS experiment [71]. Some models are proposed based on single nucleons, pion enhancement, multiquark clusters, dynamical rescaling and shadowing [72] [73]. However, none of them match the data well. The origin of the EMC effect still remains a puzzle to the physics community.

- Fermi motion ($x \gtrsim 0.8$)

The huge enhancement at large x ($x \gtrsim 0.8$) is due to the Fermi motion ($E_F \sim 33$ MeV, $p_F \sim 250$ MeV/ c for heavy ions, such as Pb and Au) of the constituent nucleons in a nucleus. This can be understood by the Fermi gas model in a nucleus. The Fermi energy is about 20 - 40 MeV, the heavier nucleus, the larger Fermi Energy. And the Fermi momentum is determined as

$$p_F = \sqrt{2mE_F}. \quad (1.48)$$

Here, m is the mass of the nucleon. Under the Fermi surface, the nucleons undergo a chaotic motion, which is the *Fermi motion*. The Fermi momentum has its own effect on nuclear reactions. In the collisions with nucleons inside of nuclei, the Fermi motion would smear the effective energy, and lower the nuclear reaction's threshold energy. Therefore, the Fermi motion enhances the particle production in the sub-threshold or near-to-threshold collisions.

The most commonly used nPDF's are EPS09 [65]. However, EPS09 is a global fit of data with all impact parameters b . Therefore, the impact parameter averaged EPS09 doesn't contain any spatial dependence. The impact parameter dependent parton distribution functions EPS09s and EKS98s are constructed and published under the assumption that the geometric dependence can be formulated as a power series (up to 4) of the nuclear thickness functions T_A [74].

1.3.2 Cronin Effect. The hadron production in the intermediate p_T range about $2 < p_T < 6$ GeV/ c in the $p+A$ collisions is enhanced compared with the scaled $p+p$ values [75] [76]. This effect is referred to as the *Cronin Effect*, named after the first discover. It is believed to be caused by the multiple scattering of the interacting partons. This Cronin effect is best shown in the R_{dA} and R_{cp} plot, see publications by PHENIX [77] [67] [68] [78], PHOBOS [79], STAR [80]. The BRAHMS result [81] shows that the Cronin peak appears at $\eta = 0$, disappears at $\eta =$

1, and the suppression happens at all p_T when $\eta = 3.2$, see Figure 1.14. Similar results are published by PHENIX [67]. Generally speaking, the R_{dA} and R_{cp} plots should show some suppression at low p_T and enhancement at intermediate p_T , then come back to 1 at large p_T . And in central Au+Au collisions, the severely suppressed R_{AA} is one signature of the jet quenching and energy loss in the quark gluon plasma [63].

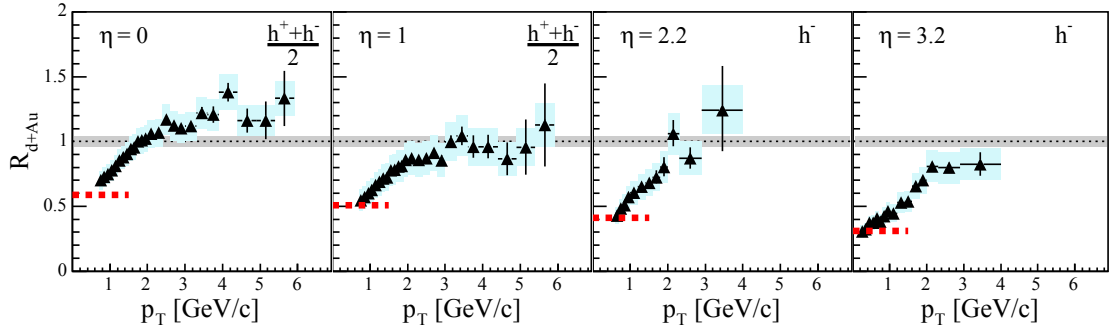


Figure 1.14: Nuclear modification factor R_{dAu} for charged hadrons at pseudorapidities $\eta = 0, 1.0, 2.2, 3.2$ [81]

Recently in d +Au collisions, a surprising enhancement was observed in R_{dA} that is qualitatively similar to the Cronin enhancements seen at RHIC in R_{AA} . However this enhancement appears only in a higher momentum region and surprisingly only in peripheral collisions, so it is not expected to be related to Cronin physics. Still the data in this thesis is relevant to the interpretation of this result and it is discussed further in Section 5.3.

1.3.3 Radiative Energy Loss. The *radiative energy loss* is the medium induced gluon bremsstrahlung, which leads to energy loss due to the gluon radiation and exchange in the medium. There are three possible scenarios. The first one is the

initial state energy loss in the nucleus before the hard scattering. This decrease the momentum of the incoming parton which undergoes the hard scattering. Essentially, it is equivalent to the change of x (shift to the left), or say, the modification of the parton distribution function. The second one is the final state energy loss where the outgoing hard scattered parton or fragmented hadron lose energy when going through the medium, which is equivalent to the change of the fragmentation function. The last one is Bertsch-Gunion radiation, where the parton experience no hard scattering in the cold nucleus. The energy loss in cold nuclear matter could be large; the initial state E-loss might be larger than the final state E-loss in the asymptotic limit; the initial and final state radiative energy loss might have different path length dependence [82]. The theoretical models are reviewed in [83].

1.3.4 Gluon Saturation. The study of the nuclear modification factor R_{dA} in d +Au collision at different rapidity and centrality shows a significant forward rapidity suppression, especially in a central collision [84]. The midrapidity-forwardrapidity and forwardrapidity-forwardrapidity two-particle correlations are observed to be suppressed for d +Au collision compared with p + p , according to a PHENIX result [85]. This effect has been predicted as a signature of the *color glass condensate* [86]. In this scenario, the short-life fluctuation partons are frozen out due to the time dilation in a fast moving nucleons, and exist as a large static source of low momentum partons, see Figure 1.15. The gluon density at a small momentum fraction x is the result from the balance of gluon recombination (reducing the number) and gluon splitting (increasing the number), and peaks about a characteristic momentum $Q_S \sim \frac{A^{1/3}}{x^\lambda}$, namely the saturation momentum (here λ is 0.3 determined from data in [85]). Such an effect is called *gluon saturation*, because below this momentum scale, no more gluons can be created due to the dominance of the recombination. It is predicted that the gluon saturation

gets prominent when the jet's p_T is close to Q_s , which is about 1-2 GeV/c in RHIC and increases with nuclear size as the formula indicates. Therefore, the large nucleus and small x , which is equivalent to the forward region, are favored to test the gluon saturation phenomena. Of course, some other theories could explain such a suppression in d +Au collisions, such as the nuclear shadowing. To distinguish between these models, the forward azimuthal correlation is suggested [87].

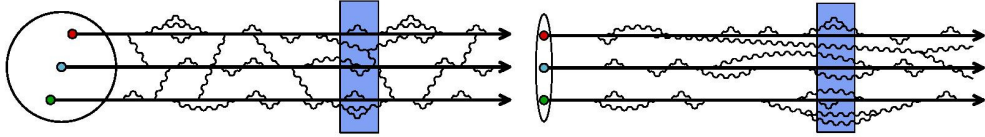


Figure 1.15: Left: a rest nucleus, the parton fluctuation is complicated, non-perturbative, and short lived. Right: a high energy nucleus, the thickness is compressed due to the length contraction, the short-lived parton fluctuation becomes a static source of parton due to the time dilation. [87].

1.3.5 k_T Effect. In the *leading order approximation* (LO) of QCD scattering, which corresponds to 2 on 2 scattering reactions, such as $q + g \rightarrow q + g$, the *transverse momentum* of one outgoing parton should be exactly balanced with the other side parton. However, due to the finite size of the nucleons and the uncertainty principle, the initial partons are expected to have a transverse momentum on the order of 300 MeV/c [88]. The p_T imbalance is further spoiled by the fact that the hard scattered parton could radiate fragmentation photons or bremsstrahlung gluons beyond the LO QCD. Moreover, γ +A and π +A collisions show that $\langle k_T \rangle$ (k_T is defined as the p_T sum of the outgoing partons) is proportional to $A^{1/3}$, which could result from the multiple scattering in the nucleus since $L \sim A^{1/3}$. In p +A collisions, $\langle k_T \rangle$ increases more slowly than $A^{1/3}$ [89]. These effects

are collectively called the k_T effect or k_T broadening . The *next-to-leading order* (NLO) pQCD calculation is insufficient to describe the magnitude of p_T imbalance measured in the experiments which is about a few GeV/ c in dimuon, diphoton and dijet pairs [90]. The relationship between the k_T effect and the presence of the nuclear matter, no matter hot or cold nuclear matter, is yet to be discovered by experiments. A previous k_T measurement by STAR has shown that there is no major k_T difference in $p+p$ and $d+Au$ collisions [91]. A systematic investigation of k_T broadening in direct photon production using fixed-target and collider data shows a pattern of deviation from NLO QCD calculation [90].

1.4 Collective Effect in $d+Au$ Collisions

Though compelling evidence supports that there is a hot and dense medium created in A+A collisions, $d+Au$ collisions are traditionally believed to be too small to create the quark-gluon plasma. Recently, an unexpected near-side long range (large pseudorapidity range) correlation was observed in high multiplicity $p+p$ collisions [92]. Then, the results in $p+A$ collisions, [93], [94] [95] [96] from $p+Pb$ at LHC, [97] [98] from $d+Au$ at RHIC, indicate some collective behaviour in the small $p+A$ systems.

The series of surprising discoveries began with “shoulder” and “ridge” structures in two particle correlation measurements at RHIC’s Au+Au data. Central Au+Au collisions show modifications to $p+p$ ’s Gaussian-like away-side peak. The away-side peak is broader and even splits to two “shoulders” in the intermediate p_T region. This was first observed in [99], then confirmed in [100] [101] [102]. For the near-side, the correlations extend a large pseudorapidity range in central Au+Au collisions, and such a structure is called “ridge”. It was first observed in [99], then [103] [104] showed that it elongates across several units in $\Delta\eta$.

Figure 1.16 1.17 visually demonstrates the ridge and shoulder structure in central A+A collisions. The spectrum of ridge particles are softer than jet particles, close to the inclusive hadrons [105]. And the fraction of baryons is close to the inclusive hadrons too [106].

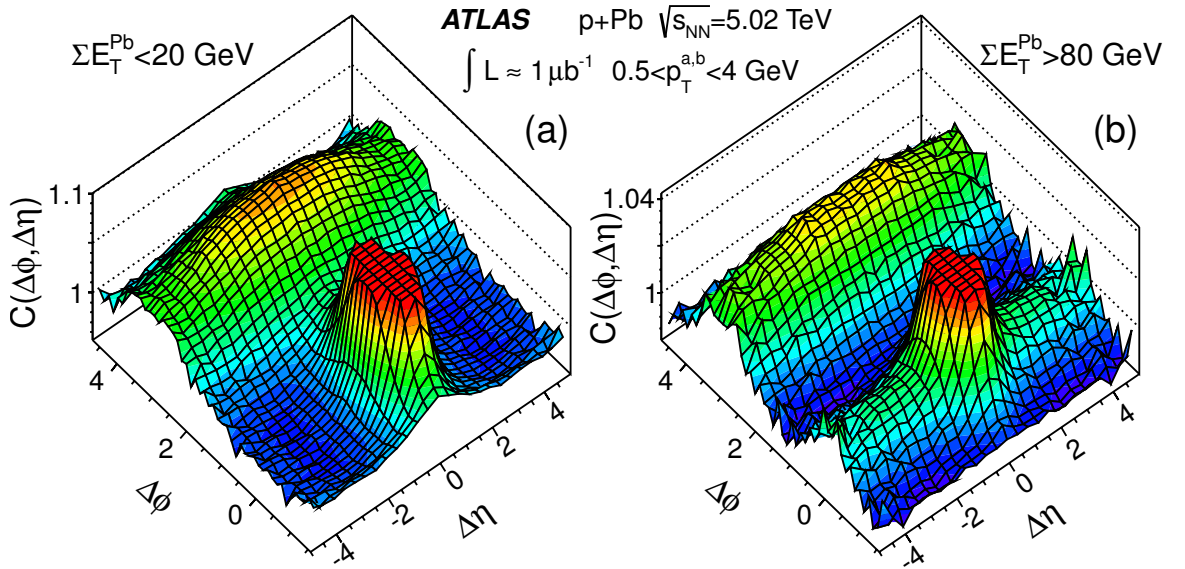


Figure 1.16: Ridge structure demonstration. In Panel (a), the ridge structure is missing in peripheral $p+Pb$ collisions. In Panel (b), the ridge structure is clear in the near side and across a large rapidity range in central $p+Pb$ collisions. Here, ATLAS classifies the central and peripheral events by summed transverse energy [95].

Theoretical interpretations of the away-side shoulder structure initially focused on the Mach cone, a final state effect. However, the Mach cone shock wave is unlikely to be observed in conical angular correlations after hadronization [107] or even before it [108] [109]. Later on, people started to realize the importance of once neglected higher order of flow harmonics, especially v_3 in the role of these structures.

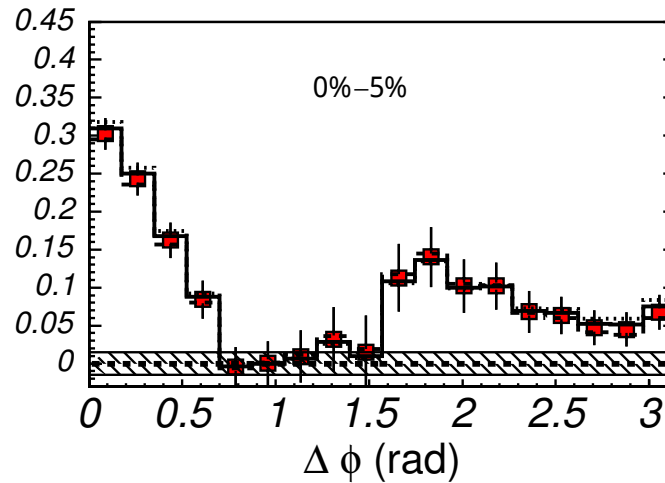


Figure 1.17: The shoulder structure in central Au+Au collisions. The deficit in $\Delta\phi \sim \pi$ is the “head”, and the excess in $\Delta\phi$ around π is the “shoulder”. The plot is adapted from [100].

Reference [110] showed that the geometry fluctuation in initial state could lead to triangular flow by a simple Glauber model (See Section 2.2.1.3) and AMPT (a multiphase transport model), then Reference [111] used fKLN model to argue that higher order flow harmonics could result from the initial state fluctuation. ALICE (A Large Ion Collider Experiment, an experiment collaboration at LHC) published their $v_2 v_3$ measurement, and agree with such idea that the double peak shoulder can be explained by v_3 [112]. PHENIX published $v_2 v_3 v_4$ measurements, and their data support the Glauber model (simple statistical fluctuation) instead of MC-KLN (a color glass condensate k_T -factorization approach) prediction [113]. Then more data of higher flow harmonics came out [114] [115] [116]. One thing to note, the n -th order event plane Ψ_n might not be the same or even correlated with the event plane Ψ_{RP} defined in Subsection 1.2.1. Figure 1.18 demonstrates that a triangular shape in the initial state could come from probabilistic fluctuations in the Glauber model.

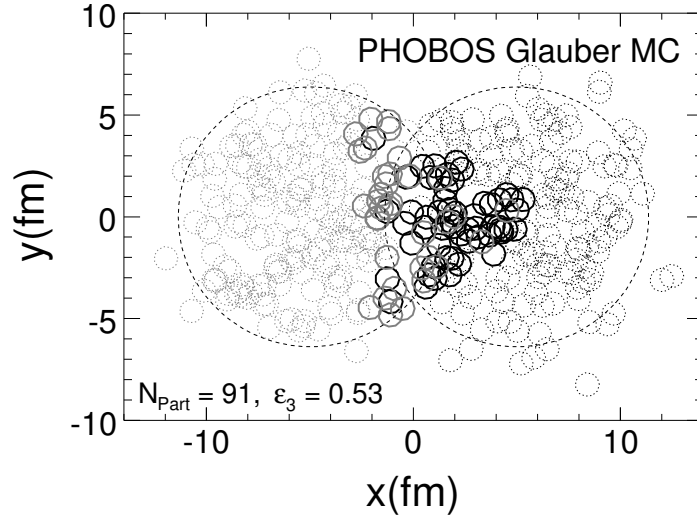


Figure 1.18: Triangular fluctuation in Glauber MC simulation. The distribution of nucleons on the transverse plane with $\varepsilon_3 = 0.53$ from Glauber model demonstrates the highly possible origin of v_3 flow. The wounded nucleons (participants) are shown in solid circles, the spectators are shown in dotted ones [110].

Various models have been proposed to explain the experiment observed ridge, see this review [117]. Now, people converge to the idea of initial geometric fluctuation and hydrodynamical flow proposed by [110]. Still, nobody anticipated such a phenomenon to happen in a small system such as $p+p$ and $d+Au$ collisions.

Another surprise came from CMS's measurement in $p+p$ collisions in 2010 [92]. They observed that in high multiplicity events ($N_{\text{trk}}^{\text{offline}} \geq 110$) in $p+p$ collisions at $\sqrt{s_{NN}} = 7$ TeV, a pronounced structure emerges in the 2-dimensional ($\Delta\phi$ and $\Delta\eta$) correlation functions for particle pairs with $1 < p_T < 3$ GeV/ c and $2.0 < |\Delta\eta| < 4.8$ and $\Delta\phi \approx 0$. This structure is very similar to the ridge structure in central Au+Au collisions.

In 2012, CMS found a similar ridge structure in $|\Delta\eta| < 4$ in high multiplicity events in $p+Pb$ collisions at $\sqrt{s_{NN}} = 5.02$ TeV collected in a short 8-hour run, but

significantly larger [93]. Later in the same year, using the same pilot p +Pb run, ALICE considered the difference between central (0-20%, higher multiplicity) and peripheral (60-100%, lower multiplicity) events in $|\Delta\eta| < 1.8$ to investigate it. The assumption here is that the non-flow contribution, such as jets, should be the same in central (high multiplicity) and peripheral (low multiplicity) events. And the long range correlation should be none or very small in the peripheral events. They found ridge-like structures in both near and away-sides with almost identical size. They projected the two-ridge structure on to $\Delta\phi$ and obtained non-zero v_2 and v_3 values [94].

LHC started their first p +Pb run in February 2013, which delivered $\approx 30 \text{ nb}^{-1}$ collisions. Using these data, ATLAS published their results in [95]. To avoid the correlation/bias from the charge particle multiplicity, they used $\sum E_T^{Pb} > 80 \text{ GeV}$ and $< 20 \text{ GeV}$ to classify the central and peripheral events respectively. Here, $\sum E_T^{Pb}$ is the transverse energy summed over $3.1 < |\eta| < 4.9$ in the direction of the Pb beam. The results were the same, close-to identical ridges on both sides and non-zero v_2 and v_3 after central-peripheral subtraction. CMS also published their results from this 5.02 TeV p +Pb run [96], with comparison to 2.76 TeV Pb+Pb collisions. To reduce the non-flow contribution on the away-side, they also used 4 particle correlations to obtain v_2 values. Their v_2 values are consistent with ATLAS from central-peripheral subtraction method (this subtraction is used to remove the jet correlations), and the difference in the low-multiplicity events used for the subtraction could explain the slight discrepancy in two experiment data. In the 4-particle correlation method results, the ones from ATLAS are systematically higher than the ones from CMS, see Figure 1.19. They found v_3 values are very similar in p +Pb and Pb+Pb collisions, see Figure 1.20.

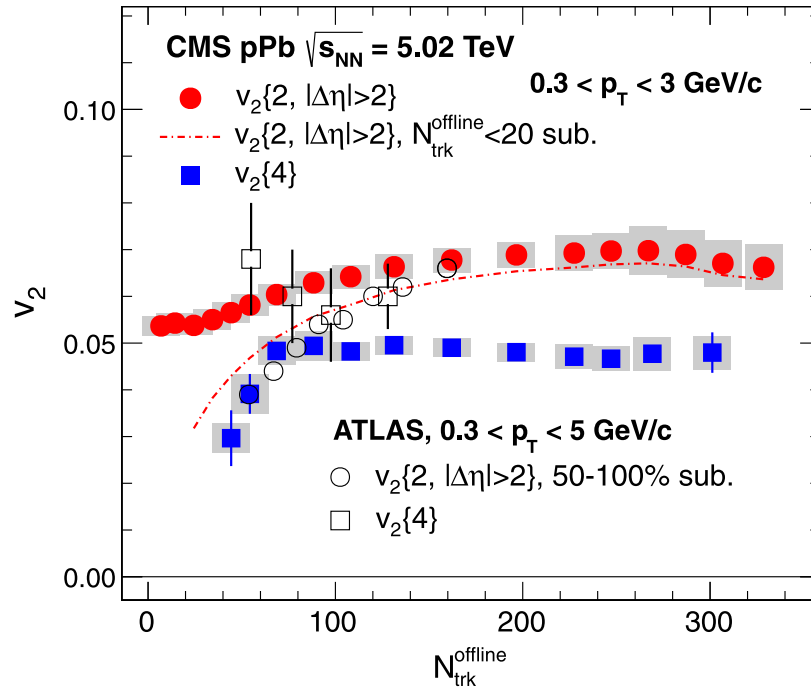


Figure 1.19: v_2 of p +Pb from CMS and ATLAS [96]. The red dotted line is from CMS central-peripheral subtraction method, and the open circle is from ATLAS with the same method. They matches with each other, and the difference can be attributed to the different choice of peripheral events. The solid and open square are the 4-particle correlation results from two experiments respectively, and they are inconsistent with each other.

PHENIX followed up with d +Au collisions at $\sqrt{s_{NN}} = 200$ GeV [97]. They found similar but larger v_2 , albeit with large uncertainties. When divided by the initial state eccentricity (from MC simulation), v_2 shows a qualitatively nice trending with the multiplicity, including the measurements of d +Au, Au+Au from RHIC and p +Pb, Pb+Pb from LHC, see Figure 1.21. This agrees with the idea that the final product anisotropy comes from the initial state geometric anisotropy. One

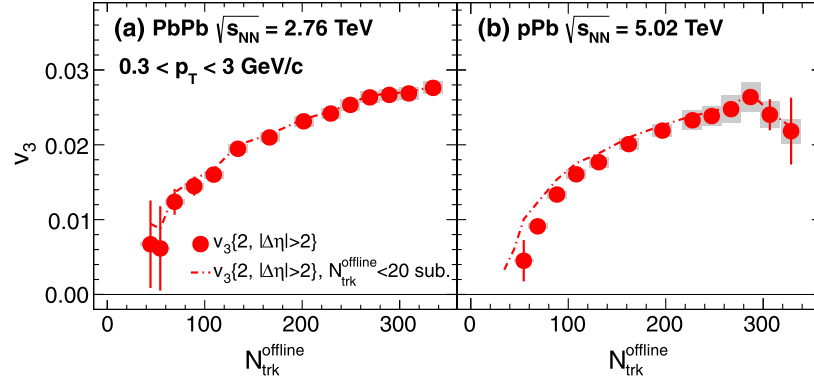


Figure 1.20: v_3 of p +Pb and Pb+Pb from CMS measurements [96]. They share similar dependence on the multiplicity.

thing to note, due to the limited acceptance in PHENIX, the pseudorapidity separation is $0.48 \leq |\Delta\eta| \leq 0.7$ and the uncertainties are large in this publication.

ALICE published their results of π^\pm , K_\pm , K_S^0 , $p(\bar{p})$ and $\Lambda(\bar{\Lambda})$ measurements at midrapidity in p +Pb collisions at $\sqrt{s_{NN}} = 5.02$ TeV. The p_T distributions for different centralities (multiplicities) shows that p_T is harder (larger) in more central (higher multiplicity) events. And a clear mass ordering was reported, where $\langle p_T \rangle^\Lambda > \langle p_T \rangle^p > \langle p_T \rangle^K > \langle p_T \rangle^{\pi^\pm}$, see Figure 1.22. Such a mass ordering phenomena were attributed to radial flow in Au+Au collisions [118] [38].

To improve the uncertainties, PHENIX published their measurements using the muon piston calorimeter(MPC) in the Au going direction [98]. They measured correlations between charged hadrons in $|\eta| < 0.35$ and energy deposited in the calorimeter towers for $-3.7 < \eta < -3.1$. The η separation is greater than 2.75 in this measurement. They used the energy deposited in Au going direction to get the event plane and calculated v_2 . Using minimum bias p + p as a control, they obtained the 2nd Fourier coefficients c_2 in the two systems. In order to eliminate the non-flow contributions, such as jets and resonance decays, they constructed c_2 as a sum of

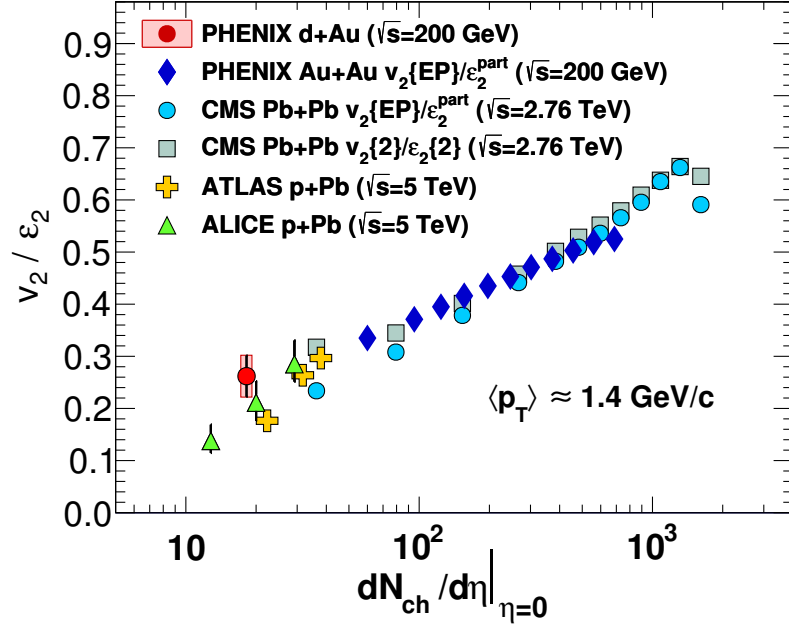


Figure 1.21: The eccentricity-scaled anisotropy v_2/ε_2 vs charged particle multiplicity ($dN_{\text{ch}}/d\eta$) for $d+Au$ and $p+Pb$ collisions. Also, $Au+Au$ and $Pb+Pb$ data are shown. v_2 are in similar p_T selections. The colored curves are for different ε_2 values from different nucleon representations in MC simulations. No systematic error is shown. And the multiplicities of $d+Au$ and $p+Pb$ are from HIJING [97] (For HIJING, see Section 5.9).

elementary (non-flow) and non-elementary (flow) parts. The elementary part is scaled by the sum of transverse energy due to dilution. They argued that the contribution from the elementary part is small. They measured v_2 from inclusive hadrons at midrapidity up to $4.5 \text{ GeV}/c$, and this result is lower than the previous one in [97] which has large uncertainties. They also measured v_2 from π^\pm and $p(\bar{p})$, and observed a mass ordering pattern similar to $Au+Au$ collisions. They compared the result with hydrodynamic model calculation and the one from ALICE measurements, see Figure 1.23.

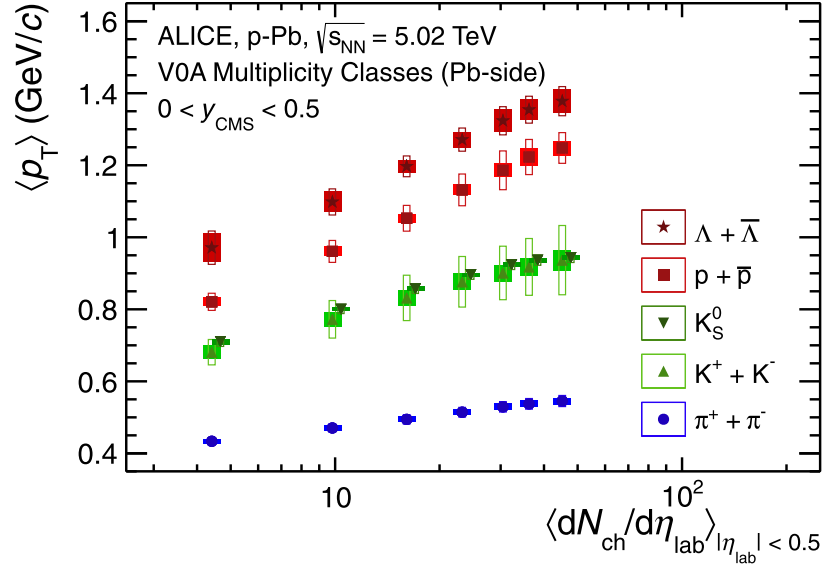


Figure 1.22: The mass ordering in $p+Pb$ collisions at $\sqrt{s_{NN}} = 5.02$ TeV [119].

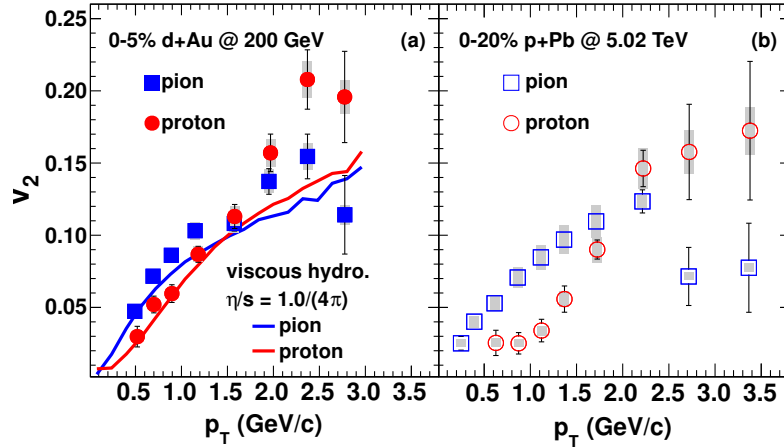


Figure 1.23: v_2 from identified π^\pm and $p(\bar{p})$ from [98]. In panel (a) the data are compared with hydrodynamic model [120] [121]. In panel (b), data are compared with $p+Pb$ collisions from ALICE measurement [94].

All experimental data support that there is some collective effect in central / high multiplicity $p+A$ collisions. Whether it comes from the final state effect, such

as a dense opaque medium, or from some initial state effect, such as cold nuclear matter effects (including gluon saturation), it has to be in a coherent way, and survive the hadronization phase. If it is flow, as indicated by model comparisons in the publications mentioned above, is there any thermal equilibrium or quasi-equilibrium in such a small system?

1.5 Statement of Purpose

In Au+Au collisions at RHIC, quite a lot QGP signatures have been found, in different approaches, such as the flow, the jet quenching, the charmonium dissociation and recombination, heavy flavor E-loss and mass hierarchy. Though there is no definite claim that QGP has been established in A+A collisions, people do believe the existence of QGP in heavy ion collisions. It's like a Bayesian inference, the more observations come in, the stronger belief we hold. Anyway, at least, all previous measurements are consistent with pQCD based model calculations and the picture that a hot dense color medium is created in such collisions. In order to disentangle the final state QGP effect from the cold nuclear matter (including both initial and final state effects), d +Au collisions serve as a promising baseline. More cold nuclear matter effects than $p+p$, and just no (or little) QGP there. Data have to be established in such a control object. This is the first objective we want to accomplish.

The observations of unexpected long range correlations show non-zero v_n from collective flow in d +Au collisions during the course of my research. The experimental data agree reasonably with hydrodynamical model calculations, though the color glass condensate theory has not yet completely ruled out for these observables. Hydrodynamic models enjoy their success in heavy ion collisions, however, the application in the small d +Au system might be still questionable. If

there are flows, there could also be energy loss, though the medium and hence the effects might be small. The two-particle correlation method is well suited for energy loss measurements, as well as the flow ones. The second object is to search for extra small E-loss effects besides the cold nuclear matter effect in $d+Au$ collisions.

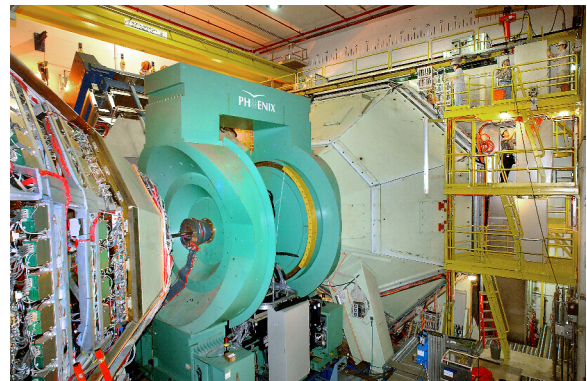
2 EXPERIMENTAL FACILITIES

2.1 RHIC

The *Relativistic Heavy Ion Collider (RHIC)*, as shown in Figure 2.1a, is a dedicated heavy ion collider at Brookhaven National Laboratory (BNL) in Upton, New York, USA. RHIC began its physical operation from the year of 2000 with highest energy $\sqrt{s_{NN}} = 200$ GeV for heavy ions and 500 GeV for protons. RHIC is capable of colliding a variety of beam species, including protons, copper, gold, and uranium nuclei, in a wide span of energy ranging from a few GeV to its highest energy level. RHIC has its own advantage to collide polarized protons for studying the spin structure of particles. Two small experiments BRAHMS and PHOBOS have finished their operation, and the other two experiments at RHIC, namely PHENIX and STAR are still in operation.



(a) RHIC with the beam line indicated



(b) PHENIX detectors

Figure 2.1: Experimental facilities (Photos from [122]).

2.2 PHENIX

PHENIX, the Pioneering High Energy Nuclear Interaction eXperiment, shown in Figure 2.1b, is a research experiment at RHIC to study the energetic collisions between heavy ions and protons, with the mission of discovery and examination of the new state of matter, namely the quark-gluon plasma, as well as exploration in the spin structure of protons. PHENIX is designed to optimize the capability to detect the rare process with better resolution and momentum range for penetrating probes, such as leptonic (including electrons and muons) and photonic channels. STAR has larger acceptance coverage due to their barrel Time Projection Chamber(TPC). Two different detector configurations in the STAR and PHENIX experiments can provide both teams their own advantages and the cross-check of their results from different techniques. This complementary setup of experiments is beneficial to the whole physics community. The future installation of new Silicon Vertex Detector(VTX) in Run11 will provide a full azimuthal coverage. The current PHENIX acceptance coverage is shown in Figure 2.2.

PHENIX is a combination of different particle detectors, which are on four spectrometer arms. The variety of PHENIX detectors provides more measurements and cross-checks for the analysis. The north-south spectrometer arms are along the beam line at the forward and backward rapidity region, with $1.15 < \eta < 2.44$ or $-2.25 < \eta < -1.15$. These two muon arms are designed specifically for muon identification and track reconstruction. The east-west spectrometer arms are on the central rapidity region, on the side of the beam line. The two central arms cover $-0.35 < \eta < 0.35$ in the rapidity and 180° in azimuthal angle. The primary goals of the central arms include photon/electron reconstruction, charged particle tracking, particle identification. The detector configuration of PHENIX Run08 is shown in Figure 2.3.

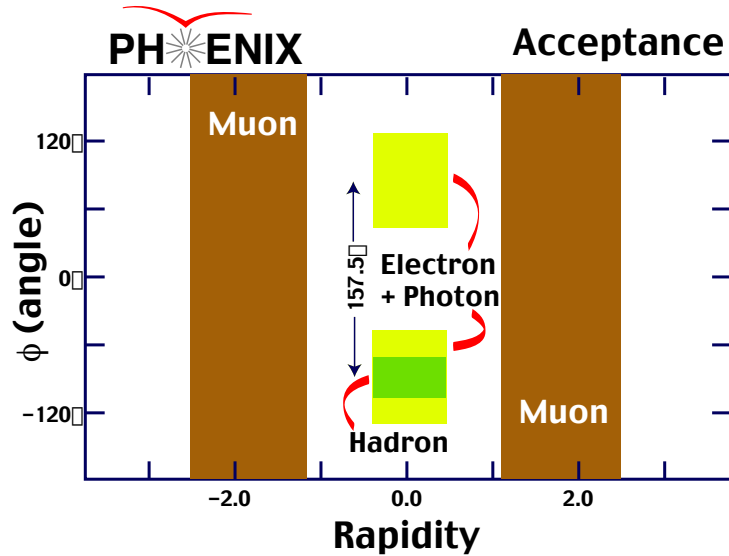


Figure 2.2: PHENIX acceptance plot, ϕ is the azimuthal angle around the beam line, rapidity is along the beam line (Plot from [122]).

2.2.1 Event Trigger and Characterization. The inner detectors consist of Beam-Beam Counters(BBCs), Zero Degree Calorimeters(ZDCs) and Reaction Plane Detector(RxNP), which are responsible for the event triggering and characterization, such as determination of the event location, centrality and the reaction plane. The condition required to trigger the data collection for an event is called a *trigger*⁷.

2.2.1.1 Beam-Beam Counters. The *BBC* detectors, shown in Figure 2.4, are placed around the beam pipe at ± 144 cm from the geometry center of PHENIX detector covering $3.1 < \eta < 3.9$ over full azimuth. The detector consists of a set of 64 *photonmultiplier tubes* (PMT) which measure the Cherenkov light from the charged particles passing through the quartz radiators in front of each PMT. The

⁷ We have two trigger concepts through out this thesis. One is the trigger condition discussed here, the other one is the trigger particle discussed in Section 3.6. The two concepts are totally different, the only common thing is their name.

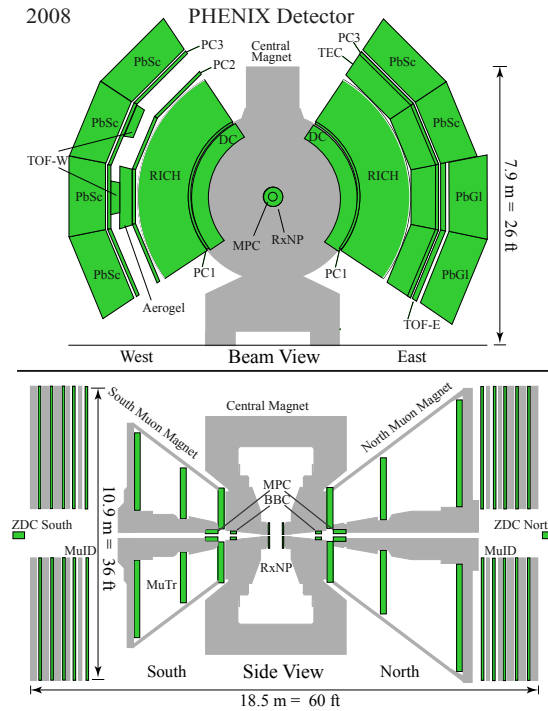


Figure 2.3: PHENIX detector configuration for Run8, top: beam view, bottom: side view (Plot from [122]).

most important feature of BBC is the excellent timing resolution, about 54 ± 4 ps for each element. The collision time T_0 is determined by the average arrival time of the leading charged particles into the South and North BBCs. This time is used by the timing synchronization, such as for the TOF detectors of PHENIX to identify hadrons. The collision location, namely Z-vertex, is determined by the difference of the time from the two BBCs with resolution about 1 cm, which is part of the Local Level 1 trigger which rejects the collision with Z-vertex outside of the center interaction region (> 30 cm). The collision vertex is also used as the origin point for tracking subsystems. The resolution gets worse for lower centrality, smaller size of beam species and lower beam energy.

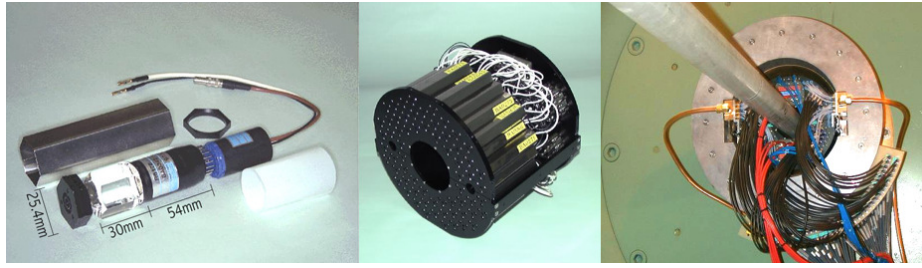


Figure 2.4: BBC detector construction: An individual BBC PMT and quartz radiator (left). A BBC bundle as constructed from 64 PMT and radiators (center). A BBC as installed around the beam pipe behind the central magnet (right) (Photos from [122]).

2.2.1.2 Zero Degree Calorimeters. The *ZDC* detectors, shown in Figure 2.5, are a pair of hadronic calorimeters located at 18 meters away from the center of PHENIX along the beam pipe, covering $\theta < 2$ mrad ($6\eta > 6$). They are positioned behind the dipole bending magnets such that the charged beam remnants are swept away from their path by the magnetic field. *ZDCs* are able to catch the spectator neutron remnants with the trajectory very close to the beam line. *ZDCs* are designed to completely contain the hadronic showers of the spectator neutrons.

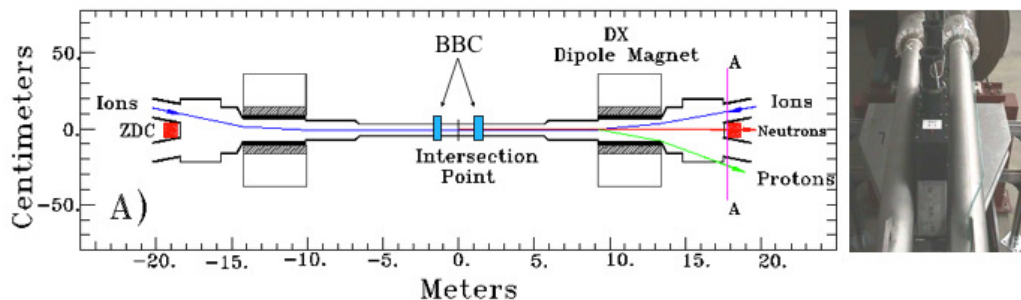


Figure 2.5: Placement of the *ZDC* beyond the forward dipole magnets(left). A *ZDC* as installed between the RHIC blue and yellow beam pipes(right) (Photos from [122]).

2.2.1.3 The Centrality Definition. PHENIX uses the concept of *centrality* to characterize the geometric quantity impact parameter b such that the centrality refers to the percentiles of the total nuclear interaction cross section (7.2 b). The centrality class can be determined from experimental observables, like the multiplicity and energy deposition. Using the Glauber model, the impact parameter b and some other collision quantities can be determined for each centrality class. For example, we can measure the charged particle multiplicity $dN_{\text{ch}}/dN_{\text{evt}}$ in the mid-rapidity $|\eta| < 1$. And the distribution of $d\sigma/dN_{\text{ch}}$ is related to $dN_{\text{evt}}/dN_{\text{ch}}$ by the relation of $N_{\text{evt}} = \sigma \int L dt$. As shown in Figure 2.6, the centrality class is defined by the fraction of the total cross section in a specific bin.

The quantity N_{part} mentioned in Figure 2.6 is a concept of the *Glauber model*. In the Glauber model, the two colliding nuclei are treated as two collections of incoming nucleons. The nucleus-nucleus collision is deemed as a superposition of multiple nucleon-nucleon collisions. The Glauber model is often calculated by a Monte Carlo simulation. The two nuclei are modeled by the computer as two bunches of independent nucleons distributed as some probability distribution function, which travel in straight lines in 3 dimensional space. A random impact parameter b is picked up with a probability according to $d\sigma/db = 2\pi b$. Each N-N collision is independent of other nucleons or any N-N collisions before, and depends only on the distance d between two participating nucleons. If $d < \sqrt{\sigma_{\text{inel}}^{\text{NN}}/\pi}$, a collision is set to happen between the two nucleons. There might be some other complicated considerations involved, such as that the nucleon space distribution is Gaussian alike. In this way, the number of participating nucleons N_{part} and the number of binary nucleon-nucleon collisions N_{coll} are clearly obtained. After many simulations, the average number $\langle N_{\text{part}} \rangle$, $\langle N_{\text{coll}} \rangle$ and other quantities for some

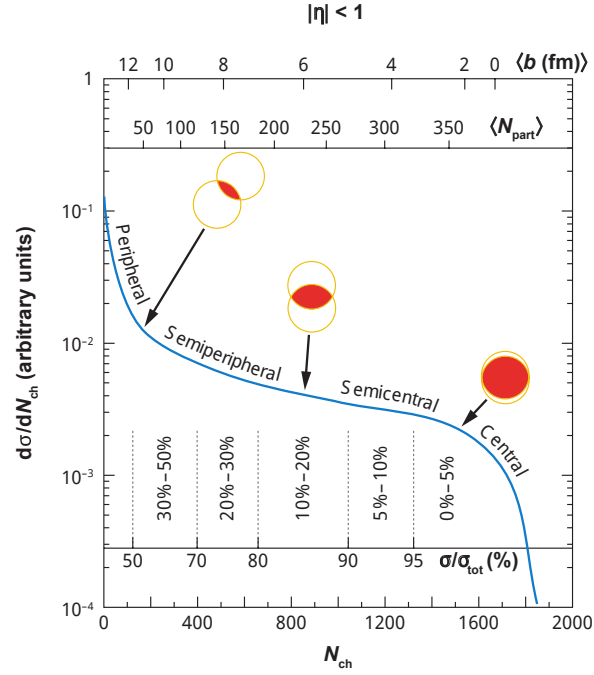


Figure 2.6: Simple example of the definition of the centrality class by the experiment observable, namely the charged particle multiplicity in mid-rapidity N_{ch} [123]. Also, the impact parameter b and the number of participating nucleons N_{part} calculated from the Glauber model are shown in the top of the figure.

specific impact parameter b , which in turn is related to the centrality, can be determined.

The underlying assumption here is that the impact parameter is monotonically related to the particle multiplicity both at the mid-rapidity and the forward-rapidity regions, or other experimental used observables, to make a one-one mapping between the impact parameter and the centrality class (or say, the experimental observables). If there is no such a monotonical relation, the centrality class obtained in the experiment is irrelevant to the impact parameter b , and can not be used to determine N_{part} , N_{coll} by the Glauber model. In the case of large impact parameter

or peripheral events, we expect a small particle multiplicity in the mid-rapidity and a larger number of spectator nucleons in the forward-rapidity. On the contrary, we expect a large particle multiplicity in the mid-rapidity and a small number of spectator nucleons in the forward-rapidity for the central events with small impact parameter.

PHENIX adopts a “clock” method to determine the centrality class by the charge collected in BBCs and the energy deposited in ZDCs. The former quantity is determined by the participating nucleons, while the later are determined by the number of neutrons coming from the colliding nuclei. Figure 2.7 shows the determination of the centrality in PHENIX by BBCs and ZDCs. The response of ZDC is quite interesting. In most central collisions, few spectator neutrons can survive in the collision and reach ZDCs. As the impact parameter increases, more and more spectator neutrons are collected by ZDCs. But, for the most peripheral collisions, though few participating neutrons are involved in the collisions, most spectator neutrons are still bound with the spectator protons, and are swept out by the magnetic field. Therefore, for the most central collisions, few spectator neutrons can hit ZDCs. The centrality can be determined by the combination of BBCs and ZDCs. As shown in Figure 2.7, the ZDCs are sensitive in the most peripheral collisions, and the BBCs are sensitive in the most central collisions.

2.2.1.4 Triggers. There are two sets of level-1 (LVL1) *event triggers* available for Run08 $d+Au$ data. One is the Minimum Bias trigger (*MB*), the other one is the EMCal/RICH Level-1 Trigger (*ERT*). The LVL1 trigger helps to remove empty beam crossing and uninterested events, and serves an essential part of PHENIX on-line system.

For Au+Au collisions, the Min Bias trigger requires at least two photomultiplier hits in each BBC for and at least one neutron detected in each ZDC (which helps to

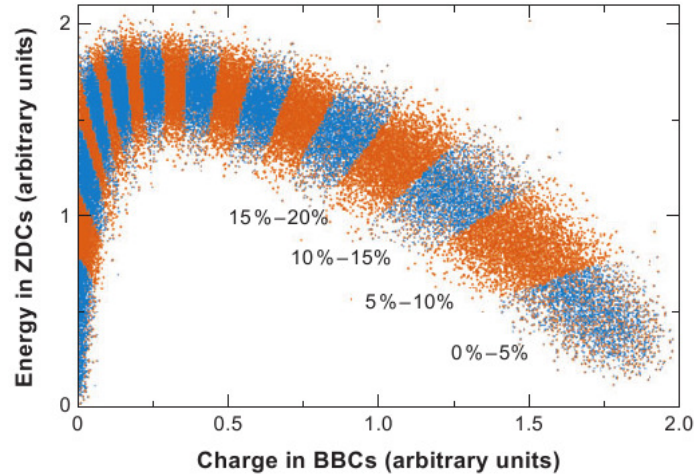


Figure 2.7: The centrality class is determined by the response of BBCs and ZDCs in PHENIX [123].

remove the background events from beam-gas interaction, but is accompanied by a efficiency lost in the most peripheral collisions due to the ZDCs' poor response in such events.). For $p+p$, $d+Au$ and $Cu+Cu$ collisions, the Min Bias trigger requires a coincidence between the BBCs with at least one hit in each BBC detector.

Besides the Min Bias trigger, PHENIX utilizes the ERT trigger, which is triggered by the events with high p_T photons or electrons. The EMCal and RICH subsystems are used in this Level 1 trigger (See Section 2.2.3.1 and 2.2.4 for details of these subsystems). In the EMCal part of the ERT trigger, an energy threshold is required for an overlapping tile of 4x4 EMCal towers in coincidence with the BBC trigger. There are 4 variants, namely 4x4a, 4x4b, 4x4c with different energy thresholds, and 2x2 with an energy thresholds on a tile of 2x2 EMCal towers. This requirement makes sure that there is at least one high p_T photon or electron hit in EMCal. In the RICH part of the ERT trigger, a threshold on the sum of photonelectrons in an unoverlapping tile of 4x5 PMTs in RICH is required. A 4x5

tile can just cover the nominal size of a ring by an electron. Since the tiles are not overlapping, to enhance the efficiency, it's good to choose a relative low threshold. All the thresholds in the ERT trigger can vary run by run. For Run 8 $d+Au$ data in this analysis, the equivalent thresholds before run 250515 are list as below: 2.8 GeV (PbSc) and 2.1 GeV (PbGl) for 4x4a, 3.5 GeV (PbSc) and 2.8 GeV (PbGl) for 4x4b, 2.1 GeV (PbSc) and 1.4 GeV (PbGl) for 4x4c, 600 MeV (PbSc) and 400 MeV (PbGl) for 2x2, and 3 photonelectrons for RICH. From run 250515, the 2x2 thresholds are raised to 800 MeV (PbSc) and 600 MeV (PbGl) according to the summary page at <http://www.phenix.bnl.gov/WWW/trigger/pp/c-arm/Run3/run8.html>.

A further Level-2 (LVL2) trigger is used in the event assembling to enhance the interested physics data. An overview of LVL2 algorithms are summarized in Table 2.1.

The Min-Bias trigger loses the efficiency in the most peripheral collisions, because ZDCs can possibly not able to get a coincidence on both sides.

2.2.2 Charged Particle Tracking. The central tracking system for charged particles consists of the Drift Chambers (DC), the Pad chambers (PC) and the Time Expansion Chamber (TEC). Two DCs are located on the east and west arm respectively, each covers $\pi/2$ in azimuth. There are three layers of Pad Chambers, PC1, PC2, PC3 on the west arm, and PC1, PC3 and TEC on the east arm respectively. DCs provide high resolution measurements of the trajectory and momentum of the charged particles, PCs can provide 3D spacial point information for pattern recognition, and TEC tracks the charged particles between RICH and EMCal, identifies them by measuring dE/dX and improves the e/π separation. The multiplicity of charged particles in the central collisions at RHIC energy level is about $dN_c/d\eta = 700$ with a spectrum peaking at 300-500 MeV for soft particles. Due

Table 2.1: Overview of LVL2 trigger algorithm

Trigger	Method
Single Electron	Match RICH rings to EMCal clusters Make EMCal energy threshold cut
Electron Pair	Calculate invariant mass of electron pairs Make invariant mass cut
Single Muon	Calculate invariant mass of electron pairs Make invariant mass cut
Muon Pair	Find roads through MuID panels
High p_T EMCal	Find EMCal clusters Make threshold cuts
High p_T Charged	Match PC and DC hits Cut on the bend angle
Coherent Peripheral Events	Look for ZDC trigger with no BBC trigger Look for PC hits
Centrality Selection	Use BBC and ZDC to estimate centrality Make centrality cuts on selected triggers

to the partial coverage in the azimuthal angle, a large number of charged particles enter the central tracking system without passing through DC. All the three detectors are essential to perform both an accurate measurement and a good pattern recognition in such a large multiplicity environment.

2.2.2.1 Drift Chamber. The *Drift Chambers* are cylinder shaped multiwire chambers, as shown in Figure 2.3. It locates at a radial distance from 2 m

to 2.4 m, and it is 2 m along the beam axis. Thus each DC can cover 90° in azimuthal angle and ± 0.35 in pseudorapidity. DCs are outside of the central magnet field, and the residual magnetic field at DCs is about 0.6kG. The central magnet field is designed to be along the beam axis, therefore it only bent the charged particles in azimuth. Accordingly, DCs have better resolution in r - ϕ than z . The single wire resolution in r - ϕ is better than $150\mu m$, while the single wire resolution in z is designed to be better than $2mm$ only.

The volume of each DC detector on the east/west arm is confined by a cylinder Ti frame defined the azimuthal and z limits, also by Five-mil Al-mylar window defining the radial limits. Each frame is divided into 20 equal sectors, and each sector extends 4.5° in azimuth, as shown Figure 2.8.. In each sector are six types of wire modules positioned radially, namely X1, U1, V1, X2, U2 and V2. In each module, there are 4 anode planes and 4 cathode planes. In the anode plane, there are other wires beside the anode wires. The anode wires are separated by the Potential wire, and surrounded by Gate wires and Back wires. Also, there are two Termination wires on both sides of the anode plane in each module. For X wire cells, there are 12 anode wires in each anode plane in a module, and for U, V wire cells, there are 4 anode wires in each plane, as shown in Figure 2.8..

The X wires are parallel to the beam pipe, and they are designed to have excellent resolution in r - ϕ plane. The U, V wires are placed with a small stereo angle (6°) respect to the X wires so that DCs are able to get the z position by those wires, see Figure 2.8. The distance between the anode wires and the location where the electrons/ions are caused by the passing charged particle can be determined by the arrive time and the drift velocity in the working gas. In DC, the working gas is mixed by 50% Argone and 50% Ethane.

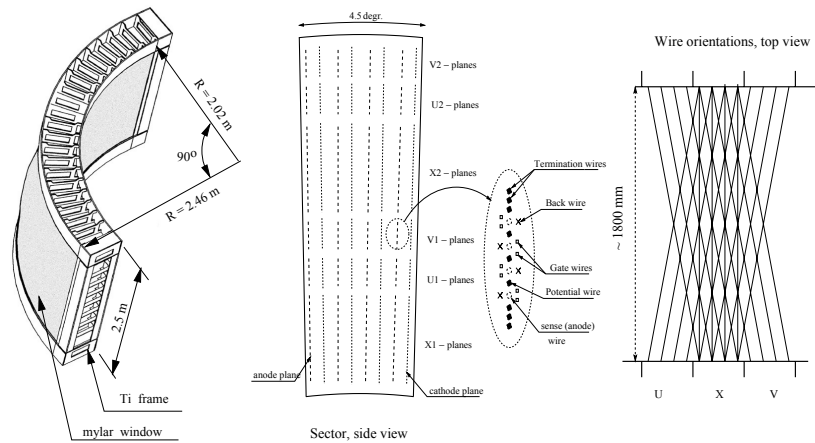


Figure 2.8: The frame of Drift Chamber (left), side view of the layout of wire arrangement in one sector and in one V1 anode plane (middle), top view of the wire orientation (right) [124].

The track in Drift Chamber is reconstructed by a combinatorial Hough transform (CHT) technique. The Drift Chamber hits are mapped into a feature space which is defined by ϕ and α , as shown in Figure 2.9. ϕ is defined by the azimuthal angle of the crosspoint of the track trajectory and the middle radius of DC, while α is defined as the inclination angle of the track at that crosspoint. α is proportional to the inverse of p_T such that it gives us a first estimation of the value of p_T . X1, X2 hits are both required for the track reconstruction, and U, V hits are needed to determine z information.

2.2.2.2 Pad Chamber. After leaving the Drift Chamber, a charged particle enters a set of separate layers of *Pad Chambers*. They are in fact multiwire proportional chambers. The first layer PC1 is located between DC and RICH, about 2.45m away from the beam, which can determine the z coordinate at the outside of DC and make a good crosscheck with U, V wire readout in DC. The third layer PC3 is located just before EMCal, 4.9m away from the beam. The second layer PC2 is

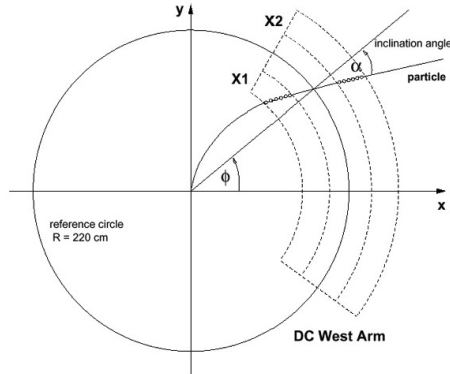


Figure 2.9: Illustration of the track reconstruction in Drift Chamber using the CHT technique. The circles near the charged particle trajectory represent the Drift Chamber hits [125].

only installed in the west central arm, as shown in Figure 2.3. PC2 and PC3 are needed to remove the particles which come from secondary interaction or hadron decay outside DC and finally enter EMCal. Also, low momentum charged particles which fly around DC and PC1 can be ruled out by PC2 and PC3 too. And the situation that three layer's hits in a straight line serves a good confirmation of a particle trajectory.

2.2.3 Photon Reconstruction.

2.2.3.1 Electromagnetic Calorimeter. The *Electromagnetic Calorimeters* (EMCal or EMC) are primarily to measure the position, energy and time-of-flight information of photons and electrons / positrons in midrapdity region. Also, the quick response to energy deposition of EMCal is useful in triggering events with high p_T photons and electrons. The underlying physics is that the photons and electrons interact with the medium by the electromagnetic shower, through cascading bremsstrahlung (for electrons) and pair production (for photons, note: photonelectric effect and Compton scattering are only important when the energy of

the incident particle is below a few MeV), while the hadrons deposit only a small fraction of the total energy by the hadronic shower, via strong interaction, which is more complicated. Two different detector technologies are adopted in the PHENIX EMCal detector, one is lead scintillator calorimeters(PbSc), as shown in Figure 2.10a, the other is lead glass Cherenkov detector(PbGl), as shown in Figure 2.10b. PbSc is a sampling calorimeter, consisting layers of lead and scintillators; while PbGl is a homogeneous calorimeter, made of a whole lead-glass Cherenkov radiator. Such a configuration provides a valuable cross-check between two technologies with different characteristics. EMCal is the outmost of the PHENIX central arm, and is 5 meters away from the beam pipe. EMCal is composed of eight sectors. Six of them are PbSc detectors, and the other two are PbGl detectors. The PbSc has great signal linearity and timing response, and the PbGl has excellent energy resolution and granularity.

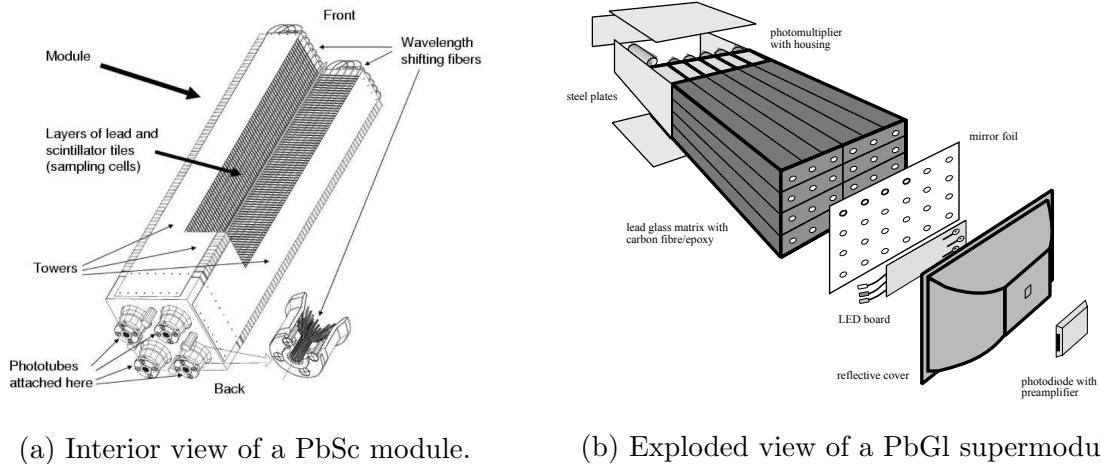


Figure 2.10: Diagrams of EMCal Detectors [126].

The PbSc detector consists of 15552 individual towers. Each tower is composed of 66 sampling cells which consists of alternating lead and scintillator layers. PMTs are attached in the backend, which are connected by optical fibers with those cells. A module of PbSc is composed of four individual towers, which are mechanically hold together. Thirty six modules are attached to a backbone and held together to form a supermodule (SM). A sector consists of eighteen supermodules. The energy resolution of PbSc was obtained by a beam test at BNL and CERN, and the fit to a quadratic formula is:

$$\frac{\sigma_E(E)}{E} = 2.1\% \oplus \frac{8.1\%}{\sqrt{E(\text{GeV})}}. \quad (2.1)$$

The position resolution can be described well by a simple formula

$$\sigma_x(E, \theta) = \sigma_0(E) \oplus \Delta \times \sin(\theta) \quad (2.2)$$

where

$$\sigma_0(E) = 1.55 \oplus \frac{5.7}{\sqrt{E(\text{GeV})}} (\text{mm}) \quad (2.3)$$

is the position resolution for normal incidence and $\Delta \sim L_{rad}$.

The PbGl detector is previously serviced for CERN experiment WA98. Each PbGl sector comprises 192 supermodules in an array of 16 SM in wide and 12 SM in height. Each supermodule consists of 24 modules in an array of 6 modules wide and 4 modules high. Each module is read out by a photomultiplier. The response of the PbGl has been studied in test beams of AGS at BNL and SPS at CERN. The energy resolution results are shown with the fit parameterization

$$\frac{\sigma(E)}{E} = \frac{[5.9 \pm 0.1]\%}{\sqrt{E/\text{GeV}}} \oplus [0.8 \pm 0.1]\%. \quad (2.4)$$

The measured position resolution can be fitted with the parameterization

$$\sigma_x(E) = \frac{[8.4 \pm 0.3]\text{mm}}{\sqrt{E/\text{GeV}}} \oplus [0.2 \pm 0.1]\text{mm}. \quad (2.5)$$

2.2.3.2 Muon Piston Calorimeter. The *Muon Piston Calorimeter* (MPC) is a small lead-tungstate (PbWO_4) based electromagnetic calorimeter with Avalanche Photodiode (APD) readout at the south and north side of PHENIX. It covers the rapidity in $3.1 < |\eta| < 3.9$, and the azimuth in 2π . MPC helps PHENIX to extend the acceptance to the forward/backward region and go further in the small x and spin physics. MPC is compact enough to be installed in the small hole just in front of the muon piston after which MPC is named, and strong enough to withstand the magnetic field there. Each MPC are composed of 8 modules, as shown in Figure 2.11, including 4 wedges (with 29 crystals each) and 4 bricks (with 19 crystals each). MPC consists of 192 crystals in total at each side.

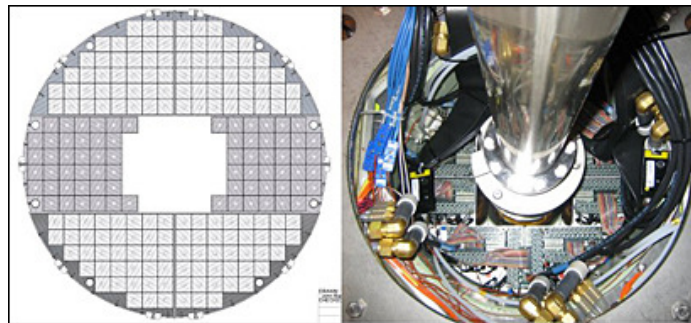


Figure 2.11: Muon Piston Calorimeter. Left: detector layout of the PbWO_4 crystals; Right: MPC is installed around the beam pipe (Photos from [122]).

2.2.4 Electron Identification. The *Ring Imaging Cherenkov detector* (RICH), shown in Figure 2.12, is the principal electron ID device in PHENIX. The RICH detects the Cherenkov light ring produced by charged particles whose speed is faster than the speed of light in the medium, and measures the speed of that fast moving charged particle. If the momentum of the particle is provided, the mass of the particle can be derived and the type of particle can be identified. The RICH

detector at PHENIX can identify the electrons above 18 MeV/ c , and the Cherenkov threshold for charged pions is 4.65 GeV/ c , which is much higher. Since the charged pions are the lightest charged hadrons, so any particles with momentum below 4.65 GeV/ c detected by the RICH are electrons uniquely. In this way, the RICH detector can be used to veto electrons from charged hadron tracks, which is useful in the hadronic jet analysis. The medium in the RICH detector is CO₂ gas at 1 atm with refractive index 1.000410. The yield of Cherenkov light is determined by the length of the radiator medium, so the RICH detector is very large due to the gas vessel volume. The RICH detector produces about 12 photons in average for a $\beta \approx 1$ particle over a path length of 1.2 meters. To reduce the size of the radiation length, a set of very thin mirrors are mounted onto the PMT array, just outside the central arm η acceptance. There are 5120 PMTs in total mounted in the RICH detector.

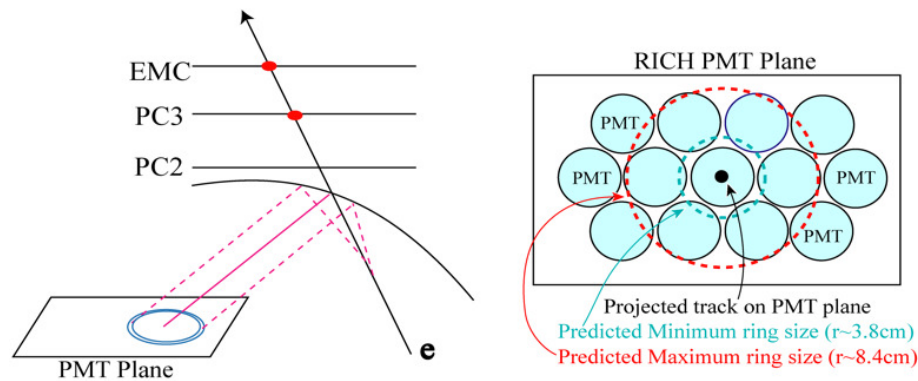


Figure 2.12: Electron signal depositions are shown in the RICH. Cherenkov radiation is reflected onto PMT array (left). Ring sizes are shown relative to PMT lattice (right). Plots from [122].

3 DATA ANALYSIS

3.1 PHENIX Data Set

Since 2000, PHENIX has collected data for each run period, see Table 3.1. In this analysis, Run08 d +Au ERT triggered data are selected, and the number of events is about 10 million.

Table 3.1: A summary of PHENIX data sets through 2008.

RHIC Run (Year)	beam species	beam energy (GeV)	sampled events	$\int Ldt$
1 (2000)	Au+Au	130	10 M	$1 \mu b^{-1}$
2 (2001/2)	Au+Au	200	170 M	$24 \mu b^{-1}$
	$p+p$	200	3.7 B	$0.15 pb^{-1}$
3 (2002/3)	d +Au	200	5.5 B	$2.74 nb^{-1}$
	$p+p$	200	6.6 B	$0.35 pb^{-1}$
4 (2003/4)	Au+Au	200	1.5 B	$241 \mu b^{-1}$
	Au+Au	62.4	58 M	$9 \mu b^{-1}$
5 (2005)	Cu+Cu	200	8.6 B	$3 nb^{-1}$
	Cu+Cu	62.4	400 M	$0.19 nb^{-1}$
	Cu+Cu	22.4	9 M	$2.7 \mu b^{-1}$
	$p+p$	200	85 B	$3.8 pb^{-1}$
6 (2006)	$p+p$	200	233 B	$10.7 pb^{-1}$
	$p+p$	62.4	28 B	$0.1 pb^{-1}$
7 (2007)	Au+Au	200	5.1 B	$813 \mu b^{-1}$
8 (2008)	d +Au	200	160 B	$80 nb^{-1}$
	$p+p$	200	115 B	$5.2 pb^{-1}$

3.2 Particle Identification

3.2.1 Choice of Particle Types. In two particle jet correlations, the final state hadrons produced in jets are the primary focus of our studies. So the charged hadrons detected by the drift chambers are used as the partners. The choice of triggers is a little bit of subtle. The initial triggers are the direct photons, especially the isolated non-decay-tagged ones, because the direct photons provide a precise assessment of the jet momenta and z_T values. However, the direct photon measurement suffers from the poor statistical uncertainties as well as low signal / background (direct / decay) ratio in inclusive photon samples. Then we move to π^0 's as the triggers in two particle correlations. First, pions, including π^0 , π^\pm , are the lightest hadrons, which are created abundantly in jets. The events analysed are not rare direct photon events any more, thus, the statistical uncertainties are improved. Second, PHENIX doesn't have any tracking detector between the beam and the drift chambers in its 2008 detector configuration (Later PHENIX has the silicon vertex detector installed to improve the tracking capability, but not for Run08). So for high p_T π^\pm particles, PHENIX has a large background which limits the capability of π^\pm - h^\pm analysis in high p_T regions. Meanwhile, PHENIX EMCAL detectors provide precise energy and position resolution for the photon detection. The π^0 can be reconstruct from two decay photons by the invariant mass method. Considering this branch ratio of $\pi^0 \rightarrow \gamma + \gamma$ decay channel is about 98.8%, the life time of the π^0 is about 8.4×10^{-17} seconds, ~ 25.1 nm, PHENIX has the capability to detect a large chunk of the π^0 's. And the combinatoric background in the π^0 detection is small (S/B > 18), see Section 3.9. Therefore, the π^0 is chosen as the trigger in our analysis.

3.2.2 Photon Identification. Clusters in the EMCAL are identified as photons with these cuts:

- shower shape cut: $\chi^2 < 3$
- track-based charged hadron veto
- hot and dead tower exclusion
- fiducial cut: $|Z_{EMC}| < 155$ cm

The shower shape for an electromagnetic shower is different from a hadronic shower. The EMCal detector's response is predicted by the simulation with PISA (PHENIX Integrated Simulation Application, which is based on GEANT3 libraries), and a predicted EM shower shape function for i -th tower (F_i) is parameterized as:

$$\begin{aligned}
 F_i &= \frac{E_i^{pred}}{E_{tot}} \\
 &= P_1(E_{tot}, \alpha) \exp\left\{-\frac{(r_i/r_0)^3}{P_2(E_{tot}, \alpha)}\right\} + P_3(E_{tot}, \alpha) \exp\left\{-\frac{(r_i/r_0)}{P_4(E_{tot}, \alpha)}\right\}
 \end{aligned} \tag{3.1}$$

Where, E_i^{pred} is the predicted energy of i -th tower, r_i is the distance between the center of i -th tower and corrected hit position, and r_0 is the surface size of a EMCal cell which is 5.5 cm. P_{1-4} are the parameterized functions of total energy E_{tot} and impact angle α . P_{1-4} are obtained in the test beam run as

$$\begin{aligned}
 P_1 &= 0.59 - (1.45 + 0.13 \ln E_{tot}) \sin^2 \alpha \\
 P_2 &= 0.27 - (0.80 + 0.32 \ln E_{tot}) \sin^2 \alpha \\
 P_3 &= 0.25 - (0.45 + 0.036 \ln E_{tot}) \sin^2 \alpha \\
 P_4 &= 0.42
 \end{aligned} \tag{3.2}$$

Then the electromagnetic showers can be identified from the hadronic shower by the shower shape profile χ^2 test,

$$\chi^2 = \sum_i \frac{(E_i^{pred} - E_i^{meas})^2}{\sigma_i^2} \tag{3.3}$$

where E_I^{meas} is the measured energy in i -th tower after the calibration, E_i^{pred} is the predicted energy by Equation 3.1, and σ_i is the variance of the predicted energy function as

$$\sigma_i^2 = A \cdot E_i^{pred} (1 + B \sqrt{E_{tot}} \sin^4 \alpha) \left(1 - \frac{E_i^{pred}}{E_{tot}}\right) + q(E_{tot}) \quad (3.4)$$

where the constant A and B are obtained by the test beam data.

Although most of the hadronic shower is removed by the shower shape cut, there is still a considerable amount of hadron contamination. The photon candidate clusters are distinguished from the charged particles (electron converted by photon or remaining hadron) by associating the photon candidate clusters with charged particle hits in Pad Chamber (PC3), which is just 5 cm away in front of EMCal. The distance between hit positions of EMCal and PC3 is given by

$$r_{emc-pc3}^{veto} = \sqrt{dx_{emc-pc3}^2 + dy_{emc-pc3}^2 + dz_{emc-pc3}^2} \quad (3.5)$$

The threshold for the charged particle veto is set to 6.5 cm based on the Moliere radius.

Any bad conditioned towers are recognized and removed by the hot/dead tower map. A tower with hit frequency higher/lower than 5σ of the averaged hit frequency per tower is tagged as a hot/dead tower. Any hot/dead tower with its 3x3 nearby towers are excluded from later analysis.

A fiducial cut on the edge could help to rule out the photons which are unable to be reconstructed correctly, if part of their energy is not deposited into the EMCal.

The efficiency of the photon identification cut is NOT studied for now, and should be done by simulation.

3.2.3 π^0 and η Identification. The π^0 and η are neutral mesons which can decay into photons. They are reconstructed by the invariant mass of photon

pairs by

$$\begin{aligned}
m_{inv} &= \sqrt{(E_1 + E_2)^2 - (\mathbf{p}_1 + \mathbf{p}_2)^2} \\
&= \sqrt{2E_1E_2\left(1 - \frac{x_1x_2 + y_1y_2 + z_1z_2}{l_1l_2}\right)} \\
&= \sqrt{2E_1E_2(1 - \cos\psi)}
\end{aligned} \tag{3.6}$$

where ψ is the opening angle between the two photons' tracks, E_i is the energy of photon i , \mathbf{p}_i is the momentum of photon i , x_i, y_i, z_i are the coordinates of photon i , l_i is the path length from the collision vertex which is determined by BBCs to the hit position of photon i . The reconstructed invariant mass should be within the mass window for π^0 or η mesons. The invariant mass spectrum of the photon pairs can be fitted by a gaussian peak of the "real" π^0 and a 3rd order polynomial of fake π^0 from the combinatorial background. The mass window for π^0 is 120-160MeV, and that for η is 530-580MeV. To reduce the combinatorial background, the two photons' energy should be greater than 1 GeV, which helps to remove the soft photons, the major source of the combinatorial background. High p_T photons which decay from the same π^0 are likely not to separate far away and to remain in the same sector of EMCal, while the random combinatorial matching of photon pairs has no such trend. Accordingly, the sub-leading photon is required to be in the same sector as the leading photon. Also, in the high p_T region, most fake π^0 s are due to the random combination of a high p_T (must be high energy) photon which comes from a real π^0 and a low energy soft photon. They can possibly be distinguished by the concept of asymmetry:

$$\text{asymmetry} = \left| \frac{E_1 - E_2}{E_1 + E_2} \right|. \tag{3.7}$$

The asymmetry cut on the photon pairs can alleviate the random combinatorial π^0 match problem. The threshold is determined by both the energy of the photons and

the centrality of the event. The background from the combinatorial match for a π^0 is pretty small in simulations. The contribution from a false match for η should be removed by side band analysis, see Section 3.9.

3.2.4 Charged Hadrons Identification. The reconstructed tracks in the drift chamber are identified as charged hadron tracks based on the following criteria:

- Track quality
- PC3 and EMCal matching
- RICH ring veto
- Drift chamber z-edge cut
- EMCal energy cut

In a high multiplicity environment, fake tracks could be reconstructed by unrelated hits in the tracking system, or, the real tracks constructed could lack hitting point in some detectors. Accordingly, the quality control in the charged track reconstruction is an important part of the analysis. In PHENIX tracking system, six bits, shown below, are used to describe the quality of the reconstructed tracks.

- ◊ bit 0 (1): X1 used
- ◊ bit 1 (2): X2 used
- ◊ bit 2 (4): UV found
- ◊ bit 3 (8): UV unique
- ◊ bit 4 (16): PC1 found

◊ bit 5 (32): PC1 unique

The tracks with quality bit of 63 or 31 are selected in this analysis . Quality 63 means hits in X1, X2 and UV wires in DC and also a unique hit in the PC1, while quality 31 doesn't require PC1 hit to be unique.

The DC/PC1 hit matching with quality selection is not a guarantee to erase the “ghost” particles which are just random matching between them. Also the background from off-vertex tracks, such as the tracks from conversion, deflection and decay, should be excluded from our analysis since the current charged track analysis assumes that all tracks are from the collision vertex. Due to these consideration, the outer PC layers are included into the charged particle selection cuts. Since PC2 is only installed on west arm, only PC3 is incorporated into the analysis at this moment. Along with the magnetic field consideration, the tracks reconstructed from DC and PC1 hit are projected to PC3, and the projection point should match a nearby PC3 hit. The matching window is determined by a Gaussian fit of the distance between the projection point and the PC3 hit position, and the PC3 matching cut is appropriately selected as 3σ of the normalized Gaussian peak, or $\sqrt{\sigma_{\Delta\phi}^2 + \sigma_{\Delta z}^2} < 3$. Actually it is a double Gaussian fit because the real match and random combinatorics have their own Gaussian peaks. The EMCAL matching is pretty similar to the PC3 matching mentioned above.

Electrons are rejected by vetoing from the RICH ring. Charged hadrons with p_T less than 4.65 GeV/ c are unable to radiate Cherenkov light in the RICH detector, and a zero coincidence with RICH radiation rings, a.k.a. $n0 \leq 0$, serves as a cut for charged tracks with p_T below this value. If a charged particle's p_T is greater than this threshold, it could still radiate Cherenkov rings based on its mass. The pions radiate first at or just above this threshold, then other heavier charged particles radiate with even higher p_T . If a charged particle is above its threshold for radiating

in the RICH, an e/p ratio cut in EMCal is applied. In this cut, the ratio between the energy deposited in EMCal by this particle and its own momentum is calculated and should be below a specific value.

It's possible that a charged particle hits the edge region of DC and crosses out of its side boundary. To prevent this case which would bring unexpected errors into the charged particle efficiency estimation, a fiducial cut (or a z-edge cut of DC) is applied as shown below

- ◇ West arm: $-0.54 < \phi_{DC} < 0.92$
- ◇ East arm: $2.25 < \phi_{DC} < 3.65$
- ◇ $Z_{ed} < 75cm$
- ◇ $\theta_0 < 0$

wher ϕ_{DC} and Z_{ed} are the ϕ and z coordinates of the hit position on DC respectively, and θ_0 is the polar angle of the reconstructed track from the collision vertex which is determined by the BBC detectors.

3.3 d +Au Centrality Categorization

After the observation of collective flow in p +Pb and d +Au collisions (see Section 1.4), and π^0 , η and jet R_{dA} (defined in Equation 1.43) anomalies in peripheral d +Au collisions (see Section 1.3.2), it is time to review how we characterize centrality and geometry parameters in such collisions . It is crucial in all R_{dA} measurements.

In A+A collisions, the centrality is defined by the particle multiplicity and summed energy deposited in some pseudorapidity range. Some quantities associated the centrality concept can be defined for each event, such as N_{coll} and N_{part} . N_{coll} is the number of binary collisions in one event, it is also called N_{binary} in some

literatures. N_{part} is the number of participant (wounded) nucleons in one event. In a more central collision event, N_{coll} and N_{part} are larger.

However, in $p+A$ collisions, the relative particle multiplicity fluctuation for some N_{coll} value is larger than A+A collisions due to the relatively small N_{coll} value range. Also, the centrality definition might be correlated with the observable, and introduce some bias. This is another reason that we need to be extra careful for centrality determination.

PHENIX has published its method of determination of centralities in $d+Au$ collisions [127]. The described method is the one adopted in this analysis. PHENIX $d+Au$ centrality is defined as the percentile based on the summed charge multiplicity measured at BBC in the Au going direction ($-3.9 < \eta < -3.0$). The Glauber model MC simulation is used to map the initial geometry parameters to the observed charge multiplicity. The transverse position of nucleons in a deuteron is decided by a Hulthén wave function

$$\psi_d(r_{pn}) = \left(\frac{\alpha\beta(\alpha + \beta)}{2\pi(\alpha - \beta)^2} \right)^{1/2} \frac{e^{-\alpha r_{pn}} - e^{-\beta r_{pn}}}{r_{pn}} \quad (3.8)$$

with $\alpha = 0.228 \text{ fm}^{-1}$ and $\beta = 1.18 \text{ fm}^{-1}$. The square of this wave function determines the probability distribution in a deuteron. For the gold nucleus, a Woods-Saxon density function is used,

$$\rho(r) = \frac{\rho_0}{1 + e^{\frac{r-R}{a}}} \quad (3.9)$$

with radius $R = 6.38 \text{ fm}$, and diffuse parameter $a = 0.54 \text{ fm}$. On an event-by-event basis, all nucleons are randomly placed. If the distance between two nucleons is smaller than σ_{NN}/π (here, σ_{NN} is the nucleon-nucleon inelastic cross section, $\sigma_{NN} = 42 \text{ mb}$), a nucleon-nucleon collision is set to occur. In this event, N_{part} , N_{coll} and all geometric information, such as spacial position and overlapping region, are collected.

In an assumption that the charge multiplicity is proportional to the number of binary collisions, and the fluctuation follows the negative binomial distribution,

$$\text{NBD}(x; \mu, \kappa) = \left(1 + \frac{\mu}{\kappa}\right) \frac{(\kappa + x - 1)!}{x!(\kappa - 1)!} \left(\frac{\mu}{\mu + \kappa}\right)^x. \quad (3.10)$$

and the charge multiplicity distribution / probability is determined as

$$P(x) = \sum_{n=1}^{N_{\text{binary}}(\text{max})} Gl(n) \times \text{NBD}(x; n\mu, n\kappa), \quad (3.11)$$

here x is the BBC charge multiplicity, $Gl(n)$ is the number of binary collisions from the Glauber model, normalized as per event quantity. μ and κ is obtained by fitting to the experimental data with x greater than 20. Data in the small x region are expected to deviate from this formula due to MB trigger requirement (one hit in d going BBC, then quite a few in Au going BBC). The results are $\mu = 3.03$ and $\kappa = 0.46$. If we set the charge multiplicity proportional to the number of participant instead of the number of binary collisions, the results are almost the same, and the difference is included into systematic uncertainties. A fit shows that the MB trigger fires $88 \pm 4\%$ of 2.19 barn inelastic d +Au cross section determined in the Glauber model.

Other quantities in the initial state, such as geometric parameters, can be determined. For example, the eccentricity ε_2 and higher moments, which represents the asymmetry of the overlapping collision region, are determined as

$$\varepsilon_n = \frac{\sqrt{\langle r^2 \cos(n\phi) \rangle^2 + \langle r^2 \sin(n\phi) \rangle^2}}{\langle r^2 \rangle}, \quad (3.12)$$

here, the average $\langle \cdot \rangle$ means an average over the spacial distribution of participating nucleons from the Glauber model. The spacial distribution is taken as point-like, disk-like, Gaussian and disk-NBD[127], and the difference between combinations are included into systematic uncertainties. The spacial overlap area is calculated as

$$S = 4\pi\sqrt{\langle x^2 \rangle \langle y^2 \rangle - \langle xy \rangle^2} \quad (3.13)$$

and the mean radius

$$\bar{R} = \frac{1}{\sqrt{1/\langle x^2 \rangle + 1/\langle y^2 \rangle}}. \quad (3.14)$$

However, there is a correlation between a trigger requirement and the charge multiplicity in BBC. Considering the nucleon-nucleon 42 mb inelastic cross section in three parts:

1. nondiffractive collisions, 28 mb
2. single diffractive collisions, 10 mb
3. double diffractive collisions, 4 mb

The particle products in diffractive events are mostly distributed around the beam, hence have small amount in the BBC, or say, a small charged distribution in the BBC. For this sake, the BBC trigger is more efficient to fire nondiffractive events, which has a large probability to emit a π^0 in midrapidity and detected by a central arm detector. Therefore, there is an autocorrelation between the charge multiplicity and a trigger requirement because our triggers tend to fire nondiffractive events. When we measure π^0 yields, we have to consider events that don't fire the trigger. Our MB trigger are selecting events with bias, it not simply "minimum bias". This effect is universal in $p+p$ and $d+Au$, and affects all yield measurements, such as R_{dA} measurements. A correction for yields is needed. You might ask why we can't simply use a clock trigger ⁸ since there is no detector issue? Because the clock trigger can't remove the beam-gas interaction background. Also, PHENIX analysis has assumptions that the events occur close to the detector center, only the MB trigger can ensure this requirement.

⁸ A clock trigger fires randomly on some time. A true randomness means no correlation. Of course, a clock trigger is correlated with time or a clock, but there is no detector issue, no physics observable correlation except it is correlated with time!

This bias has another consequence in terms of centrality determination in $d+Au$. An event with physics interests, such as a nondiffractive collision or an event with π^0 in midrapidity, has more charge multiplicity than others, and is more likely classified as large centrality. In peripheral collisions, such a centrality migration causes yields to go down. While in central collisions, it cause yields to go up. Both need corrections.

To correct the bias-factor, PHENIX first determines the charge multiplicity increase in $p+p$ events from MB and clock trigger data. The additional charge corrects μ and κ in NBD both by a factor of 1.55 ± 0.23 . Also PHENIX assumes that

1. in an event with N binary collisions, the one with a hard scattering is biased to higher charge multiplicity and higher trigger efficiency
2. the increase in $p+p$ is applicable to the one binary hard scattering in $d+Au$
3. the other $N-1$ binary collisions are unaffected

Then they calculate the invariant yields with and without this bias, and obtain the bias-factor correction. This factor could be applied in all yields measurements, such as R_{dA}

$$R_{dAu} = \frac{c dN^{dAu}/dy}{\langle N_{\text{coll}} \rangle dN^{pp}/dy}, \quad (3.15)$$

here, c is this bias-factor correction.

3.4 p_T and Centrality Selection

- Trigger binning: 5-7, 7-9, 9-12, 12-15 GeV/ c
- Partner binning: 0.6-1, 1-2, 2-3, 3-5, 5-7 GeV/ c
- Centrality class: 0-20%, 20-40%, 40-60%, 60-88%

3.5 Event and Particle Selections for Final Results

The data set is Run8dAu200ERT data set.

- Event cut:
 - $|Z_{vtx}| < 30$ cm
- Photon cuts:
 - shower shape cut $\chi^2 < 3$
 - PbSc/PbSc warnmap cut with mask 0x3fe1ce70
 - my own 3x3 hot tower cut
 - edge tower cut
 - fiducial cut: $|Z_{emc}| < 155$ cm
 - firing ERTtrigger
 - veto based on the distance to the closest charged track
- π^0 cuts:
 - two decay photons in the same arm
 - brother decay photon's energy > 0.5 GeV
 - $0.12 < \pi^0 \text{ InvMass} < 0.16$
- Charged hadron cuts:
 - quality cuts: 31 or 63
 - RICH n0 cut: $n0 \leq 0$ when $p_T < 5.0$
 - PC3 matching cuts: $|pc3sdz| < 3$ && $|pc3sdphi| < 3$ at all p_T

- no EMC matching cut
- no e/p cut
- Mixing requirements:
 - centrality within 5%
 - vertex within 5 cm
 - mixing multiplier ≥ 100

3.6 Two Particle Correlation

For heavy ion collisions, even for p+p or d+A collisions, the large amount of soft particles makes the direct jet reconstruction difficult. For the existing jet reconstruction methods, they are forced to use particles with high p_T values (as large as several GeV/c) to avoid the soft particles background. If we include these particles, the jet would be too broad and include the contamination from “underlying events”. The situation is even complicated further by the limited acceptance of PHENIX detector, because the central arm can detect the particles with $|\eta| < 0.35$ which leads to some of the jet constituents being leaked outside of the detector acceptance.

The *two-particle azimuthal correlation method* is an alternative tool to investigate the jet properties, as illustrated in Figure 3.1. A *trigger* particle is selected, usually with some conditions such as the high p_T value which indicates the presence of a jet, then we get the pair distributions from other particles in the same event, which are called *partner* particles. It could be the distribution in the azimuthal plane, such as pair angle $\Delta\phi$ distribution, or it could be distributions in a larger space such as $\Delta\phi$ and $\Delta\eta$ 2-dimensional distributions. Using the azimuthal angle is based on the fact that in Leading-Order QCD, the outgoing partons in hard

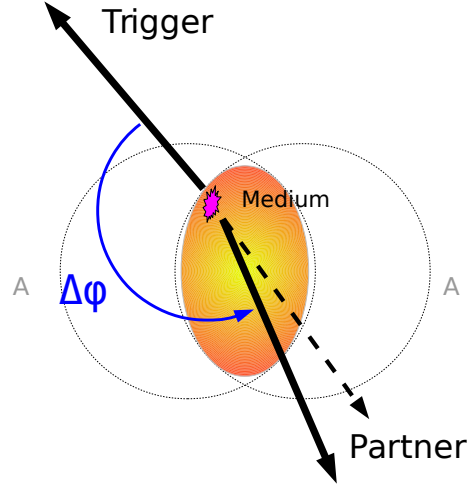


Figure 3.1: Two particle azimuthal correlation illustration

scattering events are back-to-back in the azimuthal angle. Any deviation from this should be a result from the Next-to-Leading-Order effect, soft gluon radiation, multiple scattering or the response from the medium. With carefully chosen variables, the contribution from different effects could be distinguished by the two-particle azimuthal correlation method. The result from $p+A$ collisions serves as a baseline for comparing with $A+A$, and could make a clear view of the separate contributions of the deviations coming from hot dense medium and cold nuclear medium. In our two-particle azimuthal correlation method, a high p_T ($\geq 5\text{GeV}/c$) trigger, either a photon or a π^0 is chosen as a trigger. Within this particular p_T range for the trigger, if the trigger is a direct photon, it is likely either coming directly from the hard scattering process for the prompt photon, or part of the jet, which is the fragmentation products of a hard scattering parton, for a decay photon or a π^0 . Actually, most of decay photons come from the decay mode of π^0 s as $\pi^0 \rightarrow \gamma + \gamma$. On the other hand, the charged hadrons are chosen as the associated

partners. The p_T threshold for the associated particles helps to remove some of the soft particle background which comes from the underlying events. Due to the nature of the hard scattering events, the trigger and the associated particles tends to swarm together or to fly apart almost back-to-back. This could be clearly visualized by looking at the distribution of the azimuthal angle differences between the trigger and the associated particles, as shown in Figure 3.2. The two peaks in $\Delta\phi$ distribution of the two-particle correlation are corresponding to the near- and away-side jets to which the associated partner hadron belongs. The so called near- and away-side are relative to the trigger's direction.

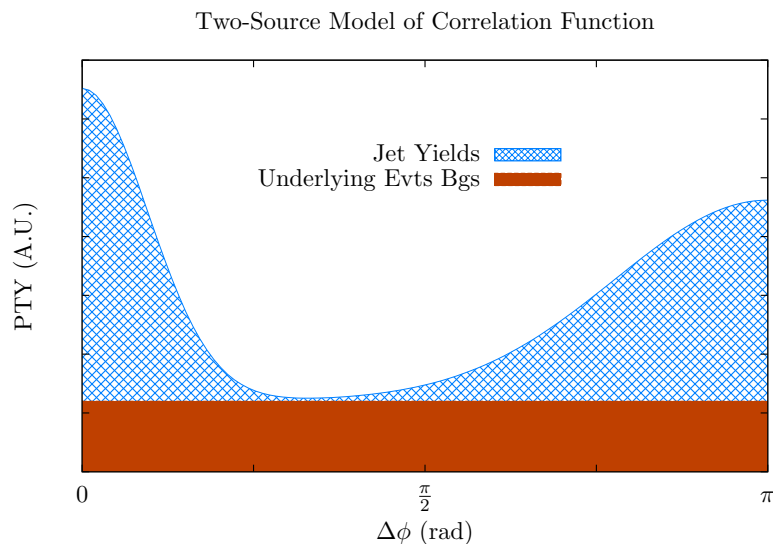


Figure 3.2: Cartoon plot of two-particle correlation distribution in $\Delta\phi$ in heavy ion collisions. The two peaks are due to the near- and away-side jets. The flat pedestal comes from the underlying events background.

Actually, the rapidity/pseudorapidity (y/η) correlation distribution is also sometimes measured, as shown in Figure 1.16, 1.17 in Section 1.4. The broadening

in $\Delta\eta$ in the near-side correlation in Au+Au collision is referred as “ridge”. The suppression at $\Delta\phi = \pi$ is referred as “head”, while the enhancement at $\Delta\phi = \pi \pm 1.1$ is referred as “shoulder”. These structures were thought as phenomena of the medium response of the jet. Later people realize that they are caused by higher order harmonics in the flow, which come from the initial state fluctuations.

3.6.1 Notations for Mathematical Framework. To make a clear introduction, this subsection is going to show the notations used in the derivation of the mathematical framework for the two-source model of jet correlation physics. All of them are following PHENIX Analysis Notes 646 [128]. To make things easy, we would like to look at the symbols and units at first.

$$[N] = \text{counts} \quad (3.16)$$

$$[\mathbb{N}] = \text{raw counts} \quad (3.17)$$

$$[n] = \text{counts/event} \quad (3.18)$$

$$[\mathfrak{n}] = \text{raw counts/event} \quad (3.19)$$

$$\left[\frac{dn}{d\Delta\phi} \right] = \text{counts/event/rad} \quad (3.20)$$

$$\left[\frac{d\mathfrak{n}}{d\Delta\phi} \right] = \text{raw counts/event/rad}. \quad (3.21)$$

The capital letter denotes total counts, while the letter in small case denotes per-event quantity. The blackboard bold letter means measured quantity, while the regular letter means the true quantity. Then the efficiencies are defined as

$$\mathfrak{n}^A = \epsilon^A n^A \quad (3.22)$$

$$\mathfrak{n}^B = \epsilon^B n^B \quad (3.23)$$

$$\mathfrak{n}_{real}^{AB} = \epsilon_{real}^{AB} n_{real}^{AB} \quad (3.24)$$

$$\mathfrak{n}_{mixed}^{AB} = \epsilon_{mixed}^{AB} n_{mixed}^{AB}. \quad (3.25)$$

The superscript A means the trigger(photon or pion), B means the associated partner(charged hadron), and AB means a two-particle pair formed by the trigger and the partner. The subscription *real* means that it is a quantity from real events, and *mixed* means that it comes from mixed events. The single particle efficiencies could be obtained by comparing the raw counts and the published PHENIX data instead of full Monte Carlo simulations.

3.6.2 Acceptance Correction and Event Mixing. The $\Delta\phi$ distribution of the two-particle correlation quantities should be corrected because of the uneven acceptance efficiency on different $\Delta\phi$ value, which results from the limited PHENIX azimuthal acceptance, shown in Figure 2.2, as well as the working condition of the detector subsystems of PHENIX and the application of various cuts in event and particle selection. To address this issue, a common procedure is to mix up different events which belong in the same group with similar characteristics, such as the centrality. Since the two particles in the pair are from different events, they are not correlated by physics. Even though, there might be some unknown residual correlation existing from the detectors, such as correlation with the reaction plane due to the reaction plane acceptance. The shape of the $\Delta\phi$ distribution from the mixed events only arises from the acceptance efficiency. Following this idea, if we divide the real event distribution of N_{real}^{pair} by the mixed event distribution of N_{mixed}^{pair} , we are able to cancel out and correct the uneven $\Delta\phi$ acceptance efficiency, which is largely due to the limited PHENIX azimuthal acceptance (See [128] [129] and Appendix A for details). Therefore, the *correlation function* $C(\Delta\phi) \equiv N_{real}^{pair}(\Delta\phi)/N_{mixed}^{pair}(\Delta\phi)$ is a good choice in the two-particle jet correlation analysis. The correlation function $C(\Delta\phi)$ could also be normalized by the

integrated yields and redefined as,

$$C(\Delta\phi) \equiv \frac{\frac{dn_{real}^{AB}}{d\Delta\phi} \int \frac{dn_{mixed}^{AB}}{d\Delta\phi} d\Delta\phi}{\frac{dn_{mixed}^{AB}}{d\Delta\phi} \int \frac{dn_{real}^{AB}}{d\Delta\phi} d\Delta\phi}. \quad (3.26)$$

The acceptance correction is defined as

$$\frac{dn_{real}^{AB}}{d\Delta\phi} = \frac{\frac{dn_{real}^{AB}}{d\Delta\phi}}{Acc(\Delta\phi)} \quad (3.27)$$

which is used to get the real number of the trigger-partner pairs. And the reason why we need the mixed events lies here. By using the sum rule from [129],

$$\int C(\Delta\phi) d\Delta\phi = \frac{\epsilon_{mixed}^{AB}}{\epsilon_{real}^{AB}} \int d\Delta\phi, \quad (3.28)$$

the ϕ acceptance correction is derived to be (The detailed derivation is in Appendix A)

$$Acc(\Delta\phi) = \frac{dn_{mixed}^{AB}}{d\Delta\phi} \frac{\epsilon_{mixed}^{AB}}{\eta_{mixed}^{AB}} \int d\Delta\phi \quad (3.29)$$

where ϵ^{AB} is essential for the evaluation of acceptance correction. To determine its value, we look at the multiplicity for mixed events

$$\eta_{mixed}^{AB} = \kappa \eta^A \eta^B \quad (3.30)$$

$$n_{mixed}^{AB} = n^A n^B \quad (3.31)$$

where κ is the pair efficiency due to the cuts in our analysis, then, we get

$$\epsilon_{mixed}^{AB} = \kappa \epsilon^A \epsilon^B. \quad (3.32)$$

In this way, the acceptance correction could be achieved by the event mixing and the evaluation of those efficiencies.

3.6.3 Two-Source Model and Combinatorial Background. As in the direct jet reconstruction, the soft background products still play a role in the two-particle correlation analysis. Apart from the jet correlation, the random

combination of uncorrelated particles, at least uncorrelated through the hard scattering (or say, the partner hadrons come from the underlying events), build up the pedestal background. The correlation function could be decomposed into two parts, one from the pair yields of two-particle jet correlation (so called *jet function*), the other from the combinatorial background from the underlying events. This decomposition could be expressed by

$$\frac{dN_{real}^{AB}(\Delta\phi)}{d\Delta\phi} = \frac{dN_{comb}^{AB}(\Delta\phi)}{d\Delta\phi} + \frac{dN_{jet}^{AB}(\Delta\phi)}{d\Delta\phi} \quad (3.33)$$

or, using per event quantities,

$$\frac{dn_{real}^{AB}(\Delta\phi)}{d\Delta\phi} = \frac{dn_{comb}^{AB}(\Delta\phi)}{d\Delta\phi} + \frac{dn_{jet}^{AB}(\Delta\phi)}{d\Delta\phi}. \quad (3.34)$$

The correlation function $C(\Delta\phi)$ could have other variants, such as the one normalized by the number of events or even by the number of triggers. Per event quantities and per-trigger quantities are two common way to evaluate the azimuthal correlations. In this analysis, the different types of triggers have different efficiencies. By using the per-trigger quantities, we are about to remove such difference across the different trigger types because dividing the pair number related quantities by the number of triggers can cancel the trigger efficiency. This advantage gets more prominent, especially when the direct photon result is obtained by subtracting the decay photon result (which is derived from π^0 meson result) from the inclusive one. Therefore we define the per-trigger yield (PTY),

$$\frac{1}{n^A} \frac{dn^{AB}}{d\Delta\phi} = \frac{1}{n^A} \left[\frac{dn_{jet}^{AB}}{d\Delta\phi} + \frac{dn_{comb}^{AB}}{d\Delta\phi} \right] \quad (3.35)$$

using the measurable quantities

$$\frac{1}{n^A} \frac{dn_{jet}^{AB}}{d\Delta\phi} = \frac{\epsilon^A}{n^A} \left[\frac{\frac{dn_{real}^{AB}}{d\Delta\phi}}{Acc(\Delta\phi)} - \frac{dn_{comb}^{AB}}{d\Delta\phi} \right]. \quad (3.36)$$

The only remaining part is the combinatorial background term. It is evaluated by various methods, such as the *zero yields at minimum* (ZYAM) method, the *absolute subtraction* (ABS) method and the *mean-seeds mean-partner* (MSMP) method.

The idea of ZYAM is that we assume the pair yield of the jet correlation approaches to zero at some minimum point $\Delta\phi_{min}$, *i.e.*

$$\left. \frac{dn_{comb}^{AB}}{d\Delta\phi} \right|_{\Delta\phi_{min}} = 0. \quad (3.37)$$

The minimum value for PTY corresponds to the combinatorial background from dAu collision which has no elliptical flow, since it is only a constant value without any v_2 term. The jet correlation could be fitted by two Gaussian peak after subtraction of the combinatorial backgrounds.

The effectiveness of ZYAM could be impaired by the situation lacking of statistics, such as the region $\Delta\phi$ near $\pi/2$ in high p_T bins either for the trigger or the associated partners.

In the ABS methods, we assume that the multiplicity of combinatoric pairs in the real event could be represented by the one in mixed events after a centrality-multiplicity correlation correction. The mixed event method counts the pair multiplicity in mixed events

$$\mathfrak{n}_{comb}^{AB} = \mathfrak{n}_{mixed}^{AB} \cdot \xi \quad (3.38)$$

divided by ϵ_{mixed}^{AB} , we get a similar form,

$$n_{comb}^{AB} = n_{mixed}^{AB} \cdot \xi \quad (3.39)$$

or the differential form,

$$\frac{dn_{comb}^{AB}(\Delta\phi)}{d\Delta\phi} = \frac{dn_{mixed}^{AB}(\Delta\phi)}{d\Delta\phi} \cdot \xi. \quad (3.40)$$

The mean-seeds mean-partner method (MSMP) could be derived by using Equation 3.30. It measures the single particle multiplicity and the pair cut loss in mixed events.

$$\mathfrak{n}_{comb}^{AB} = \mathfrak{n}^A \mathfrak{n}^B \kappa \cdot \xi. \quad (3.41)$$

In d +Au collision, the combinatorial background is a constant over all $\Delta\phi$, so

$$\frac{d\mathfrak{n}_{comb}^{AB}(\Delta\phi)}{d\Delta\phi} = \frac{\mathfrak{n}^A \mathfrak{n}^B \kappa \cdot \xi}{\int d\Delta\phi} \quad (3.42)$$

consequently,

$$\frac{dn_{comb}^{AB}(\Delta\phi)}{d\Delta\phi} = \frac{\mathfrak{n}^A \mathfrak{n}^B}{\epsilon^A \epsilon^B} \frac{1}{\int d\Delta\phi} \cdot \xi. \quad (3.43)$$

The introducing of ξ roots in the fact that the central events contribute more pairs than the peripheral events, or say the multiplicity is uneven with the centrality. In the process of event mixing, the events within the same centrality bin (see Line 200 of `combOnetriggerTrack.C`) are randomly selected for mixing. The event on the up edge of the centrality bin is under-weighted for the multiplicity by event mixing procedure. “The correction modifies the background level by $\approx 0.2\%$ in the most central and $\approx 25\%$ in the most peripheral Au+Au collisions” according to [130]. To determine the value of ξ , we start from the integrated two-particle pair yield in mixed events

$$\int \frac{dN_{mixed}^{AB}(\Delta\phi)}{d\Delta\phi} d\Delta\phi = N_{mixed}^{AB} = N_{mixed}^{evt} n^A n^B, \quad (3.44)$$

then based on the two-source model Equation 3.33, we could decompose the two-particle pair yield into the jet correlation part and the combinatorial background

$$\frac{dN_{real}^{AB}(\Delta\phi)}{d\Delta\phi} = \frac{dN_{jet}^{AB}(\Delta\phi)}{d\Delta\phi} + N_{real}^{evt} \frac{dn_{comb}^{AB}(\Delta\phi)}{d\Delta\phi} \quad (3.45)$$

using Equation 3.40

$$\frac{dN_{real}^{AB}(\Delta\phi)}{d\Delta\phi} = \frac{dN_{jet}^{AB}(\Delta\phi)}{d\Delta\phi} + N_{real}^{evt} \cdot \xi \cdot \frac{dn_{mixed}^{AB}(\Delta\phi)}{d\Delta\phi} \quad (3.46)$$

integrated by $\Delta\phi$

$$N_{real}^{AB} = N_{jet}^{AB} + N_{real}^{evt} \cdot \xi \cdot n_{mixed}^{AB} \quad (3.47)$$

by using Equation 3.31

$$N_{real}^{AB} = N_{jet}^{AB} + N_{real}^{evt} \cdot \xi \cdot n^A n^B. \quad (3.48)$$

Also, as we discussed above, the combinatorial background comes from the residual correlation from the finite centrality bin, we could write

$$N_{real}^{AB} = N_{jet}^{AB} + N_{real}^{evt} \langle n^A(c) n^B(c) \rangle \quad (3.49)$$

Here the second term stands for the residual correlation in the mixed events, arising from the finite centrality bin correlation. Therefore the angle brace means the average value over the centrality bin, and n^A , n^B are the functions of the centrality c . Comparing the two equations above, we derive [102]

$$\xi = \frac{\langle n^A(c) n^B(c) \rangle}{n^A n^B}. \quad (3.50)$$

3.7 Quality Assurance

These runs are excluded from the final results

- EMC: 247787 248149 248173 248174 249252 249255 249257 249258 249259
246483 246484 246492 246544 247055 247169 247247 247815 248149 249115
249252 249255 249257 249258 249259 249405 249496 249839 249843 250005
250016 250875 251063 251416 251486 251502 251836 251840 251971 252102
252117 252201 252259 252773 253440 253523 253629 [131] 249252 249255
249256 249257 249258 249259 [132]
- DC: 249865 249866 248380 [133]

- Acceptance Correction: No runs. We get $\frac{dN}{d\phi}$ for each run from the TTree data saved in disk. Then we do a chi-square test on each runs by comparing with the overall one. During the chi-square test, we stripe off all the bins which might be zero in any runs, then the degree of freedom is the same for all runs' test. The chi-square value is shown in Figure 3.3. Some runs might have high χ^2 value. However, the χ^2 value for the acceptance correction remains consistent with the overall one. The worst run is 249866. The efficiency and acceptance correction are shown in Figure 3.4 3.5 by comparing with the overall ones. The acceptance correction remains consistent with the overall, so we decide to keep those runs.

3.8 Dead and Hot Towers

In order to identify the dead and hot towers, we register the hit number of each tower in different energy range, starting from 1 GeV to 20 GeV in a step of 1 GeV. Then we apply an iteration algorithm for similar towers. The towers are group in two different ways, one is by sector, the other one is by the type (PbSc or PbGl). In taxi, we use the one from 8 sectors with energy 1 - 2 GeV. We calculate the mean and variance of the towers in one group. Since the hot towers are extremely "hot", which makes the mean deviated towards a high hit number, and the standard deviation to be a large number too. We throw away the towers whose hit number is out of 3σ range, then do this calculate again, until the remaining towers, the mean and the variance converged in the iterations, see Figure 3.6. The results of the dead / hot tower could be verified in Figure 3.7.

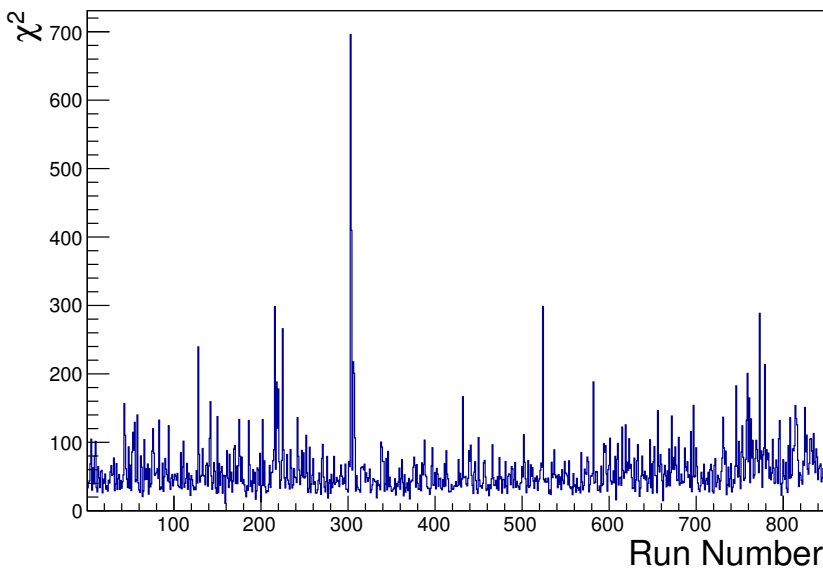


Figure 3.3: The chi-square value for each run's DC efficiency. The X axis is the *run number* (a run number denotes a section of data collected in a period where all detector configurations are kept almost the same) in the data, and the Y axis is the χ^2 value of each run. The zero bins are stripped off, they have the same degree of freedom.

3.9 Combinatorics for Reconstructed π^0

The *combinatoric background in π^0 reconstruction* is studied by fitting the data with a Gaussian peak plus a linear combinatoric background, see Figure 3.8. The fitted coefficients are list in Table 3.2. The meaning of the coefficients are: C0 \Rightarrow Gaussian peak weight, C1 \Rightarrow Gaussian peak location, C2 \Rightarrow Gaussian peak width, C3 \Rightarrow intercept in the linear function, C4 \Rightarrow slope in the linear function. The signal background ratio is determined from the fit, and listed in Table 3.2.

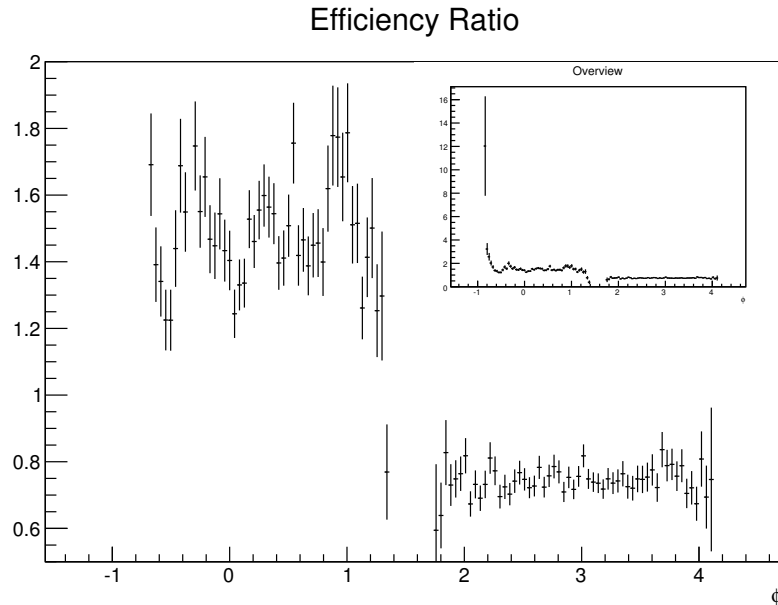


Figure 3.4: The DC efficiency ratio between a bad run 249866 and the overall. The big plot shows the zoomed-in view, and the small plot shows the overview.

Table 3.2: S/B Ratio and Fitting Coefficients of π^0 Combinatorics

Trigger(GeV/c)	S/B	C0	C1	C2	C3	C4
5 - 7	18.2	18190.5	0.139955	0.00909	422.606	1236.81
7 - 9	19.1	2236.56	0.140285	0.00931	56.3296	98.6971
9 - 12	19.8	498.05	0.1407	0.00973	9.36018	40.4933
12 - 15	21.5	65.92	0.141575	0.01040	1.20428	4.76524

The residual correlation between the mis-reconstructed fake π^0 and the charged hadrons is studied by the *side band analysis* [134]. The choice of the side bands are:

- low band: $0.065 \text{ GeV} < \text{InvMass} < 0.115 \text{ GeV}$

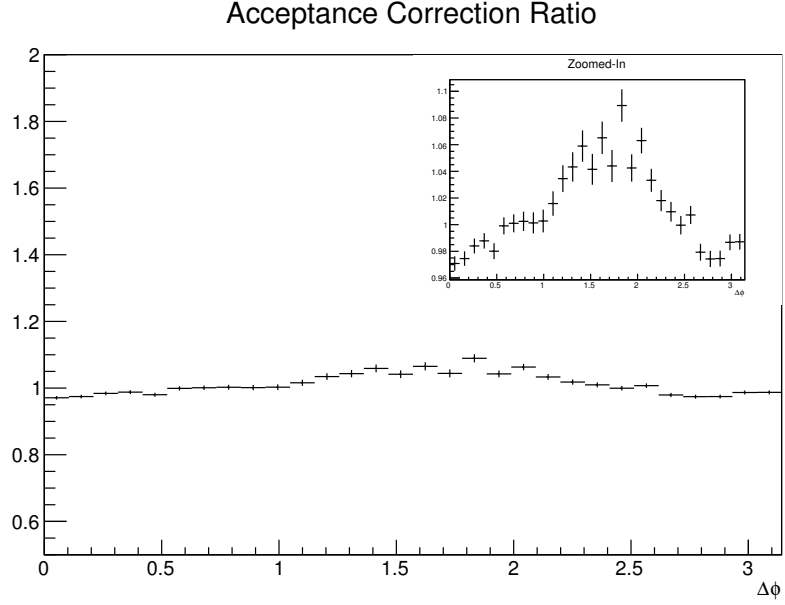


Figure 3.5: The acceptance correction ratio between a bad run 249866 and the overall. The big plot shows the overview, and the small plot shows the zoomed-in view.

- high band: $0.165 \text{ GeV} < \text{InvMass} < 0.200 \text{ GeV}$

The low band and high band correlations are shown in the jet functions in Figure 3.9, 3.10. The residual correlation of the reconstructed fake π^0 's is obtained by combining the high and low band jet function weighted by the number of triggers. Then the true π^0 's jet function is calculated by the measured π^0 - h and fake π^0 - h correlations, see Equation 3.52.

$$\frac{S \cdot Y^{\pi^0} + B \cdot Y^{\text{fake}}}{S + B} = Y^{\text{meas}} \quad (3.51)$$

$$Y^{\pi^0} = \left(1 + \frac{1}{S/B}\right) \cdot Y^{\text{meas}} - \frac{1}{S/B} \cdot Y^{\text{fake}} \quad (3.52)$$

$$= Y^{\text{meas}} + \frac{1}{S/B} (Y^{\text{meas}} - Y^{\text{fake}}). \quad (3.53)$$

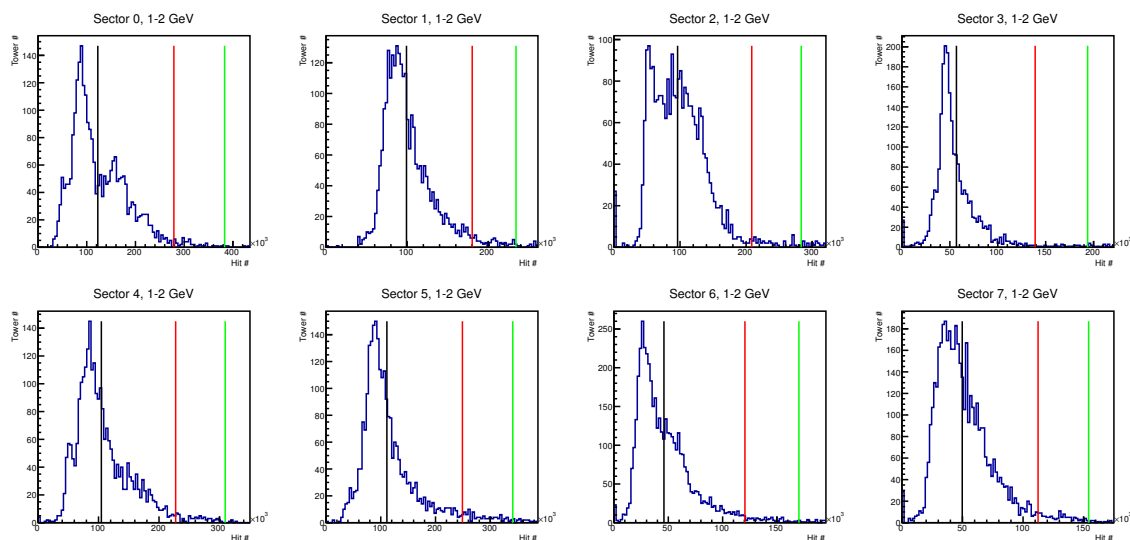


Figure 3.6: The EMCAL tower hit number distribution in different sectors with the energy in 1 - 2 GeV. The black, red and green lines represent the mean, 3σ , and 5σ respectively.

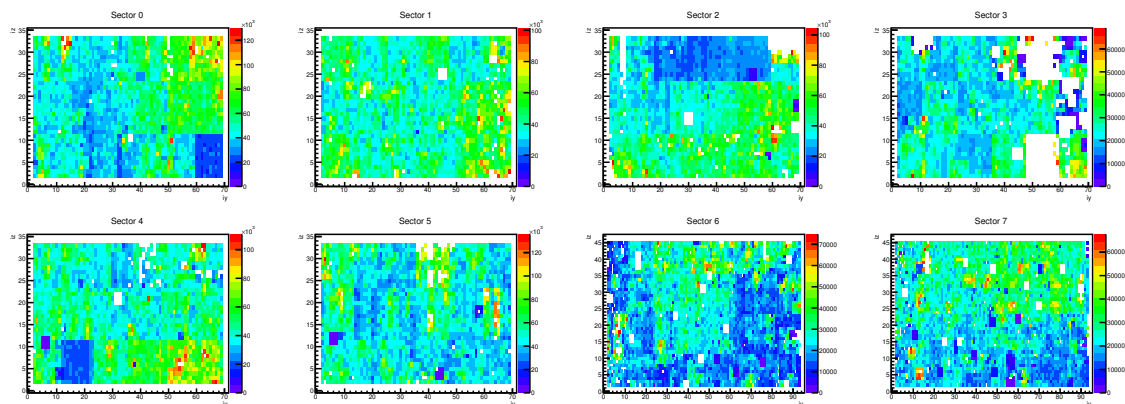


Figure 3.7: The dead/hot tower maps for all EMCAL sectors. The X axis is the column index in a sector called “iy”, and the Y axis is the row index within a sector called “iz”. Sector 0 - 5 are PbSc, Sector 6 - 7 are PbGl.

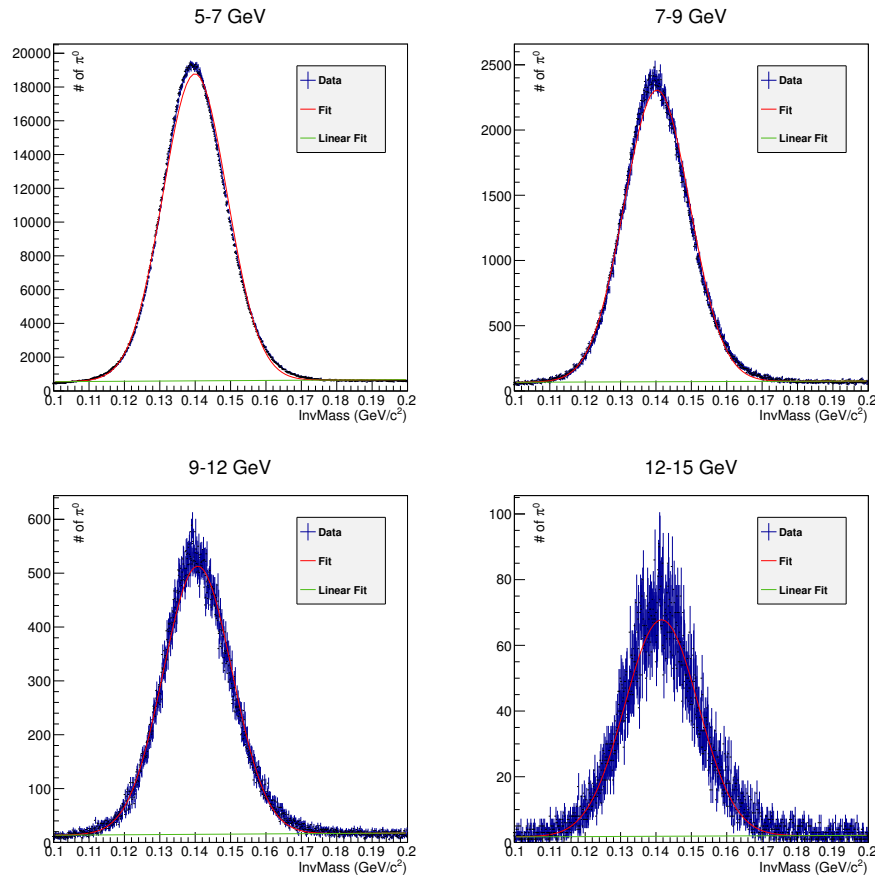


Figure 3.8: The π^0 combinatoric background is obtained by combining all sectors' data. The red line is the fitting function, which is a Gaussian π^0 peak + linear background. The green line is the linear function for background.

Here, Y means the jet function. Currently, we don't have the reconstructed fake π^0 - h correlation results for p+p collisions, so we include this as systematic error into the final results. It will be updated once we have such data ready.

The size of the correction itself is small, see Figure 3.11. We decide use 100% of this needed correction as the uncertainty, and include it in all the jet function plots, IdA plots, jet width plots, RI plots(See Section 4.4). Considering the similar shape of the π^0 combinatorics correction and the type B systematics (see Section 3.12 for

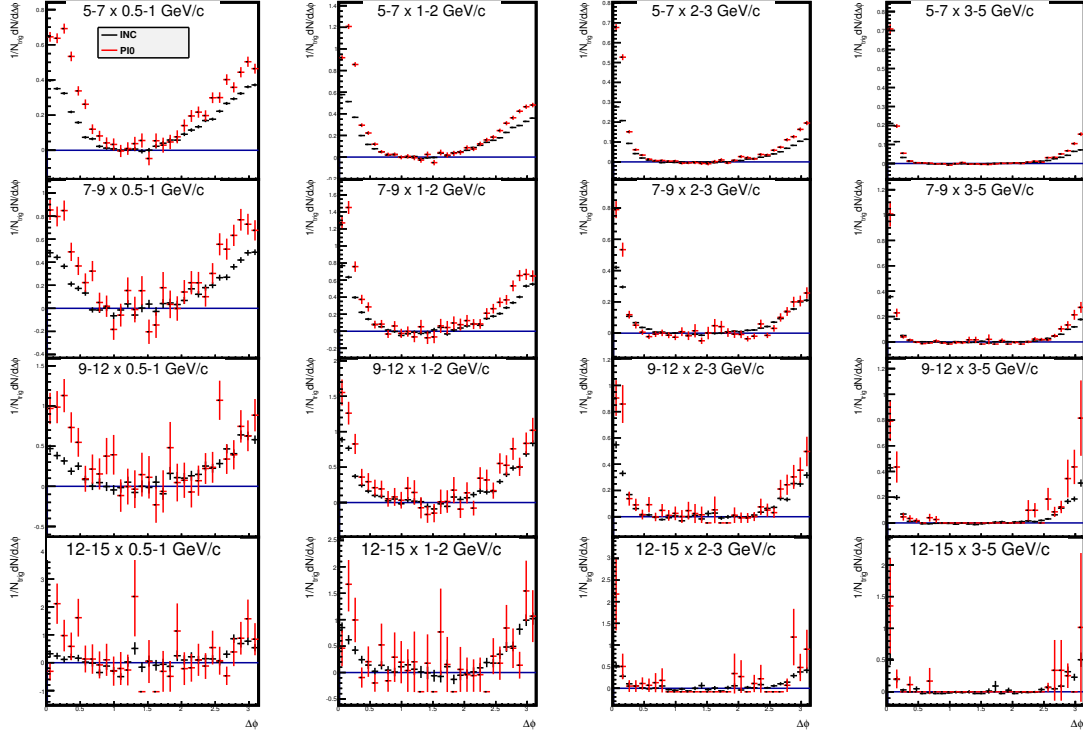


Figure 3.9: The residual correlations are shown in the jet functions between the mis-constructed fake π^0 in low band mass region and the charged tracks in 0-20% centrality.

the definitions of Type A, B, C uncertainties) from uncorrelated efficiency uncertainty and the ZYAM, the fitting won't change much by including the π^0 combinatorics systematics. The systematic errors of the fitted width are below 1% except a few p_T bins. In the fitting process, the uncertainty of the width is determined as:

1. fit with all corrections and statistical uncertainty, type B part of efficiency uncertainty, ZYAM uncertainty
2. fit with all the uncertainties mentioned above, plus the one from π^0 combinatorics

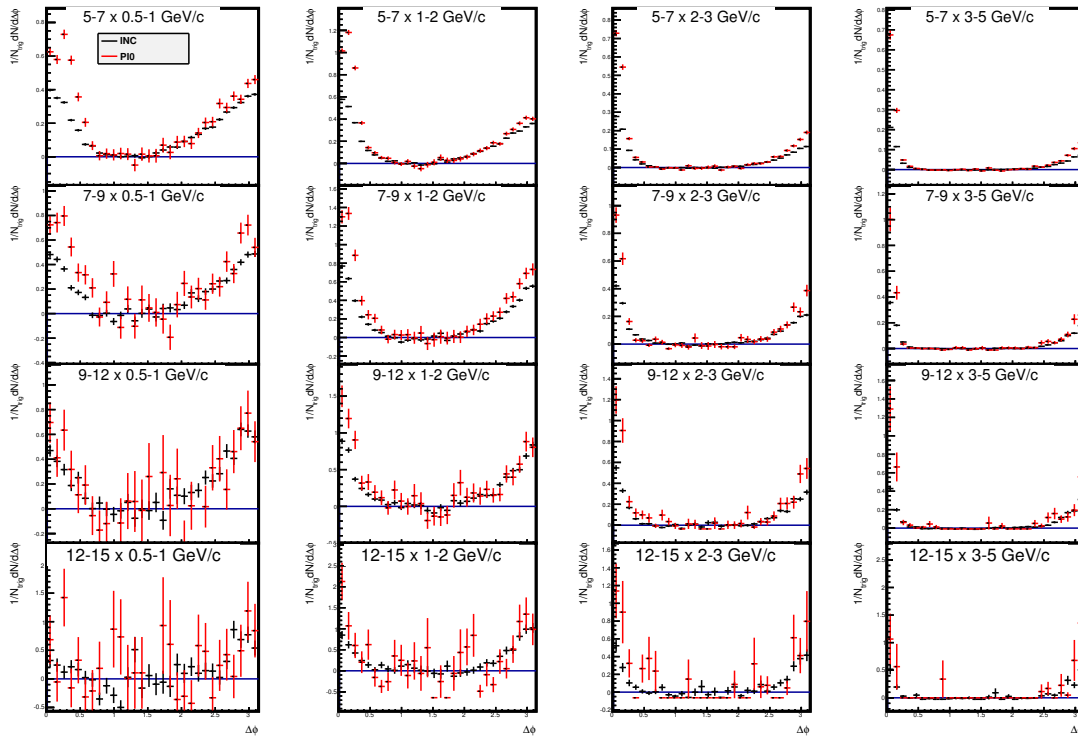


Figure 3.10: The residual correlations are shown in the jet functions between the mis-constructed fake π^0 in high band mass region and the charged tracks in 0-20% centrality.

3. the deviation of the fitted width \Rightarrow err1
4. fit with the systematics only from π^0 combinatorics
5. the fitted parameter error \Rightarrow err2
6. err1 is from the different relative uncertainty distribution between π^0 combinatorics and other uncertainty
7. err2 is from the size of the π^0 combinatorics uncertainty

8. err1 and err2 should be uncorrelated to each other, so the width uncertainty from π^0 combinatorics is $\sqrt{\text{err1}^2 + \text{err2}^2}$

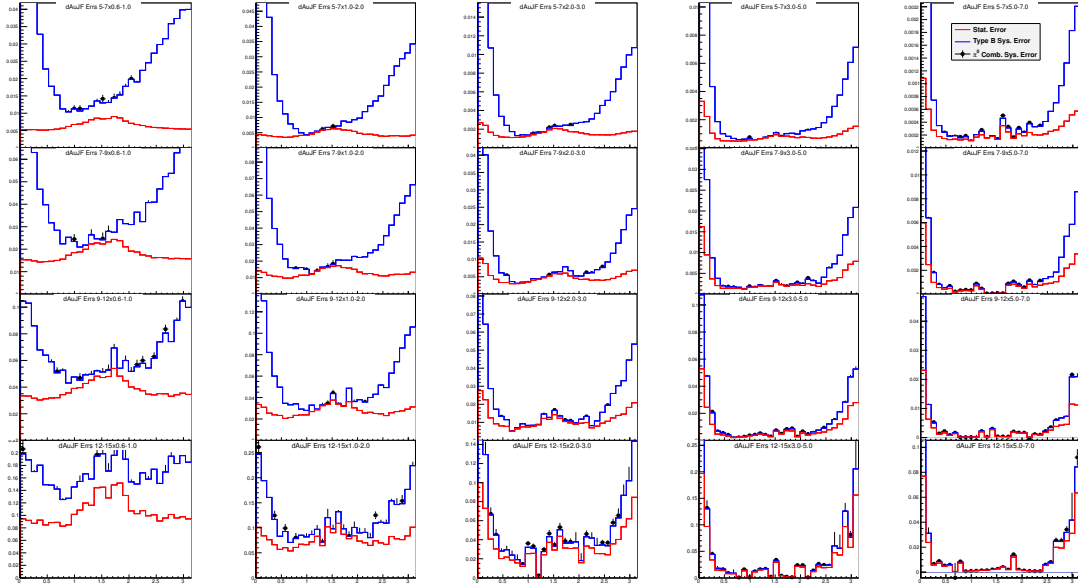


Figure 3.11: The uncertainty associated with the jet functions. The first is the statistical uncertainties, the second is the uncertainties from Type B efficiency uncertainty and ZYAM. The last is from the residual π^0 -h combinatorics correlation, for which we assign the uncertainty as 100% of this correction.

3.10 Charged Hadron Efficiency

There is no tracking detector before the Drift Chambers, so the detected charged hadrons contains sizeable backgrounds. The backgrounds come from the conversion electrons ($\gamma + \gamma \rightarrow e^+ + e^-$), secondary decay particles whose vertices are far from the event vertex (mainly from Λ) and weak decays of short lived particles (mainly K_S^0 , Λ and $\bar{\Lambda}$).

In practice, there are two options to determine the charged hadron efficiencies. One is by Monte Carlo simulation (Geant/PISA), the other one is by comparison between the measured spectra and the published ones. The later one is called the bootstrap method in the PHENIX analysis notes [135–137]. The results of the bootstrap method in the PHENIX analysis notes [135–137]. The results of the bootstrap method have been compared with the Monte Carlo method, and the two approaches agree well with each other within the systematic error [135, 137]. See Figure 3.12 from [135], and the figures showned in [137]. Considering the agreement shown by the above mentioned previous studies and the computation costs of the simulation method, we decide to determine the charged hadron efficiencies by the bootstrap method.

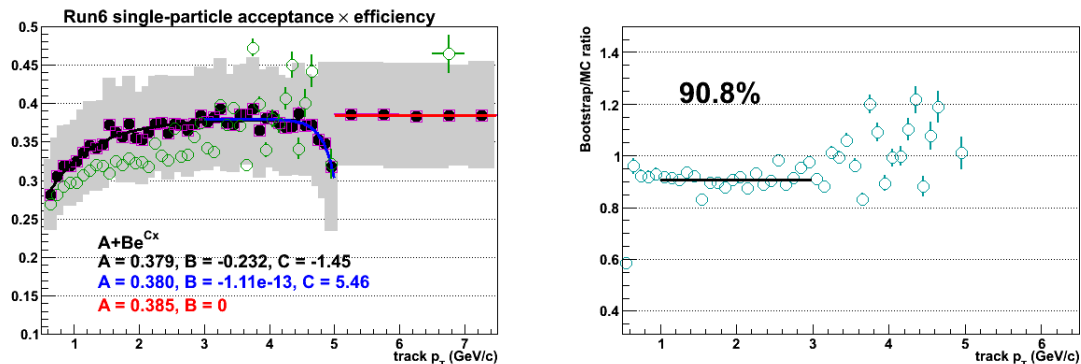


Figure 3.12: Comparison between the MC and bootstrap methods for Run 6 p+p collisions. The agreement is within the systematic uncertainties of the two methods [135].

3.10.1 d+Au Collisions. The charged hadron yields for Minimum Bias events in d+Au collisions at $\sqrt{S} = 200$ GeV have been published by PHENIX [68]. The measured spectra are determined by the histograms in the mixed events, where the charged hadrons are from the Minimum Bias events. We assume the efficiency

in ERT triggered events and the Minimum Bias events are the same, so the efficiencies determined by these Minimum Bias events are still applicable in our analysis. One subtle thing here is the occupancy effect, whose origin is the multiplicity. The occupancy effect is determined to be less than 10% in Au+Au events with centralities above 40% at 200 GeV, see [137]. We decide to add 10% into our systematic error of the efficiencies for 0-20%, 20-40% d+Au events. Both the measured and published spectra for the charged hadrons in the d+Au Minimum Bias events at $\sqrt{s} = 200$ GeV are shown in the left panel of Figure 3.13, 3.14, 3.15, 3.16, and the efficiencies are shown in the right panel of them. The error bar in the fine binning contains both errors from the experiment data and the published data. The error bar in the coarse binning is divide into two parts, one is the statistical errors from the experiment data, the other is the systematic error from the published data. There are two types of systematics in [68]. One is correlated in different p_T bins (Type B), the other one is correlated and constant in different p_T bins, which is constant 8.7% in all p_T bins (Type C). The 2nd type of systematics are definitely irreducible when combining multiple p_T bins. We treat the 1st type of systematics (Type B) as uncorrelated uncertainty when combining the p_T bins. The calculated result (4.1%) in 4.5-5.5 GeV/ c from the data in [68] website's `dAuDataTables.pdf` is larger than the one listed in [68] (3.4%). The method we are using here should be more conservative than the actual one. We compare our efficiencies with the parametrization result from [136], they agree within the systematics. The result is shown in Figure 3.17. When $p_T^h > 3$ GeV/ c , our bootstrap efficiencies start to get higher than [136], though still within the systematics errors. Because the most systematics come from the 2nd type (Type C), which is constant, we believe that we are getting mis-constructed tracks when $p_T^h > 3$ GeV/ c instead of getting fluctuations from the uncertainties (statistical + systematic). Since we

believe that the junk tracks are not part of jets, and remain constant in all $\Delta\phi$, they should be removed automatically by ZYAM procedure and not appear in the jet functions and all the measured quantities related to the jet functions. Therefore, we think it is appropriate to use the efficiency determined in 2 - 3 GeV/ c for higher partner p_T bins (and we still use the larger systematic uncertainties from those higher partner p_T bins), which are shown as red points in Figure 3.17. There are two components in the systematic errors on the d+Au efficiencies. One is p_T independent, which is 8.7% in all bins. The other one is p_T dependent. In all the following plots, the 8.7% systematics is not shown.

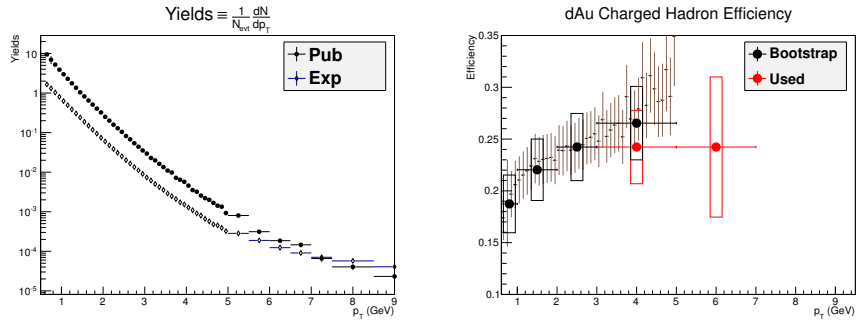


Figure 3.13: The charged hadron efficiency in 0-20% centrality d+Au Collisions. The fine binning is for [68], the coarse binning is for this analysis. This centrality class contains extra 10% systematics due to the occupancy effect. The red ones are the efficiencies we use in the bins where $p_T^h > 3.0$ GeV/ c .

3.10.2 p+p Collisions. The charged hadron cross section for Minimum Bias events in p+p collisions at $\sqrt{s_{NN}} = 200$ GeV have been published by PHENIX [138]. The yields is calculated from the published cross section by Equation 3.54

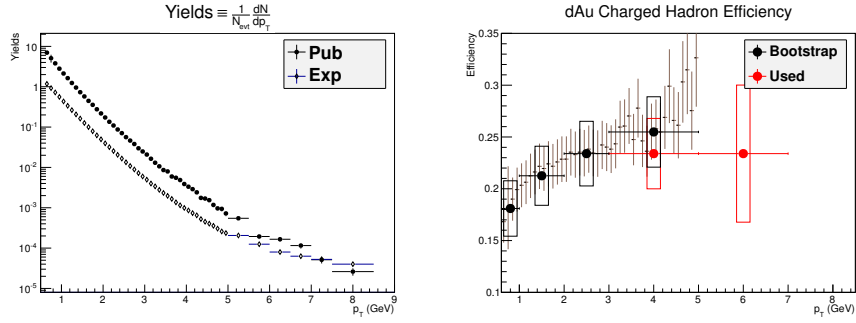


Figure 3.14: The charged hadron efficiency in 20-40% centrality d+Au Collisions. The fine binning is for [68], the coarse binning is for this analysis. This centrality class contains extra 10% systematics due to the occupancy effect. The red ones are the efficiencies we use in the bins where $p_T^h > 3.0 \text{ GeV}/c$.

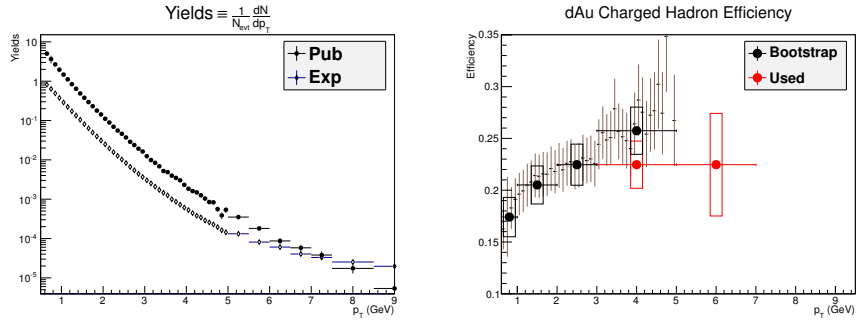


Figure 3.15: The charged hadron efficiency in 40-60% centrality d+Au Collisions. The fine binning is for [68], the coarse binning is for this analysis. The red ones are the efficiencies we use in the bins where $p_T^h > 3.0 \text{ GeV}/c$.

from [139].

$$E \frac{d^3 \sigma_X^{\text{Unbiased}}}{d^3 p} = \frac{\sigma_{\text{BBC}}}{N_{\text{BBC}}^{\text{Total}}} \cdot \frac{1}{2\pi} \frac{1}{p_T} \cdot C_{p+p}^{\text{BBC Bias}}(p_T, y) \cdot \frac{d^2 N_X^{\text{Total Biased}}}{dp_T dy}. \quad (3.54)$$

Then the efficiency is determined by the experiment data and this calculated yields.

The p+p efficiency is shown in Figure 3.18. There are p_T independent errors in the

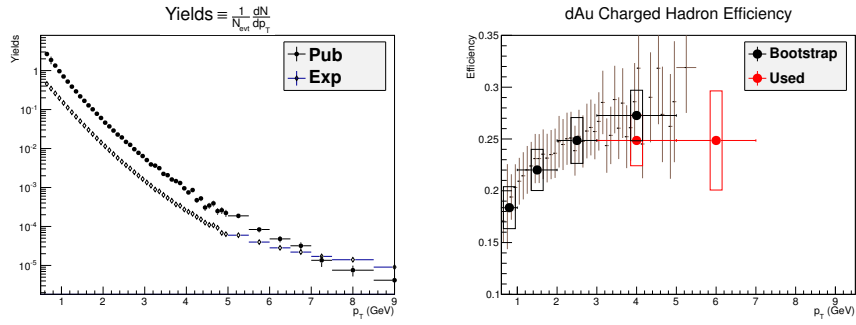


Figure 3.16: The charged hadron efficiency in 60-88% centrality $d+Au$ Collisions. The fine binning is for [68], the coarse binning is for this analysis. The red ones are the efficiencies we use in the bins where $p_T^h > 3.0$ GeV/ c .

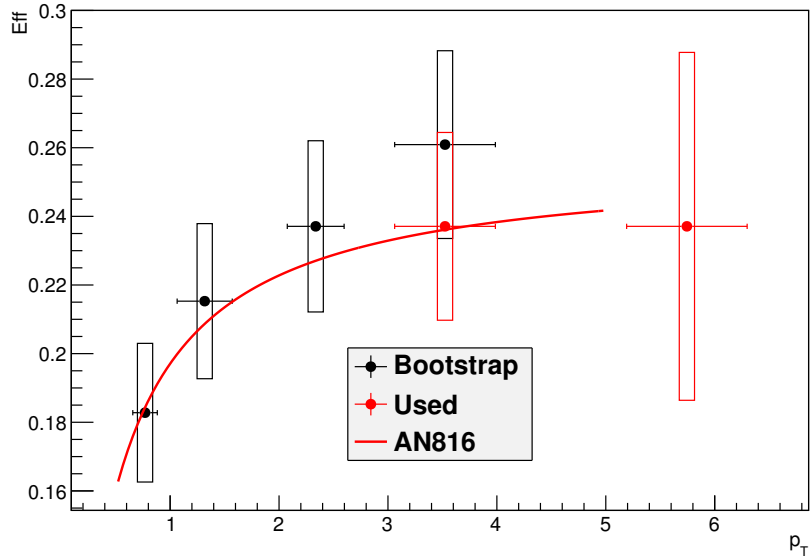


Figure 3.17: The charged hadron efficiencies (0-88%) in $d+Au$ collisions are compared with [136], they agree within the systematics. The red ones are the efficiencies we use in the bins where $p_T^h > 3.0$ GeV/ c .

systematics errors of p+p efficiencies. One comes for BBC efficiency, which is about 9.6%, the other is the trigger bias, which is 3%. These two errors are not shown in all the plots below. The remaining errors are p_T dependent.

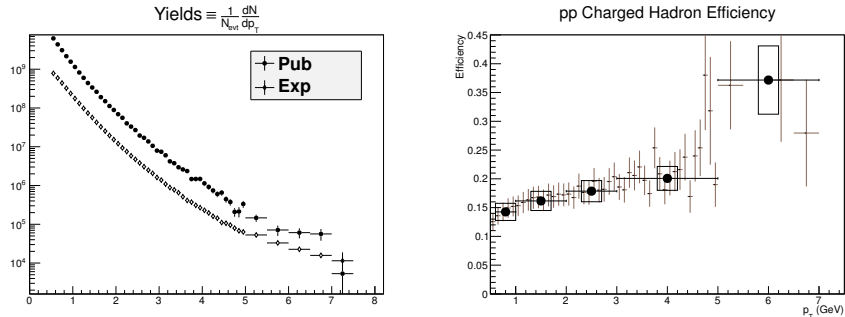


Figure 3.18: The charged hadron efficiency in pp collisions. The fine binning is for [138], the coarse binning is for this analysis.

3.11 Rapidity Acceptance Correction

Besides the ϕ acceptance correction, we need the η *acceptance correction*, see [89]. The function of $\Delta\eta$ correction is shown in Figure 3.19. The awayside jet yields correction is simply 2. And the nearside jet yields correction relies on the *width of the nearside jet*. It is determined by fitting the jet function with two Gaussian plus a pedestal background. The nearside Gaussian peak widths are shown in Figure 3.20, 3.21, 3.22, 3.23. Also, we show the awayside Gaussian peak widths in Figure 3.24, 3.25, 3.26, 3.27. These plots show a subtle modification in d+Au collisions. The nearside η acceptance correction values are shown in Figure 3.28, 3.29, 3.30, 3.31. The $\Delta\eta$ correction relies on the nearside width, which is not sensitive to the small π^0 combinatorics uncertainty. The thing that matters is the ratio between the nearside width of d+Au and p+p. In order to evaluate it, we move d+Au and

p+p's width away from each other to make the ratio larger. We try two sets of parameters. In the first parameter settings, we make the difference between d+Au and p+p's width twice larger than the fitted values. The changes of $R_{\Delta\eta}$ are all well below 1%. In the other parameter settings, we move d+Au and p+p's width away from each other by the size of their own uncertainties. The uncertainty of $R_{\Delta\eta}$ values from this setting in 0-20% d+Au collisions are shown in Table 3.3. This uncertainty is projected into I_{dA} and RI plots' systematics uncertainty as uncorrelated uncertainties (uncorrelated with other uncertainties, such as type B efficiency uncertainty, ZYAM, π^0 combinatorics).

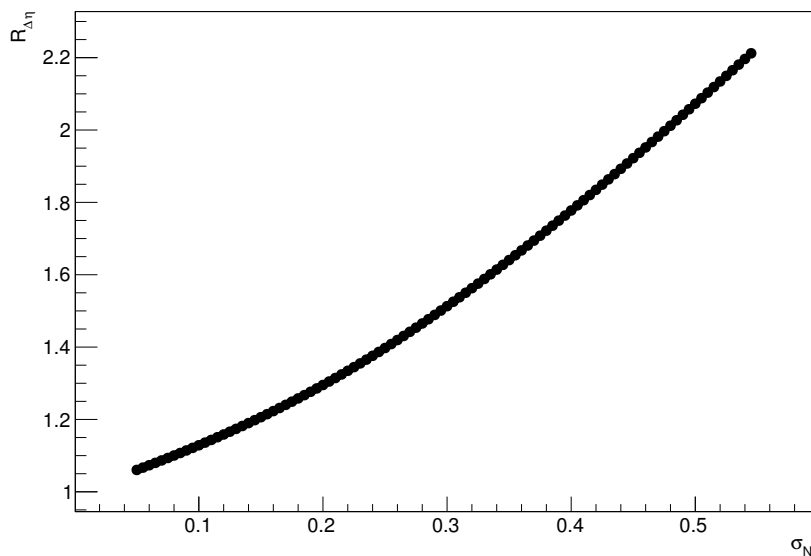


Figure 3.19: The function of the near-side $\Delta\eta$ correction, which is close to a linear function.

Nearside Width

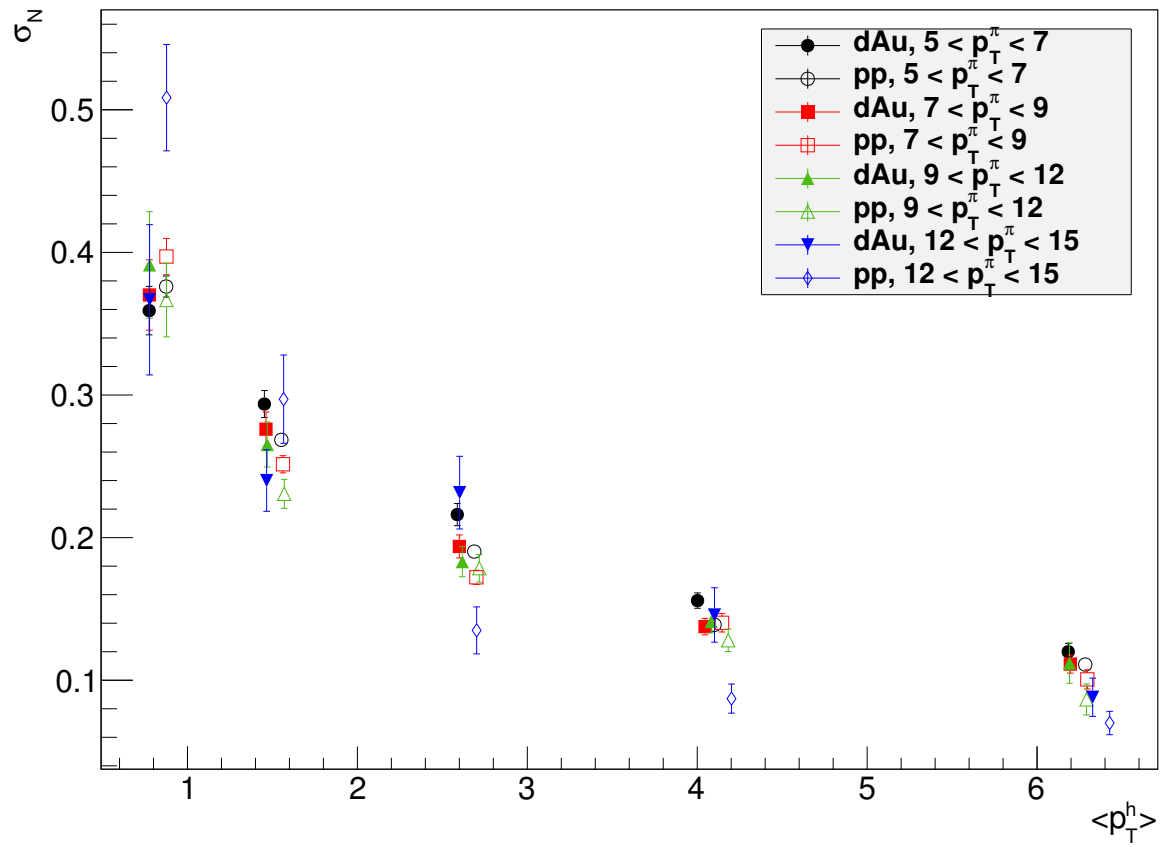


Figure 3.20: Nearside width for 0-20% centrality used for $R_{\Delta\eta}$ from gaussian fits. The $p+p$ p_T^h values are shifted to the right by 0.1.

Nearside Width

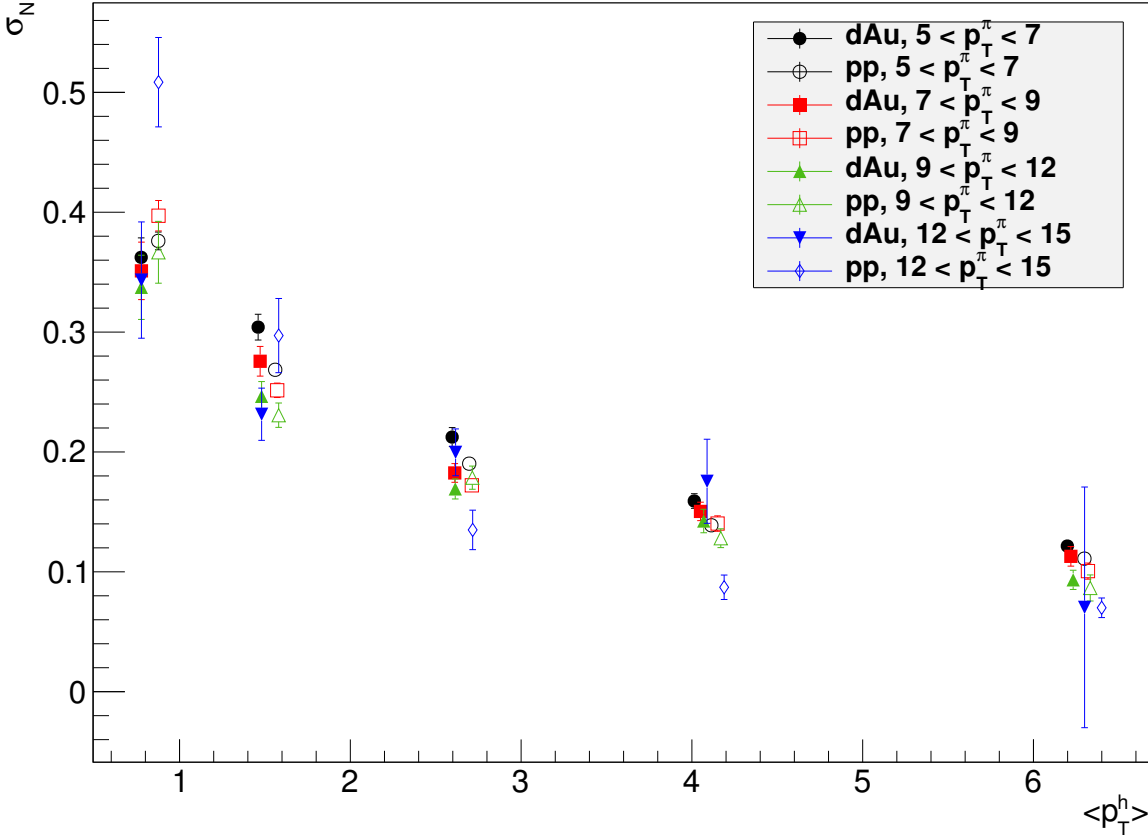


Figure 3.21: Nearside width for 20-40% centrality used for $R_{\Delta\eta}$ from gaussian fits. The $p+p$ p_T^h values are shifted to the right by 0.1.

Nearside Width

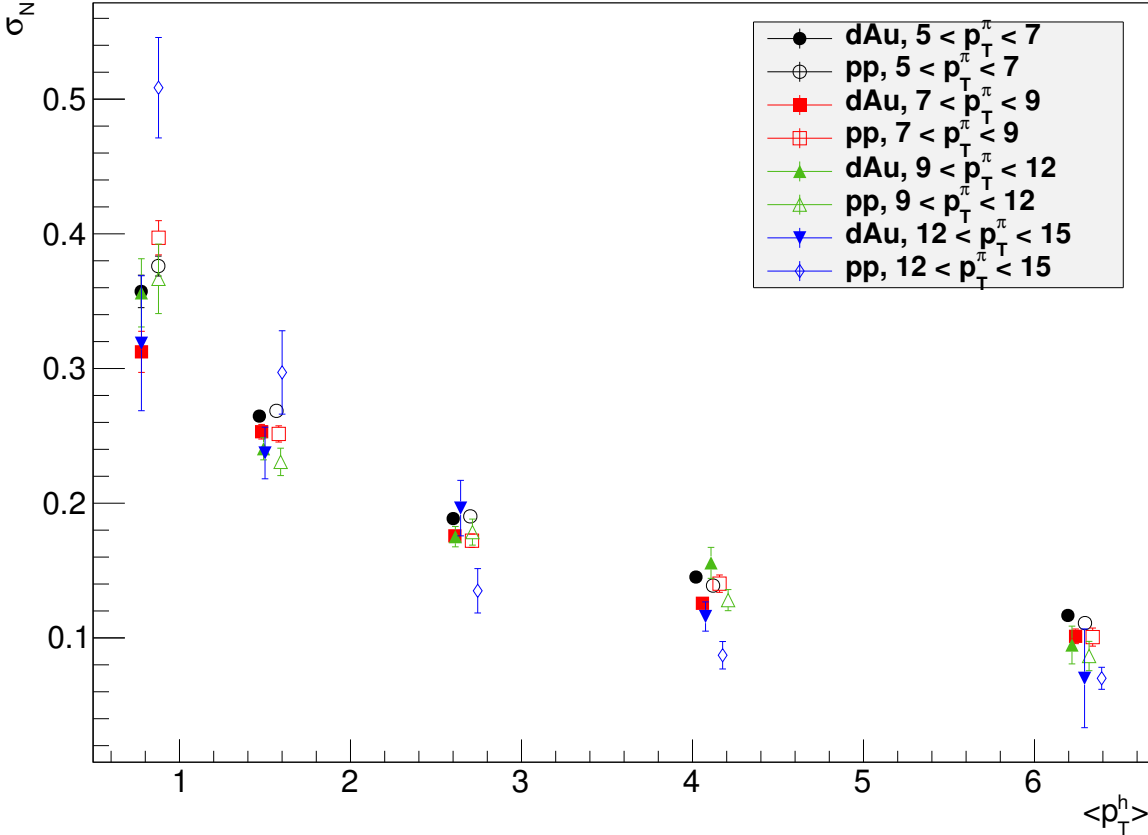


Figure 3.22: Nearside width for 40-60% centrality used for $R_{\Delta\eta}$ from gaussian fits. The $p+p$ p_T^h values are shifted to the right by 0.1.

Nearside Width

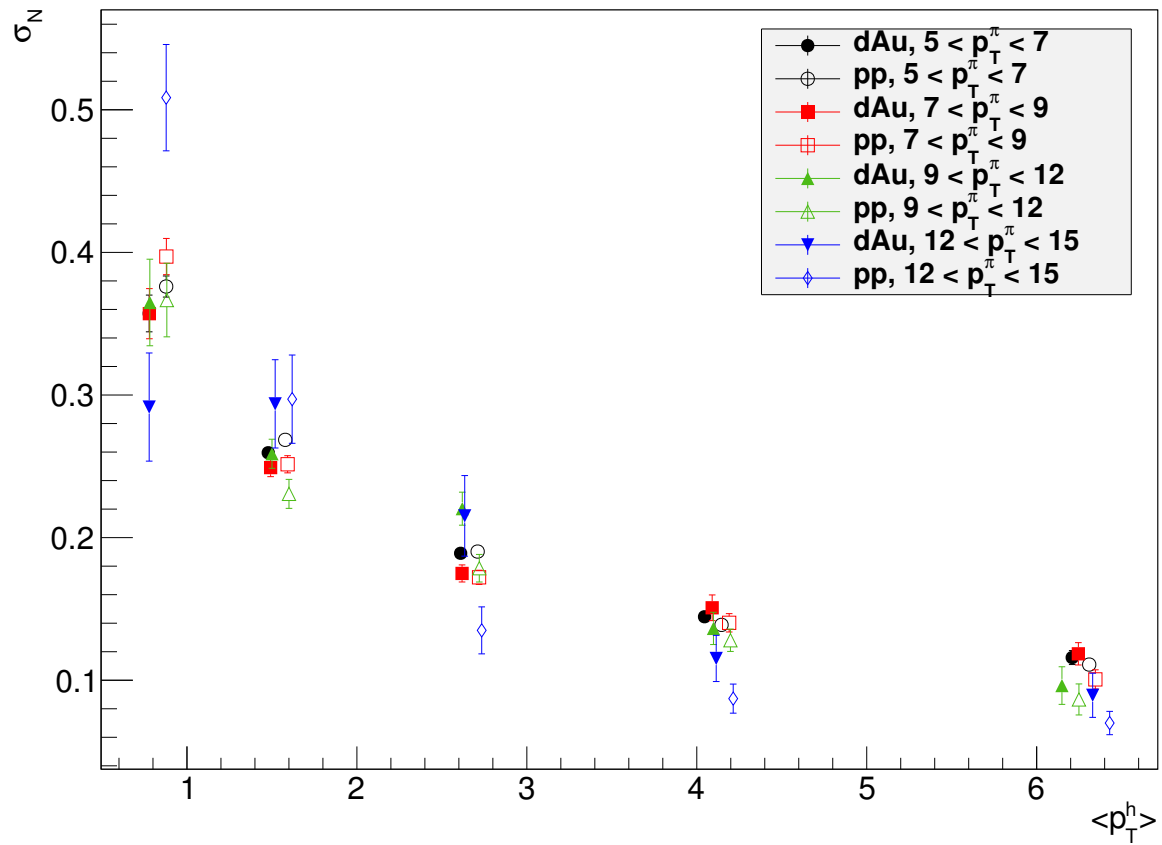


Figure 3.23: Nearside width for 60-88% centrality used for $R_{\Delta\eta}$ from gaussian fits. The $p+p$ p_T^h values are shifted to the right by 0.1.

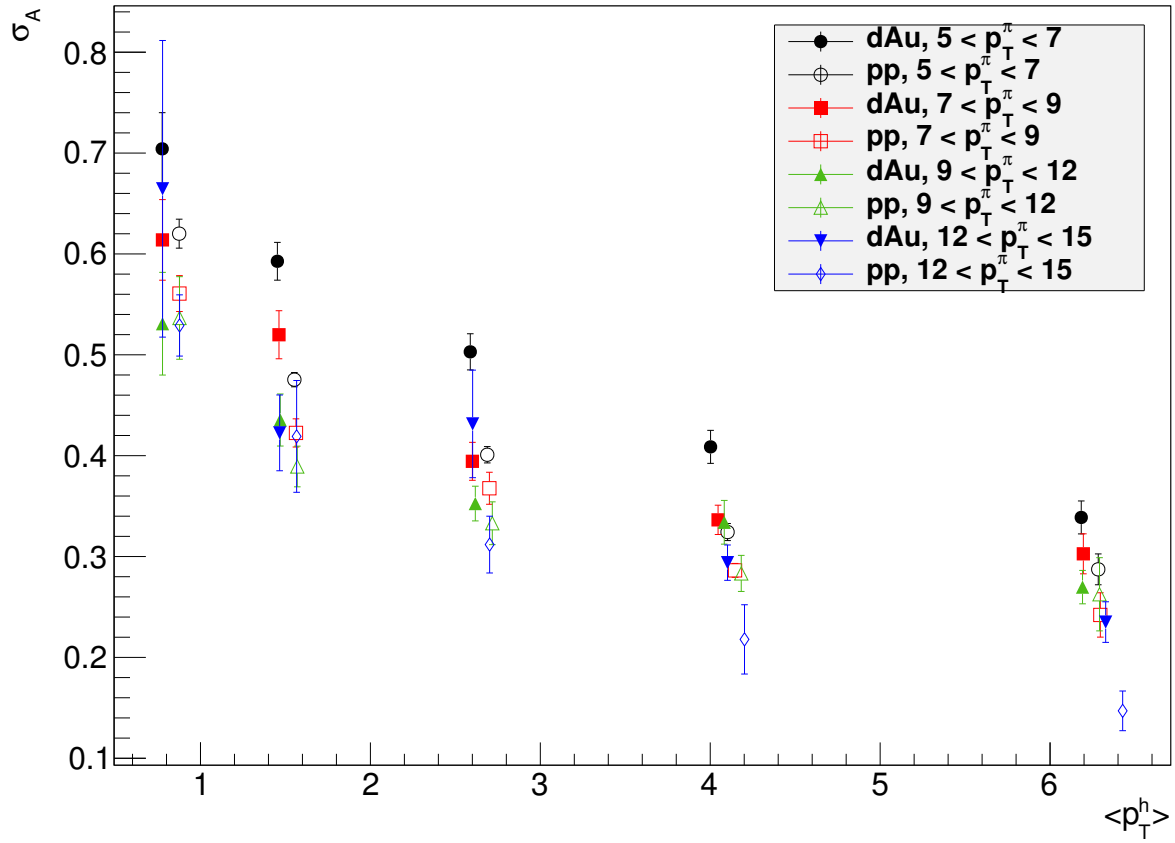


Figure 3.24: Awayside width for 0-20% centrality used for $R_{\Delta\eta}$ from gaussian fits. The $p+p$ p_T^h values are shifted to the right by 0.1.

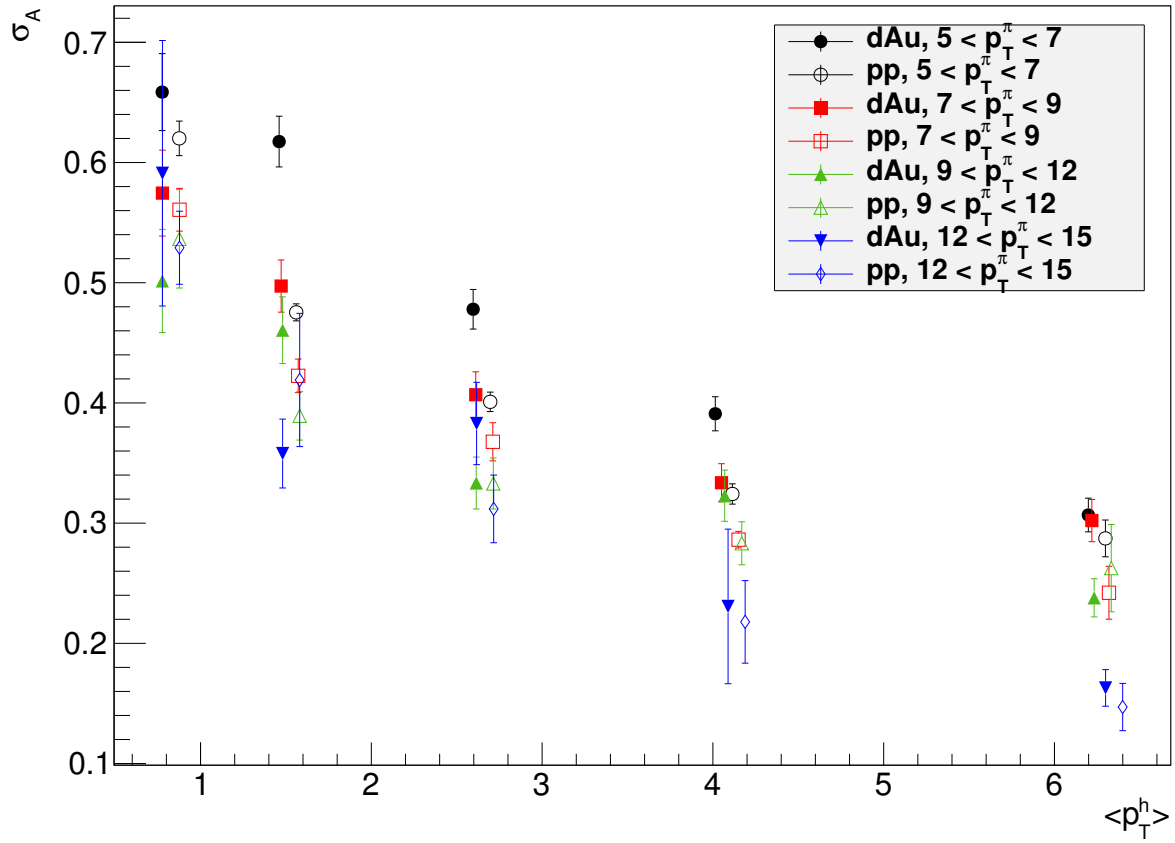


Figure 3.25: Awayside width for 20-40% centrality used for $R_{\Delta\eta}$ from gaussian fits. The $p+p$ p_T^h values are shifted to the right by 0.1.

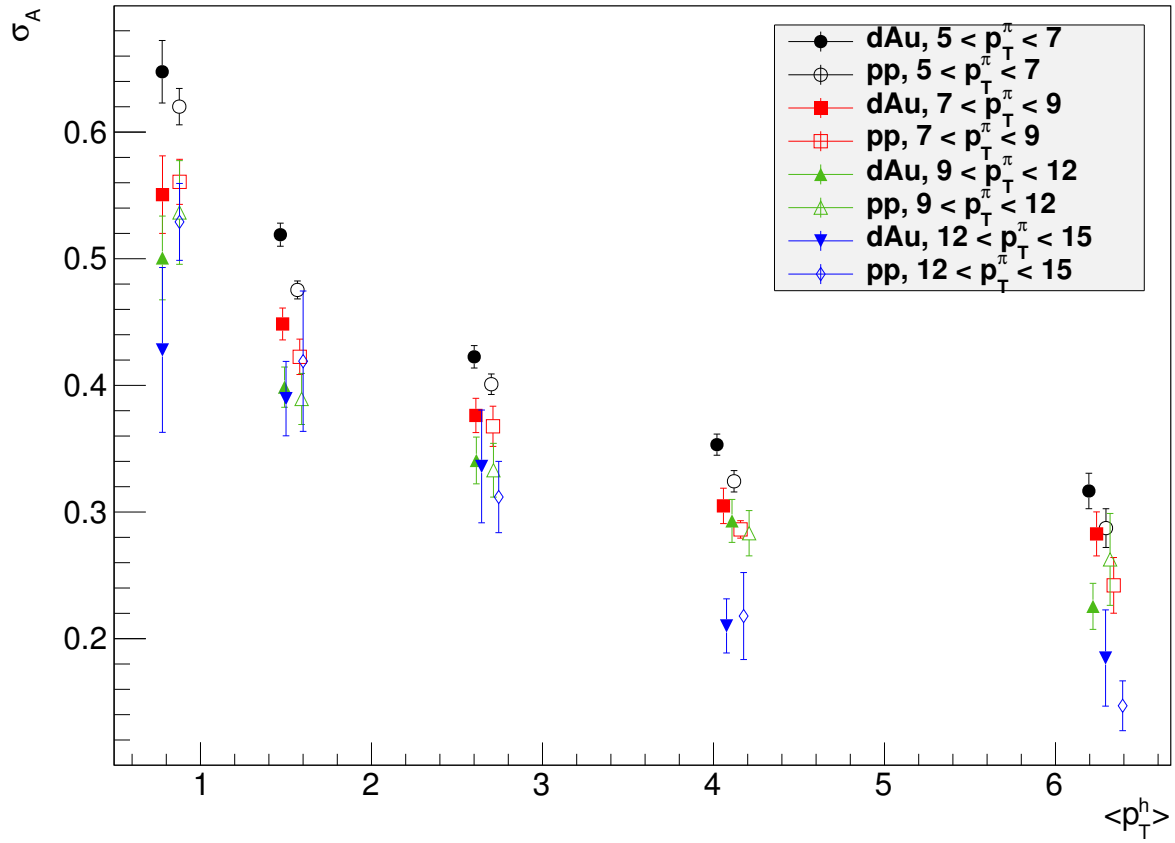


Figure 3.26: Awayside width for 40-60% centrality used for $R_{\Delta\eta}$ from gaussian fits. The $p+p$ p_T^h values are shifted to the right by 0.1.

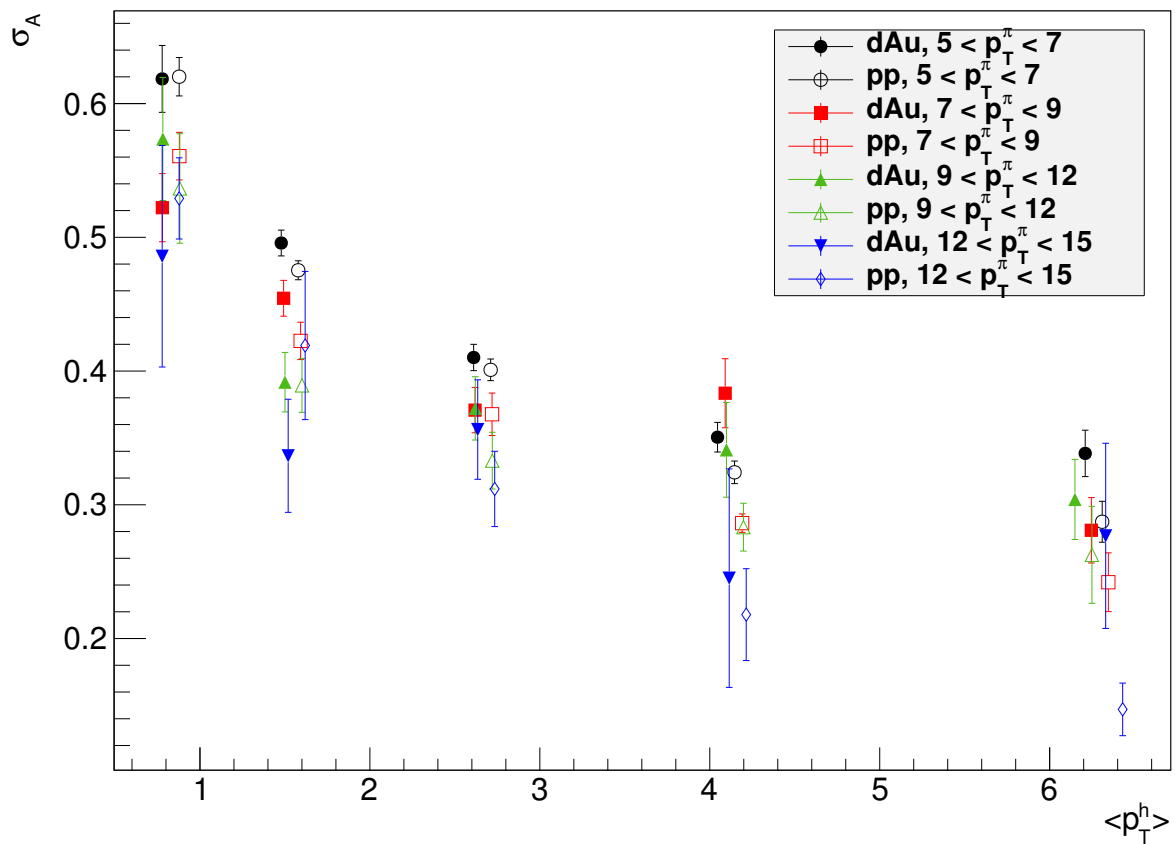


Figure 3.27: Away-side width for 60-88% centrality used for $R_{\Delta\eta}$ from gaussian fits. The $p+p$ p_T^h values are shifted to the right by 0.1.

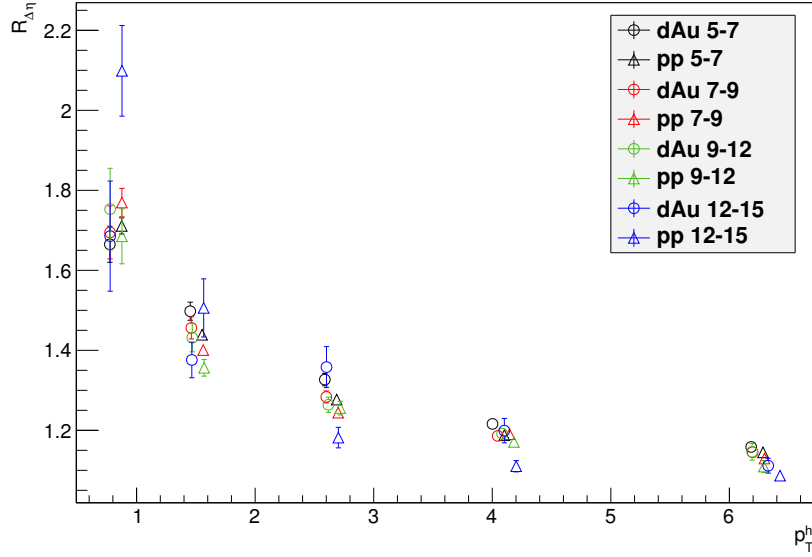


Figure 3.28: Nearside Rapidity Acceptance Correction for 0 - 20% Centrality. The $p+p$ p_T^h values are shifted to the right by 0.1.

Table 3.3: The uncertainty of $R_{\Delta\eta}$ corrections in 0-20% d+Au collisions

%	$0.6 < p_T^h < 1$	$1 < p_T^h < 2$	$2 < p_T^h < 3$	$3 < p_T^h < 5$	$5 < p_T^h < 7$
$5 < p_T^\pi < 7$	3.86	1.99	1.56	1.11	1.24
$7 < p_T^\pi < 9$	5.82	2.91	1.91	1.64	1.71
$9 < p_T^\pi < 12$	10.6	4.14	2.96	2.15	3.29
$12 < p_T^\pi < 15$	13	7.96	6.34	4	2.76

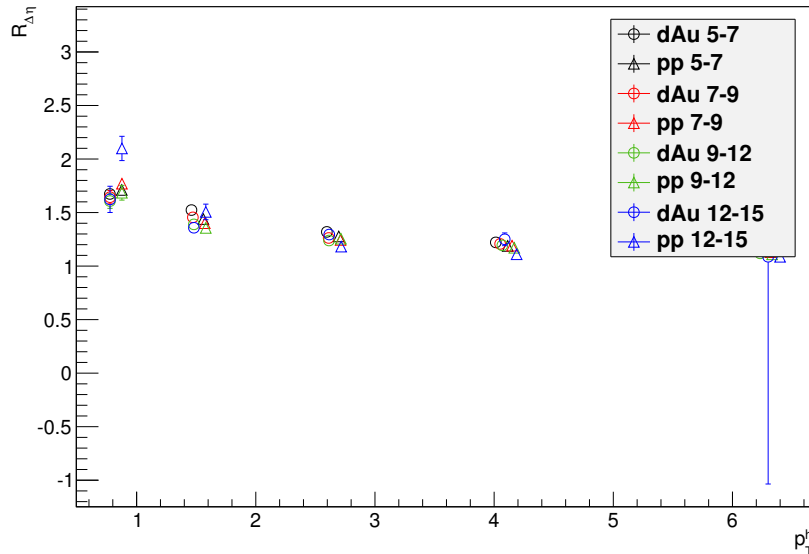


Figure 3.29: Nearside Rapidity Acceptance Correction for 20 - 40% Centrality. The p+p p_T^h values are shifted to the right by 0.1.

3.12 Uncertainties in Measurements

Before discussion of uncertainty treatment in this analysis, let's define some terms used widely in PHENIX [140] [141]. We can classify the systematic uncertainties into three classes, *Type A*, *B*, and *C*. Type A systematic uncertainty means that the uncertainty is uncorrelated from point to point. Type B means the uncertainty is correlated from point to point, and Type C means the uncertainty can be represented by an overall normalization factor.

In this analysis, the uncertainties associated with each measured variable are different, especially for *RI* (Section 4.4), where most of the systematics are cancelled out, completely or mostly. In *RI*, any uncertainty from efficiency is cancelled entirely. Some of other systematics uncertainties are correlated with each other, which dramatically reduce the size of systematic uncertainty. The

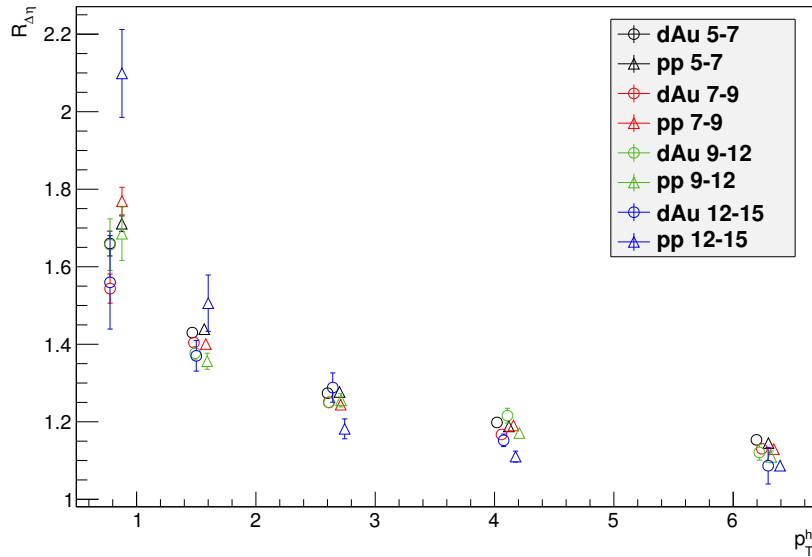


Figure 3.30: Nearside Rapidity Acceptance Correction for 40 - 60% Centrality. The p+p p_T^h values are shifted to the right by 0.1.

uncertainties deserve a separate section in any measurement, inside or outside physics. Here is a list of uncertainties considered in this analysis.

- Statistical uncertainty
- Type B uncertainties from the efficiency
- Type C uncertainties from the efficiency
- Uncertainty from the mis-constructed π^0 combinatorics
- Uncertainty from ZYAM
- Uncertainty from the bleeding correction
- Uncertainty from $R_{\Delta\eta}$

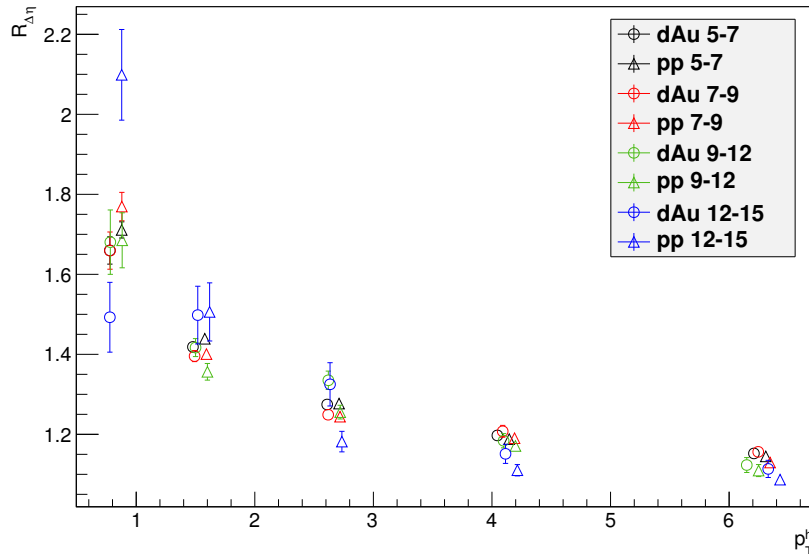


Figure 3.31: Nearside Rapidity Acceptance Correction for 60 - 88% Centrality. The p+p p_T^h values are shifted to the right by 0.1.

- Uncertainty from v_3 contribution

The statistical uncertainty is treated by ROOT, one possible concern is that we haven't update the statistical errors in the histograms when we perform the ZYAM. The necessary of the procedure is not pursued, and won't be discussed here. One uncertainty may be categorized into different types in terms of different quantities analysed. For example, all the uncertainties associated with efficiency are all type C uncertainties for the correlation function with a certain p_T bin (such as 5-7 GeV \otimes 1-2 GeV). However, they may be categorized into type B and type C uncertainties when we are analyzing I_{dA} or RI . Since the main quantities that we are trying to get physics information from are I_{dA} and RI values, so the later discussion is based on the point view of these quantities.

The type C uncertainties (both in terms of I_{dA} RI and the correlation/jet functions) from the efficiency come from three parts. The first comes from the d+Au yields published by [68], there is a 8.7% uncertainties in all p_T [68]. The second comes from the p+p cross-section published by [138], there is 9.6% uncertainties from BBC efficiency affecting all p_T [138]. The third comes from the trigger bias determination when converting p+p cross-section to yields [139]. The size of it is 3%. Since these uncertainties are constant in any p_T , z_T , N_{part} , and not correlated with any other uncertainty, so we decide leave them alone. They are not shown in any plots except in I_{dA} plots, where I put a shaded box to indicate the size of these uncertainties.

There are other p_T dependent and correlated uncertainties in the efficiency determination, or say type B, in terms of I_{dA} and RI (Attention, they are type C uncertainties in terms of the correlation function for one p_T bin). They are treated as independent to each other when we determine the average efficiency for one p_T bin in this analysis, which is more conservative than the actual one (since they are correlated somehow, at least partially, due to the same method utilized for those fine p_T bins in the previous efficiency measurements), see Section 3.10.1. And this uncertainty has the largest fraction in the combined systematic uncertainty. In RI , it is completely cancelled out. The main reason we choose RI as the measurement variable is the small systematic uncertainty. The other reason is that it is sensitive to the physics we are trying to measure. The final results of RI are shown in Section 4.4. This uncertainty is shown in the systematics graphs in all jet function plots, the near/away side yields plots, the near-away side width plots, the near/away side I_{dA} plots, and the RI plots.

The mis-constructed π^0 has its correlation in $\Delta\phi$. They should be corrected in the jet function, then in the away/near-side yields, I_{dA} , and RI . However, we don't

have the p+p data available right now. So we decide not to correct it for both d+Au and p+p, and assign the size of this uncertainty as 100% of the relative size of π^0 combinatorics correction in d+Au. This uncertainty is shown in the systematics graphs in all jet function plots, the near/away side yields plots (if I put them in this notes), the near-away side width plots, the near/away side I_{dA} plots, and the RI plots. The corrections are usually uncorrelated with others in most of the quantities I list, however, they are correlated in RI . They are both subtracted in near and away side peaks, which make the effect less in RI . The relative size of this systematics in d+Au and p+p is calculated by Equation 3.55.

$$\frac{\Delta RI_\pi}{RI} = \left| \frac{Y_\pi^A}{Y^A} - \frac{Y_\pi^N}{Y^N} \right| \quad (3.55)$$

where, Y is the integrated yields in either near or away side in d+Au, and Y_π is the correction from π^0 combinatorics in near or away side in d+Au. And we notice that $\frac{Y_\pi}{Y}$ is small in both side, and almost a constant, which makes the uncertainty even smaller. This is one more small reason we want to choose RI because of the partial carelessness in the π^0 combinatorics uncertainty and the b_0 uncertainty.

The uncertainty of the ZYAM level is determined by the size of the b_0 parameter error from fit during ZYAM procedure. It is uncorrelated with any other systematics in terms of the jet function, the near/away side yields, I_{dA} . However, the effect of ZYAM uncertainty on near and away-side yields are partially cancelled, see Equation 3.56

$$\frac{\Delta RI_{b_0}}{RI} = \sqrt{\left(\frac{\Delta Y_{b_0}^{A,pp}}{Y^{A,pp}} - \frac{\Delta Y_{b_0}^{N,pp}}{Y^{N,pp}} \right)^2 + \left(\frac{\Delta Y_{b_0}^{A,dAu}}{Y^{A,dAu}} - \frac{\Delta Y_{b_0}^{N,dAu}}{Y^{N,dAu}} \right)^2}. \quad (3.56)$$

The reason we combine p+p and d+Au as the root of sum of squares because we believe the uncertainty of b_0 in p+p and d+Au fitting are uncorrelated with each

other. And the yields in integrated in $0 - \pi/2$ and $\pi/2 - \pi$, so we may rewrite it as

$$\sqrt{\left(\frac{1}{Y^{A,pp}} - \frac{1}{Y^{N,pp}}\right)^2 \left(\frac{\Delta b_0^{pp} \cdot \pi}{2}\right)^2 + \left(\frac{1}{Y^{A,dAu}} - \frac{1}{Y^{N,dAu}}\right)^2 \left(\frac{\Delta b_0^{dAu} \cdot \pi}{2}\right)^2}. \quad (3.57)$$

This uncertainty is shown in the systematics graphs in all yields plot (if I put them in this notes), I_{dA} plots and RI plots.

The uncertainty of the bleeding effect is estimated as 50% the size of the correction itself because of the small correction, see Section 4.3. We assign this as 100% of the correction in my previous analysis note. However, since we've correct it, we could go with a little bit of less conservative. In the lowest partner bins, especially 5-7 x 0.6-1 GeV/c one, the correction is relative large, which might need a careful treatment. In general, the shape and width of d+Au, p+p jets are similar, so the effect of the bleeding correction is similar for the two yields. Therefore, the bleeding correction in d+Au and p+p partially cancels each other. The bleeding correction in near-side and away-side are also correlated. The loss in one side is exactly the gain in the other side, which makes the contribution somewhat larger than independent variables. So, all four corrections to the yields (near/away side \otimes d+Au/pp) are not independent variables. Right now, we use 50% size of the correction as the uncertainty. In principle, we could use the uncertainties of the fitted width to propagate into this correction, and use this to evaluate the uncertainties, and possibly reduce the systematics. This uncertainty is shown in the systematics graphs in all yields plot (if I put them in this notes), I_{dA} plots and RI plots.

The uncertainty of $R_{\Delta\eta}$ is evaluated by the function of $R_{\Delta\eta}(\sigma_N)$, shown in Figure 3.19. We vary the nearside width by the error from the fitting, and obtain the uncertainty of $R_{\Delta\eta}$, and propagate it into the nearside yields, nearside I_{dA} and RI . The contribution of p+p and d+Au uncertainties into nearside I_{dA} and RI is

treated as uncorrelated uncertainties, and calculated as square root of sum of squares. This uncertainty is shown in the systematics graphs in all yields plot (if I put them in this notes), I_{dA} plots and RI plots.

The v_3 could cause an enhancement of awayside nearside ratio. v_3 should be generally small, however, [97], [98] don't rule out a possibility of large v_3 . So for this systematics, we choose v_3 values as large as v_2 ones, such as $v_3 = 0.05$ in 0.6 - 1 GeV/ c , and $v_3 = 0.07$ in 5 - 7 GeV/ c , and propagate it into yields, I_{dA} , RI . The uncertainty is about 2% for the awayside nearside ratio. In high partner p_T 's, it remains about 2% if we assume a rising v_3 as v_2 . So we assign a 2% type C uncertainty for v_3 contribution. This uncertainty is shown in the systematics graphs in all yields plot (if I put them in this notes), I_{dA} plots and RI plots.

Table 3.4 shows the uncertainties and how they contribute to the final results.

Table 3.4: Uncertainties and Their Contributions. Here, C means corrected and the systematics is included. Y means the systematics is included. P means the systematics is included and treated carefully because of partial cancelness. 0 means the systematics is cancelled out. We believe that all Type B uncertainties are uncorrelated with each other, so we use the square root of the quadratic sum of all Type B uncertainties as the final over-all Type B uncertainty.

Uncertainty	Yields	I_{dA}	RI
Type B Eff	C	C	0
π^0 Combinatorics	Y	Y	P
ZYAM	C	C	CP
Bleeding	C	C	CP
$R_{\Delta\eta}$	C	C	C
v_3	N	Y	YP

4 RESULTS

4.1 Correlation Functions and Jet Functions

The correlation function, as we have discussed in Section 3.6, is defined as

$$C(\Delta\phi) \equiv \frac{\frac{dn_{real}^{AB}}{d\Delta\phi} \int \frac{dn_{mixed}^{AB}}{d\Delta\phi} d\Delta\phi}{\frac{dn_{mixed}^{AB}}{d\Delta\phi} \int \frac{dn_{real}^{AB}}{d\Delta\phi} d\Delta\phi}. \quad (4.1)$$

The correlation functions are ϕ acceptance corrected by dividing the mixed background. In simple words, the correlation function is an acceptance-corrected $dN^{AB}/d\Delta\phi$ π^0 - h^\pm pair distribution.

One thing to note, for the highest partner pt bin (5-7 GeV/ c), the mixing method fails due to extremely low statistics. The worst case is 12-15 \otimes 5-7 GeV/ c in 60-88% centrality, there are only 22 entries in my mixing histogram. The amount of computation in the taxi might be prohibitive considering the quick falling of the partner spectrum in Minimum Bias events. So we decide to use the one from one lower partner pt bin (3-5 GeV/ c), and triple the error bars. The difference between the two partner pt bins are checked in the lowest trigger pt bin, where the statistics are better. The two acceptance corrections are consistent with each other, well within the statistical errors, see Figure 4.1. One thing could break this validity, the distribution of the triggers. We check the number of triggers, which have large statistics, so we believe this won't cause the break down of this substitution.

The per trigger correlation functions for 0-5%, 0-20%, 20-40%, 40-60%, 60-88% centrality bins are shown in Figure 4.3, 4.4, 4.5, 4.6, 4.7 respectively.

We could separate the $dN^{AB}/d\Delta\phi$ pair distributions, a.k.a. the correlation functions, into two parts, one from the jets, the other one from the combinatorial backgrounds. This two source model could be described by the equation below

$$\frac{dn_{real}^{AB}(\Delta\phi)}{d\Delta\phi} = \frac{dn_{jet}^{AB}(\Delta\phi)}{d\Delta\phi} + \frac{dn_{comb}^{AB}(\Delta\phi)}{d\Delta\phi}. \quad (4.2)$$

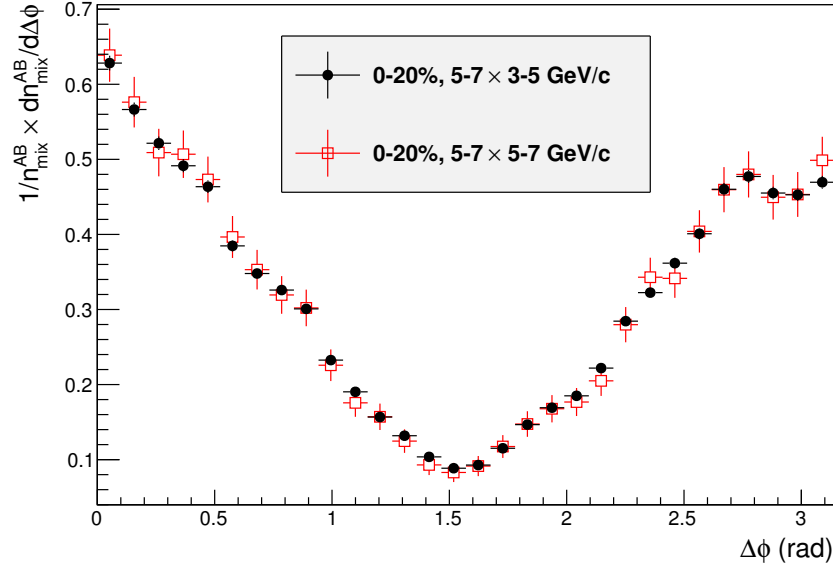


Figure 4.1: The acceptance correction of $5-7 \otimes 3-5$ GeV/ c and $5-7 \otimes 5-7$ GeV/ c in 0-20% centrality. The X axis is $\Delta\phi$, and the Y axis is $1/n_{\text{mix}}^{AB} \times dn_{\text{mix}}^{AB}/d\Delta\phi$. They are consistent with each other. This should validate our substitution of 5-7 GeV/ c mixing partners with 3-5 GeV/ c ones.

We could obtain the jet function by removing the combinatoric backgrounds from the correlation function. The ZYAM method, which is described in Section 3.6, is used to remove the background pedestal. Since the π^0 - h correlation functions are very clean in the central region, we simply pick up the lowest bin content from the histogram as the ZYAM level. We also tried fitting the data with a function containing both background pedestal and near-/away-side Gaussian peaks. Both methods agree with each other. The systematic error from the ZYAM is determined by the error of the fitted background parameter.

The jet function reveals the structure of jets, and the possible jet / fragmentation modifications in heavy ion collisions with the presence of nuclear

medium. In our d +Au data, we observe that in central events the away side jet has a clear suppression for high p_T partners, and a delicate enhancement in low p_T partners. A zoomed-in plots for the jet functions are shown in Figure 4.2 to show the small effects we are describing. This feature is similar to the data in Au+Au collisions which is due to the energy loss in the opaque quark gluon plasma, but in a much smaller scale. We will discuss this later in Chapter 5. And the near side jet has a small suppression in high p_T partners, which might comes from a bias effect. If there is some energy loss mechanism, no matter it is from cold or hot nuclear medium, the triggered events have a bias that the trigger survived with some probability while the other near side high p_T partners suffer from this energy loss.

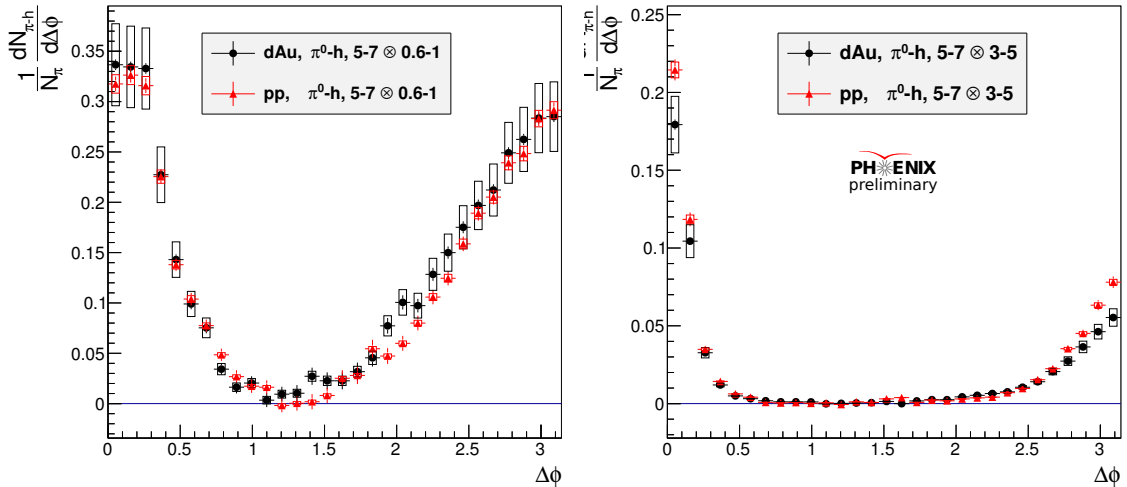


Figure 4.2: Two examples of d +Au and p + p jet functions for 0 - 20% Centrality. It shows some delicate enhancements and suppressions in central d +Au collisions. The suppression happens in the high partner p_T plots on the right side. The enhancement happens in the low partner p_T plots on the left side. And this enhancement is spread into a wider range.

The jet functions for 0-5%, 0-20%, 20-40%, 40-60%, 60-88% centrality bins are shown in Figure 4.8, 4.9, 4.10, 4.11, 4.12 respectively.

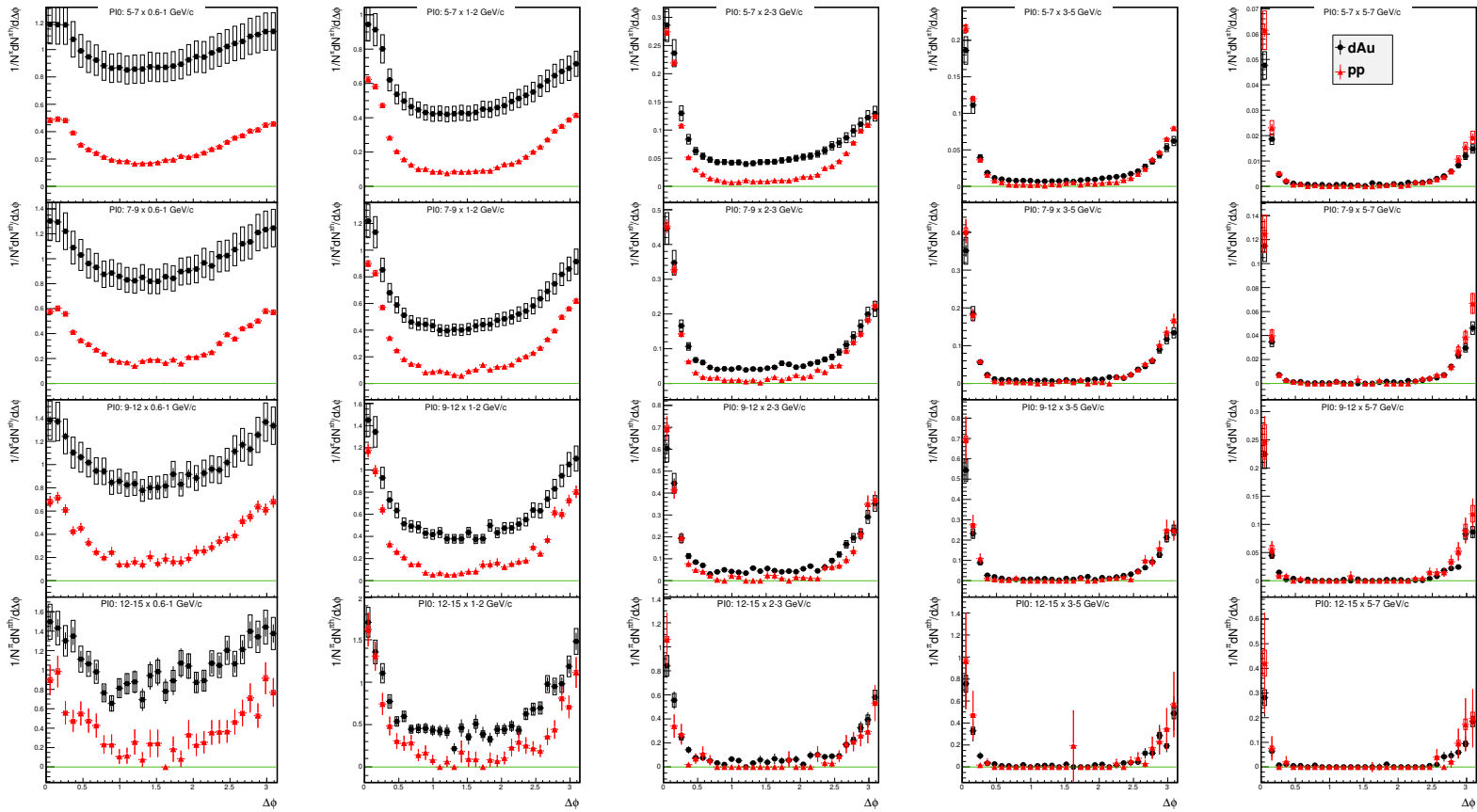


Figure 4.4: $d+Au$ and $p+p$ Correlation Functions for 0 - 20% Centrality. The systematic error is shown by the box markers, which includes efficiency, π^0 combinatorics. Both are Type C systematics in terms of $\Delta\phi$. The efficiency systematics have the same relative errors, and the ZYAM systematics have the same absolute errors.

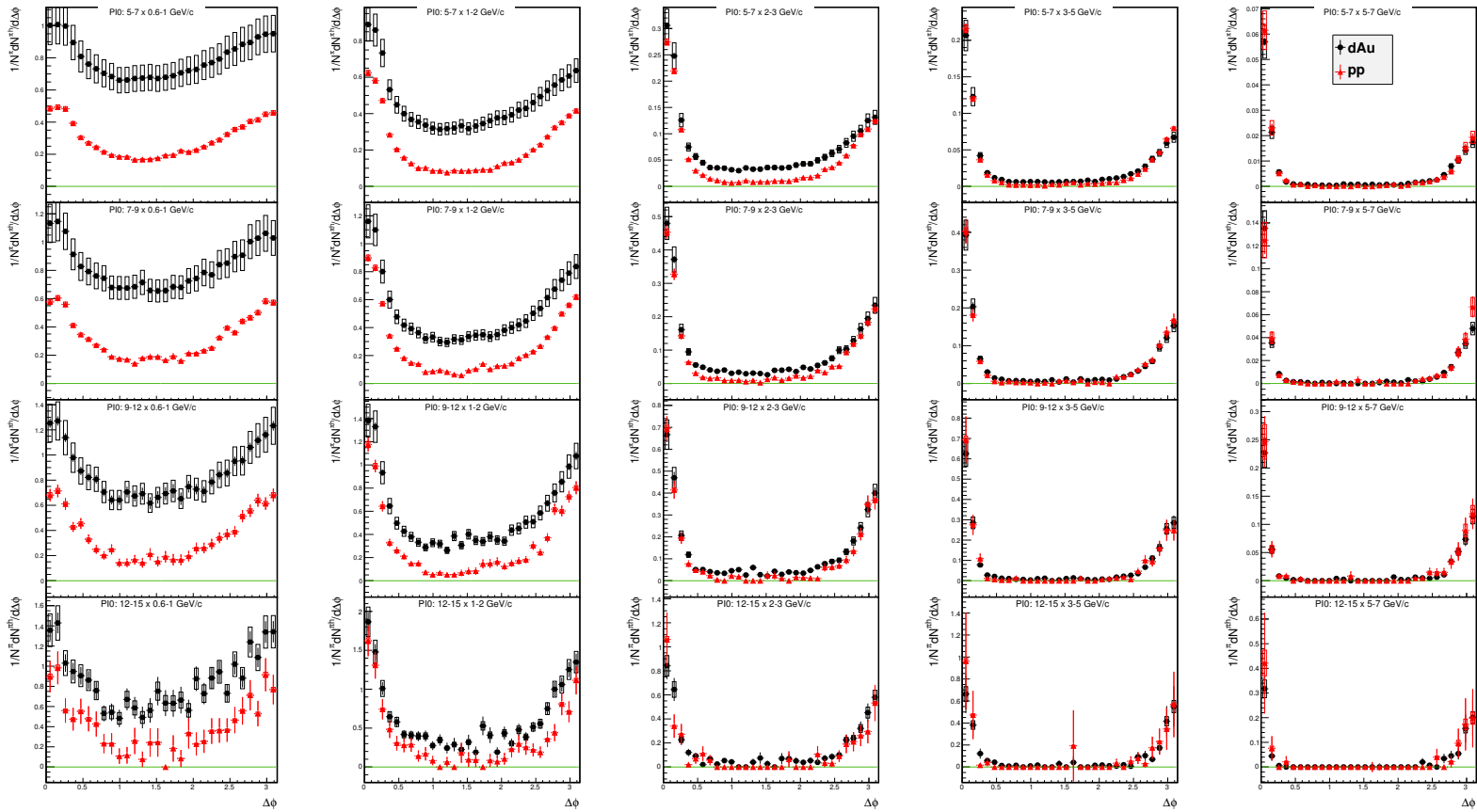


Figure 4.5: $d+Au$ and $p+p$ Correlation Functions for 20 - 40% Centrality. The systematic error is shown by the box markers, which includes efficiency, π^0 combinatorics. Both are Type C systematics in terms of $\Delta\phi$. The efficiency systematics have the same relative errors, and the ZYAM systematics have the same absolute errors.

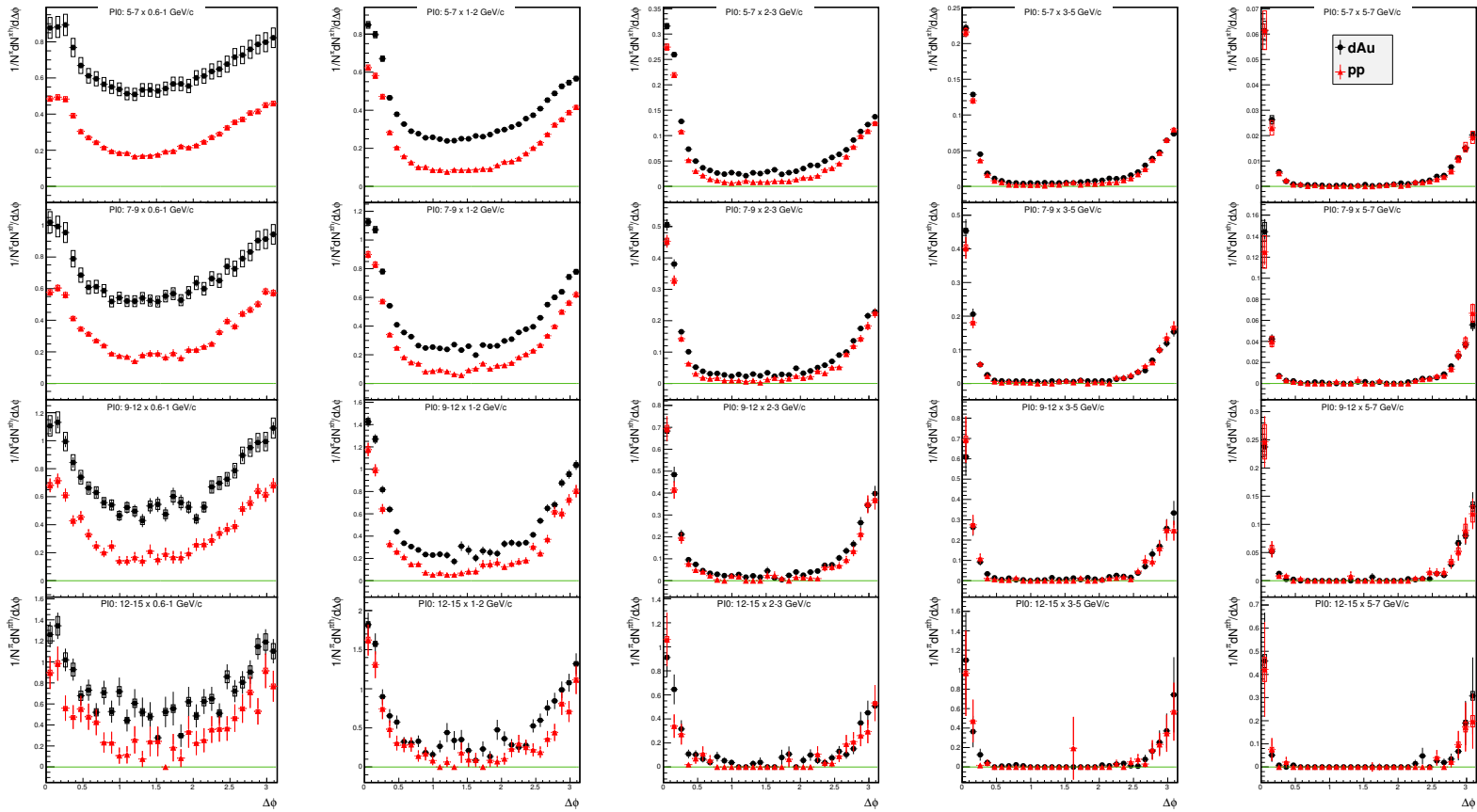


Figure 4.6: $d+Au$ and $p+p$ Correlation Functions for 40 - 60% Centrality. The systematic error is shown by the box markers, which includes efficiency, π^0 combinatorics. Both are Type C systematics in terms of $\Delta\phi$. The efficiency systematics have the same relative errors, and the ZYAM systematics have the same absolute errors.

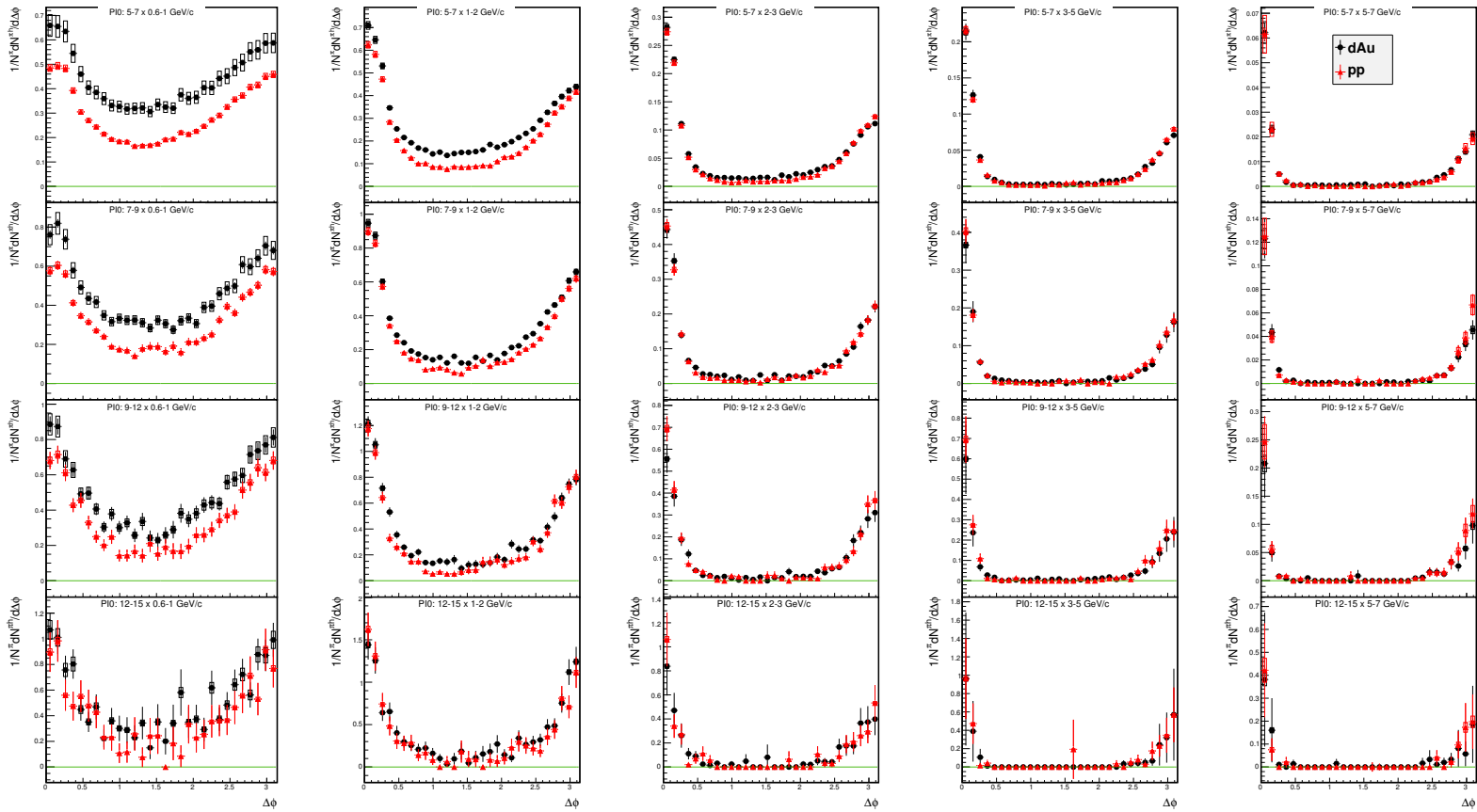


Figure 4.7: $d+Au$ and $p+p$ Correlation Functions for 60 - 88% Centrality. The systematic error is shown by the box markers, which includes efficiency, π^0 combinatorics. Both are Type C systematics in terms of $\Delta\phi$. The efficiency systematics have the same relative errors, and the ZYAM systematics have the same absolute errors.

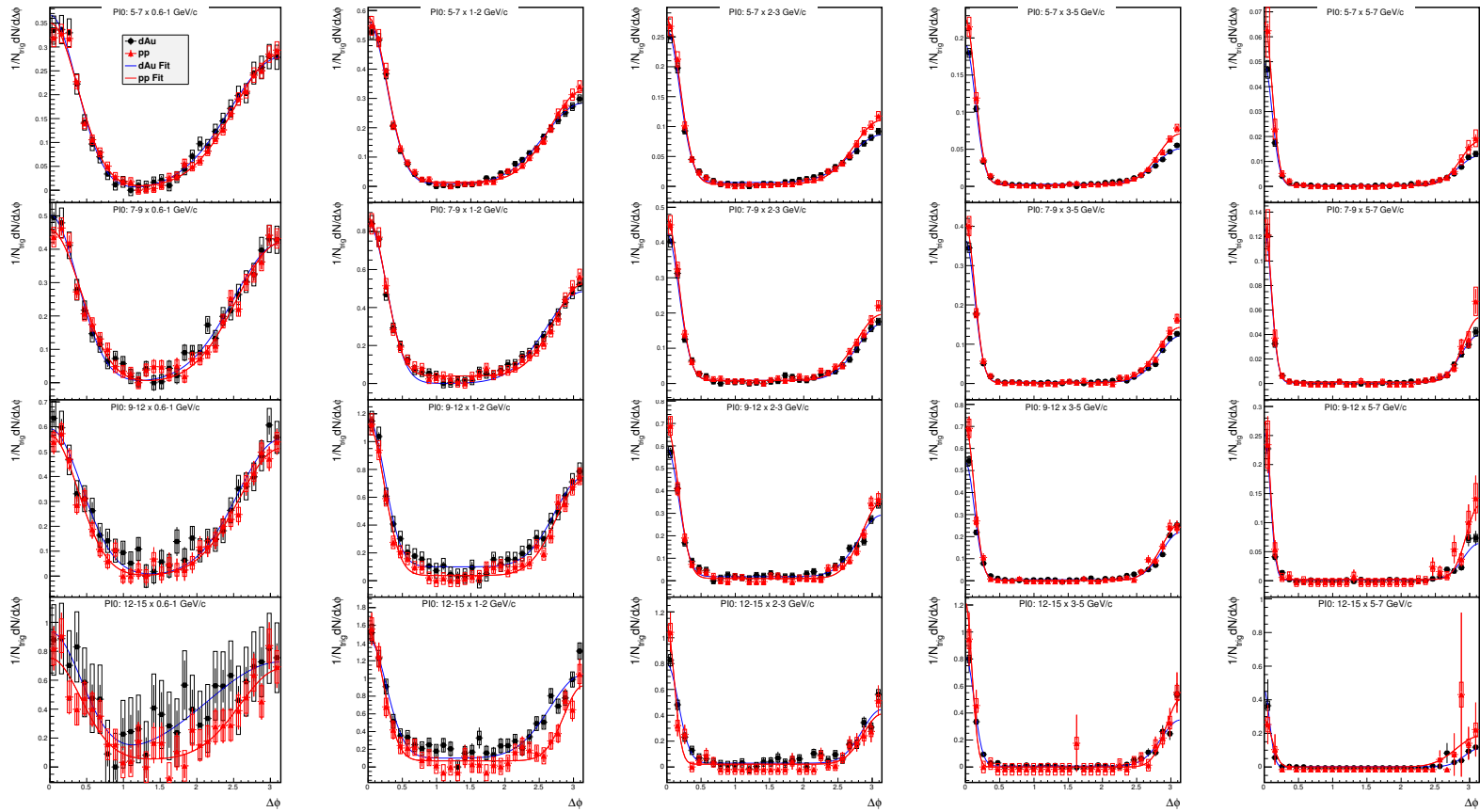


Figure 4.8: d +Au and p + p jet functions for 0 - 5% centrality. The systematic error is shown by the box markers, which includes efficiency, π^0 combinatorics and ZYAM.

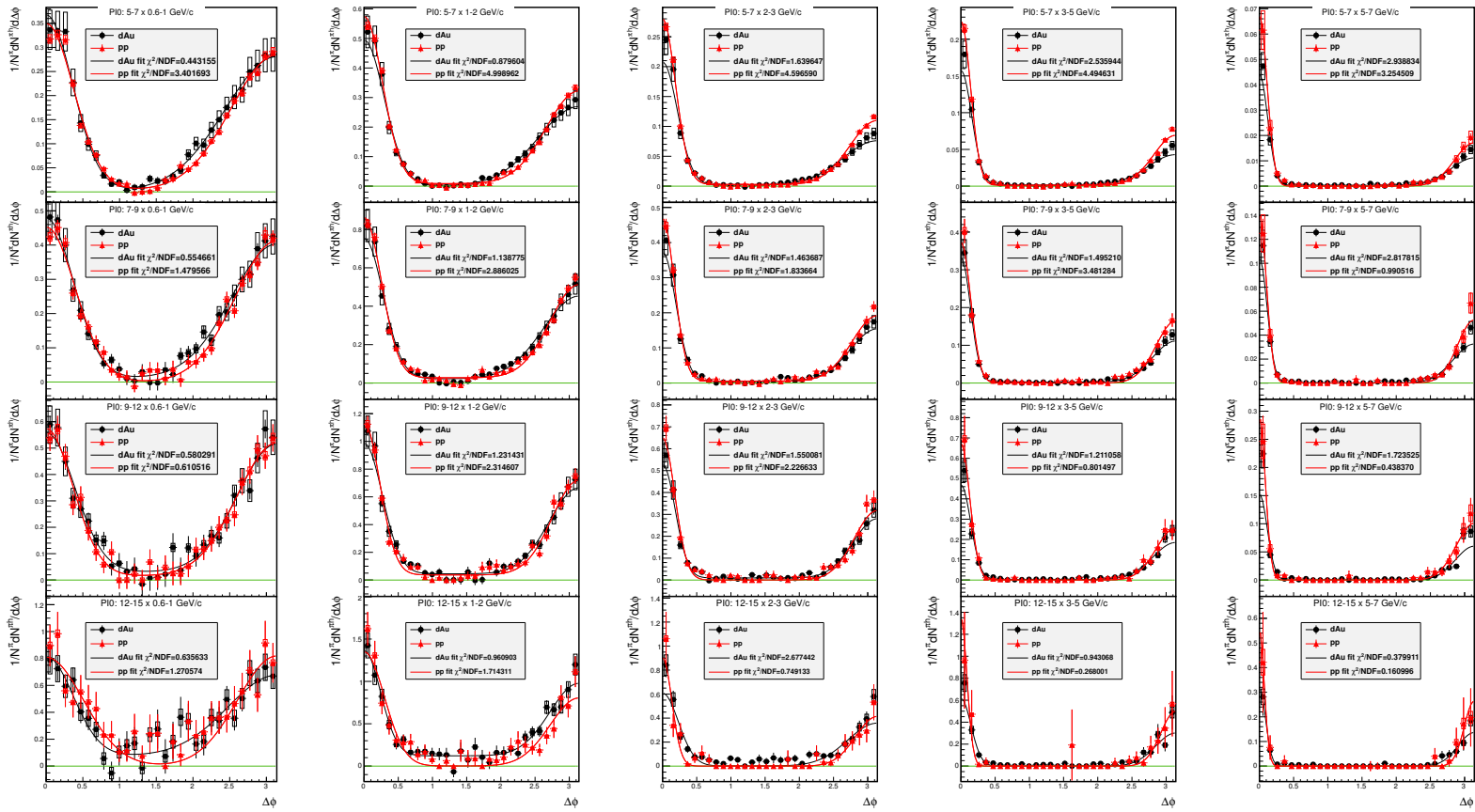


Figure 4.9: $d+Au$ and $p+p$ jet functions for 0 - 20% centrality. The systematic error is shown by the box markers, which includes efficiency, π^0 combinatorics and ZYAM.

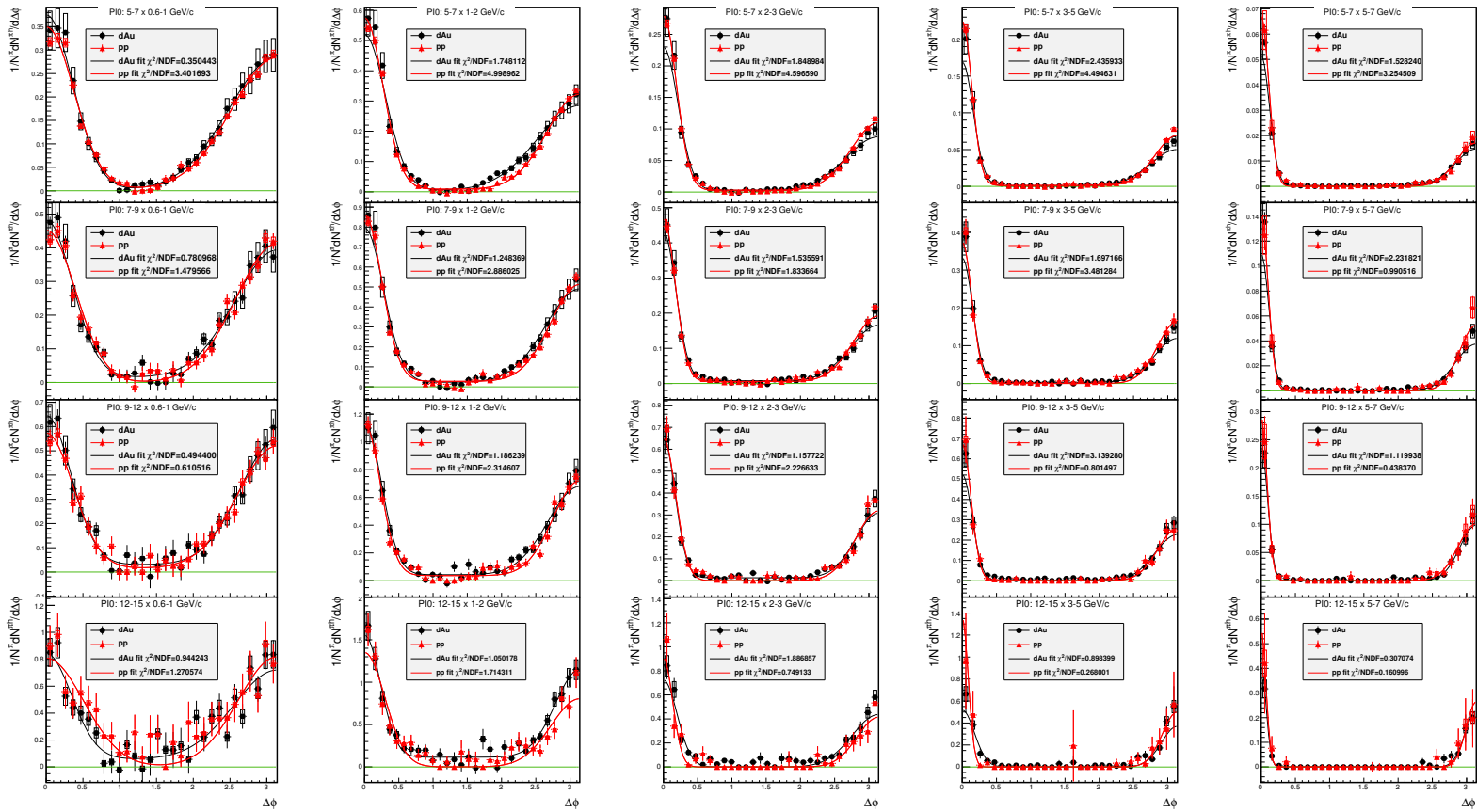


Figure 4.10: $d+Au$ and $p+p$ jet functions for 20 - 40% centrality. The systematic error is shown by the box markers, which includes efficiency, π^0 combinatorics and ZYAM.

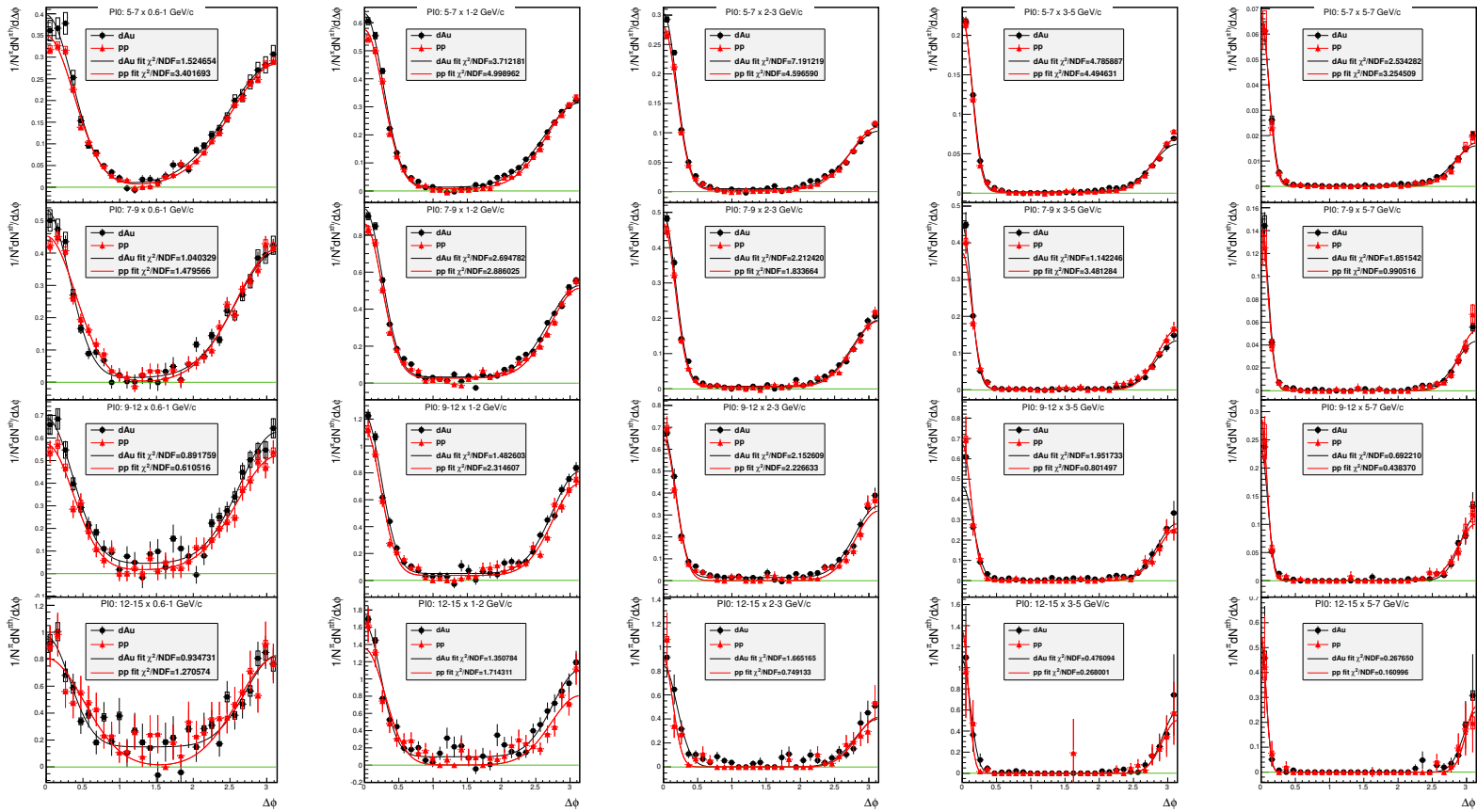


Figure 4.11: $d+Au$ and $p+p$ jet functions for 40 - 60% centrality. The systematic error is shown by the box markers, which includes efficiency, π^0 combinatorics and ZYAM.

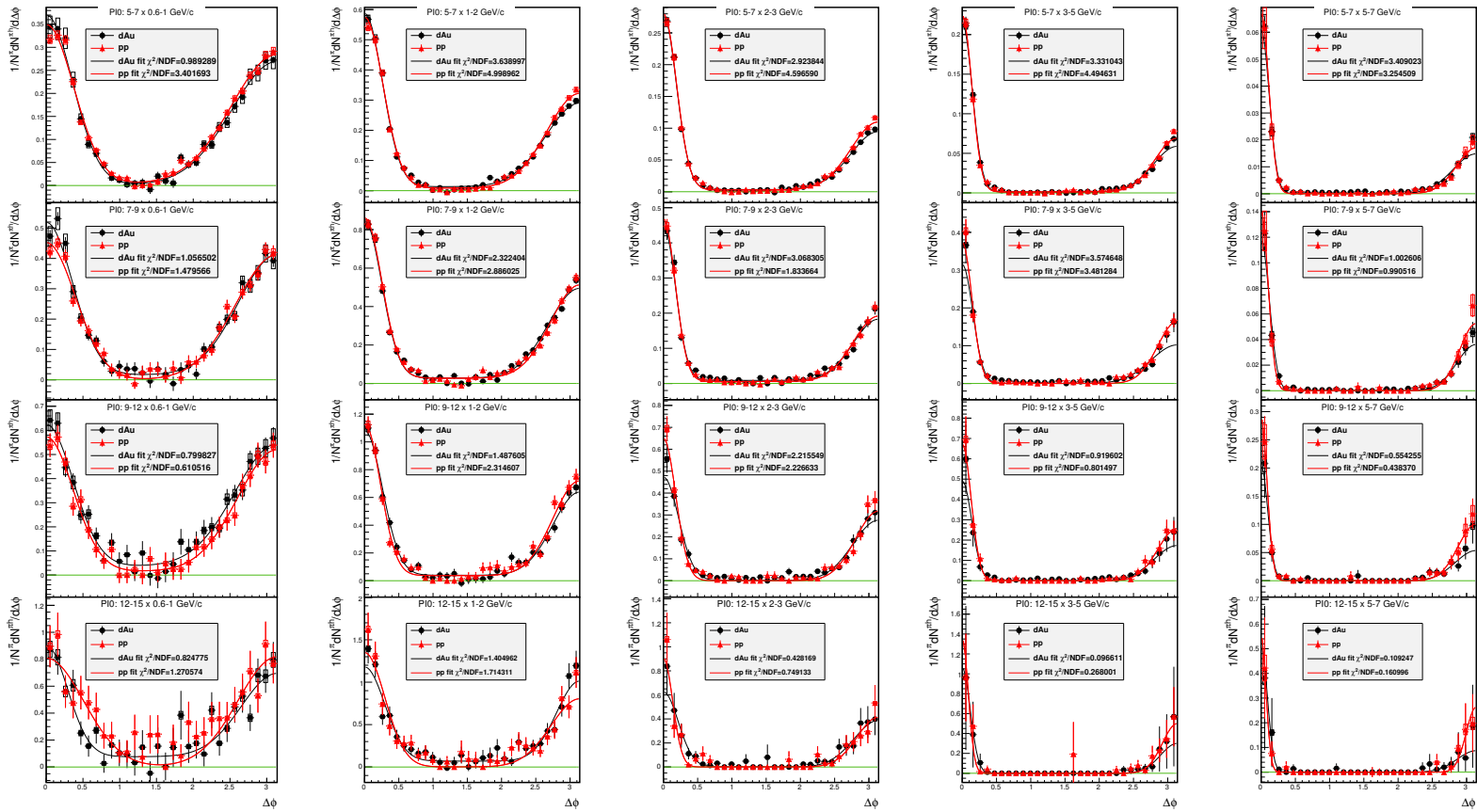


Figure 4.12: $d+Au$ and $p+p$ jet functions for 60 - 88% centrality. The systematic error is shown by the box markers, which includes efficiency, π^0 combinatorics and ZYAM.

4.2 Jet Widths

In Section 3.11, we have obtained the near and away-side jet width by fitting the jet function with a function representing the two source model. The results are shown in Figure 3.20 - 3.27. This method depends on the validity of the two source model. In order to avoid such issues, we use the *root of mean square (RMS)* method to evaluate the widths of the near and away-side jets. The near-side *jet width* are shown in Figure 4.13, 4.14, 4.15, 4.16, and the away-side jet width are shown in Figure 4.17, 4.18, 4.19, 4.20. As we can see, the most uncertainties come from the statistical fluctuations.

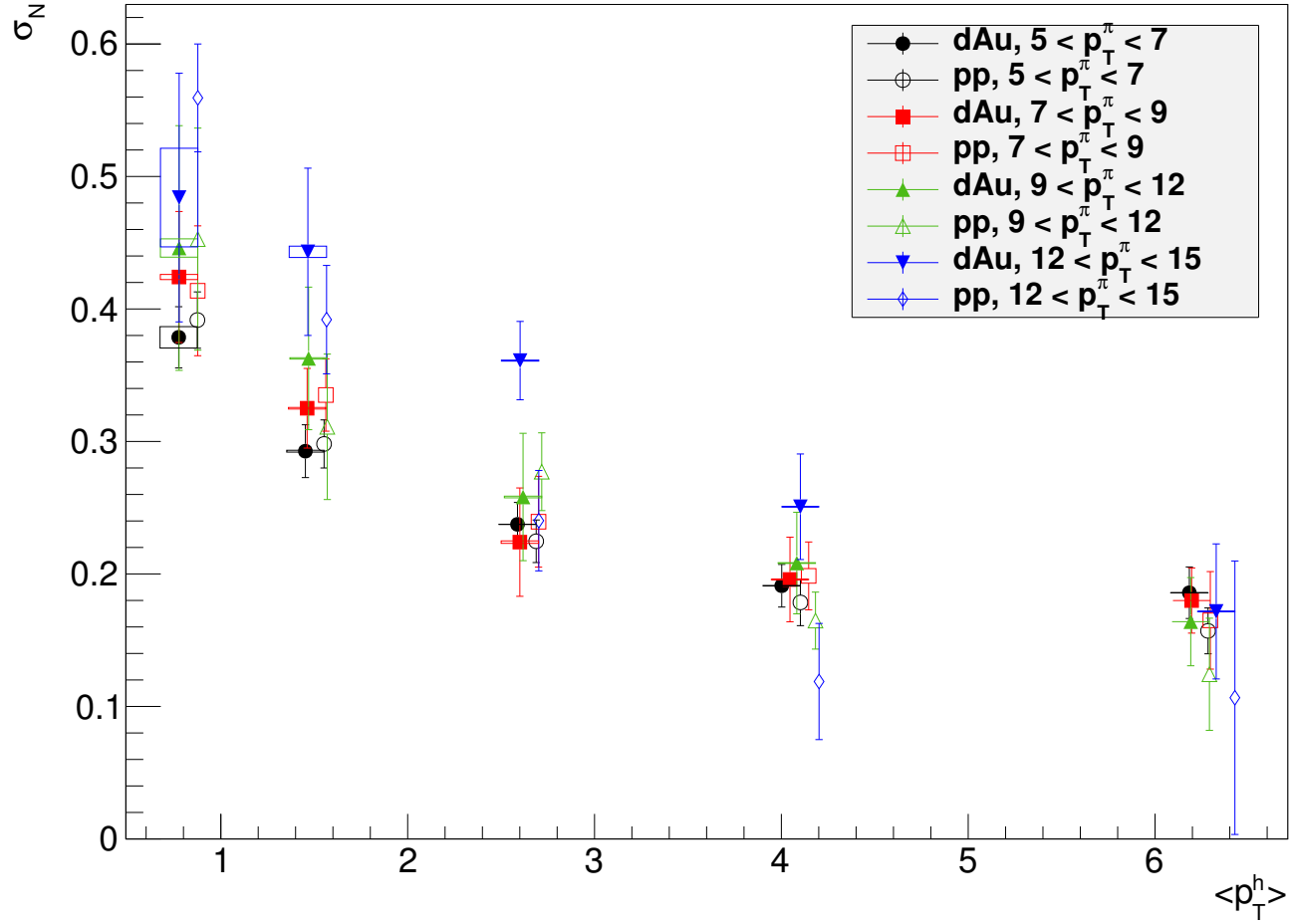


Figure 4.13: Nearside width for 0-20% centrality from RMS calculation. The $p+p$ p_T^h values are shifted to the right by 0.1. The systematic uncertainties are represented by the boxes.

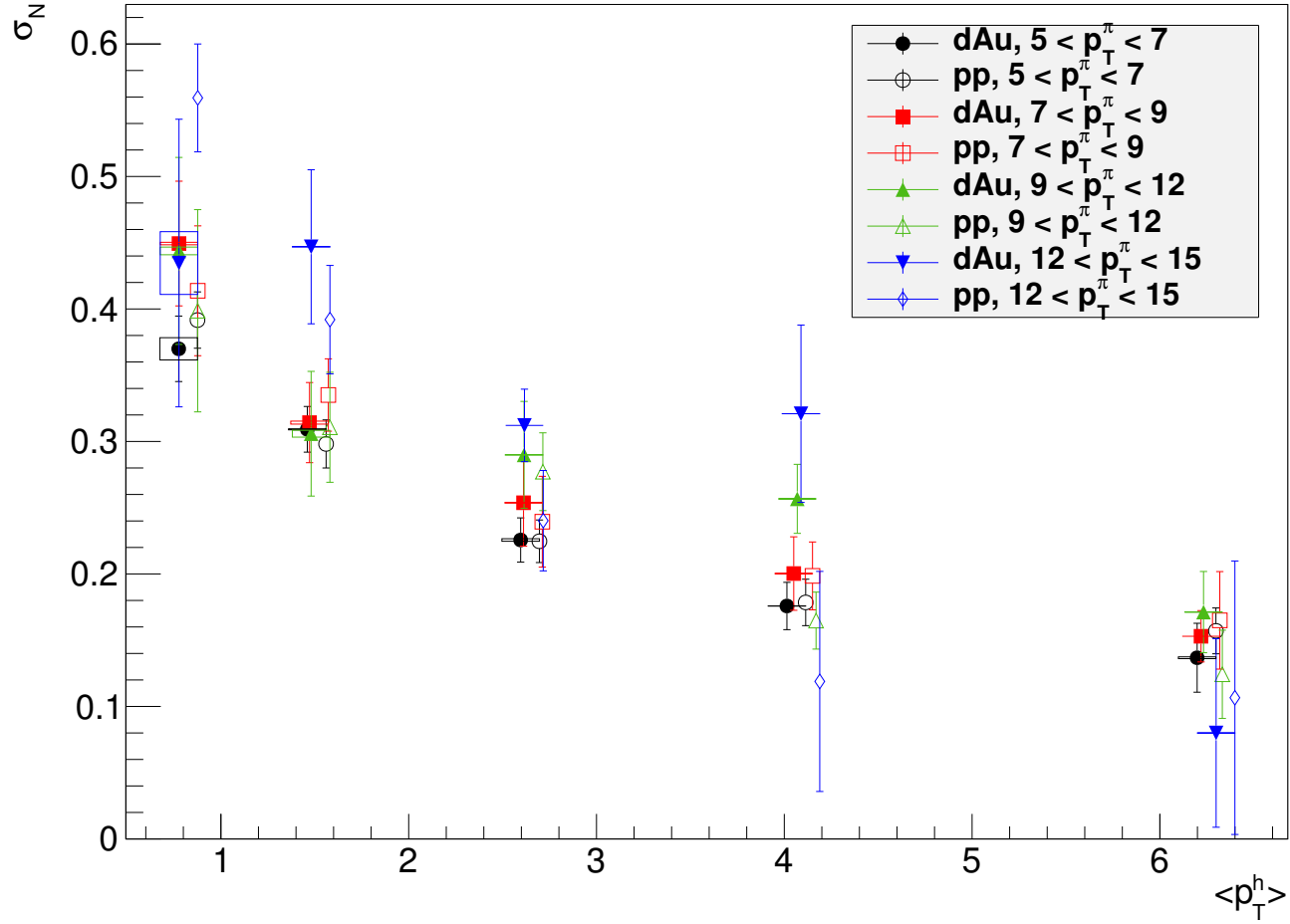


Figure 4.14: Nearside width for 20-40% centrality from RMS calculation. The $p+p$ p_T^h values are shifted to the right by 0.1. The systematic uncertainties are represented by the boxes.

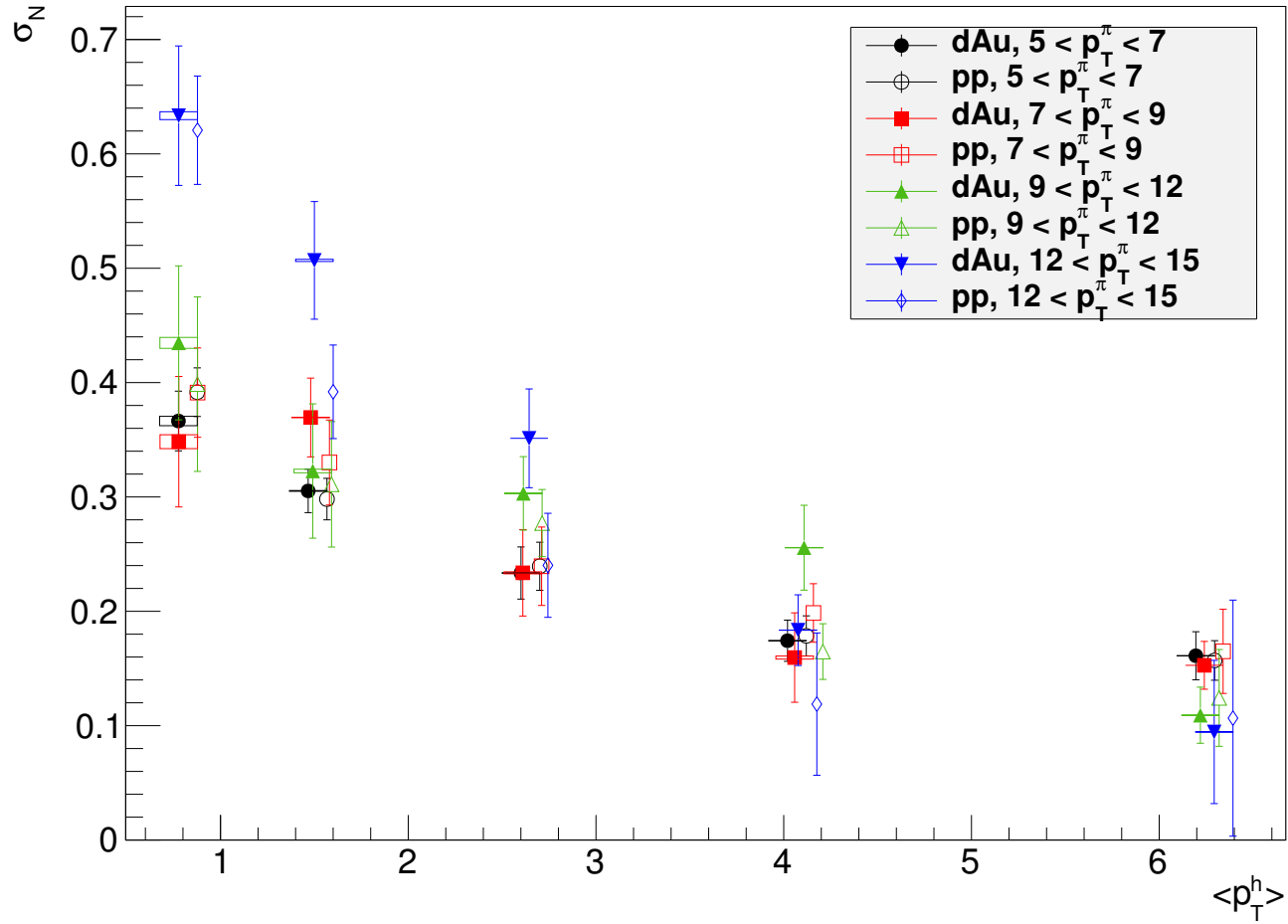


Figure 4.15: Nearside width for 40-60% centrality from RMS calculation. The $p+p$ p_T^h values are shifted to the right by 0.1. The systematic uncertainties are represented by the boxes.

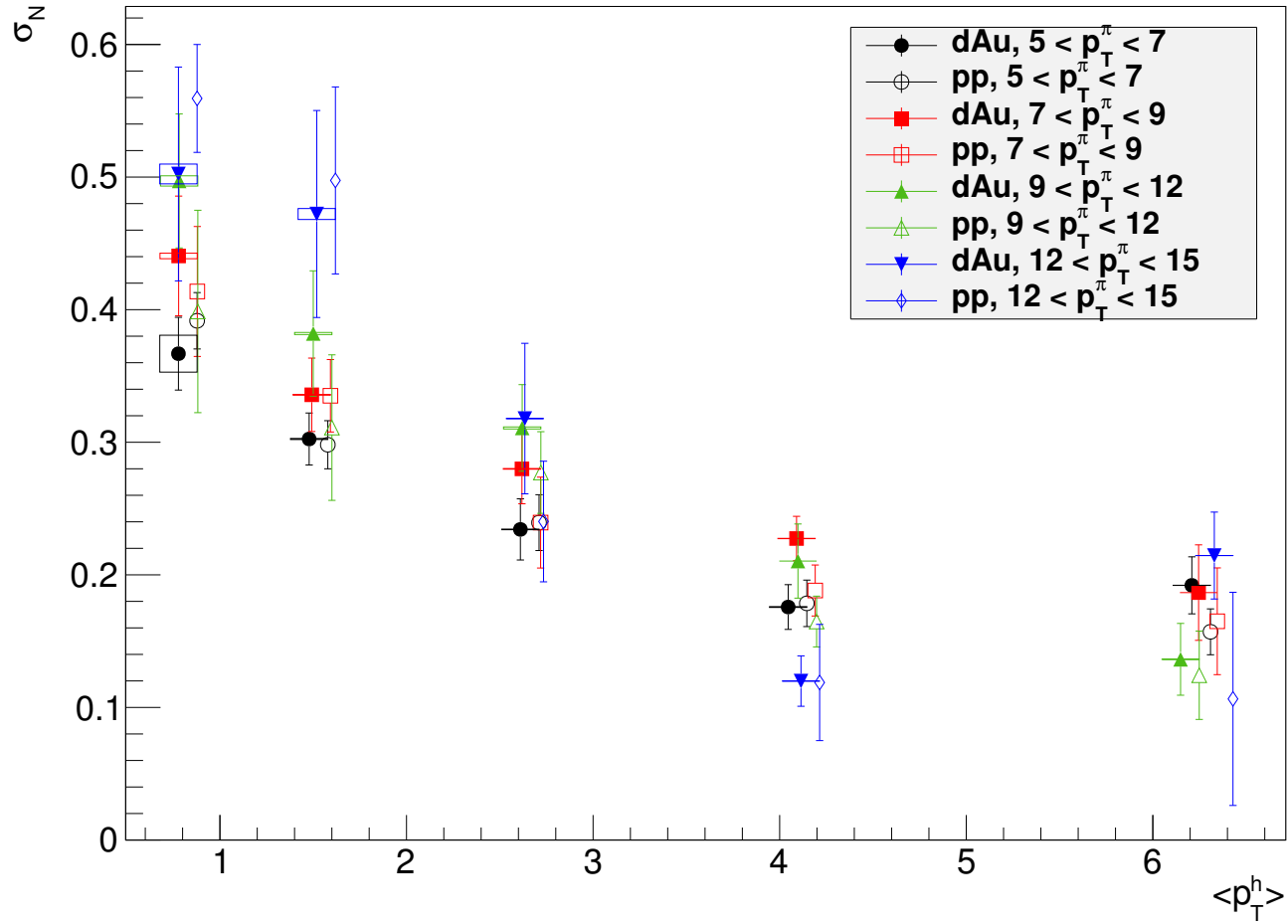


Figure 4.16: Nearside width for 60-88% centrality from RMS calculation. The $p+p$ p_T^h values are shifted to the right by 0.1. The systematic uncertainties are represented by the boxes.

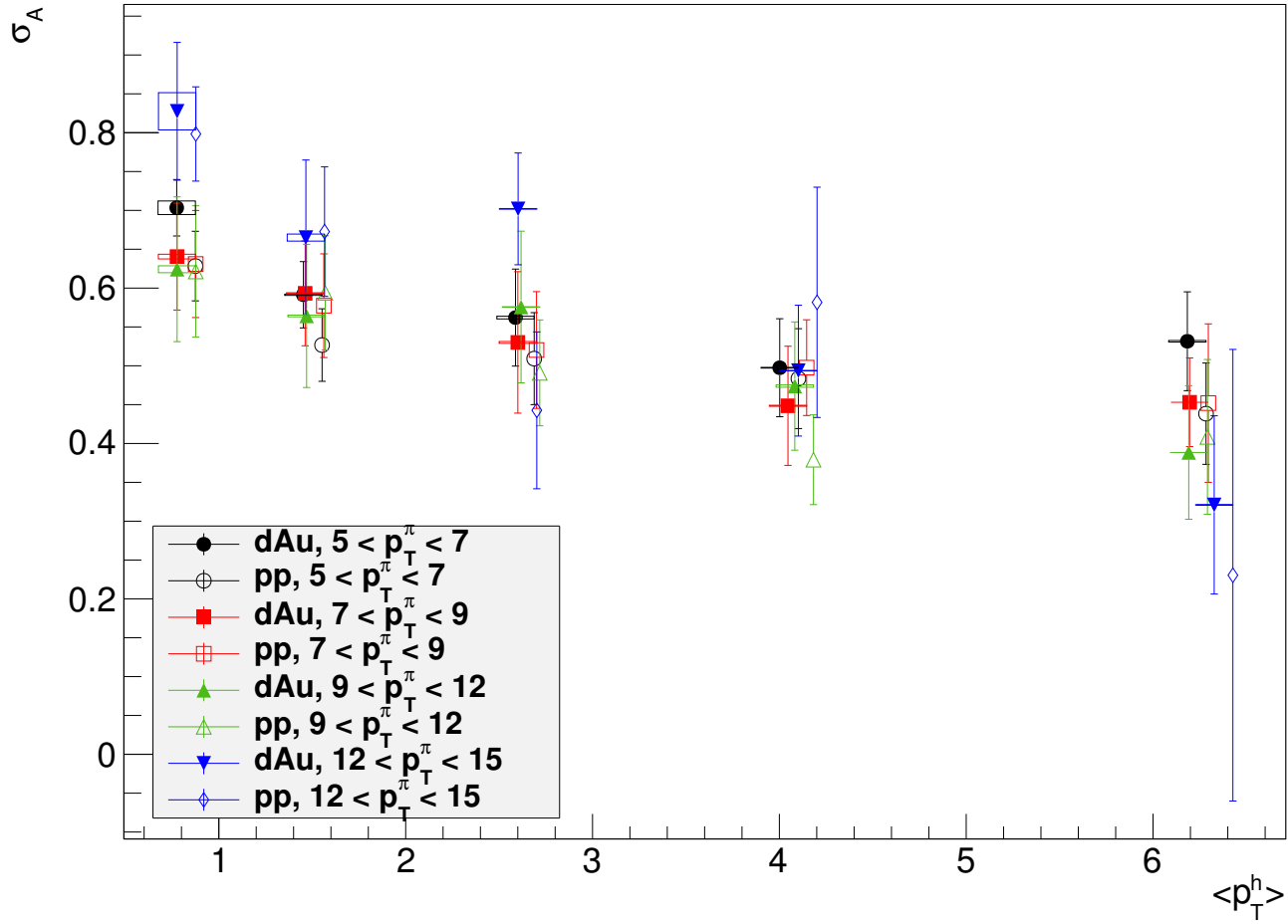


Figure 4.17: Awayside width for 0-20% centrality from RMS calculation. The $p+p$ p_T^h values are shifted to the right by 0.1. The systematic uncertainties are represented by the boxes.

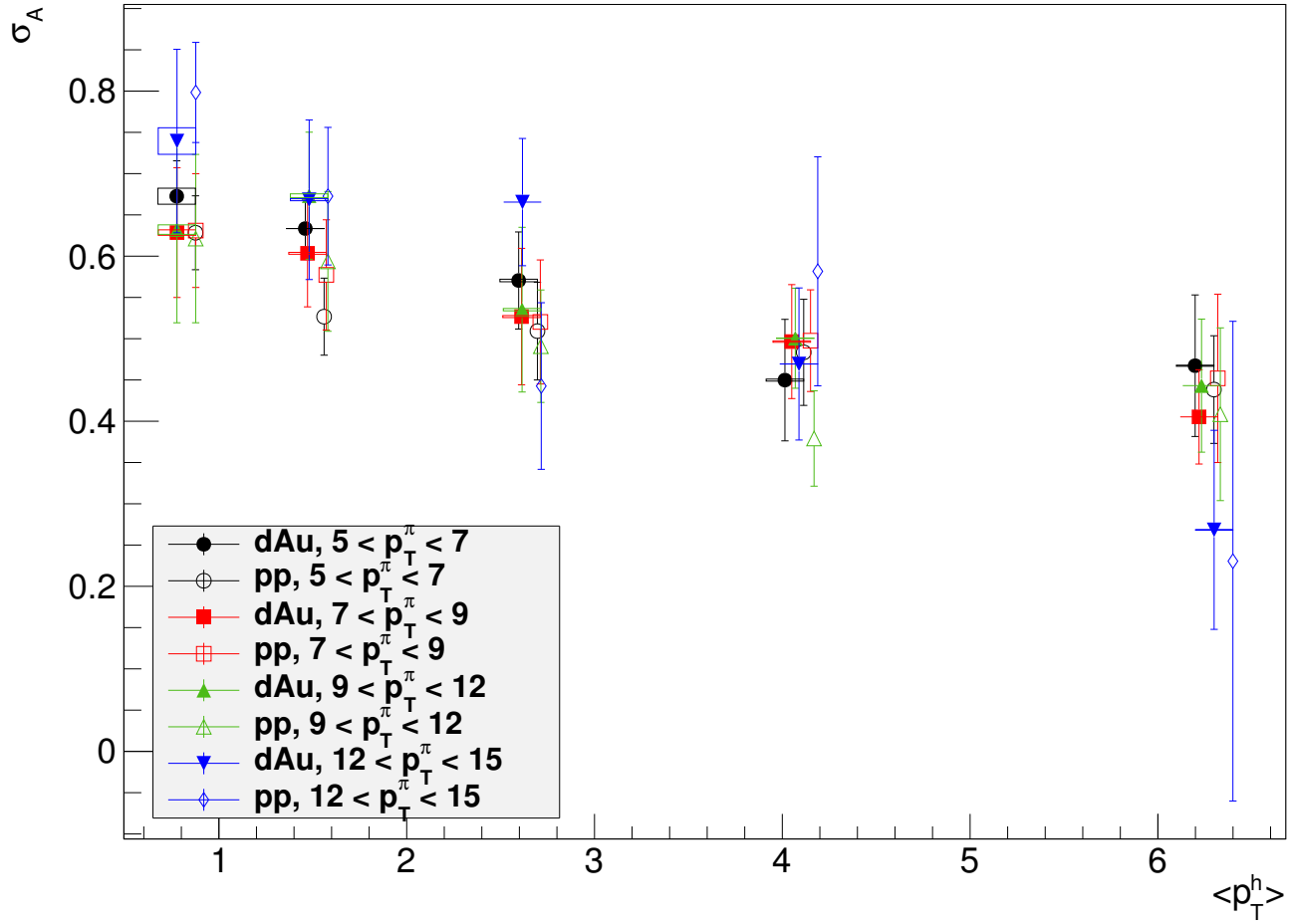


Figure 4.18: Away-side width for 20-40% centrality from RMS calculation. The $p+p$ p_T^h values are shifted to the right by 0.1. The systematic uncertainties are represented by the boxes.

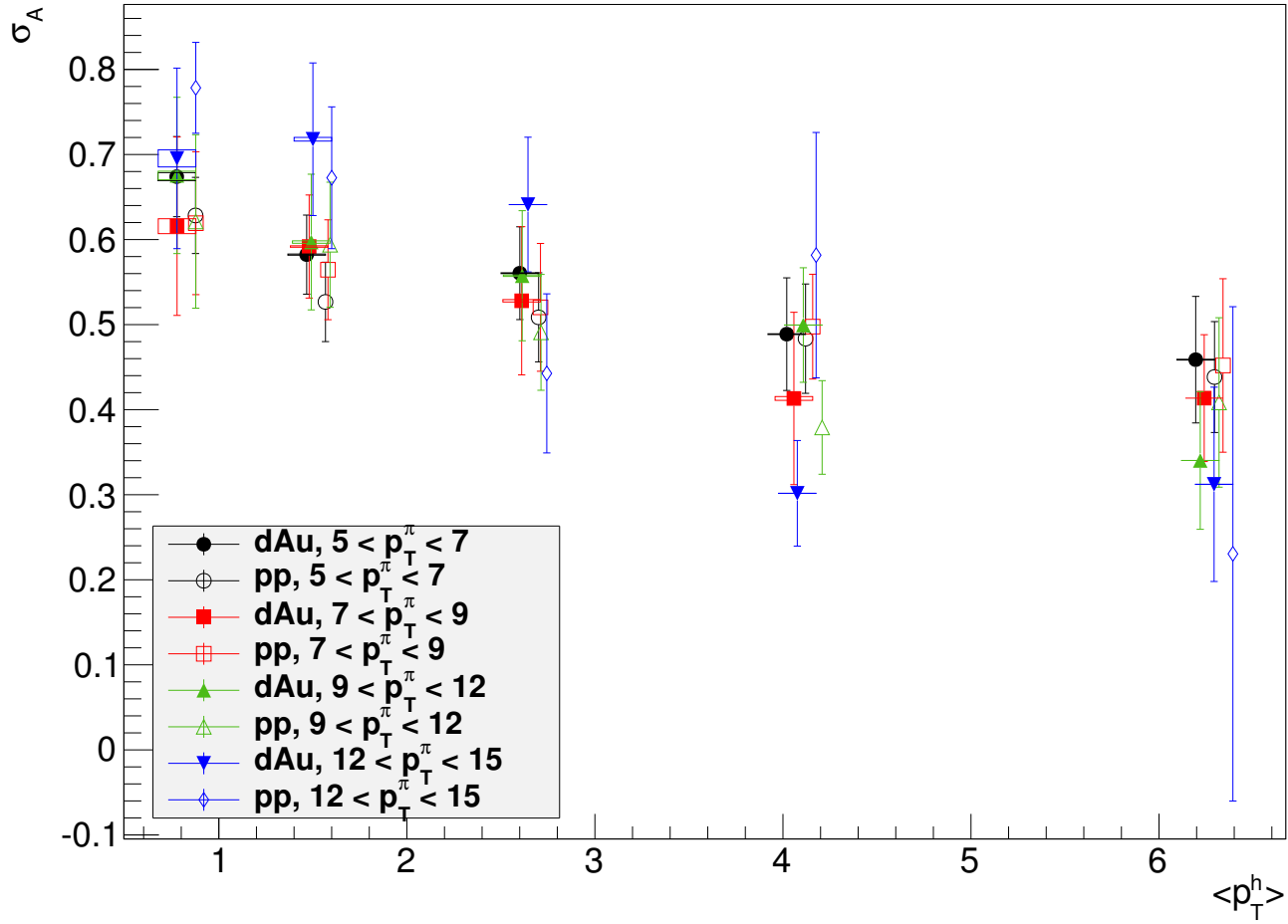


Figure 4.19: Awayside width for 40-60% centrality from RMS calculation. The $p+p$ p_T^h values are shifted to the right by 0.1. The systematic uncertainties are represented by the boxes.

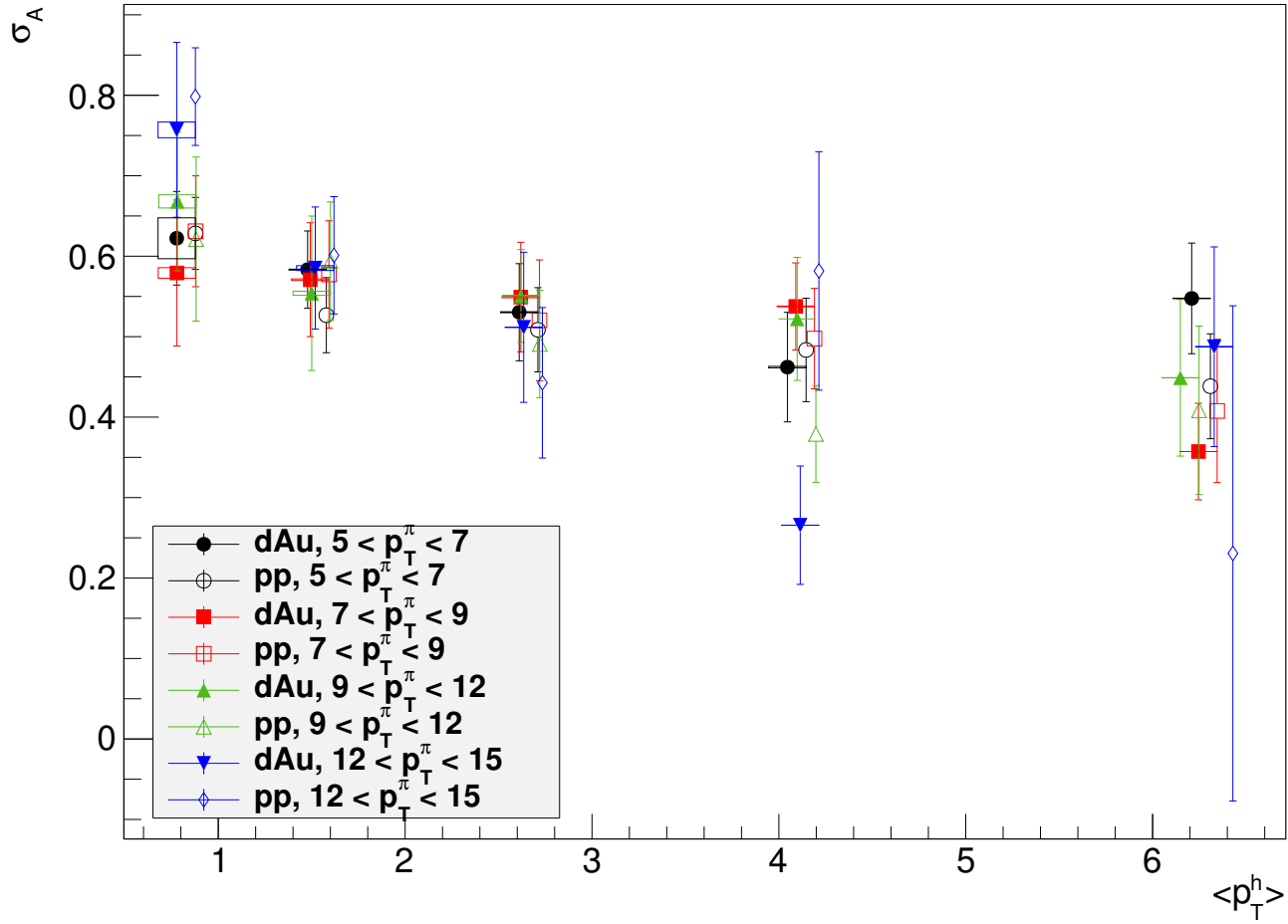


Figure 4.20: Away-side width for 60-88% centrality from RMS calculation. The $p+p$ p_T^h values are shifted to the right by 0.1. The systematic uncertainties are represented by the boxes.

4.3 Near and Away Side I_{dA}

The near and away side per trigger yields are obtained by integrating the two peaks and the bleeding effect correction, the rapidity acceptance correction (see Sub-Section 3.11). The idea of the bleeding effect is that the tail of the near/away-side Gaussian peaks could extend to the other side. It is corrected by subtracting the residual yields from the other side's fitted Gaussian peak and adding up the tail from the same side Gaussian peak. Since we are correcting the tails of the Gaussian peaks, we decide to use $\pi/2$ as the integration range.

$$Y_N = \int_0^{\pi/2} \text{JF}(\Delta\phi) d\Delta\phi - \int_0^{\pi/2} \text{Gaus}_A(\Delta\phi) d\Delta\phi + \int_{\pi/2}^{\pi} \text{Gaus}_N(\Delta\phi) d\Delta\phi$$

$$Y_A = \int_{\pi/2}^{\pi} \text{JF}(\Delta\phi) d\Delta\phi - \int_{\pi/2}^{\pi} \text{Gaus}_N(\Delta\phi) d\Delta\phi + \int_0^{\pi/2} \text{Gaus}_A(\Delta\phi) d\Delta\phi.$$

The first term is from the histograms, and the later two terms are calculated from the fitted Gaussian function. The uncertainty from the bleeding effect is set as 50% of this correction itself. The size of the bleeding effect correction in RI is shown in Table 4.1, which is very small considering the much larger yields and its effect on both sides and both $d+Au$, $p+p$ yields.

The effect of the nuclear matters in $d+Au$ collisions could be quantified by I_{dA} , the ratio of per trigger yields between $d+Au$ and $p+p$ collisions, see Equation 1.44. The deviation from unity denotes the departure from a vacuum QCD process.

The near side I_{dA} plots in different centralities are shown in Figure 4.21, 4.22, 4.23, 4.24, and the awayside I_{dA} are shown in Figure 4.25, 4.26, 4.27, 4.28. The X axis here is z_T , which is defined as

$$z_T \triangleq \frac{p_T^{\text{partner}}}{p_T^{\text{trigger}}}. \quad (4.3)$$

Table 4.1: The size of the bleeding effect correction on the awayside in 0-20% $d+Au$ collisions (The unit of p_T is GeV/ c)

%	$0.6 < p_T^h < 1$	$1 < p_T^h < 2$	$2 < p_T^h < 3$	$3 < p_T^h < 5$	$5 < p_T^h < 7$
$5 < p_T^\pi < 7$	2.54	0.783	0.161	0.0103	2.87e-4
$7 < p_T^\pi < 9$	0.97	0.22	5.78e-3	2.62e-4	1.77e-05
$9 < p_T^\pi < 12$	0.25	0.025	7.17e-4	2.14e-4	4.43e-07
$12 < p_T^\pi < 15$	1.4	0.0137	0.0207	6.93e-06	1.99e-09

z_T is a proxy of z in the fragmentation function. The systematic errors, shown as box in the plots, are determined by propagating the systematic errors from the $d+Au$, $p+p$ efficiencies and the ZYAM background. The ZYAM systematics are relatively low from the correlation functions shown in Section 4.1.

The $5-7 \otimes 5-7$ GeV/ c (an abbreviation of 5-7 GeV/ c trigger p_T and 5-7 GeV/ c partner p_T bin) data points in I_{dA} plots are close to unity, which might come from a possible kinematic bias. When the partner's p_T is close the trigger's p_T , it gets close to the jet's p_T . It takes away most of the jet energy, and there is less probability find other particle productions in the jet. Therefore, there is little room for a jet modifications. Besides this kinematic bias, another reason might comes from a trigger bias when the energy loss in a nuclear medium exists. A partner with p_T similar to the trigger might suggest that the partner undergoes a minimum energy loss, which is essentially an ‘‘anti’’ surface bias.

In principle, the I_{dA} plots should quantitatively display the modifications we've seen in the jet functions. However, the large systematic uncertainties associated in I_{dA} determination prevent us to get a definite conclusion. We see some tantalizing

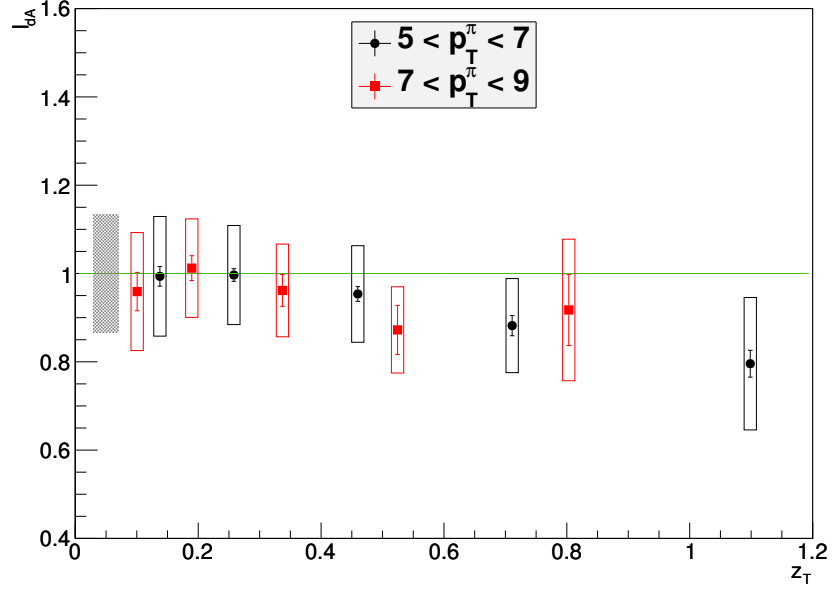


Figure 4.21: Nearside I_{dA-z_T} Plot in $d+Au$ with 0 - 20% Centrality.

signal here, but not in a conclusive way. Therefore, we propose a new quantity RI to cancel out the major sources of systematic uncertainties, see Table 3.4.

4.4 Double Ratio RI

The systematic uncertainty is large in the I_{dA} plots. The small modification effect in $d+Au$ collisions is hard to extract from those plots. In order to cancel out most of the systematics, we define a double ratio RI

$$RI \triangleq \frac{Y_{away}^{dAu} / Y_{near}^{dAu}}{Y_{away}^{pp} / Y_{near}^{pp}} \quad (4.4)$$

where, Y is the per trigger yields integrated from the jet function. RI cancels out the systematics from the efficiency completely (which is the major source of systematic uncertainties), and the relatively smaller one from ZYAM remains. The systematic uncertainties from ZYAM are plotted in two different ways: the first is

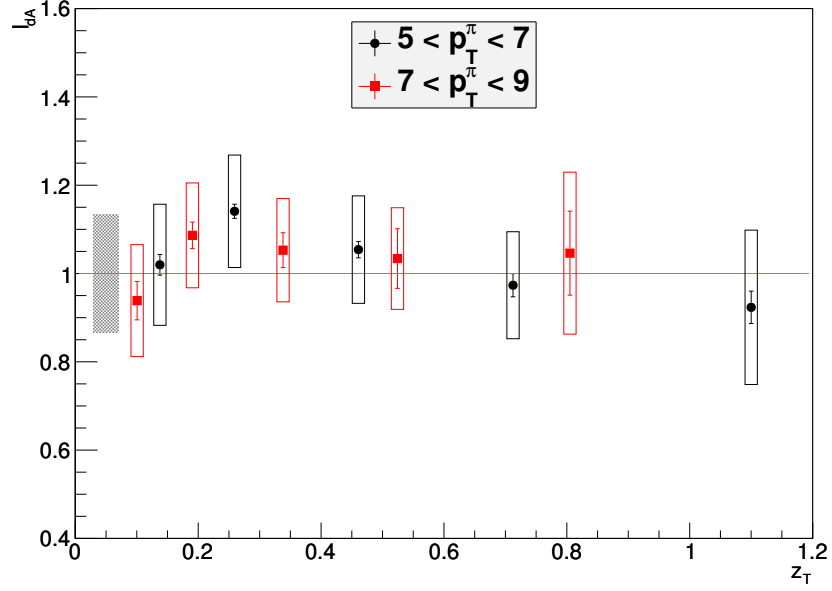


Figure 4.22: Nearside I_{dA} - z_T Plot in d +Au with 20 - 40% Centrality.

using ErrorHigh and ErrorLow calculated from YieldsHigh and YieldsLow, the other one is by propagating the errors from ZYAM into RI . The formula for d +Au away- / near-side yields ratio is

$$\begin{aligned}
 y &= \frac{a + c\delta}{b + d\delta} = \frac{a}{b} \frac{1 + \frac{c}{a}\delta}{1 + \frac{d}{b}\delta} \\
 &\sim \frac{a}{b} \left(1 + \frac{c}{a}\delta\right) \left(1 - \frac{d}{b}\delta\right) \\
 &\sim \frac{a}{b} \left[1 + \left(\frac{c}{a} - \frac{d}{b}\right)\delta\right].
 \end{aligned}$$

The one for RI should be

$$\sigma_{RI}^{ZYAM} = RI \cdot \sqrt{\left(\left(\frac{R_{dAu}^A}{Y_{dAu}^A} - \frac{R_{dAu}^N}{Y_{dAu}^N}\right) * \delta_{dAu}^{ZYAM}\right)^2 + \left(\left(\frac{R_{pp}^A}{Y_{pp}^A} - \frac{R_{pp}^N}{Y_{pp}^N}\right) * \delta_{pp}^{ZYAM}\right)^2} \quad (4.5)$$

where, Y means the per trigger yields, R means the integral range. The one from error propagation is a littler bit larger, so we use this one in our plots for conservative reasons. The RI vs z_T plots are shown in Figure 4.29, 4.30, 4.31, 4.32.

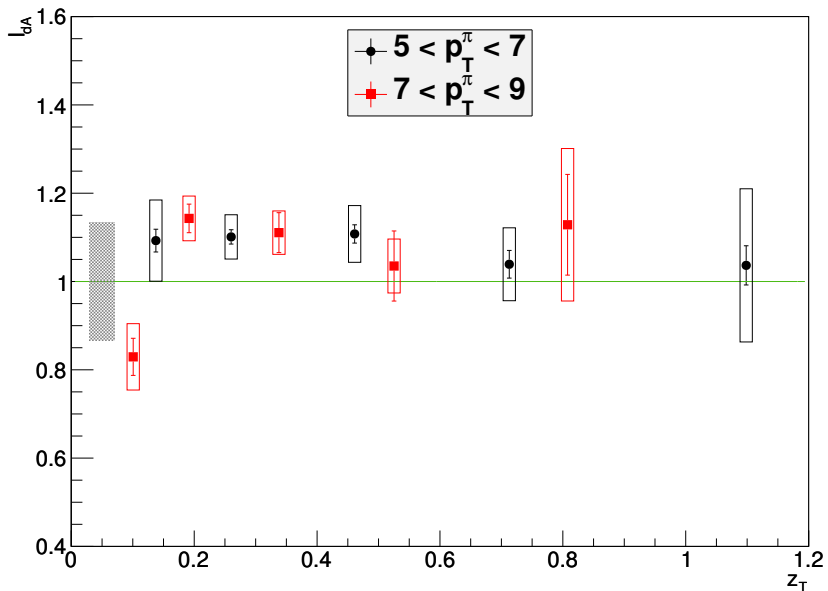


Figure 4.23: Nearside I_{dA} - z_T Plot in d +Au with 40 - 60% Centrality.

The $5-7 \otimes 5-7$ GeV/ c data points show some rising in RI plots, which might come from a possible kinematic bias, see discussions in Section 4.3.

The plots reveal subtle suppression in high z_T and enhancement in low z_T regions in central d +Au collisions. These RI plots shows the feature described in the jet functions in a qualitative way. The suppression in high z_T and enhancement in low z_T are about 2σ , which is about 95% probability for the presence of deviation from $p+p$ collisions.

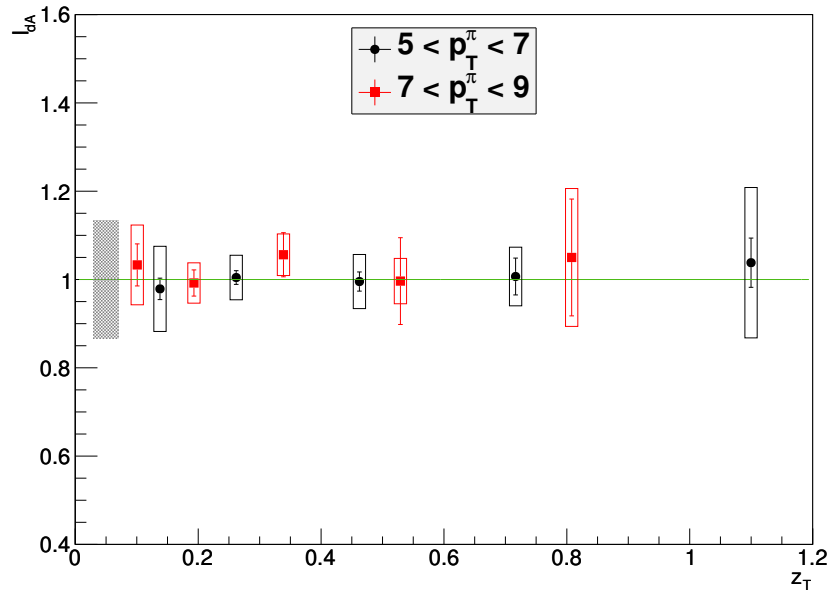


Figure 4.24: Nearside I_{dA} - z_T Plot in d +Au with 60 - 88% Centrality.

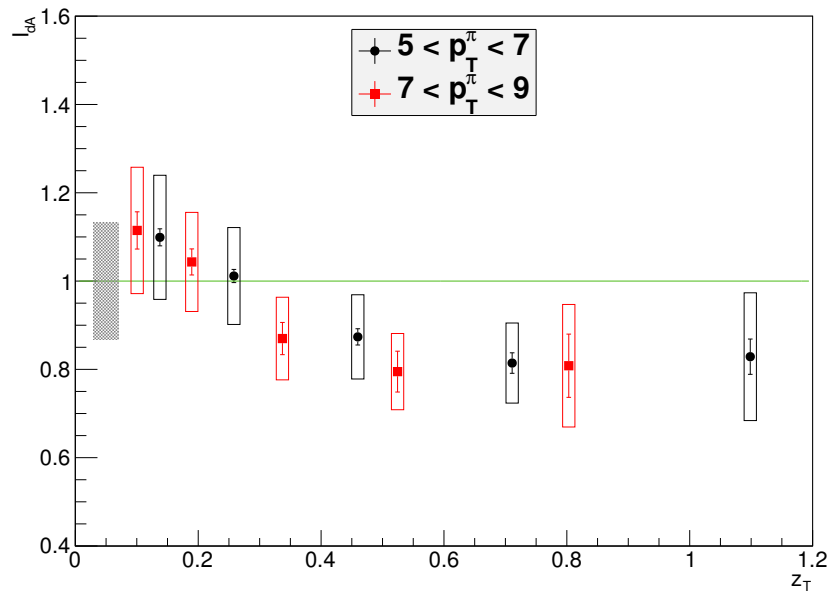


Figure 4.25: Awayside I_{dA} - z_T Plot in d +Au with 0 - 20% Centrality.

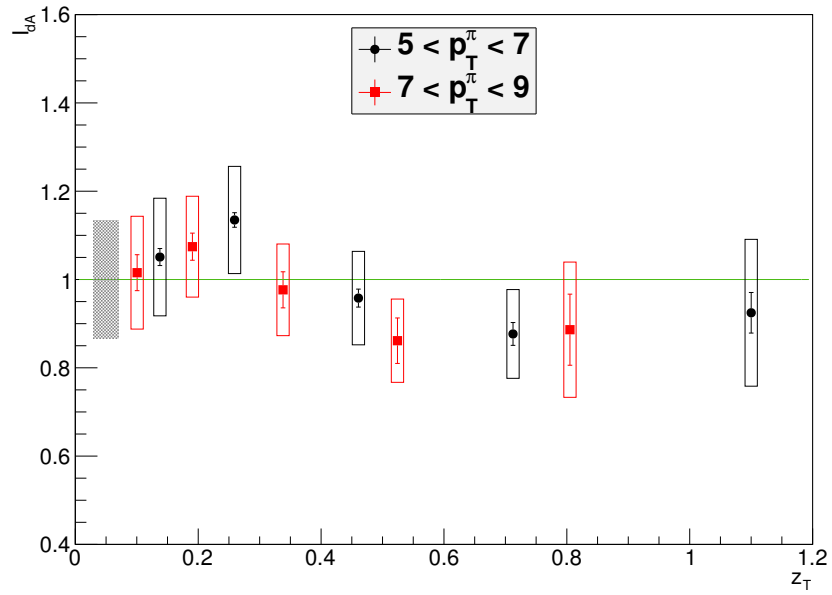


Figure 4.26: Away-side I_{dA} - z_T Plot in d +Au with 20 - 40% Centrality.

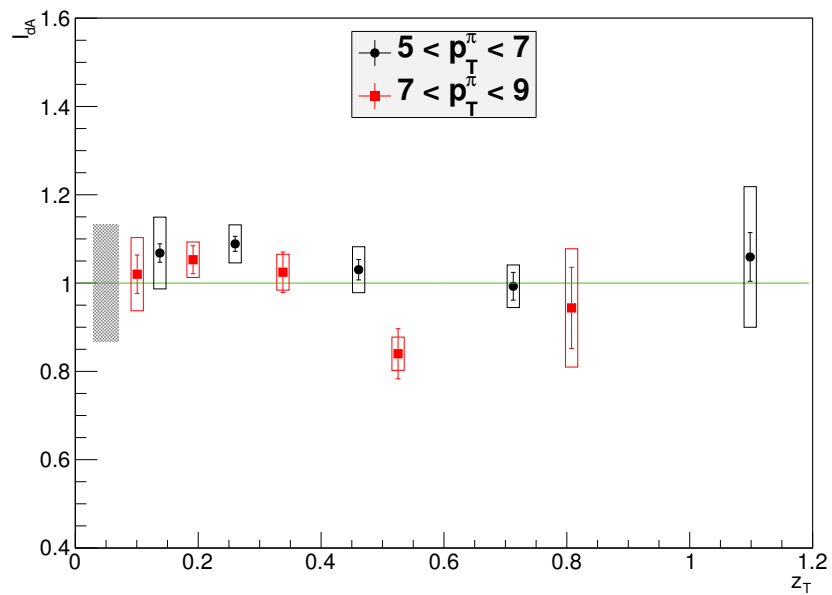


Figure 4.27: Away-side I_{dA} - z_T Plot in d +Au with 40 - 60% Centrality.

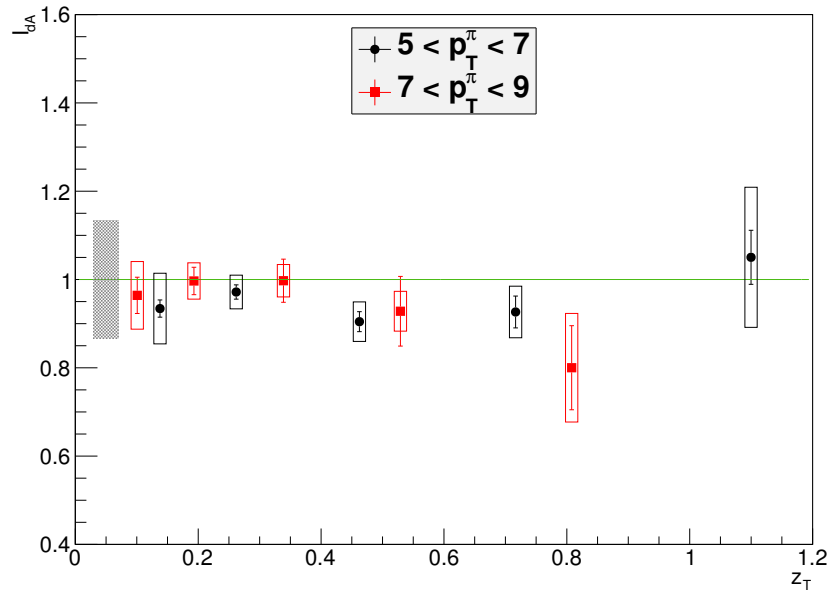


Figure 4.28: Away-side I_{dA} - z_T Plot in d +Au with 60 - 88% Centrality.

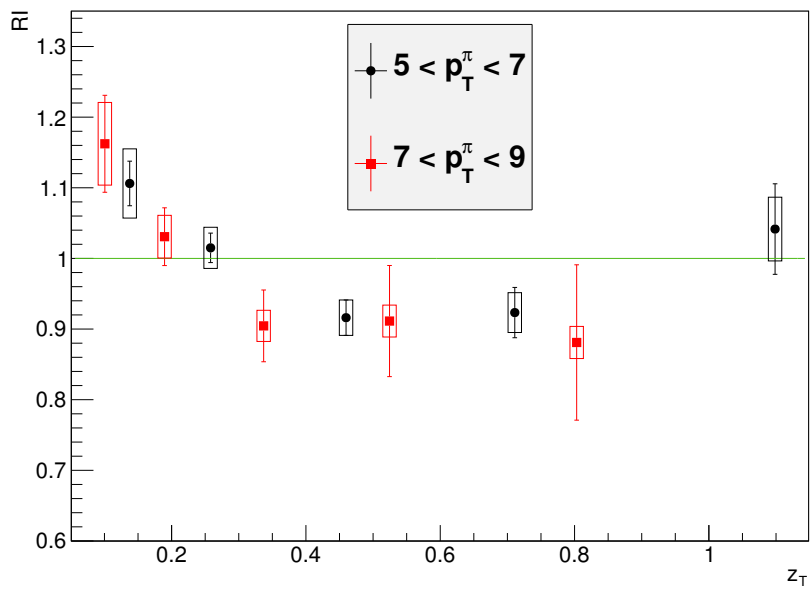


Figure 4.29: RI vs z_T Plot in d +Au with 0 - 20% Centrality.

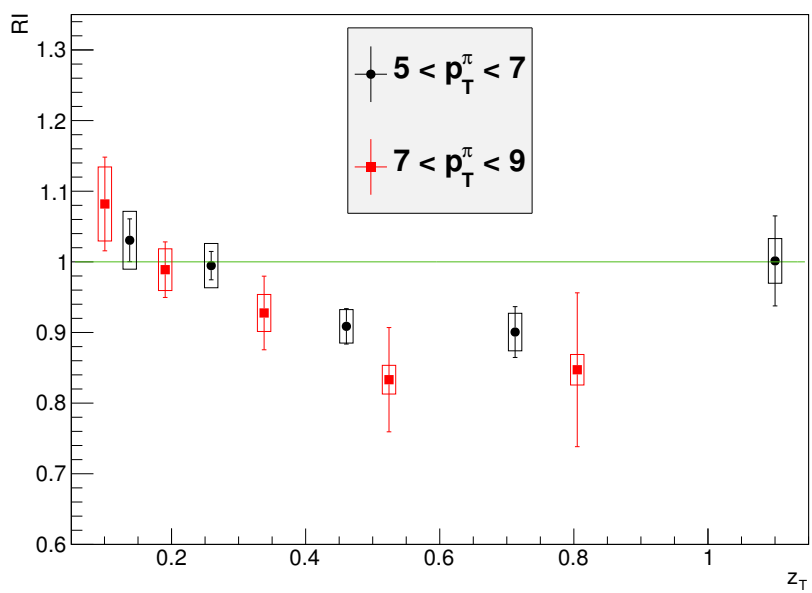


Figure 4.30: RI vs z_T Plot in $d+Au$ with 20 - 40% Centrality.

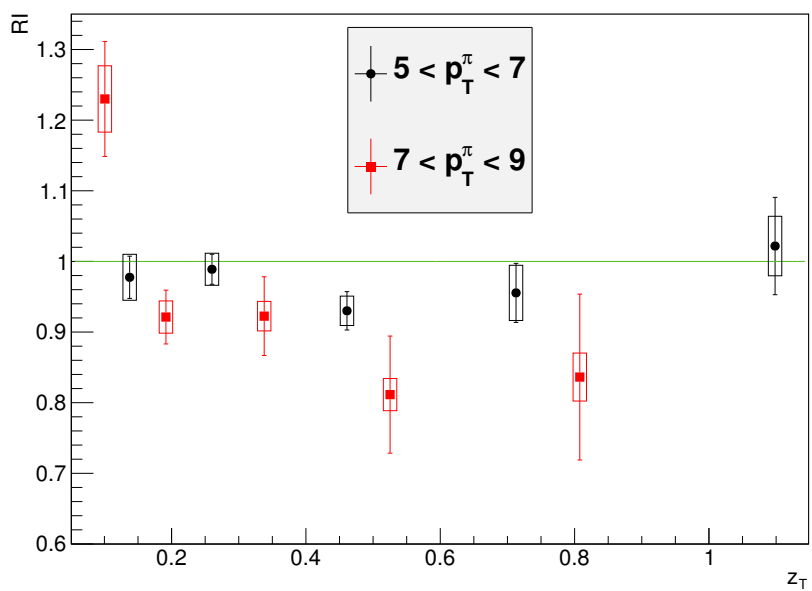


Figure 4.31: RI vs z_T Plot in $d+Au$ with 40 - 60% Centrality.

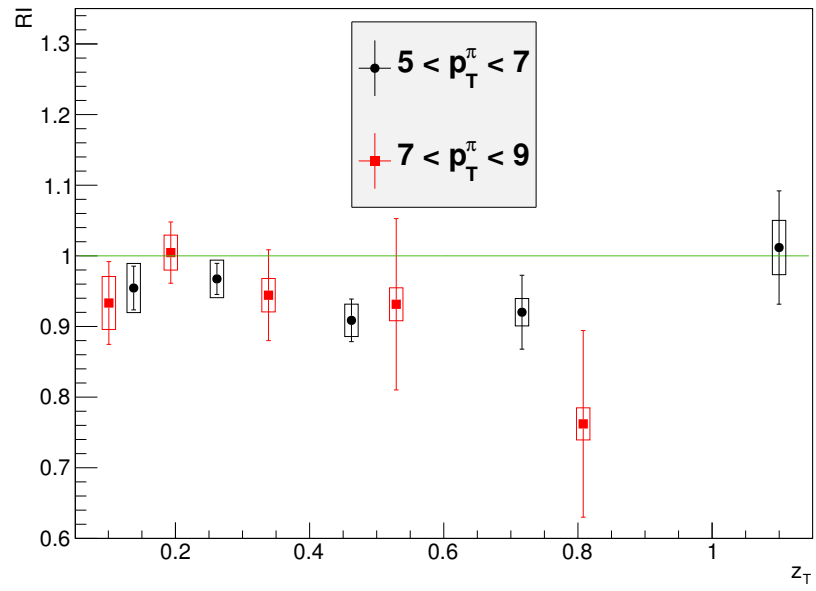


Figure 4.32: RI vs z_T Plot in $d+Au$ with 60 - 88% Centrality.

5 DISCUSSIONS

5.1 Introduction to Discussion

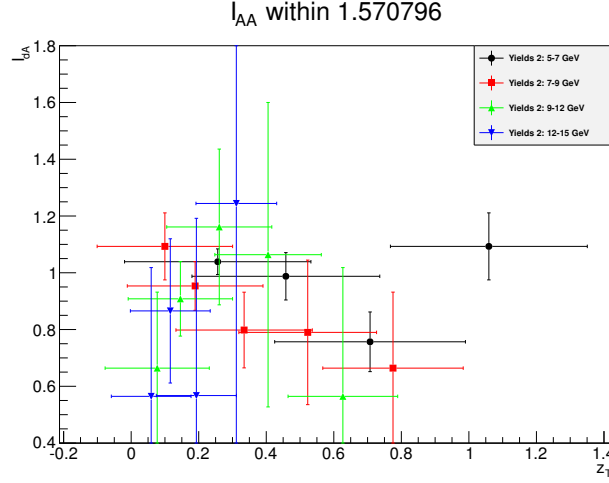


Figure 5.1: Away-side I_{dA} in peripheral d +Au collisions from isolated γ - h^\pm analysis. The black data point with z_T above one comes from 5-7 \otimes 5-7 GeV/ c bin, where the average $\langle z_T^{\text{partner}} \rangle > \langle z_T^{\text{trigger}} \rangle$, and the jet information is diluted by other contributions.

Originally the research conducted for this thesis included the use of isolated direct photons as triggers. In this measurement, single direct photons are identified through a requirement of being relatively isolated from other particles in angular cones of chosen sizes around the candidate. Direct photon measurements would give more accurate jet momenta and z_T assessment because the momentum of the away jet should be exactly balanced by the direct photon triggers in the leading order. However, direct photon measurements suffer from two factors. Firstly, the direct photon events are rare which causes large statistical uncertainties. The away-side I_{dA} plot, see Figure 5.1, demonstrated the size of the statistical uncertainties in the

isolated photon analysis. We may compare it with Figure 5.3 from the previous section. The π^0 - h^\pm measurement offers more statistical precision. Secondly, the inclusive photon samples, even with the isolation cut still have substantial background contributions from decay photons from π^0 and η 's, which causes low signal / background ratio. For a delicate modification observed in this d +Au analysis, direct photon study might not be the ideal one. The first set of results from the direct photon analysis indicate the advantage of hadron-hadron correlations for this delicate effect in d +Au collisions we are searching for.

5.2 New Questions for Small Heavy Ion Collision Systems

As explained in the Introduction, recently new questions have arisen about the physics present in smaller Heavy Ion collisions systems like d +Au and p +Pb with many observations of new effects not previously observed in such high energy nuclear collisions. These include azimuthal asymmetries consistent with the presence of a hydrodynamic flow similar to the quark gluon plasma (QGP) flow in Au+Au collisions, as well as an apparent abnormal enhancement in the peripheral high p_T jet production yield.

The full set of I_{dA} , RI , jet yields and widths presented in the previous section can be used to constrain the size of nuclear effects, and give more insight into many of these questions.

5.3 Comparison to Peripheral R_{dA} Results

As a first example of insights this thesis data can address concerning the new questions in small collision systems, we consider new peripheral jet R_{dA} measurements that show surprising enhancement. We have discussed in Section 1.3.2, in peripheral d +Au collisions R_{dA} and R_{cp} in p + p collisions should show some suppression at low p_T and enhancement at intermediate p_T , due to the Cronin

effects then come back to 1 at large p_T . And in central Au+Au collisions, because of the jet quenching and energy loss in the quark gluon plasma, R_{AA} is severely suppressed. For example, R_{AA} values of π^0 in central d +Au collisions are down to about 0.3 for $p_T > 2$ GeV. Interestingly, a few anomalies in the large p_T region are reported by PHENIX in peripheral d +Au collisions. One is π^0 and η 's R_{dA} measurements [142], the other one is a full jet reconstruction analysis [143]. Both surprisingly show some enhancement at large p_T in the midrapidity region in peripheral collisions, see Figure 5.2. This is another example of some of the new questions about d +Au which this thesis data can address.

The general feeling in the field is that in peripheral collisions there should not be much modification to jets from any nuclear effects, because the collisions are generally between single nucleons just as in a $p+p$ collision. Instead, R_{dA} relies on a scaling factor to multiply $p+p$ yields to equal the equivalent number of nucleon-nucleon collisions comprising an d +Au collision. The nuclear modification factor R_{dA} determination needs N_{coll} (or N_{binary} in some literatures), which might cause the anomalies observed in π^0 and jet measurements in peripheral d +Au collisions. However it still is yet to be confirmed that there is not more complicated types of modifications of high p_T jet properties.

One possible comparison is the peripheral away-side I_{dA} with high trigger p_T plots from our measurement in Figure 5.3. In contrary to the R_{dA} results, there is no enhancement in large p_T bins in I_{dA} plots of peripheral d +Au collisions. Since the I_{dA} measurement avoids the scale factor issue in R_{dA} , it gives a different picture in peripheral d +Au collisions. We have not observed any abnormal enhancement in peripheral d +Au collisions. Thus our data favors an issue with the understanding of the scale factor.

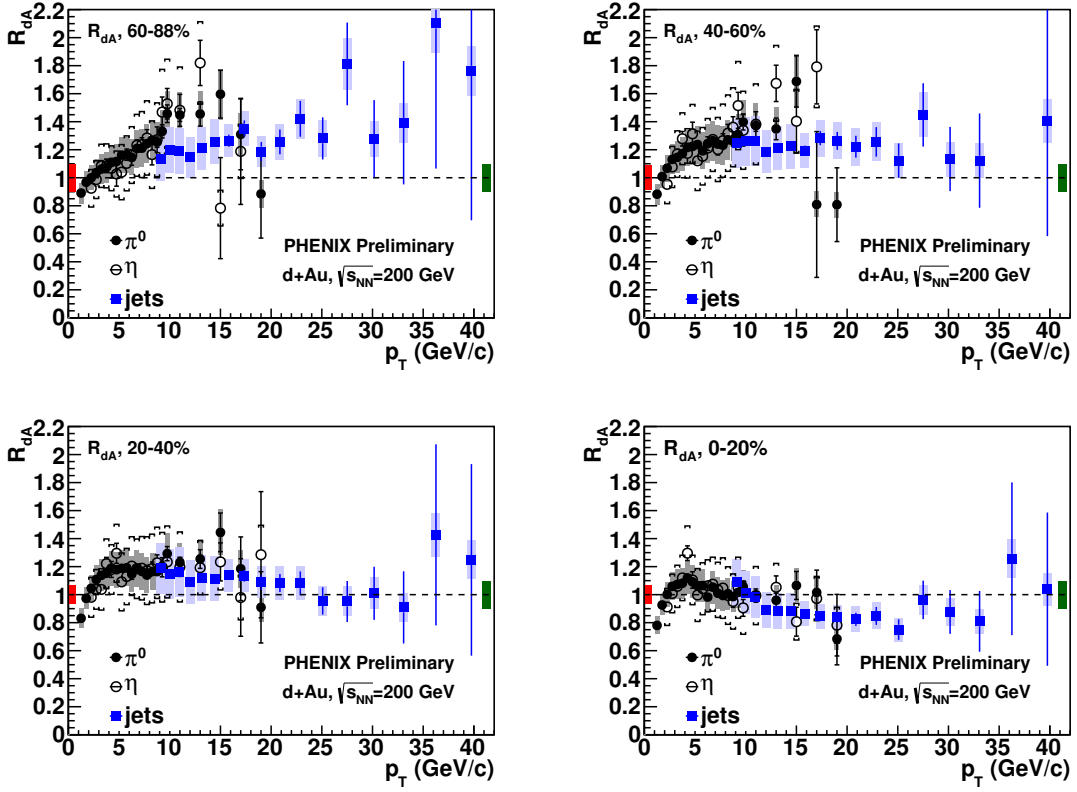


Figure 5.2: Nuclear modification factor R_{dA} from π^0 , η and full jet reconstruction measurements by PHENIX. The peripheral results show some enhancement at large p_T [142] [143].

5.4 Establishment of Centrality Dependent Nuclear Effect for RI

Our data show the presence of delicate suppressions at high z_T and enhancements at low z_T in central $d+Au$ collisions. Such jet modifications are not present in peripheral $d+A$ collisions. By eye the I_{AA} and RI ratio itself for different centralities seems to indicate a nuclear effect, that is to say, a non-flat shape, with values different than one. But to what level are these features statistically significant and how do they evolve with how deeply within the Au nucleus the deuteron strikes.

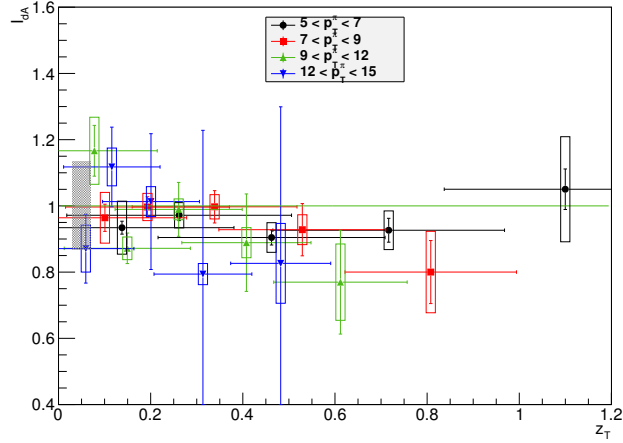


Figure 5.3: Away-side I_{dA} in peripheral $d+Au$ collisions. There is no evidence for an enhancement in high partner p_T regions in peripheral $d+Au$ collisions. The black data point with z_T above one comes from 5-7 \otimes 5-7 GeV/ c bin, where the average $\langle z_T^{\text{partner}} \rangle > \langle z_T^{\text{trigger}} \rangle$, and the jet information is diluted by other contributions.

First we may observe the RI ratios themselves and quantify the non-flatness of their shape. By cancelling out the major systematic uncertainties, RI plots show these modifications in a quantitative way. We may use a linear function to fit the lowest trigger p_T bin, and a non-zero slope value will therefore give some indication of the level to which the jet function is non-flat. We find that significance of a non-zero slope value for the most central bins is better than about 2σ , corresponding to 95% probabilities. Furthermore, we can view the full centrality dependence of these jet modifications in a clearer way. The plot of fitted slope values shows a centrality dependence, see Figure 5.4. The 0-20% and 20-40% centrality bins show a deviation from 0 about 2σ , and the other two 40-60%, 60-88% are still consistent with zero, showing no such modifications.

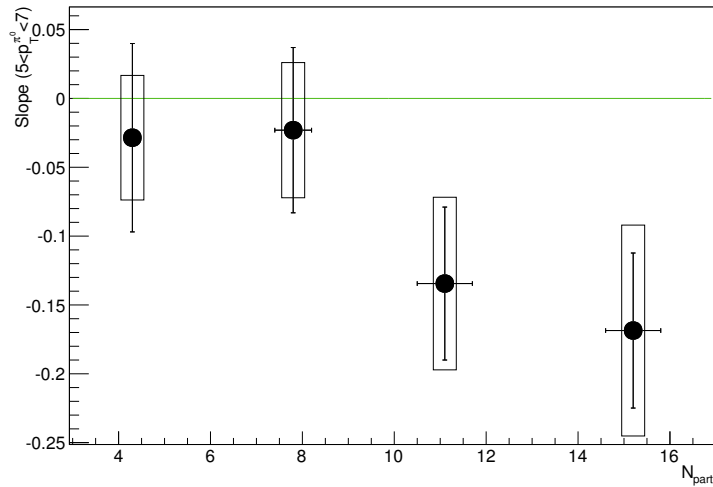


Figure 5.4: Centrality dependence of the slope fitted with the RI vs z_T plot in 5-7 GeV/c trigger pt bin. The statistical uncertainties are represented by vertical bars, and the systematic uncertainties are represented in boxes. The 0-20% and 20-40% data points are the ones on the right. The 40-60% and 60-88% data points are the ones on the left. The two central data points show $\sim 2\sigma$ deviations from zero. The two peripheral data points are still consistent with zero within uncertainties.

To differentiate the roles of the modifications in high and low z_T region, we use a constant to fit RI vs z_T plot in these two regions (low $z_T < 0.4$, high $z_T > 0.5$) after combining the statistical and systematic errors. The fitted value means $\langle RI \rangle_{z_T}$. The behaviour of the double ratio in different z_T regions are different, see Figure 5.5. The RI in low z_T increase as the collision goes to more central. However, the RI in high z_T doesn't show a clear trend of changes in different centralities. The ratio of the two values in low and high z_T regions is shown in Figure 5.6. The difference between the two regions are clear in the central two bins.

The two central data points deviate from unity by 2σ , while the two peripheral data points are consistent with unity within uncertainties.

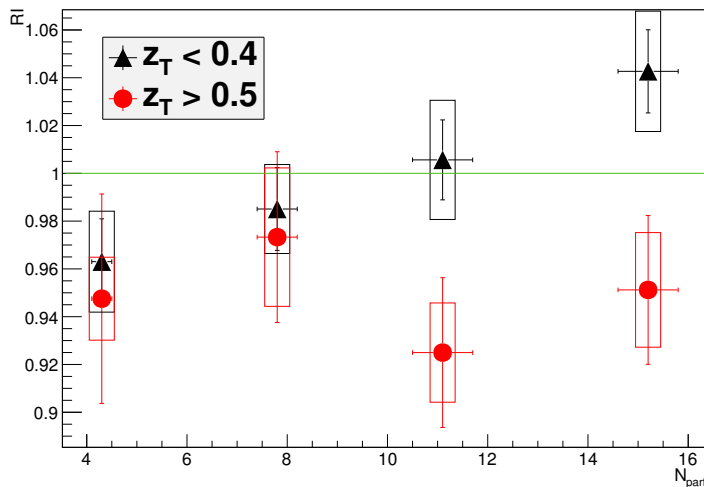


Figure 5.5: Centrality dependence of the double ratio values in low and high z_T region. The statistical uncertainties are represented by vertical bars, and the systematic uncertainties are represented in boxes. The low z_T RI increases in a seemingly systematic way when the centrality increases. The high z_T RI doesn't show a clear trend in changes.

In summary, this two-particle jet measurement shows a picture of suppression at high z_T and a slight enhancement at low z_T in central $d+\text{Au}$ collisions. This feature observed in data is qualitatively similar, but much smaller, to the one in $\text{Au}+\text{Au}$ collisions.

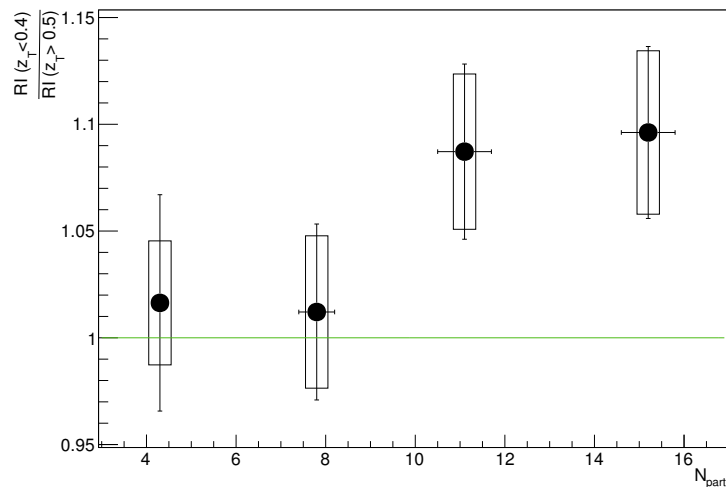


Figure 5.6: Ratio of the double ratio values in low and high z_T region. The statistical uncertainties are represented by vertical bars, and the systematic uncertainties are represented in boxes. The ratio is consistent with unity in peripheral collisions. It deviate from unity about 2σ in central collisions.

5.5 Interpretation of RI

Now that we've established a centrality dependent modification of the correlations in $d+\text{Au}$ collisions, we can naturally ask the question to what physics is it due to?

If QGP or something similar exists in $d+\text{Au}$ collisions, it could have other signals indicating its presence such as jet energy loss. In $\text{Au}+\text{Au}$ collisions, the suppression in high z_T is attributed to the jet energy loss in a quark gluon plasma, and the enhancement in low z_T is explained by the recovery of energy lost in the medium. Figure 5.7 from [102] shows that the away side jet disappears in the central $\text{Au}+\text{Au}$ collisions. This phenomena is used to demonstrate the presence of a quark gluon plasma, which causes the loss of energy of the away side jet. Figure 5.8

from [144] shows that the excess in low z_T in central Au+Au collisions is a large effect ($I_{AA} \sim 2$ in large cone sizes). Also, the deficit in high z_T in central Au+Au collisions is large too ($I_{AA} \sim 0.2$ in large cone sizes). This plot also shows the modification gets larger when the integration range increases, which is consistent with the idea that the redistributed energy is spread into a wider area. Full jet reconstruction measurements show the similar feature in heavy ion collisions. Figure 5.9 shows that the ratios of charged hadron fragmentation functions between central and peripheral events in Pb+Pb collisions have similar enhancements in low z . The lack of a large suppressions in high z is because the jet reconstruction method require the existence of a jet which introduces a bias to remove the large suppression in central collisions [145].

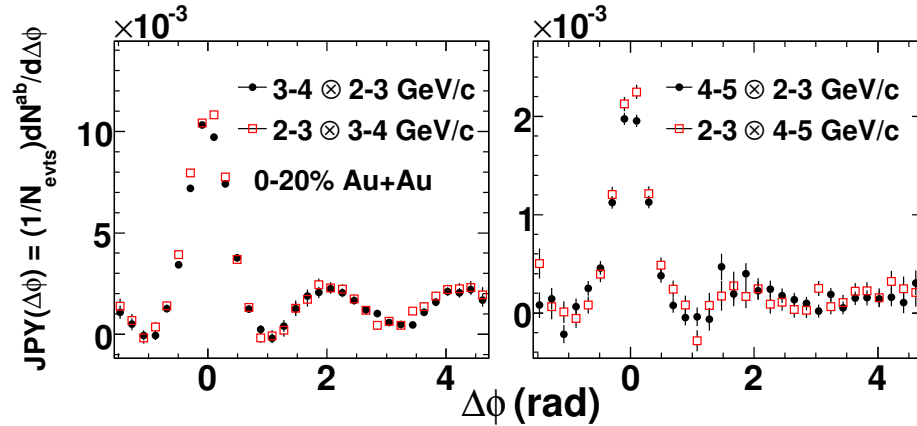


Figure 5.7: Correlation functions in central Au+Au collisions [102]. The away side jet peak is disappeared in central Au+Au collisions. This is believed to be caused by the jet energy loss into the medium when the away side jet travel trough the quark gluon plasma.

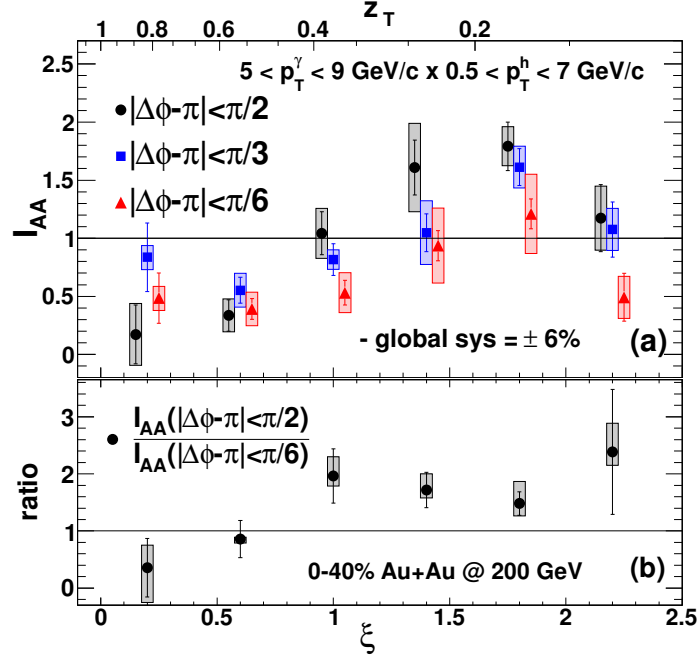


Figure 5.8: Away side I_{AA} plot in central Au+Au collisions, which shows the prominent energy loss and recovery in a quark gluon plasma [144]. Here $\xi = \ln(1/z_T)$.

One possible explanation for the phenomena observed in the RI ratio in this analysis is an energy loss mechanism from nuclear medium. It might come from a possible quark gluon plasma, especially when the collective flow is discovered in p +Pb and d +Au collisions in LHC and RHIC respectively (see the discussion in Section 1.4). A direct comparison with Au+Au result is obtained by using the v_n subtracted $4 < p_T^\pi < 10 \text{ GeV}/c$ data from [146]. We compared our $5 < p_T^\pi < 7 \text{ GeV}/c$ d +Au results with the Au+Au ones in Figure 5.10 to show the relative size of effects in both systems.

It is clear that a qualitatively similar effect as seen in RI in d +Au is also seen in Au+Au data. In Au+Au collisions we know this is due to energy loss. One goal of the current research is to determine to what extent the similar looking d +Au

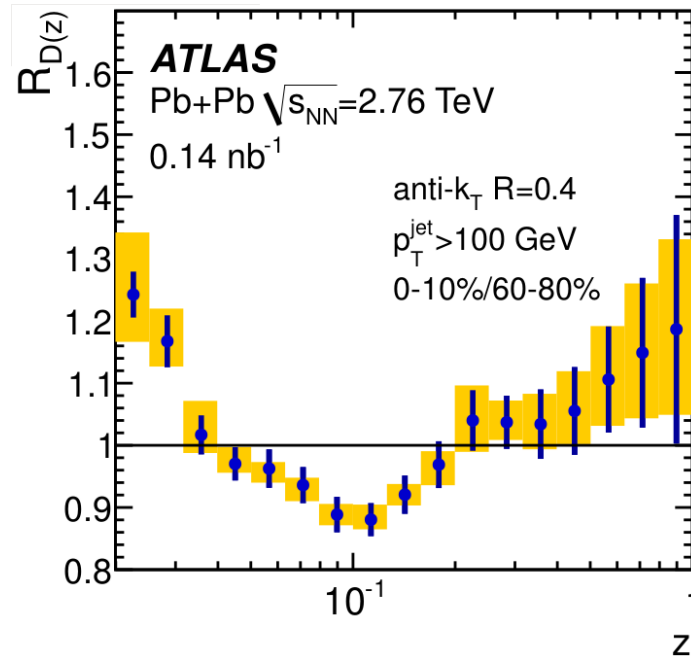


Figure 5.9: Ratio of charged hadron fragmentation function $D(z)$ between central and peripheral Pb+Pb collisions from ATLAS reconstructed jet measurements [145].

result might also be attributed to an energy loss. This means looking into what other known physics besides this could cause similar modifications to RI .

However, the feature observed in our $d+Au$ RI data might merely or mainly come from the cold nuclear matter effects partially because a quark gluon plasma is not traditionally believed to exist in $d+Au$ collisions. In order to constrain the possible cold nuclear matter origins, we use Monte Carlo simulations to compare with the data. We first investigate the k_T effect, because a large k_T value in hard scattering (or say, triggered events) could cause jet imbalance in mid-rapidity and RI 's departure from unity. Then we check the effects of nuclear modifications of the parton distribution functions by EPS09 nPDF sets, because the shadowing / anti-shadowing effect there might cause an enhancement or suppression in certain z_T regions. To incorporate the collision geometry effect, we apply EPS09s nPDF

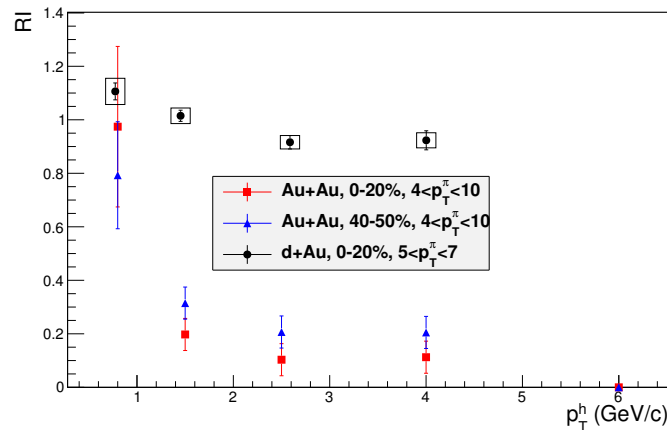


Figure 5.10: R_I results compared between d +Au and v_2 v_3 corrected Au+Au data. The d +Au 5-7 \otimes 5-7 GeV/ c data point is removed due to possible kinematic bias (see discussions in Section 4.3). The size of R_I modifications in d +Au collisions are much smaller than Au+Au ones.

sets too. HIJING has the capability to simulate the jet quenching (or say, jet energy loss) and soft interactions (by mini-jets) in A+A collisions, also contains the shadowing / anti-shadowing effects from nPDF, so we adopt HIJING to simulate d +Au collisions too, and measure the size of enhancement / suppression effects. Even if we find a cold nuclear matter effect that is qualitatively similar, the data, due to its precision should still have relevance to the possible existence of energy loss effects in d +Au since by constraining the cold nuclear effects, we can then provide limits on the possible size of any additional energy loss effects.

5.6 PYTHIA Studies of the k_T Effect

PYTHIA (not an acronym) is a high energy particle collision event generator [147] [148] which is especially accurate for elementary hadron-hadron collisions. It simulates leading order 2 to 2 perturbative QCD parton scattering processes

including parton probability distributions for various colliding hadrons and hadronization of any partons that form jets in the processes. All known QCD and QED scattering processes can be included and PYTHIA provides the correct sampling of the processes based on the perturbative cross sections. It also includes many known physics effects that occur in the hadron-hadron collisions such as models for soft particle production, remnants of the hadrons which do not participate in the hard scattering, etc. It has been used to study several possible “cold” nuclear matter effects that we think could potentially cause the observed modifications seen in the data.

The first effect investigated was nuclear k_T effect. The k_T effect was mentioned in the introduction. In this context k_T is net transverse momentum of the two jets produced in a single 2 to 2 jet process. Normally this should be 0 assuming each initially scattered parton carries only longitudinal momentum in the beam direction. This is the average effect which causes near and awayside peaks 180 degrees from each other in the measured jet production. However event by event, an effective non-zero k_T can be observed which fluctuates around 0. It is expected that in large nuclei, due to net transverse momentum of the nucleons themselves and other effects, a larger should be observed. STAR has measured this extra nuclear k_T effect in 2011, which is integrated over all centralities of 10-20 GeV/ c di-jet measurement in d+Au collisions, see Figure 5.11. The measurement shows about 1σ larger k_T in d+Au compared to p+p. In the 2-p angular correlations measured in this thesis, this larger di-jet k_T will result in larger awayside angular distribution widths since the jet fragmentation hadrons we measure are approximately on average in the same direction as the underlying jets measured shown in Figure 5.11.

The PYTHIA study on the potential nuclear k_T effect is as follows. PYTHIA 6 is used with a set up of 200 GeV, using the default set of input parameters which

control many features of the many physics processes involved in the full event generation described above. The default parameter set is known to reproduce hadron-hadron collisions over a wide range of collision energies and should be sufficient for this study. The degree to which the event generators used in this and the other studies match the relevant features of the data is discussed below in the HIJING section. We investigate the k_T effect on the awayside/nearside ratio. Because the largest effect is in the lowest trigger pt bin, we focus on 5-7 GeV/c triggers for the study. The double ratio RI is calculated in different k_T settings in PYTHIA, see Figure 5.12. The rapidity acceptance is $-1 \leq \eta \leq 1$ to increase the statistics, which is larger than PHENIX acceptance. We also check with PHENIX central arm acceptance, the result remains the same within statistical uncertainties. The triggers are chosen as π^0 and π^\pm to increase the statistics, as expected, the π^0 trigger result is consistent this with a relatively low statistical precision.

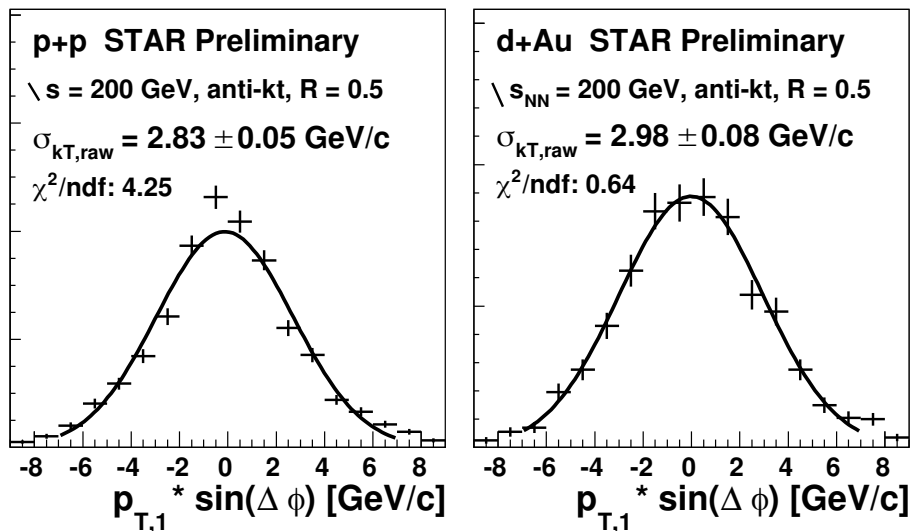


Figure 5.11: k_T Effect in p+p,d+Au collisions measured by STAR [91].

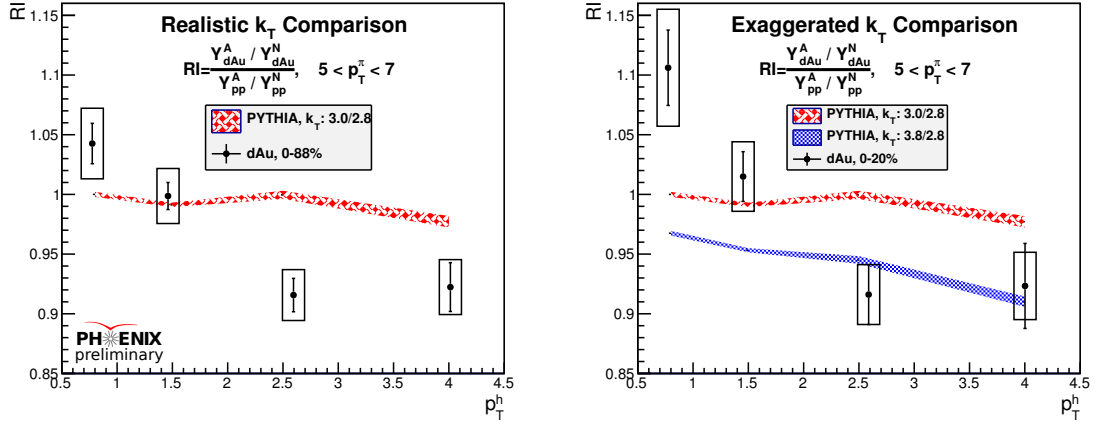


Figure 5.12: The modification of RI due to different k_T settings in PYTHIA study. We show the double ratio RI from two possible scenarios. One realistic setting is $k_T = 3$ GeV/ c versus $k_T = 2.8$ GeV/ c , and the other exaggerated setting is $k_T = 3$ GeV/ c versus $k_T = 2$ GeV/ c . The size of effect is averaged in all centralities.

The realistic extra nuclear k_T values, based on the values of k_T measured by STAR result in nearly negligible effect which is not consistent with our data—note that for this plot we combine results from all centralities into a single bin, which is still dominated by the more central events in order to match the centrality of the STAR measurement. In more central collisions due to the larger nuclear density sampled, one may expect the nuclear k_T to increase. The central collisions k_T value has not been measured, but it is expected to be only slightly larger due to the fact that 2- p correlations awayside widths in many previous measurements, and such as those given in this thesis data in Figure 4.13-4.14 generally do not appear to increase greatly with centrality. In order to demonstrate what a relatively large increase of the nuclear k_T value in central collisions could do, we choose to test an increase of one 1 GeV/ c in PYTHIA from the measured $p+p$ value of 2.8 GeV/ c . We

find that such a large increase can cause some suppression of away-side / near-side ratio, but the p_T^h dependence is generally too small for an explanation of slope we see in data. From this study, we believe that k_T effect is not the major source of the enhancements in low z_T and the suppressions in high z_T observed in our data.

5.7 PYTHIA Study of Quark Gluon Jet Mixing

The feature observed in central d +Au data is somewhat similar to our knowledge of gluon jets. Gluon jets are known to be softer and broader than quark jets. If some physics caused there to be more gluon jets emitted from central d +Au collisions than from normal p + p or neutron-proton collisions—we actually also doubled checked in PYTHIA that p + p vs. n + p showed no differences, since central d +Au involves a substantial number of n + p collisions as well—then this could potentially mimic the effect we see in RI . To investigate into increased gluon jet effects in RI , we use PYTHIA to generate all QCD di-jet hard scattering events, which includes

- Subprocess 11: $q_i + q_j \rightarrow q_i + q_j$
- Subprocess 12: $q_i + \bar{q}_i \rightarrow q_k + \bar{q}_k$
- Subprocess 13: $q_i + \bar{q}_i \rightarrow g + g$
- Subprocess 28: $q_i + g \rightarrow q_i + g$
- Subprocess 53: $g + g \rightarrow q_k + \bar{q}_k$
- Subprocess 68: $g + g \rightarrow g + g$

In this study, we categorize the interactions based on the scattered (outgoing) partons,

- Class A: $g + g$

- Class B: $q + g$
- Class C: $q + q$

Class A includes the subprocess 68 and 13, where subprocess 68 dominates due to the fact that the valence quarks dominate the sea quarks. Class B includes the subprocess 28, which is called the Compton Scattering. Class C includes the subprocess 11, 12, and 53. The probability distributions for these subprocesses in high p_T π^0 triggered events are shown in Figure 5.13. The Compton scattering and the qq scattering dominate the π^0 triggered events.

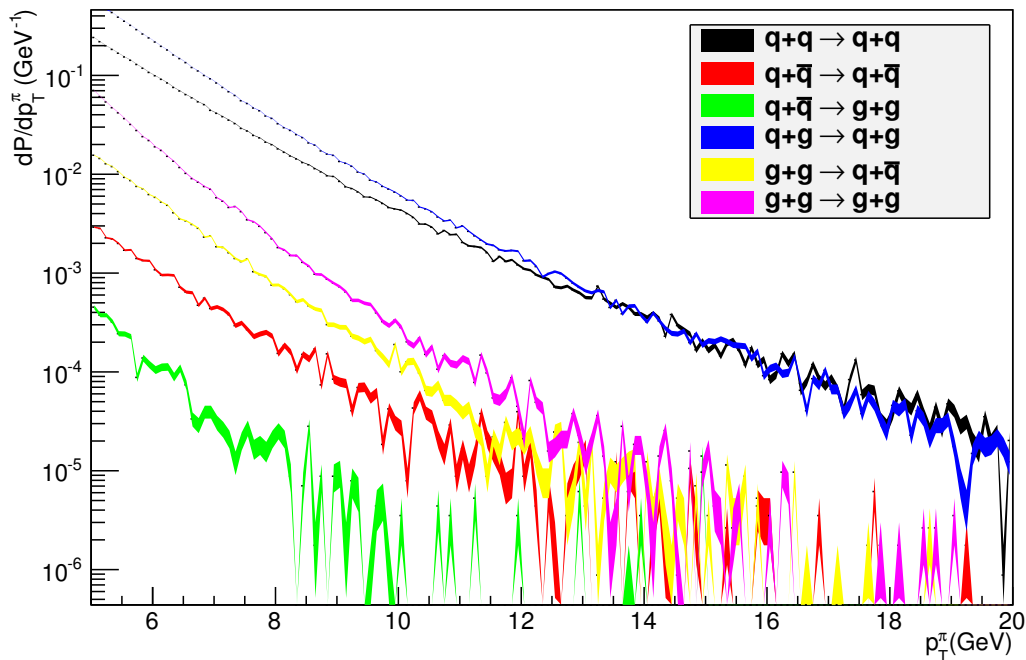


Figure 5.13: Probability distributions for hard scattering subprocesses in π^0 triggered events.

First, to demonstrate the basic concept of softer gluon jet fragmentation compared to quark jets, we compare cases with only gluon jets in the final awayside jets to cases where only quark jets comprise the awayside. The result is shown in Figure 5.14 which is explained in more detail below.

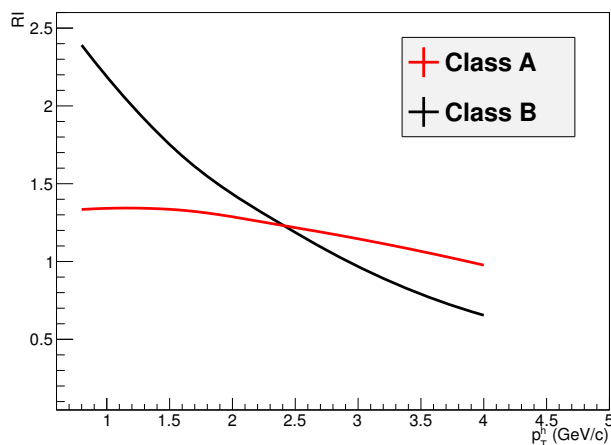


Figure 5.14: RI modifications in Class A and Class B events due to the gluon jets. This is like the ratio of gluon to quark jet fragmentation functions in two different cases of production processes and shows that gluon jets generally have softer fragmentation than quark jets.

Class A and B includes gluon jets in their final state productions on the awayside. For Class A there are only gluon jets in the final state, so we divide this by Class C which only has quark jets in the final state to do a more straightforward gluon to quark comparison. Note that these effects may also include effects of the different production processes. If we define

$$RI_{\text{Class A}} \triangleq \frac{Y_{g-g}^A / Y_{g-g}^N}{Y_{q-q}^A / Y_{q-q}^N} \quad (5.1)$$

where $g-g$ means the events with gluon jets on both near and away-sides, $q-q$ means the events with quark jets on both sides. Thus this is a demonstration of gluon jets having softer fragmentation on average than quark jets.

For Class B in the same figure, which involves the Compton scattering where both a quark and gluon are present in the final state, we compare the cases where the gluon and quark appear in opposite configurations with respect to the near and away-side. We compare the RI ratio (away-side/near-side yields ratio) between the events with a quark in near-side and a gluon in away-side to the events with a gluon in the near-side and a quark in the away-side, and define RI as

$$RI_{\text{Class B}} \triangleq \frac{Y_{q-g}^A / Y_{q-g}^N}{Y_{g-q}^A / Y_{g-q}^N} \quad (5.2)$$

Here, $q-g$ means the events with near-side quark jets and away-side gluon jets, vice versa for $g-q$. Figure 5.14 is just meant to demonstrate the direction of the effects we should expect if more gluon jets were present than quark jets for any unspecified reason in the nuclear collisions. The modification of RI in this plot is much larger than we should expect any such modifications to cause in our data measurement of RI however, because our $p+p$ reference there will always contain the normal mixture of quark and gluon jets, not exclusively just quark jets.

Instead the realistic possible modification of A/N ratio in $d+Au$ collisions (or say RI 's deviation from 1) only comes from the potential q and g jets conversions in the numerator $d+Au$ ratio. By using PYTHIA to simulate changes to the numerator only, we may evaluate the size of RI 's modification in extreme cases. In the most realistic but still extreme scenario, suppose we assume there is some final state process that converts all quark jets after they are produced into gluon jets, but does not affect the original gluon jets. That is if we assume that all q jets are converted to g jets, i.e. $q-q$ converts to $q-g$ and $g-q$ converts to $g-g$, the modification

of RI is shown in Figure 5.15. This effect is seen to be unlike our measured RI with an enhancement at low z of slightly less than observed but no suppression. Keep in mind that this would still represent an extreme conversion of all quark jets, thus more realistic conversion types would likely be far less in the magnitude of the modifications. Based on this we conclude that the origin of the modification in A/N ratio in central $d+Au$ collisions is not likely to come from changes to the quark to gluon mix.

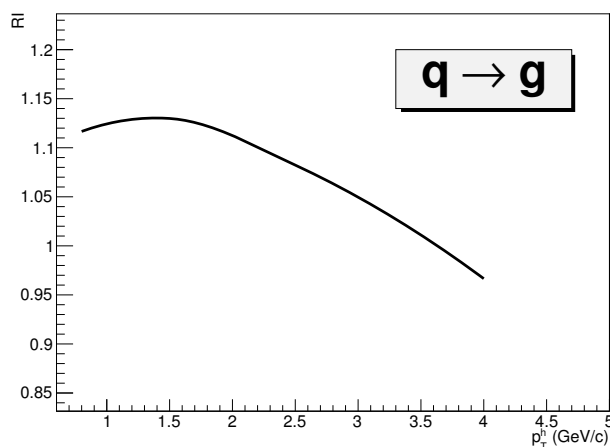


Figure 5.15: RI modifications if we assume all q jets are converted to g jets.

We end by noting, however, that other more exotic types of changes to the quark to gluon jet mixture could at least result in larger modifications which are qualitatively similar to our measured RI . For example if we assume many “double conversions”, where a substantial number of q and g jets converted to each other simultaneously (qg pairs go to qg , $q \leftrightarrow g$), the RI modifications are shown in Figure 5.16. Note though, that even in this case, the enhancement in the simulation results

extends to a much larger z_T values and thus has a different shape than our measured RI .

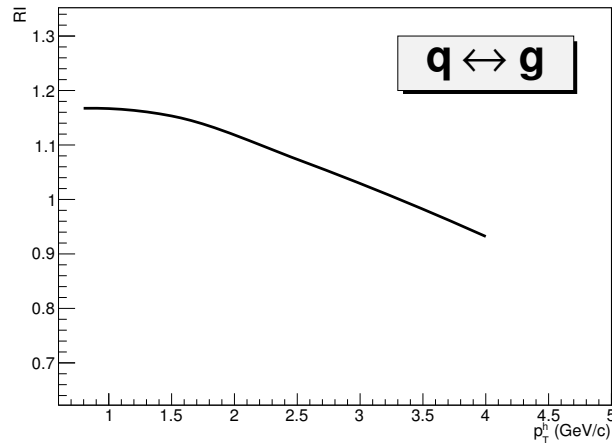


Figure 5.16: RI modifications if we assume substantial “double conversion” which is the same as the other plot, but where simultaneously g jets are also converted into q jets at large rates.

5.8 Nuclear Modification of Parton Distribution Functions

Nuclear modifications of parton distribution functions are major sources of initial state cold nuclear matter effects. The shadowing and anti-shadowing effects could cause enhancements and suppressions at certain z_T regions in final state products. EPS09 is the most widely accepted nuclear PDF set, therefore, we use PYTHIA + EPS09 to investigate the effects from the nuclear modifications of PDF’s. In this study, we pick a realistic k_T setting of 2.0 GeV/ c as well as a minimum 0.2 GeV settings (both show the same results). We turn on hard and semi-hard scattering processes. The value of x and Q^2 passed to leading order

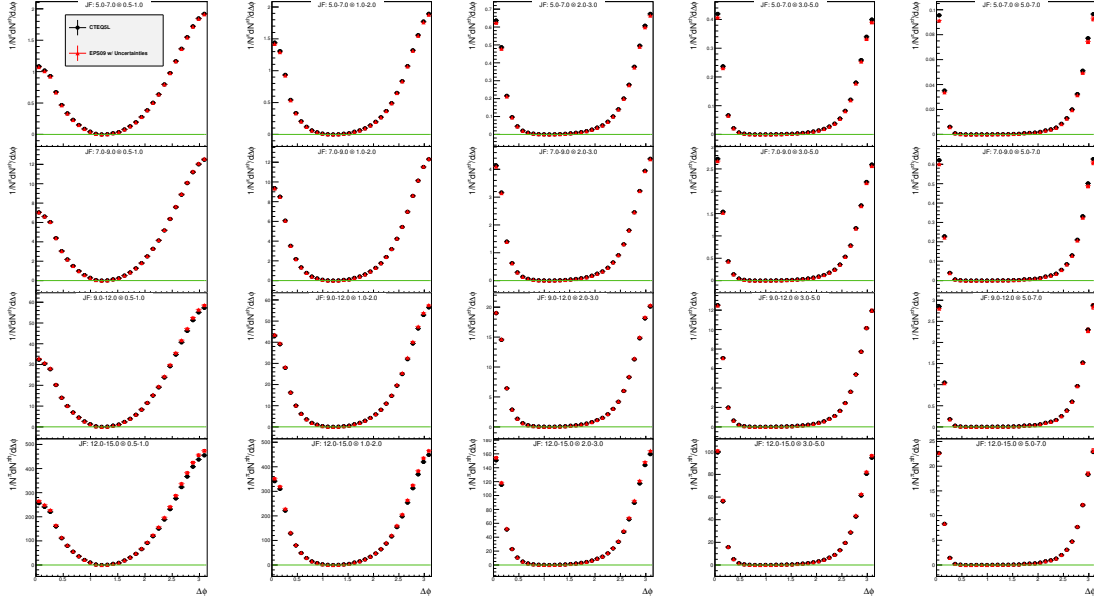


Figure 5.17: The modification of jet functions caused by nuclear modifications in parton distribution functions. CTEQ5L is a PDF set without any nuclear modification, which is the default one in PYTHIA6. EPS09 is a widely used nuclear nPDF set. The uncertainties from EPS09 is represented by the boxes around the data points, which is pretty small.

EPS09 PDF sets are from PYTHIA's PARI(34) and PARI(15) perspective. To prevent possible ordering of x_1 and x_2 in PYTHIA, we switch them by choosing PARI(33) as x , and the result remains the same. PYTHIA has multiple definition of Q^2 , as explained in MSTP(32). We choose $-\hat{t}$ as the definition of Q^2 in PYTHIA to make it consistent with EPS09. The uncertainties of EPS09 are evaluated and we take a quadratic sum of all 30 uncertainties since they are calculated from a Hessian matrix.

The jet functions shows that the modifications have larger effects in higher partner p_T bins, as shown in Figure 5.17. And the size of modification is close to the uncertainties.

In accordance, RI 's plot shows that the size of modification is very small ($\lesssim 1\%$), see Figure 5.18. The RI modification from EPS09 nuclear PDF is inconsistent

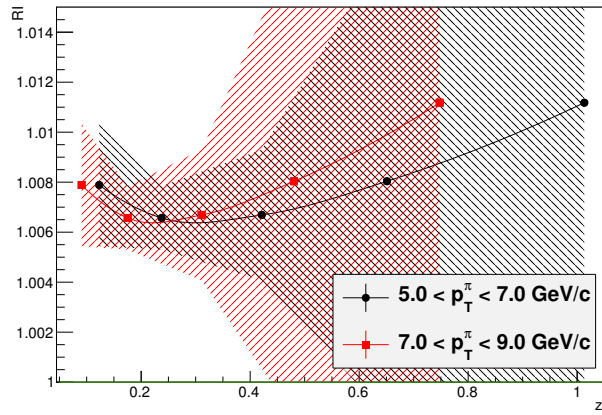


Figure 5.18: The modification of RI caused by nuclear modifications in parton distribution functions. The shaded area is the uncertainties from EPS09 nuclear nPDF set. The black area is for triggers with $5 < p_T < 7$ GeV/ c . The red area is for triggers with $7 < p_T < 9$ GeV/ c .

with our data, since there is no suppression in the EPS09 simulation at all. To investigate the reason for such a small nuclear effect, we plot x vs Q^2 in triggered events (x_1 and x_2 are essentially symmetric as we expected), see Figure 5.19. We can see the most probable events are those with $x \approx 0.02$ and $Q^2 \approx 30 \sim 50$ (GeV/ c)² or $Q \approx 6 \sim 7$ GeV/ c . If we plot the EPS09 nPDF sets with such momentum transfer values, for example, $6 \leq Q \leq 7$ GeV/ c (See Figure 5.20), we would find that $x \approx 0.02$

area is about in between of the shadowing and anti-shadowing regions, where R_i^{Au} values of u d valence quark and gluon are pretty close to unity. This explains the small size of the effect from nuclear modifications in PDF. The reason to use valence u and d quarks is based on CTEQ6M PDF sets shown in Figure 5.21 from [69], where the valence quarks' $f(x)$ is always higher than the sea quarks' in all relevant kinematic ranges. One possible concern is that the nuclear modification around $x \sim 0.02$, $Q \sim 6$ GeV/ c is large, and $f(x)$ from NNLO MSTW2008 shows larger sea quarks' $xf(x)$, which is different than CTEQ6, see Figure 5.22 from [31] (Possibly, this is normalized in x space). Anyway, we use sea u d quark in EPS09 nPDF sets, the results are still small, see Figure 5.23.

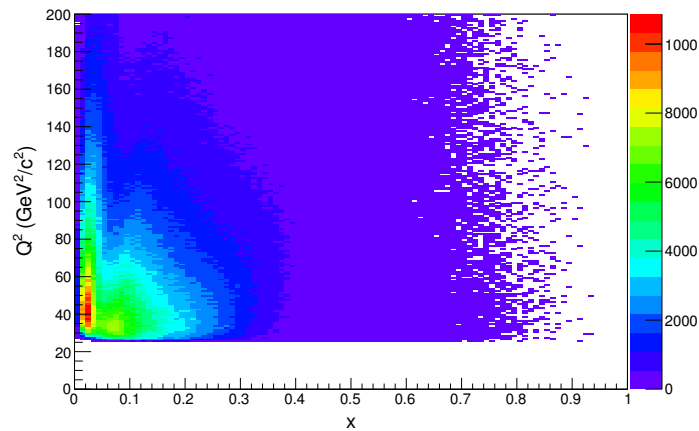


Figure 5.19: x vs Q^2 of triggered events in PYTHIA study. The most probable events are those with $x \approx 0.02$ and $Q^2 \approx 30 \sim 50$ (GeV/ c)² or $Q \approx 6 \sim 7$ GeV/ c . The cut-off of Q^2 is due to CKIN(3) setting for minimum p_T values in PYTHIA.

There are nPDF sets with spacial information available, such as EPS09s. In principle, we can use Glauber model to calculate the thickness function and sample

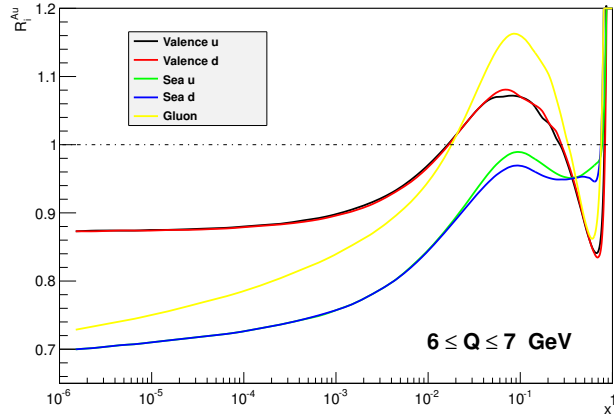


Figure 5.20: R_i^{Au} of EPS09 nPDF sets for various partons when $6 \leq Q \leq 7$ GeV/c. We can see that when $x \approx 0.02$, the nuclear modifications for the valence u , d and gluon are close to 1, which cause a small effect in modifications of jets and RI values.

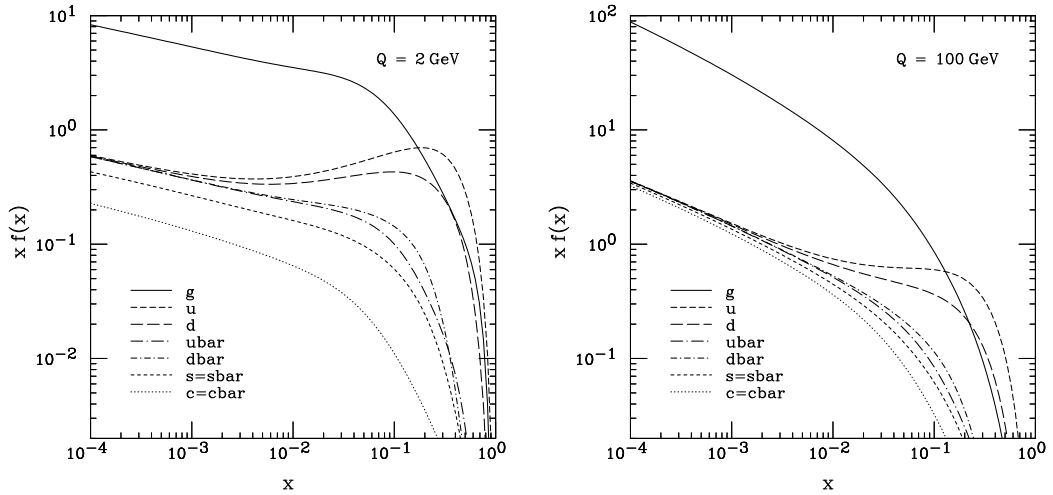


Figure 5.21: Overview of CTEQ6M PDF sets at $Q = 2$ and 100 GeV/c² [69].

the distribution of the impact parameter b , then use PYTHIA + EPS09s to investigate the nPDF modifications and their centrality dependence. HIJING uses similar optical Glauber model in its calculations, so the impact parameter

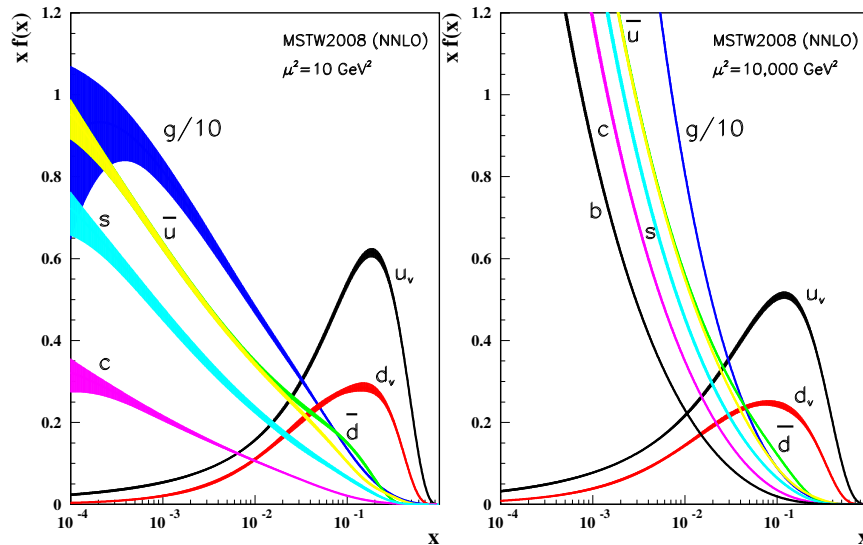


Figure 5.22: Overview of NNLO MSTW2008 PDF sets at $Q = 10$ and $10,000 \text{ GeV}/c^2$ [31].

distributions are obtained from our HIJING simulations. Potentially EPS09s nPDF sets could have more features from spacial dependence, see Figure 5.24. It is reasonable to check EPS09s to see if there is a large effect. The result is shown in Figure 5.25, where the effect is still small. The distribution of the impact parameter b is roughly linear due to the geometry settings, so the most b values are close to 5 fm, where R_u^{Au} is still close to unity. So the nuclear PDF modifications have a very small effect in RI and are not able to explain the observed enhancement/suppression in central $d+Au$ events.

5.9 HIJING Simulations

HIJING (not an acronym) is a simulation program incorporating collision geometries, nuclear shadowing effect, multiple collision scenarios, multiple mini-jets and jet quenching [149] [150] [151] [152]. With jet quenching turned off, HIJING

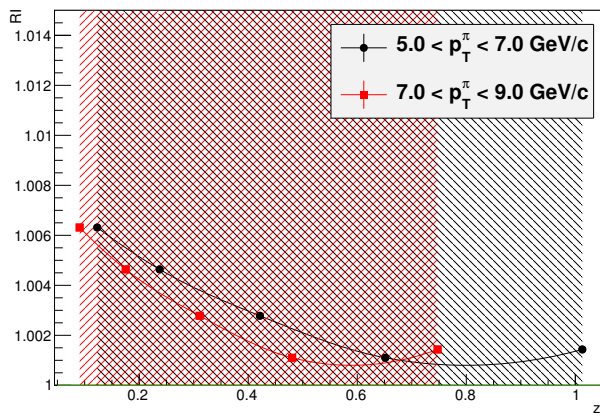


Figure 5.23: The modification of RI caused by nuclear modifications in parton distribution functions with sea u d quarks. The shaded area is the uncertainties from EPS09 nuclear nPDF sets. The black area is for triggers with $5 < p_T < 7$ GeV/ c . The red area is for triggers with $7 < p_T < 9$ GeV/ c . The uncertainties for sea quarks are much larger than the ones for valence quarks.

would be an ideal tool to study the possible cold nuclear effect origin of the observed jet modifications in central d +Au data. HIJING uses PYTHIA 6 code to generate many aspects of its nuclear events for each nucleon-nucleon collision. To simulate the collision geometries, we use the collision parameter $0 < b < 5$ fm for central d +Au collisions and $5 < b < 11$ fm for peripheral d +Au collisions.

First of all, HIJING reproduces asymmetric particle production in rapidity for d +Au collisions, see Figure 5.26, which is similar to PHOBOS measurement in Figure 5.27. This uneven η distribution might cause a problem in our η acceptance correction. In our previous analysis in Section 3.11, we assume that the η distribution is flat, then get the triangle distribution in $\Delta\eta$. We've observed such uneven η distribution in particle production, and we will see that HIJING still produce RI values very close to unity, which demonstrates that the η acceptance

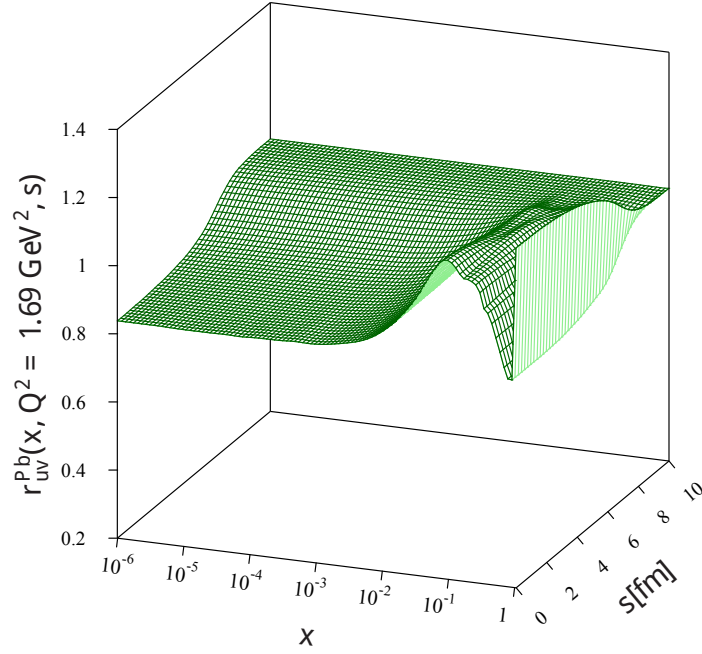


Figure 5.24: EPS09s nPDF for valence u quarks when $Q = 1.3 \text{ GeV}/c$ [74].

effect on RI is pretty small. However, though the systematic uncertainty is small, if the measured signal is minute, we still need to take care of η acceptance correction effect.

In HIJING, the default k_T setting is 0.44 GeV . The results are shown in Figure 5.28. As we can tell, the default k_T setting can not reproduce the features in data. There is almost no suppression from the out-of-box HIJING simulation. However it does not match some features of the data very well. Generally since HIJING and its underlying PYTHIA are based on leading order perturbative QCD, they are known not to reproduce the normalization of particle yields seen in data. For example in both cases, PYTHIA and HIJING $p+p$, the normalization of jet function per trigger yields seems to be off by about a factor of 1.5-2.0. However we do see that the relative changes of the yields with the associated hadron momentum is similar to the data. Since our ratio RI will cancel out any such normalization difference it is

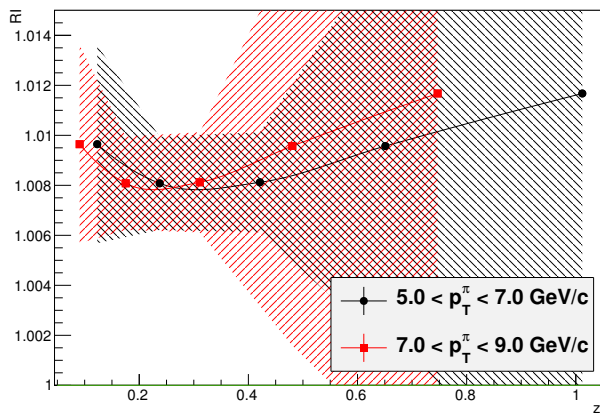
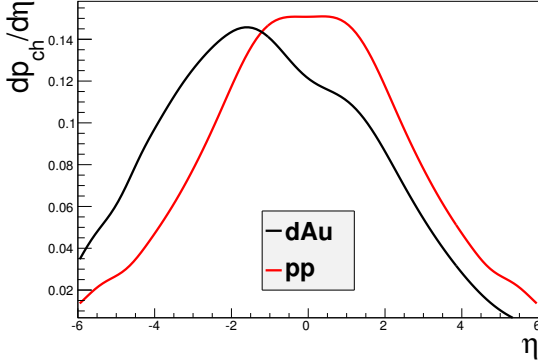


Figure 5.25: The modification of RI caused by EPS09s nuclear parton distribution functions. The shaded area is the uncertainties from EPS09 nuclear nPDF set. The black area is for triggers with $5 < p_T < 7 \text{ GeV}/c$. The red area is for triggers with $7 < p_T < 9 \text{ GeV}/c$.

not important to demand that the simulations reproduce the normalization. Instead we deem the simulation to data matching acceptable if it reproduces such relative changes, and especially we focus more on requiring primarily that the simulations reproduce the shape of the correlations.

HIJING doesn't provide an interface to change the k_T value. And as far as our current understanding of its code, HIJING might not have k_T effect included in its main design. In order to study the k_T effect in HIJING, we tried to modify HIJING code and introduce larger k_T effects in the remnants, which is the only place HIJING adds the additional parton level k_T kick. The setting value might not be the real k_T value in effect. The multiple application of k_T kick in HIJING code might introduce a larger k_T value than the settings. We tried multiple k_T settings, starting from the default values $0.44 \text{ GeV}/c$, to $1.2 \text{ GeV}/c$, $2.0 \text{ GeV}/c$, and $2.8 \text{ GeV}/c$. We investigated into the systematic changes of jet widths and I_{dA} when we turned up k_T values.



(a) Charged hadrons in central HIJING

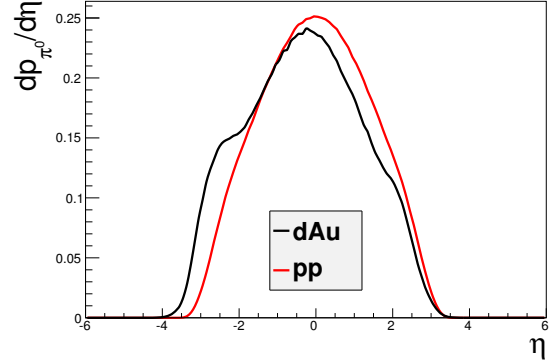
(b) π^0 triggers in central HIJING

Figure 5.26: HIJING particle production in η distributions with an normalization similar to the probability distribution function. Panel (a) shows the charged hadron pseudorapidity distribution in central HIJING simulation ($0 < b < 5$ fm). Panel (b) shows the π^0 trigger pseudorapidity distribution in central HIJING simulation ($0 < b < 5$ fm).

The near and away-side jet width for $k_T = 0.44, 1.2, 2.0, 2.8$ GeV/ c are shown in Figure 5.32. As we can see, the near-side jet widths of $p+p$ and $d+A$ collisions are both much smaller than the data (See Section 4.2) when k_T values are the default 0.44 GeV/ c . When k_T value increases, $p+p$ width doesn't change. The away-side width of $d+Au$ gets larger, while the near-side width of $d+Au$ remains the same. The near-side widths match the data reasonably (See the data plots in Section 3.11, 4.2), and their insensitiveness on the k_T values reflects the fact that the near-side jet width depends on j_T instead of k_T . The partner p_T dependence of the away-side width seems follow the same feature in data. When the partner p_T increases, the away-side jet broadens. Therefore, in order to tune the k_T effect to a realistic one, we compare the away-side jet widths. Meanwhile, we checked the near

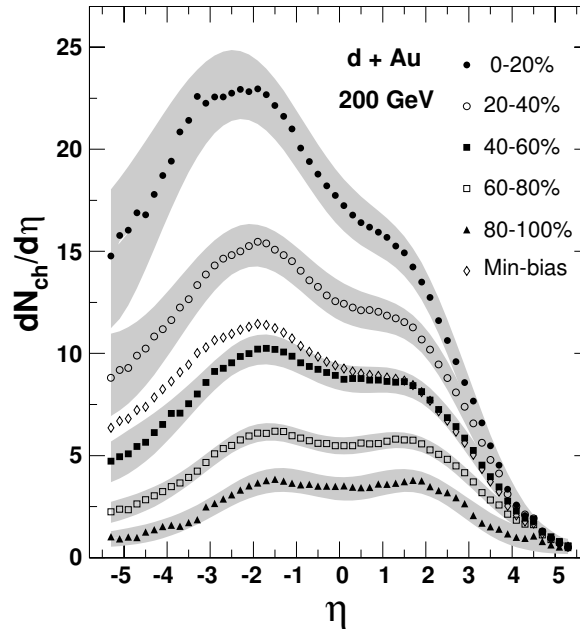


Figure 5.27: The charged hadron pseudorapidity distribution from PHOBOS measurement in [153].

and away-side I_{dA} values to make sure they are in a reasonable values and to peek into the underlying parts of RI 's modifications.

Lacking of k_T dependence in $p+p$ results, HIJING seems have not implemented this effect in a good way. This is consistent with our current knowledge of HIJING that it introduces the parton level k_T only in the remnants. PYTHIA has implemented k_T effect in a better way, and known to match quite a bit experimental data. One possible solution would be looking into PYTHIA's $p+p$ results. By comparing away-side with between HIJING $d+Au$ and PYTHIA $p+p$ results, we found a best match when $k_T = 2.0$ GeV in central $d+Au$ in HIJING. The pp 's k_T value in PYTHIA is taken as a realistic value 2.8 GeV/ c , close to the experimental measurement value, see Section 5.6. The away-side jet width of both are shown in Figure 5.29. It indicates that the effective k_T value in $d+Au$ HIJING is similar to

2.8 GeV/ c set in PYTHIA. When we look into the modification of RI in this case (see Figure 5.30), it is different from the data, and similar to the exaggerated k_T result in PYTHIA's study (see Section 5.6). There is no enhancement in low z_T region at all, only suppression in high z_T region. To demonstrate the modification difference, we show the jet functions in Figure 5.31.

In summary, based on current understanding of HIJING, we don't believe HIJING could reproduce our data in central $d+Au$ simulations.

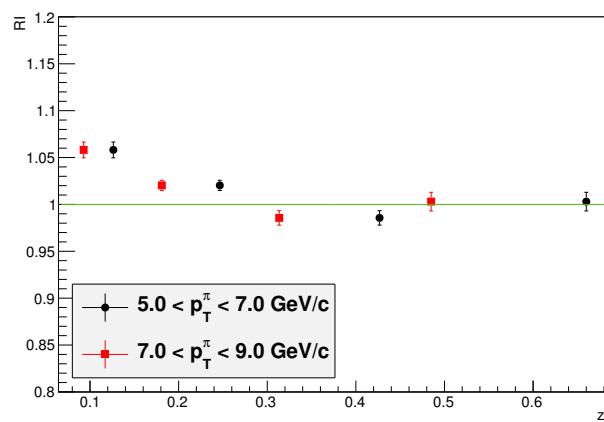


Figure 5.28: The modification of RI from HIJING simulation with default $k_T = 0.44$ GeV/ c for both $d+Au$ and $p+p$.

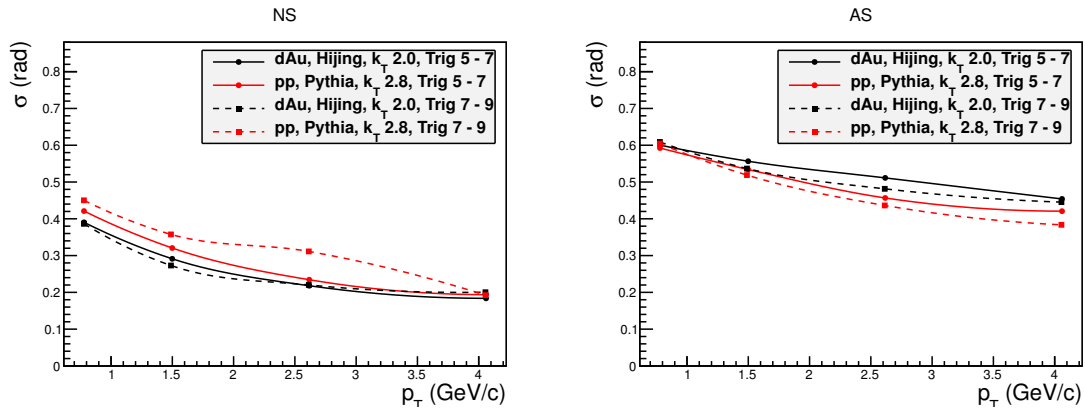


Figure 5.29: Width comparison between HIJING $d+Au$ with $k_T = 2.0$ GeV/ c and PYTHIA $p+p$ with $k_T = 2.8$ GeV/ c . The match of the away-side width is used to tune HIJING k_T settings.

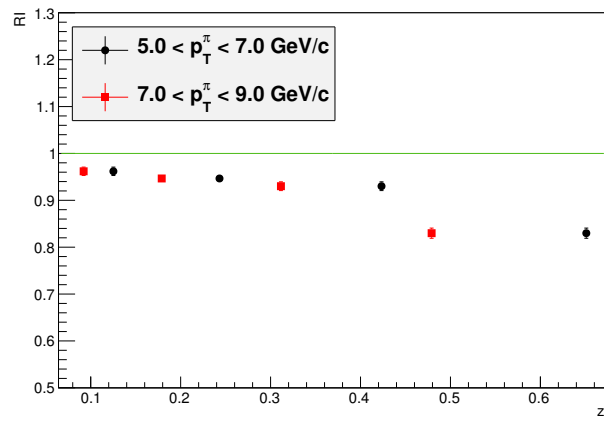


Figure 5.30: The modification of RI from HIJING $d+Au$ with $k_T = 2.0$ GeV/ c and PYTHIA $p+p$ with $k_T = 2.8$ GeV/ c .

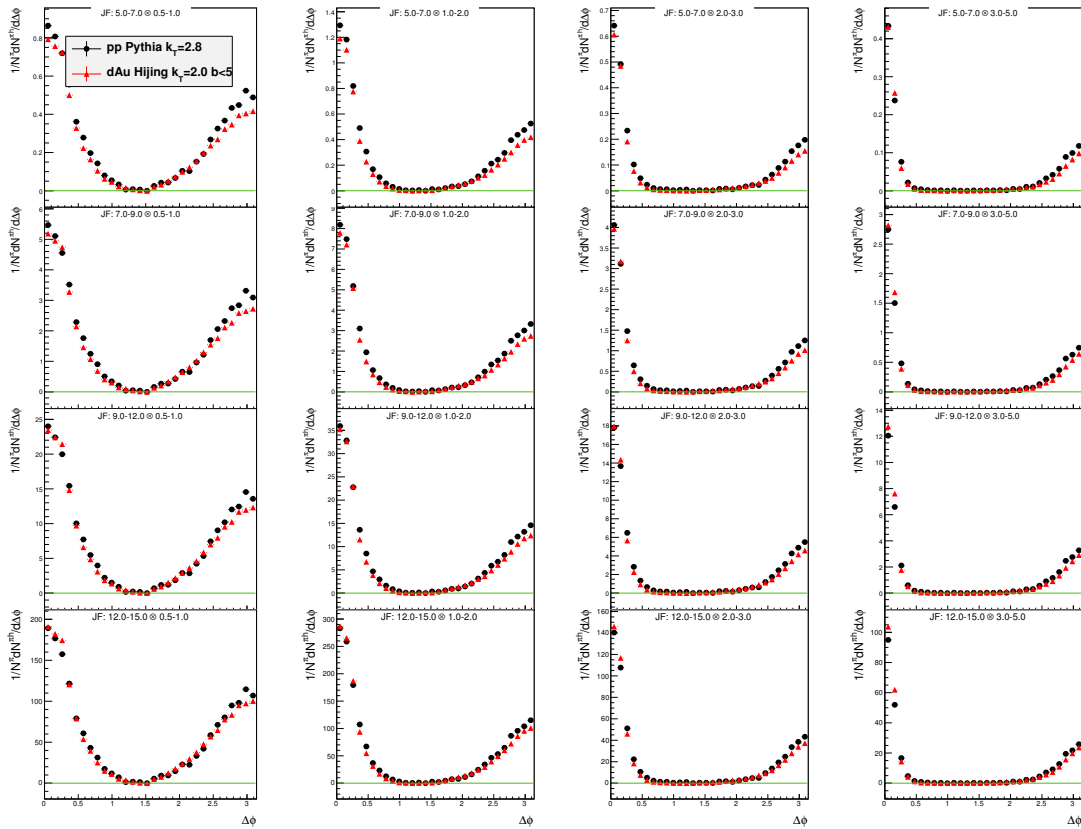


Figure 5.31: The modification of jet functions from HIJING $d+Au$ with $k_T = 2.0$ GeV/ c and PYTHIA $p+p$ with $k_T = 2.8$ GeV/ c .

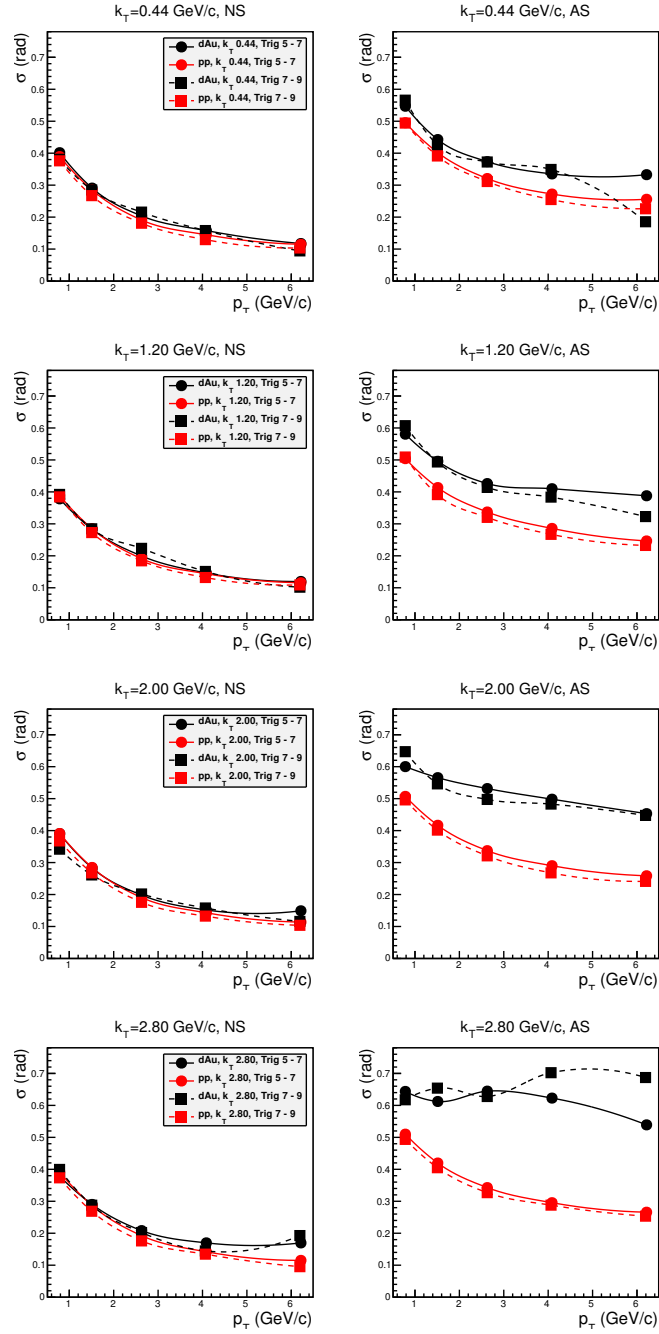


Figure 5.32: Near and away-side jet widths with different k_T and trigger p_T values in $d+Au$ and $p+p$ HIJING simulations. The left is the near-side width, the right is the away-side width. From top to bottom, the k_T values are 0.44, 1.2, 2.0, 2.8 GeV/c. The trigger p_T values are 5-7 GeV/c and 7-9 GeV/c.

5.10 Summary

We have analyzed PHENIX data from Run08 $d+Au$ and Run06 $p+p$ collisions at $\sqrt{s_{NN}} = 200$ GeV by using two particle azimuthal correlation method, and have measured the jet properties, such as the jet yields, width and observed some clear suppression and delicate enhancement in jet modifications in central $d+Au$ collisions, which are qualitatively similar but much smaller in magnitude to central A+A heavy ion collisions.

Our initial direct photon study suffers from low statistics. We use π^0 triggers to decrease the uncertainties from statistic fluctuations which helps to see the small effect in $d+Au$ collisions. Conventional I_{dA} comparison shows relatively large systematic uncertainties. In order to partially cancel out systematic uncertainties, we proposed and constructed a double ratio quantity RI to test the jet modifications in $d+Au$ collisions.

In peripheral $d+Au$ collisions, our data show no significant yield enhancement compared to pp in the high p_T trigger regime. This is different from the single π^0/η and jet reconstruction R_{dA} results previously presented by PHENIX which do reveal an unexpected enhancement in large p_T region. My peripheral results suggest that those enhancements in peripheral $d+Au$ collisions might just come from the determination of N_{coll} parameters instead of modifications of the jets.

In central $d+Au$ collisions, our RI measurements have the precision to test subtle jet modifications, especially the one in low z_T region. We observed a clear suppression of RI in the large z_T region and a small enhancement in the low z_T region. The enhancement at low z_T is about 2σ , which means the probability of the existence of such a modification instead of a statistical fluctuation is about 95% . The observed central $d+Au$ modifications are qualitatively similar to the features in central Au+Au or Pb+Pb collisions, where it is attributed to the jet quenching and

energy loss/recovery in a quark gluon plasma. The modifications in d +Au collisions are on a much smaller scale compared to Au+Au, which is no surprise because of the relatively small nuclear medium in d +Au systems. Considering the recent discovery of the collective flow in central p +A collisions both in LHC and RHIC, this measurement could be another piece of information to indicate a possible existence of QGP-like medium in central p +A collisions. There are currently few model calculations, if any, describing such modifications in central d +Au collisions, neither with the quark gluon plasma picture nor with just cold nuclear matter effects.

In order to constrain or test the possible physics origin of these modifications in central d +Au collisions, we investigate into a few possible causes related to this near / away-side ratio modifications.

- Firstly, one candidate is the nuclear k_T effect which is known to exist in p + p and d +Au collisions. We use the PYTHIA to test large nuclear k_T effects in RI . The realistic k_T values are unable to reproduce the large suppression in the high z_T region. An exaggerated k_T value in central events could cause a similar sized suppression, however, it does not appear to show a substantial excess in low z_T . Considering the lack of any enhancement feature and, under the assumption that the exaggerated k_T values are likely unrealistic, we believe that k_T alone could not cause such modifications in data.
- Secondly, we test the gluon jet contribution in this modifications. By assuming conversion of all quark jets to gluon jets or vice versa, RI modifications show either much smaller modifications or different features with the extreme settings. Therefore, we don't believe the gluon jet mixture mechanism could play an important role in the jet modifications.

- Thirdly, we utilize EPS09 nPDF set to study the nuclear modifications of parton distribution functions in the initial state. The effect turns out very small, and has totally different features. We believe the nuclear modifications in PDF are insufficient to cause RI 's deviation observed in the data.
- Lastly, we use HIJING to simulate d +Au cold nuclear matter effects. We depend on the jet function's shape to tune the k_T settings in HIJING. The realistic k_T settings show similar effect as PYTHIA k_T studies, there is no enhancement in low z_T regions. With current knowledge of HIJING, we can't reproduce the data by simulations.

In the prospectus of future experiment progress, we see a series of new runs set up in both RHIC and LHC. In 2014, RHIC has a new 2.4 weeks run for He+Au collisions at $\sqrt{s_{NN}} = 200$ GeV, which delivers 134 nb^{-1} data. In 2015, RHIC will have a p +Au run at $\sqrt{s_{NN}} = 200$ GeV⁹. In 2017, LHC will have a run either for Pb+Pb or p +Pb. In 2020, LHC will have a definite p +Pb run¹⁰. We can expect more data of the small collision systems coming from experiment around the world. The experiments at LHC certainly have the capability to detect π^\pm as well as π^0 in a large region of p_T values by using their vertex tracking detectors. The Figure 5.33 shows the statistical precision of CMS measurement in LHC p +Pb data collected in the 2013 LHC p +Pb run about 31 nb^{-1} .

In the end, we observed some jet modifications in central d +Au collisions qualitatively similar to energy loss effects in the quark gluon plasma. No correct theory calculations currently directly address this kind of modification. Our simulations that incorporated various cold nuclear matter effects are unable to reproduce this phenomena observed in the data. However we expect that further

⁹ <http://www.agrhome.bnl.gov/RHIC/Runs/>

¹⁰ <http://lhc-commissioning.web.cern.ch/lhc-commissioning/>

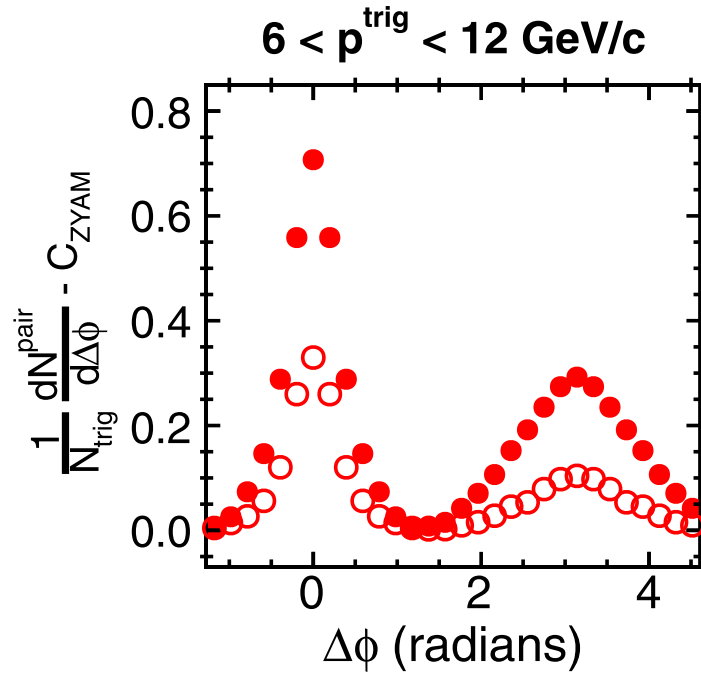


Figure 5.33: Statistical precision of CMS p +Pb measurement. This plot is adapted from the one from [96]. This is the correlation functions for 5.02 TeV p +Pb collisions within the multiplicity range $220 \leq N_{\text{trk}}^{\text{offline}} \leq 260$ (filled squares) and $N_{\text{trk}}^{\text{offline}} \leq 20$ (open squares) for pairs with short-range region ($|\Delta\eta| < 1$) with $1 < p_T^{\text{assoc}} < 2\text{GeV}/c$ and $6 < p_T^{\text{trig}} < 12\text{GeV}/c$. It shows the good statistical precisions CMS has been able to achieve with LHC 2013 p +Pb data.

development of theoretical or model calculations of many of these effects can be constrained by comparison to our data, especially the precise RI ratio data. Such constraints should be able to set concrete limits on the contributions of various cold nuclear or possibly hot QGP-like effects.

REFERENCES

- [1] F. Englert and R. Brout, *Phys.Rev.Lett.* **13**, 321 (1964).
- [2] P. W. Higgs, *Phys.Rev.Lett.* **13**, 508 (1964).
- [3] G. Guralnik, C. Hagen, and T. Kibble, *Phys.Rev.Lett.* **13**, 585 (1964).
- [4] G. Aad *et al.* (ATLAS Collaboration), *Phys.Lett.* **B716**, 1 (2012),
arXiv:1207.7214 [hep-ex] .
- [5] S. Chatrchyan *et al.* (CMS Collaboration), *Phys.Lett.* **B716**, 30 (2012),
arXiv:1207.7235 [hep-ex] .
- [6] G. 't Hooft, *Nucl.Phys.* **B33**, 173 (1971).
- [7] G. 't Hooft, *Nucl.Phys.* **B35**, 167 (1971).
- [8] G. 't Hooft and M. Veltman, *Nucl.Phys.* **B44**, 189 (1972).
- [9] H. Yukawa, *Proc. Phys. Math. Soc. Japan* **17**, 48 (1935).
- [10] M. E. Peskin and D. V. Schroeder, *An Introduction to Quantum Field Theory*
(Addison-Wesley Publishing Company, 1995).
- [11] W. Heisenberg, *Zeitschrift für Physik* **77**, 1 (1932).
- [12] D. Griffiths, *Introduction to Elementary Particles* (Wiley-VCH, 2008).
- [13] M. Gell-Mann, (1961).
- [14] V. Barnes, P. Connolly, D. Crennell, B. Culwick, W. Delaney, *et al.*,
Phys.Rev.Lett. **12**, 204 (1964).
- [15] M. Gell-Mann, *Phys.Lett.* **8**, 214 (1964).

- [16] G. Zweig, (1964).
- [17] G. Zweig, , 22 (1964).
- [18] T.-P. Cheng and L.-F. Li, *Gauge Theory of Elementary Particle Physics* (Oxford University Press, 1988).
- [19] O. Greenberg, Phys.Rev.Lett. **13**, 598 (1964).
- [20] M. Han and Y. Nambu, Phys.Rev. **139**, B1006 (1965).
- [21] W. Cottingham and D. Greenwood, *An Introduction to the Standard Model of Particle Physics* (Cambridge University Press, 1998).
- [22] T. Muta, World Sci.Lect.Notes Phys. **57**, 1 (1998).
- [23] F. Halzen and A. D. Martin, *Quarks and Leptons* (John Wiley & Sons, 1984).
- [24] C.-N. Yang and R. L. Mills, Phys.Rev. **96**, 191 (1954).
- [25] H. Weyl, Annals of Physics **59**, 101 (1919).
- [26] Gerardus 't Hooft, *50 Years of Yang-Mills Theory* (World Scientific Publishing Co., 2005).
- [27] H. D. Politzer, Phys.Rev.Lett. **30**, 1346 (1973).
- [28] D. J. Gross and F. Wilczek, Phys.Rev.Lett. **30**, 1343 (1973).
- [29] D. Gross and F. Wilczek, Phys.Rev. **D8**, 3633 (1973).
- [30] H. D. Politzer, Phys.Rept. **14**, 129 (1974).
- [31] J. Beringer *et al.* (Particle Data Group), Phys.Rev. **D86**, 010001 (2012).

- [32] T. van Ritbergen, J. Vermaseren, and S. Larin, Phys.Lett. **B400**, 379 (1997), arXiv:hep-ph/9701390 [hep-ph] .
- [33] M. Czakon, Nucl.Phys. **B710**, 485 (2005), arXiv:hep-ph/0411261 [hep-ph] .
- [34] S. Bethke, Eur.Phys.J. **C64**, 689 (2009), arXiv:0908.1135 [hep-ph] .
- [35] J. C. Collins, D. E. Soper, and G. F. Sterman, Adv.Ser.Direct.High Energy Phys. **5**, 1 (1988), arXiv:hep-ph/0409313 [hep-ph] .
- [36] K. G. Wilson, Phys.Rev. **D10**, 2445 (1974).
- [37] J. C. Collins and M. Perry, Phys.Rev.Lett. **34**, 1353 (1975).
- [38] K. Adcox *et al.* (PHENIX Collaboration), Nucl.Phys. **A757**, 184 (2005), arXiv:nucl-ex/0410003 [nucl-ex] .
- [39] F. Karsch, Lect.Notes Phys. **583**, 209 (2002), arXiv:hep-lat/0106019 [hep-lat] .
- [40] H. Satz, Nucl.Phys. **A715**, 3 (2003), arXiv:hep-ph/0209181 [hep-ph] .
- [41] A. Adare *et al.* (PHENIX Collaboration), Phys.Rev.Lett. **104**, 132301 (2010), arXiv:0804.4168 [nucl-ex] .
- [42] B. Abelev *et al.* (ALICE Collaboration), Phys.Rev.Lett. **109**, 072301 (2012), arXiv:1202.1383 [hep-ex] .
- [43] B. B. Abelev *et al.* (ALICE Collaboration), Phys.Lett. **B734**, 314 (2014), arXiv:1311.0214 [nucl-ex] .
- [44] G. Roland, K. Safarik, and P. Steinberg, Prog.Part.Nucl.Phys. **77**, 70 (2014).
- [45] S. Chatrchyan *et al.* (CMS Collaboration), Phys.Rev. **C84**, 024906 (2011), arXiv:1102.1957 [nucl-ex] .

- [46] G. Aad *et al.* (ATLAS Collaboration), Phys.Lett. **B719**, 220 (2013),
arXiv:1208.1967 [hep-ex] .
- [47] B. Abelev *et al.* (ALICE Collaboration), JHEP **1403**, 013 (2014),
arXiv:1311.0633 [nucl-ex] .
- [48] S. Chatrchyan *et al.* (CMS Collaboration), Phys.Rev.Lett. **106**, 212301
(2011), arXiv:1102.5435 [nucl-ex] .
- [49] S. Chatrchyan *et al.* (CMS Collaboration), Phys.Lett. **B715**, 66 (2012),
arXiv:1205.6334 [nucl-ex] .
- [50] G. Aad *et al.* (ATLAS Collaboration), Phys.Rev.Lett. **110**, 022301 (2013),
arXiv:1210.6486 [hep-ex] .
- [51] K. Ackermann *et al.* (STAR Collaboration), Phys.Rev.Lett. **86**, 402 (2001),
arXiv:nucl-ex/0009011 [nucl-ex] .
- [52] I. C. Park *et al.* (PHOBOS Collaboration), Nucl.Phys. **A698**, 564 (2002),
arXiv:nucl-ex/0105015 [nucl-ex] .
- [53] K. Adcox *et al.* (PHENIX Collaboration), Phys.Rev.Lett. **89**, 212301 (2002),
arXiv:nucl-ex/0204005 [nucl-ex] .
- [54] P. Danielewicz and M. Gyulassy, Phys.Rev. **D31**, 53 (1985).
- [55] G. Policastro, D. T. Son, and A. O. Starinets, Phys.Rev.Lett. **87**, 081601
(2001), arXiv:hep-th/0104066 [hep-th] .
- [56] J. Adams *et al.* (STAR Collaboration), Nucl.Phys. **A757**, 102 (2005),
arXiv:nucl-ex/0501009 [nucl-ex] .

- [57] J. Adams *et al.* (STAR Collaboration), Phys.Rev.Lett. **92**, 052302 (2004),
arXiv:nucl-ex/0306007 [nucl-ex] .
- [58] J. Castillo (STAR Collaboration), J.Phys. **G30**, S1207 (2004),
arXiv:nucl-ex/0403027 [nucl-ex] .
- [59] E. Fermi, Prog.Theor.Phys. **5**, 570 (1950).
- [60] R. Hagedorn, Nuovo Cim.Suppl. **3**, 147 (1965).
- [61] M. Kaneta and N. Xu, (2004), arXiv:nucl-th/0405068 [nucl-th] .
- [62] R. Baier, D. Schiff, and B. Zakharov, Ann.Rev.Nucl.Part.Sci. **50**, 37 (2000),
arXiv:hep-ph/0002198 [hep-ph] .
- [63] K. Adcox *et al.* (PHENIX Collaboration), Phys.Rev.Lett. **88**, 022301 (2002),
arXiv:nucl-ex/0109003 [nucl-ex] .
- [64] C. Adler *et al.* (STAR Collaboration), Phys.Rev.Lett. **90**, 082302 (2003),
arXiv:nucl-ex/0210033 [nucl-ex] .
- [65] K. Eskola, H. Paukkunen, and C. Salgado, JHEP **0904**, 065 (2009),
arXiv:0902.4154 [hep-ph] .
- [66] I. Vitev, Phys.Lett. **B562**, 36 (2003), arXiv:nucl-th/0302002 [nucl-th] .
- [67] S. Adler *et al.* (PHENIX Collaboration), Phys.Rev.Lett. **94**, 082302 (2005),
arXiv:nucl-ex/0411054 [nucl-ex] .
- [68] S. Adler *et al.* (PHENIX Collaboration), Phys.Rev. **C77**, 014905 (2008),
arXiv:0708.2416 [nucl-ex] .
- [69] J. Pumplin, D. Stump, J. Huston, H. Lai, P. M. Nadolsky, *et al.*, JHEP **0207**,
012 (2002), arXiv:hep-ph/0201195 [hep-ph] .

- [70] A. Adare *et al.* (PHENIX Collaboration), Phys.Rev. **D82**, 072001 (2010), arXiv:1006.1347 [hep-ex] .
- [71] J. Aubert *et al.* (European Muon Collaboration), Phys.Lett. **B123**, 275 (1983).
- [72] P. Norton, Rept.Prog.Phys. **66**, 1253 (2003).
- [73] K. Rith, (2014), arXiv:1402.5000 [hep-ex] .
- [74] I. Helenius, K. J. Eskola, H. Honkanen, and C. A. Salgado, JHEP **1207**, 073 (2012), arXiv:1205.5359 [hep-ph] .
- [75] J. Cronin, H. J. Frisch, M. Shochet, J. Boymond, P. Piroue, *et al.*, Phys.Rev.Lett. **31**, 1426 (1973).
- [76] J. Cronin, H. J. Frisch, M. Shochet, J. Boymond, R. Mermod, *et al.*, Phys.Rev. **D11**, 3105 (1975).
- [77] S. Adler *et al.* (PHENIX Collaboration), Phys.Rev.Lett. **91**, 072303 (2003), arXiv:nucl-ex/0306021 [nucl-ex] .
- [78] H. Busching (PHENIX Collaboration), J.Phys. **G31**, S473 (2005), arXiv:nucl-ex/0410002 [nucl-ex] .
- [79] B. Back *et al.* (PHOBOS Collaboration), Phys.Rev.Lett. **91**, 072302 (2003), arXiv:nucl-ex/0306025 [nucl-ex] .
- [80] J. Adams *et al.* (STAR Collaboration), Phys.Rev.Lett. **91**, 072304 (2003), arXiv:nucl-ex/0306024 [nucl-ex] .
- [81] I. Arsene *et al.* (BRAHMS Collaboration), Phys.Rev.Lett. **93**, 242303 (2004), arXiv:nucl-ex/0403005 [nucl-ex] .

- [82] I. Vitev, Phys.Rev. **C75**, 064906 (2007), arXiv:hep-ph/0703002 [hep-ph] .
- [83] N. Armesto, B. Cole, C. Gale, W. A. Horowitz, P. Jacobs, *et al.*, Phys.Rev. **C86**, 064904 (2012), arXiv:1106.1106 [hep-ph] .
- [84] I. Arsene *et al.* (BRAHMS Collaboration), Phys.Rev.Lett. **93**, 242303 (2004), arXiv:nucl-ex/0403005 [nucl-ex] .
- [85] A. Adare *et al.* (PHENIX Collaboration), Phys.Rev.Lett. **107**, 172301 (2011), arXiv:1105.5112 [nucl-ex] .
- [86] L. D. McLerran and R. Venugopalan, Phys.Rev. **D49**, 3352 (1994), arXiv:hep-ph/9311205 [hep-ph] .
- [87] D. Kharzeev, E. Levin, and L. McLerran, Nucl.Phys. **A748**, 627 (2005), arXiv:hep-ph/0403271 [hep-ph] .
- [88] R. Feynman, R. Field, and G. Fox, Nucl.Phys. **B128**, 1 (1977).
- [89] S. Adler *et al.* (PHENIX Collaboration), Phys.Rev. **C73**, 054903 (2006), arXiv:nucl-ex/0510021 [nucl-ex] .
- [90] L. Apanasevich, C. Balazs, C. Bromberg, J. Huston, A. Maul, *et al.*, Phys.Rev. **D59**, 074007 (1999), arXiv:hep-ph/9808467 [hep-ph] .
- [91] J. Kapitan (STAR Collaboration), Nucl.Phys. **A855**, 412 (2011), arXiv:1012.1804 [nucl-ex] .
- [92] V. Khachatryan *et al.* (CMS Collaboration), JHEP **1009**, 091 (2010), arXiv:1009.4122 [hep-ex] .
- [93] S. Chatrchyan *et al.* (CMS Collaboration), Phys.Lett. **B718**, 795 (2013), arXiv:1210.5482 [nucl-ex] .

- [94] B. Abelev *et al.* (ALICE Collaboration), Phys.Lett. **B719**, 29 (2013),
arXiv:1212.2001 [nucl-ex] .
- [95] G. Aad *et al.* (ATLAS Collaboration), Phys.Rev.Lett. **110**, 182302 (2013),
arXiv:1212.5198 [hep-ex] .
- [96] S. Chatrchyan *et al.* (CMS Collaboration), Phys.Lett. **B724**, 213 (2013),
arXiv:1305.0609 [nucl-ex] .
- [97] A. Adare *et al.* (PHENIX Collaboration), Phys.Rev.Lett. **111**, 212301 (2013),
arXiv:1303.1794 [nucl-ex] .
- [98] A. Adare *et al.* (PHENIX Collaboration), (2014), arXiv:1404.7461 [nucl-ex] .
- [99] J. Adams *et al.* (STAR Collaboration), Phys.Rev.Lett. **95**, 152301 (2005),
arXiv:nucl-ex/0501016 [nucl-ex] .
- [100] S. Adler *et al.* (PHENIX Collaboration), Phys.Rev.Lett. **97**, 052301 (2006),
arXiv:nucl-ex/0507004 [nucl-ex] .
- [101] A. Adare *et al.* (PHENIX Collaboration), Phys.Rev.Lett. **98**, 232302 (2007),
arXiv:nucl-ex/0611019 [nucl-ex] .
- [102] A. Adare *et al.* (PHENIX Collaboration), Phys.Rev. **C78**, 014901 (2008),
arXiv:0801.4545 [nucl-ex] .
- [103] F. Wang (STAR Collaboration), Int.J.Mod.Phys. **E16**, 3168 (2007),
arXiv:0707.0815 [nucl-ex] .
- [104] B. Alver *et al.* (PHOBOS Collaboration), Phys.Rev.Lett. **104**, 062301 (2010),
arXiv:0903.2811 [nucl-ex] .

- [105] B. Abelev *et al.* (STAR Collaboration), Phys.Rev. **C80**, 064912 (2009), arXiv:0909.0191 [nucl-ex] .
- [106] C. Nattrass, Nuovo Cim. **C034N2**, 31 (2011), arXiv:1012.2907 [nucl-ex] .
- [107] J. Noronha, M. Gyulassy, and G. Torrieri, Phys.Rev.Lett. **102**, 102301 (2009), arXiv:0807.1038 [hep-ph] .
- [108] R. Neufeld and I. Vitev, Phys.Rev. **C86**, 024905 (2012), arXiv:1105.2067 [hep-ph] .
- [109] L. Satarov, H. Stoecker, and I. Mishustin, Phys.Lett. **B627**, 64 (2005), arXiv:hep-ph/0505245 [hep-ph] .
- [110] B. Alver and G. Roland, Phys.Rev. **C81**, 054905 (2010), arXiv:1003.0194 [nucl-th] .
- [111] R. A. Lacey, R. Wei, N. Ajitanand, and A. Taranenko, Phys.Rev. **C83**, 044902 (2011), arXiv:1009.5230 [nucl-ex] .
- [112] K. Aamodt *et al.* (ALICE Collaboration), Phys.Rev.Lett. **107**, 032301 (2011), arXiv:1105.3865 [nucl-ex] .
- [113] A. Adare *et al.* (PHENIX Collaboration), Phys.Rev.Lett. **107**, 252301 (2011), arXiv:1105.3928 [nucl-ex] .
- [114] S. Chatrchyan *et al.* (CMS Collaboration), Eur.Phys.J. **C72**, 2012 (2012), arXiv:1201.3158 [nucl-ex] .
- [115] G. Aad *et al.* (ATLAS Collaboration), Phys.Rev. **C86**, 014907 (2012), arXiv:1203.3087 [hep-ex] .

- [116] L. Adamczyk *et al.* (STAR Collaboration), Phys.Rev. **C88**, 014904 (2013), arXiv:1301.2187 [nucl-ex] .
- [117] J. Nagle, Nucl.Phys. **A830**, 147C (2009), arXiv:0907.2707 [nucl-ex] .
- [118] P. Huovinen, P. Kolb, U. W. Heinz, P. Ruuskanen, and S. Voloshin, Phys.Lett. **B503**, 58 (2001), arXiv:hep-ph/0101136 [hep-ph] .
- [119] B. B. Abelev *et al.* (ALICE Collaboration), Phys.Lett. **B728**, 25 (2014), arXiv:1307.6796 [nucl-ex] .
- [120] J. Nagle, A. Adare, S. Beckman, T. Koblesky, J. O. Koop, *et al.*, (2013), arXiv:1312.4565 [nucl-th] .
- [121] M. Luzum and P. Romatschke, Phys.Rev. **C78**, 034915 (2008), arXiv:0804.4015 [nucl-th] .
- [122] <http://www.phenix.bnl.gov/>.
- [123] M. L. Miller, K. Reygers, S. J. Sanders, and P. Steinberg, Ann.Rev.Nucl.Part.Sci. **57**, 205 (2007), arXiv:nucl-ex/0701025 [nucl-ex] .
- [124] K. Adcox *et al.* (PHENIX Collaboration), Nucl.Instrum.Meth. **A499**, 489 (2003).
- [125] J. Mitchell *et al.* (PHENIX Collaboration), Nucl.Instrum.Meth. **A482**, 491 (2002), arXiv:nucl-ex/0201013 [nucl-ex] .
- [126] L. Aphecetche *et al.* (PHENIX Collaboration), Nucl.Instrum.Meth. **A499**, 521 (2003).
- [127] A. Adare *et al.* (PHENIX Collaboration), (2013), arXiv:1310.4793 [nucl-ex] .

- [128] M. P. McCumber (PHENIX Collaboration), “Practical jet mathematics,” (2007), Analysis Note 646.
- [129] P. Stankus (PHENIX Collaboration), “Mathematical Framework for Interpreting Pair Angular Correlations in a Two-Source Model,” (2003), Technical Note 412.
- [130] S. Adler *et al.* (PHENIX Collaboration), Phys.Rev. **C71**, 051902 (2005), arXiv:nucl-ex/0408007 [nucl-ex] .
- [131] B. Meredith, M. Chiu, and M. Perdekamp (PHENIX Collaboration), “Run8 $\sqrt{s}=200\text{GeV}$ d+Au, p+p rapidity separated correlations using the MPC and central arm detectors,” (2011), Analysis Note 961.
- [132] N. Grau and B. Cole (PHENIX Collaboration), “Di-jet $\delta\phi$ distributions using the anti- k_T algorithm in Run-8 d+Au,” (2009), Analysis Note 855.
- [133] Private corresponding with J.Jia, there are quite a few runs excluded in AN961. We decide not to exclude them.
- [134] J. Frantz, M. Nguyen, J. Chen, and M. Connors (PHENIX Collaboration), “Final analysis of the run 4 Au+Au and runs 5+6 p+p direct photon-hadron correlations,” (2009), Analysis Note 718.
- [135] A. Adare, M.Connors, J.Nagle, A. Sickles (PHENIX Collaboration), “Single-particle and embedding h^\pm acceptance and efficiency corrections for central arm analyses in run 6 and 7,” (2009), Analysis Note 808.
- [136] N. Grau, Z. Citron, J. Jia (PHENIX Collaboration), “Run-8 d+au and p+p single charged hadron efficiency,” (2009), Analysis Note 816.

- [137] A. S. M. Connors (PHENIX Collaboration), “Efficiency and occupancy corrections for run 6 & 7,” (2010), Analysis Note 879.
- [138] S. Adler *et al.* (PHENIX Collaboration), Phys.Rev.Lett. **95**, 202001 (2005), arXiv:hep-ex/0507073 [hep-ex] .
- [139] F. Matathias (PHENIX Collaboration), “dear boris,” (2005), Analysis Note 350.
- [140] A. Adare *et al.* (PHENIX Collaboration), Phys.Rev. **C77**, 064907 (2008), arXiv:0801.1665 [nucl-ex] .
- [141] A. Adare *et al.* (PHENIX Collaboration), Phys.Rev. **C87**, 034904 (2013), arXiv:1204.0777 [nucl-ex] .
- [142] B. Sahlmueller (PHENIX Collaboration), Nucl.Phys. **A904-905**, 795c (2013), arXiv:1210.5547 [nucl-ex] .
- [143] D. V. Perepelitsa (PHENIX Collaboration), Nucl.Phys. **A904-905**, 1003c (2013).
- [144] A. Adare *et al.* (PHENIX), Phys.Rev.Lett. **111**, 032301 (2013), arXiv:1212.3323 [nucl-ex] .
- [145] G. Aad *et al.* (ATLAS Collaboration), (2014), arXiv:1406.2979 [hep-ex] .
- [146] T. Todoroki (PHENIX Collaboration), “Measurements of Two-Particle Correlations with respect to Higher-Order Event Planes in $\sqrt{s} = 200$ GeV Au+Au Collisions,” (2014), Analysis Note 991.
- [147] T. Sjostrand, S. Mrenna, and P. Z. Skands, JHEP **0605**, 026 (2006), arXiv:hep-ph/0603175 [hep-ph] .

- [148] T. Sjostrand, S. Mrenna, and P. Z. Skands, *Comput.Phys.Commun.* **178**, 852 (2008), arXiv:0710.3820 [hep-ph] .
- [149] X.-N. Wang and M. Gyulassy, *Phys.Rev.* **D44**, 3501 (1991).
- [150] X.-N. Wang and M. Gyulassy, *Phys.Rev.Lett.* **68**, 1480 (1992).
- [151] X.-N. Wang and M. Gyulassy, *Phys.Rev.* **D45**, 844 (1992).
- [152] M. Gyulassy and X.-N. Wang, *Comput.Phys.Commun.* **83**, 307 (1994), arXiv:nucl-th/9502021 [nucl-th] .
- [153] B. Back *et al.* (PHOBOS Collaboration), *Phys.Rev.* **C72**, 031901 (2005), arXiv:nucl-ex/0409021 [nucl-ex] .

APPENDIX A: ACCEPTANCE CORRECTION

The acceptance correction is crucial in the two-particle azimuthal correlation measurement, since there is no perfect detector, or say, no detector's efficiency is isotropic. In order to deal with it, we could use the event mixing technique. In the toy model below, we consider only the azimuthal angle dependence for all quantities to keep everything short. In real events, the distribution of true physics pairs is represented by

$$\frac{d^2 N^{AB}}{d\phi^A d\phi^B} = N^{AB} \frac{d^2 p^{AB}}{d\phi^A d\phi^B} \quad (\text{A.1})$$

Here, $\frac{d^2 N^{AB}}{d\phi^A d\phi^B}$ is a joint probability density function, whose integral should be unity, and it is meaningful statistically. p itself is probability mass function. It can represent the distribution of the physical quantities, such as N^{AB} , if we have a large enough sample. And the per event quantity is

$$\frac{d^2 n^{AB}}{d\phi^A d\phi^B} = \frac{N^{AB}}{N^{evt}} \frac{d^2 p^{AB}}{d\phi^A d\phi^B} = n^{AB} \frac{d^2 p^{AB}}{d\phi^A d\phi^B} \quad (\text{A.2})$$

Considering the the efficiency of detectors and cuts for particle type A and B , the distribution of detected pairs should be

$$\frac{d^2 \mathbb{N}^{AB}}{d\phi^A d\phi^B} = N^{AB} \frac{d^2 p^{AB}}{d\phi^A d\phi^B} \epsilon^A(\phi^A) \epsilon^B(\phi^B) \quad (\text{A.3})$$

$$\frac{d^2 \mathbb{n}^{AB}}{d\phi^A d\phi^B} = n^{AB} \frac{d^2 p^{AB}}{d\phi^A d\phi^B} \epsilon^A(\phi^A) \epsilon^B(\phi^B) \quad (\text{A.4})$$

And the pair angle distribution could be evaluated by

$$\frac{dN^{AB}}{d\Delta\phi} = N^{AB} \iint \frac{d^2 p^{AB}}{d\phi^A d\phi^B} \delta(\text{PA}(\phi^A - \phi^B) - \Delta\phi) d\phi^A d\phi^B \quad (\text{A.5})$$

$$\frac{dn^{AB}}{d\Delta\phi} = n^{AB} \iint \frac{d^2 p^{AB}}{d\phi^A d\phi^B} \delta(\text{PA}(\phi^A - \phi^B) - \Delta\phi) d\phi^A d\phi^B \quad (\text{A.6})$$

Here we defined a function called PA (i.e. PHENIX Angle), which calculates the pair angle between ϕ^A and ϕ^B and maps it into $[0, \pi]$. We may understand

$\delta(\text{PA}(\phi^A - \phi^B) - \Delta\phi)$ as a formal formulation of $\delta(\phi^A - \phi^B - \Delta\phi)$. The detected pair angle distribution is

$$\frac{dN^{AB}}{d\Delta\phi} = N^{AB} \iint \frac{d^2p^{AB}}{d\phi^A d\phi^B} \epsilon^A(\phi^A) \epsilon^B(\phi^B) \delta(\text{PA}(\phi^A - \phi^B) - \Delta\phi) d\phi^A d\phi^B \quad (\text{A.7})$$

$$\frac{dn^{AB}}{d\Delta\phi} = n^{AB} \iint \frac{d^2p^{AB}}{d\phi^A d\phi^B} \epsilon^A(\phi^A) \epsilon^B(\phi^B) \delta(\text{PA}(\phi^A - \phi^B) - \Delta\phi) d\phi^A d\phi^B \quad (\text{A.8})$$

In the previous equations, the joint distribution $\frac{d^2p^{AB}}{d\phi^A d\phi^B}$ could be evaluated by the conditional distribution

$$\frac{d^2p^{AB}(\phi^A, \phi^B)}{d\phi^A d\phi^B} = \frac{dp^A(\phi^A)}{d\phi^A} \cdot \frac{dp^{B|A}(\phi^B; \phi^A)}{d\phi^B} \quad (\text{A.9})$$

Then we may rewrite the $\Delta\phi$ distribution as

$$\begin{aligned} \frac{dn^{AB}}{d\Delta\phi} = n^{AB} \cdot & \int \frac{dp^A(\phi^A)}{d\phi^A} \epsilon^A(\phi^A) d\phi^A \\ & \cdot \int \frac{dp^{B|A}(\phi^B; \phi^A)}{d\phi^B} \epsilon^B(\phi^B) \delta(\text{PA}(\phi^A - \phi^B) - \Delta\phi) d\phi^B \end{aligned} \quad (\text{A.10})$$

$\frac{dn^{AB}}{d\Delta\phi}$ is a quantity we can measure in experiments, however ϵ^A and ϵ^B are hard to evaluate in experiments, because the true physics quantities $\frac{dn^A}{d\phi^A}$, $\frac{dn^B}{d\phi^B}$ are hard to quantify. In this case, we could use a simplest but reasonable assumption that the particle B 's conditional distribution $\frac{dp^{B|A}(\phi^B; \phi^A)}{d\phi^B}$ depends on $\Delta\phi$ only or say $\text{PA}(\phi^A - \phi^B)$. If this assumption is true, we may get

$$\boxed{\frac{dp^{B|A}(\phi^B; \phi^A)}{d\phi^B} = \frac{dp^{B|A}(\text{PA}(\phi^A - \phi^B))}{d\phi^B} = \frac{dp^{B|A}(\Delta\phi)}{d\Delta\phi}} \quad (\text{A.11})$$

Note, p is probability mass function, so the derivative of $\Delta\phi$, or say the PDF, should still be positive, and PA is just $|\phi_A - \phi_B| + C$. Substitute it into the previous

pair angle distribution,

$$\frac{d\mathfrak{n}^{AB}}{d\Delta\phi} = n^{AB} \cdot \int \frac{dp^A(\phi^A)}{d\phi^A} \epsilon^A(\phi^A) d\phi^A \quad (\text{A.12})$$

$$\cdot \int \frac{dp^{B|A}(\text{PA}(\phi^A - \phi^B))}{d\phi^B} \epsilon^B(\phi^B) \delta(\text{PA}(\phi^A - \phi^B) - \Delta\phi) d\phi^B$$

$$= n^{AB} \cdot \int \frac{dp^A(\phi^A)}{d\phi^A} \epsilon^A(\phi^A) d\phi^A \quad (\text{A.13})$$

$$\cdot \int \frac{dp^{B|A}(\Delta\phi)}{d\Delta\phi} \epsilon^B(\phi^B) \delta(\text{PA}(\phi^A - \phi^B) - \Delta\phi) d\phi^B$$

$$= n^{AB} \cdot \frac{dp^{B|A}(\Delta\phi)}{d\Delta\phi} \cdot \int \frac{dp^A(\phi^A)}{d\phi^A} \epsilon^A(\phi^A) d\phi^A \quad (\text{A.14})$$

$$\cdot \int \epsilon^B(\phi^B) \delta(\text{PA}(\phi^A - \phi^B) - \Delta\phi) d\phi^B$$

$\frac{dp^{B|A}(\Delta\phi)}{d\Delta\phi}$ is really what we want to measure, which shows the true physics correlation between the two classes of particles A and B . n^{AB} is relatively easy to obtain by measuring single particle multiplicity, $n^{AB} = n^A n^B$. So the problem goes to how to quantify this part:

$$\boxed{f(\Delta\phi) \triangleq \int \frac{dp^A(\phi^A)}{d\phi^A} \epsilon^A(\phi^A) d\phi^A \cdot \int \epsilon^B(\phi^B) \delta(\text{PA}(\phi^A - \phi^B) - \Delta\phi) d\phi^B} \quad (\text{A.15})$$

The per event $\Delta\phi$ distribution could be simplified as

$$\frac{d\mathfrak{n}^{AB}}{d\Delta\phi} = n^{AB} \cdot \frac{dp^{B|A}(\Delta\phi)}{d\Delta\phi} \cdot f(\Delta\phi) \quad (\text{A.16})$$

The job relies on the event mixing technique. In this method, we mix the particle A and B from different events, which should break the angular correlation between them. In practice, we choose the same A particles, such as the trigger in this analysis. And we choose slightly different particle B in mixed events, say, B' . We will come back to it later to see how different it could be, and how similar it must be. In this analysis, B' is the same type of particles h^\pm , similar p_T and from events with similar collision vertex. Then **statistically** (don't forget this), it would

be

$$\begin{aligned}
\frac{d\mathbb{N}_{mix}^{AB'}}{d\Delta\phi} &= N^A \int \frac{dp^A}{d\phi^A} \epsilon^A(\phi^A) d\phi^A \\
&\quad \cdot n^{B'} \int \frac{dp^{B'}}{d\phi^{B'}} \epsilon^{B'}(\phi^{B'}) \delta(\text{PA}(\phi^A - \phi^{B'}) - \Delta\phi) d\phi^{B'} \\
&= N^A \cdot n^{B'} \cdot g(\Delta\phi) \\
&= N^{evt} n^A n^{B'} \cdot g(\Delta\phi) \\
&= N^{evt} n^{AB'} \cdot g(\Delta\phi)
\end{aligned} \tag{A.17}$$

And the per event

$$\frac{d\mathbb{N}_{mix}^{AB'}}{d\Delta\phi} = n^{AB'} \cdot g(\Delta\phi) \tag{A.18}$$

Here, we define a function g as

$$\boxed{g(\Delta\phi) \triangleq \int \frac{dp^A(\phi^A)}{d\phi^A} \epsilon^A(\phi^A) d\phi^A \int \frac{dp^{B'}}{d\phi^{B'}} \epsilon^{B'}(\phi^{B'}) \delta(\text{PA}(\phi^A - \phi^{B'}) - \Delta\phi) d\phi^{B'}} \tag{A.19}$$

When we compare $f(\Delta\phi)$ with $g(\Delta\phi)$, we would find that they are pretty similar to each other. If we can make $\epsilon^{B'}$ the same as ϵ^B , and make $\frac{dp^{B'}}{d\phi^{B'}}$ independent of $\phi^{B'}$, then we can easily use $g(\Delta\phi)$ to replace $f(\Delta\phi)$. This is the reason why we wanted to choose B' the same class of particle as B , i.e., the same particle type h^\pm , similar p_T , similar event vertex. Also, the other key part is that $\frac{dp^{B'}}{d\phi^{B'}}$ should be flat in ϕ , which requires a well sampled mixed events. At least, we should have a large enough sample to ensure this. Then one of our QA should be monitoring this quantity $\frac{dp^{B'}(\phi^{B'})}{d\phi^{B'}}$ to be flat.

$$\boxed{\frac{dp^{B'}(\phi^{B'})}{d\phi^{B'}} = \text{const.}} \tag{A.20}$$

The true physics distribution, $\frac{dn^A}{d\phi^A}$ and $\frac{dn^B}{d\phi^B}$, should be isotropic, however the trigger in experiments might break it. In our analysis, we are interested in rare physics events, such as high p_T jet events, direct photon events, so besides the Minimum

Bias trigger, we utilize the ERT trigger, which trigger event recording by the combination of high energy hits in EMCal and RICH detectors. Therefore, the ERT trigger tends to select more events in or close to the acceptance of EMCal and RICH in the central arm. This causes a bias in the azimuthal angle distribution of both A and B . Based on Equation A.20, we need our B' 's distribution on ϕ to be flat. To achieve this, we have to choose B' from events triggered by the Minimum Bias trigger. And for each trigger A , we mix it with a large number of Minimum Bias events to make sure that the sample is large enough and the sample's ϕ distribution is flat. Therefore, we should keep an eye on the number of triggers, or particle A , which should be an indication of the size of B' sample. By an alternative method, we can increase the number of events to mix with for the runs that has fewer triggers. And we should be able to tell the necessary number of events to mix with if we want the relative error of the acceptance correction function to be within some extent.

There is one more thing we should be cautious. The efficiency ϵ fluctuates between runs and changes with time. The acceptance correction, $f(\Delta\phi) \sim g(\Delta\phi)$, should be applied based on the efficiency. Meanwhile, if the number of A is limited in a run, $\frac{dn^A}{d\phi^A}$ could fluctuate quite a lot between runs. These factors make the desired acceptance correction much different. The best strategy is to apply the acceptance correction separately for individual run. However, this strategy suffers from the statistics, which makes $\frac{dn^{B'}}{d\phi^{B'}}$ in each run not perfectly flat, or we have to mix a trigger with a very large number of mixed events. A practical way would be grouping runs by the closeness of their efficiency and the particle A 's ϕ distribution, then applying the acceptance correction for each run group. This should balance the two seemingly contradictory requirements (efficiency + $\frac{dn^A}{d\phi^A}$ closeness versus statistics). To ensure the sample size, we may simply reject runs with a small number of n 's, or

say, A 's, if we fix the number of events to mix with one trigger. To ensure the closeness of efficiency, we can monitor $\frac{dn^{B'}}{d\phi^{B'}}$ for each runs in a run group. Because if we got enough statics, or say $\frac{dn^{B'}}{d\phi^{B'}}$ was close to flat, then the similarity of $\frac{dn^{B'}}{d\phi^{B'}}$ reflects the similarity of $\epsilon^{B'}$. The other way to verify $\epsilon^{B'}$ is to look into the overall distribution of B' in the Minimum Bias events for each run, which means looking into the distribution in the partner data (singles TTree) in each run. For $\frac{dn^A}{d\phi^A}$ and ϵ^A , this could be taken care of by monitoring $\frac{dn^A}{d\phi^A}$ of each run in a run group.

By requiring $\frac{dn^{B'}}{d\phi^{B'}}$ of each run is close to the overall average, such as requiring the ratio to be within [90%, 110%], it won't ensure a correct acceptance correction for a run. Because a different $\frac{dn^A}{d\phi^A}$ or ϵ in that run should make the acceptance correction deviated from the average.

APPENDIX B: MEAN AND VARIANCE ESTIMATION IN HISTOGRAMS

The statistics calculation could be performed in histograms with precision, if the binning is fine enough or the statistics (bin content) in bins are high.

Considering a histogram, whose X axis is x , contain bins starting from 1 to K , we could label a bin with $i \in [1, K]$, the bin content of bin i is N^i , and the total bin content is $N \equiv \sum_1^K N^i$. The filled x quantities are denoted by x_j^i , as the diagram shown below.

$$\underbrace{1, \dots, x_j^1, \dots, x_{N^1}^1}_{N^1} \quad \dots \quad \underbrace{x_1^i, \dots, x_j^i, \dots, x_{N^i}^i}_{N^i} \quad \dots \quad \underbrace{x_1^K, \dots, x_j^K, \dots, x_{N^K}^K}_{N^K}$$

$\underbrace{\hspace{15em}}_N$

Then the mean $\mu \equiv \bar{x}$ is defined as

$$\mu \equiv \bar{x} \triangleq \frac{1}{N} \sum_{i=1}^K \sum_{j=1}^{N^i} x_j^i \quad (\text{B.1})$$

Here, x_j^i is the x value of the j th element in bin i .

$$\mu \equiv \bar{x} \triangleq \frac{1}{N} \sum_i \sum_j x_j^i \quad (\text{B.2})$$

$$= \frac{1}{N} \sum_i N^i \left(\frac{1}{N^i} \sum_j x_j^i \right) \quad (\text{B.3})$$

$$= \frac{1}{N} \sum_i N^i \mu^i \quad (\text{B.4})$$

$$= \sum_i \left(\frac{1}{N} N^i \right) \mu^i \quad (\text{B.5})$$

$$= \sum_i w^i \mu^i \quad (\text{B.6})$$

Here we define

$$\mu^i \triangleq \frac{1}{N^i} \sum_j x_j^i \quad (\text{B.7})$$

$$w^i \triangleq \frac{N^i}{N} \quad (\text{B.8})$$

and

$$\text{Var}^i \triangleq \frac{1}{N^i} \sum_{j=1}^{N^i} (x_j^i - \mu^i)^2 \quad (\text{B.9})$$

The variance $\text{Var} \triangleq \overline{(x - \mu)^2}$ is

$$\text{Var} \triangleq \overline{(x - \mu)^2} = \frac{1}{N} \sum_i \sum_j (x_j^i - \mu)^2 \quad (\text{B.10})$$

$$= \frac{1}{N} \sum_i \sum_j (x_j^i - \mu^i + \mu^i - \mu)^2 \quad (\text{B.11})$$

$$= \frac{1}{N} \sum_i \sum_j [(x_j^i - \mu^i)^2 + (\mu^i - \mu)^2 + 2(\mu^i - \mu)(x_j^i - \mu^i)] \quad (\text{B.12})$$

$$= \frac{1}{N} \sum_i \left[\sum_j (\mu^i - \mu)^2 + \sum_j 2(\mu^i - \mu)(x_j^i - \mu^i) + \sum_j (x_j^i - \mu^i)^2 \right] \quad (\text{B.13})$$

$$= \frac{1}{N} \sum_i \left[N^i (\mu^i - \mu)^2 + 2(\mu^i - \mu) \sum_j (x_j^i - \mu^i) + \sum_j (x_j^i - \mu^i)^2 \right] \quad (\text{B.14})$$

$$= \frac{1}{N} \sum_i [N^i (\mu^i - \mu)^2 + 0 + N^i \text{Var}^i] \quad (\text{B.15})$$

In the last step we use the definition of μ^i and Var^i . Then we get

$$\text{Var} = \frac{1}{N} \sum_i [N^i (\mu^i - \mu)^2 + N^i \text{Var}^i] \quad (\text{B.16})$$

$$= \sum_i [w^i (\mu^i - \mu)^2 + w^i \text{Var}^i] \quad (\text{B.17})$$

If the bin width is small enough or the bin content is large enough, we should be able to model the distribution inside a bin by a uniform distribution. Then μ^i is the i th bin center, and Var^i is $\frac{1}{12} \cdot (\text{BinWidth}^i)^2$. Let's look at our assumption in a simple example, the distribution inside a bin is a linear function, $x \in [a, b]$, and

$\frac{dN}{dx} = f(x) = C_1x + C_0$. The mean in the bin is

$$\mu = \frac{\int_a^b (C_1x + C_0)x dx}{\int_a^b (C_1x + C_0) dx} \quad (\text{B.18})$$

$$= \frac{\left(\frac{C_1}{3}x^3 + \frac{C_0}{2}x^2\right)\Big|_a^b}{\left(\frac{C_1}{2}x^2 + C_0x\right)\Big|_a^b} \quad (\text{B.19})$$

$$= \frac{\frac{C_1}{3}(b^3 - a^3) + \frac{C_0}{2}(b^2 - a^2)}{\frac{C_1}{2}(b^2 - a^2) + C_0(b - a)} \quad (\text{B.20})$$

$$= \frac{\frac{C_1}{3}(a^2 + b^2 + ab) + \frac{C_0}{2}(a + b)}{\frac{C_1}{2}(a + b) + C_0} \quad (\text{B.21})$$

$$(\text{B.22})$$

Now we take a look at the difference between the actual mean and the one from an uniform distribution, then compare it with the typical size of x , or say, compare it with $b - a$ to evaluate the relative error of our mean estimation.

$$\Delta_\mu = \mu - \frac{a + b}{2} \quad (\text{B.23})$$

$$= \frac{\frac{C_1}{3}(a^2 + b^2 + ab) + \frac{C_0}{2}(a + b)}{\frac{C_1}{2}(a + b) + C_0} - \frac{\frac{C_1}{4}(a^2 + 2ab + b^2) + \frac{C_0}{2}(a + b)}{\frac{C_1}{2}(a + b) + C_0} \quad (\text{B.24})$$

$$= \frac{\frac{C_1}{12}(a + b)^2 - \frac{C_1}{3}ab}{\frac{C_1}{2}(a + b) + C_0} \quad (\text{B.25})$$

$$= \frac{\frac{C_1}{12}(b - a)^2}{\frac{C_1}{2}(a + b) + C_0} \quad (\text{B.26})$$

and

$$\frac{\Delta_\mu}{b - a} = \frac{\frac{C_1}{12}(b - a)}{\frac{C_1}{2}(a + b) + C_0} \ll 1 \quad (\text{B.27})$$

$$\Leftrightarrow \quad (\text{B.28})$$

$$\frac{C_1}{12}(b - a) \ll \frac{C_1}{2}(a + b) + C_0 \quad (\text{B.29})$$

$$\Leftrightarrow \quad (\text{B.30})$$

$$b - a \ll \frac{a + b}{2} + \frac{C_0}{C_1} \quad (\text{B.31})$$

This would be satisfied if the binning is fine enough (\sim small $b - a$) or we have a pretty evenly distribution (\sim small C_1) or we have large statistics (\sim large C_0) or large x (\sim large $(a + b)/2$).

One more thing is notable for the estimation of variance. We may apply Bessel's correction for an unbiased estimation of the sample's variance to account that we don't have the true mean, or say one less degree of freedom.

INDEX

Symbols

β -Function, 27

η Acceptance Correction, 115

ϕ Acceptance Correction, 96

$\sqrt{s_{NN}}$, 32

v_2 , *see also* v_n

v_3 , *see also* v_n

v_n , 34

I_{dA} , *see also* Nuclear Modification Factor

N_{coll} , 85

N_{part} , 85

p_T , *see also* Transverse Momentum

R_{dA} , *see also* Nuclear Modification
Factor

RI , 159

k_T Broadening, *see* k_T Effect

k_T Effect, 49

z_T , 157

5-7 \otimes 5-7 GeV/ c , 158

A

ABS, *see also* Absolute Subtraction

Absolute Subtraction, 98

ALICE, 51

Alternating Gradient Synchrotron, AGS,
32

Anti-Shadowing Effect, 44

Asymptotic Freedom, 27

ATLAS, 16

B

BBC, Beam-Beam Counter, 62

Bjorken Scaling, 21

Bjorken Scaling Variable x , 21

Brookhaven National Laboratory, BNL,
32

C

Callan-Gross Relation, 21

Centrality, 65

d +Au Centrality, 85

CMS, 16

Cold Nuclear Matter Effect, CNM effect,
39

Color, 20

Color Glass Condensate, 47

Combinatorial Hough Transform, CHT,
72

Combinatoric Background of π^0

Reconstruction, 102

Correlation Function, 95

Cosmic Microwave Background, 32

Coupling Constant

QCD, 26

Covariant Derivative, Gauge Covariant

Derivative, 24

Cronin Effect, 45

D

DC, Drift Chamber, 70

Deep Inelastic Scattering, DIS, 19

Drell-Yan Process, 41

E

Elementary Particles, 15

Elliptical Flow, 33

EMC Effect, 44

EMCal, EMC, Electromagnetic

Calorimeter, 73

Energy Loss, 37

ERT, 67

European Organization for Nuclear

Research, CERN, 32

Event Trigger, 67

F

Factorization Theorem, 29

Fermi Motion, 45

Fine Structure Constant, α , 20

Form Factor, 21

G

Gauge Boson, 15

Gauge Field, 24

Glauber Model, 65

Gluon Field, 24

Gluon Saturation, 47

H

Heavy Ion Collider, 32

Heavy Ion Collision, 32

Higgs Boson, 15

Higgs Mechanism, 17

HIJING, 192

I

Isospin, 18

J

Jet, 21

Jet Function, 97

Jet Quenching, 37

- Jet Width
- Fitting Method, 115
 - RMS Method, 148
- L**
- Lagrangian Density
- Gluon, 25
 - QCD, 25
 - Quark, 22
 - Yukawa Theory, 18
- Large Hadron Collider, 33
- Lattice QCD, LQCD, 30
- Lawrence Berkeley National Laboratory, LBNL, 32
- Leading Order Approximation, LO, 48
- Lepton, 15
- LHC, *see also* Large Hadron Collider
- Longitudinal Momentum Fraction x , *see also* Bjorken Scaling Variable x
- M**
- MB, 67
- Mean-Seeds Mean-Partner, 98
- MPC, Muon Piston Calorimeter, 76
- MSMP, *see also* Mean-Seeds Mean-Partner
- Muon Piston Calorimeter, MPC, 55
- N**
- Neutrino, 15
- Next-to-Leading Order, NLO, 49
- Nuclear Modification Factor
- I_{AA} , 37
 - R_{AA} , 37
- Nuclear Parton Distribution Function, nPDF, 41
- P**
- Partner, 91
- Parton, 40
- Parton Distribution Function, 41
- PC, Pad Chamber, 72
- Perturbative QCD, pQCD, 29
- PHENIX, 61
- Photonmultiplier Tube, 62
- PMT, *see also* Photonmultiplier Tube
- PYTHIA, 178
- Q**
- QCD Scale, 28
- QGP, *see also* Quark-Gluon Plasma
- Quantum Chromodynamics, 17
- Quantum Chromodynamics, QCD, 17
- Quantum Electrodynamics, QED, 17
- Quantum Field Theory, QFT, 17

- Quark, 15
- Quark Model, 19
- Quark-Gluon Plasma, 30
- R**
- Radiative Energy Loss, 46
- Rapidity Acceptance Correction, *see also*
 η Acceptance Correction
- Reaction Plane, 34
- Relativistic Heavy Ion Collider, 60
- RHIC, *see also* Relativistic Heavy Ion
 Collider
- RI, *see also* RI
- RICH, Ring Imaging Cherenkov
 Detector, 76
- RMS, *see also* Root of Mean Square
- Root of Mean Square, 148
- Run Number, 102
- Running Coupling, 27
- S**
- Shadowing Effect, 42
- Side Band Analysis, 103
- Spontaneous Symmetry Breaking, 17
- sQGP, *see also* Strongly Coupled
 Quark-Gluon Plasma
- Standard Model, 15
- Strongly Coupled Quark-Gluon Plasma,
 33
- Super Proton Synchrotron, SPS, 32
- Surface Bias, 38
- T**
- Transverse Momentum, 48
- Trigger
 Trigger Condition, 62
 Trigger Particle, 91
- Two Particle Correlation, 91
- Type A, B, C Systematic Uncertainty,
 126
- Y**
- Yang-Mills Theory, 22
- Z**
- ZDC, Zero Degree Calorimeter, 64
- Zero Yields at Minimum, 98
- ZYAM, *see also* Zero Yields at Minimum